NASA/CR—2000-210672

Mixing and NOx Emission Calculations of Confined Reacting Jet Flows in Cylindrical and Annular Ducts

Victor L. Oechsle and Christopher H. Connor
Allison Engine Company, Indianapolis, Indiana

December 2000

The NASA STI Program Office . . . in Profile

Since its founding, NASA has been dedicated to the advancement of aeronautics and space science. The NASA Scientific and Technical Information (STI) Program Office plays a key part in helping NASA maintain this important role.

The NASA STI Program Office is operated by Langley Research Center, the Lead Center for NASA's scientific and technical information. The NASA STI Program Office provides access to the NASA STI Database, the largest collection of aeronautical and space science STI in the world. The Program Office is also NASA's institutional mechanism for disseminating the results of its research and development activities. These results are published by NASA in the NASA STI Report Series, which includes the following report types:

- TECHNICAL PUBLICATION. Reports of completed research or a major significant phase of research that present the results of NASA programs and include extensive data or theoretical analysis. Includes compilations of significant scientific and technical data and information deemed to be of continuing reference value. NASA's counterpart of peer-reviewed formal professional papers but has less stringent limitations on manuscript length and extent of graphic presentations.

- TECHNICAL MEMORANDUM. Scientific and technical findings that are preliminary or of specialized interest, e.g., quick release reports, working papers, and bibliographies that contain minimal annotation. Does not contain extensive analysis.

- CONTRACTOR REPORT. Scientific and technical findings by NASA-sponsored contractors and grantees.

- CONFERENCE PUBLICATION. Collected papers from scientific and technical conferences, symposia, seminars, or other meetings sponsored or cosponsored by NASA.

- SPECIAL PUBLICATION. Scientific, technical, or historical information from NASA programs, projects, and missions, often concerned with subjects having substantial public interest.

- TECHNICAL TRANSLATION. English-language translations of foreign scientific and technical material pertinent to NASA's mission.

Specialized services that complement the STI Program Office's diverse offerings include creating custom thesauri, building customized data bases, organizing and publishing research results . . . even providing videos.

For more information about the NASA STI Program Office, see the following:

- Access the NASA STI Program Home Page at ***http://www.sti.nasa.gov***

- E-mail your question via the Internet to help@sti.nasa.gov

- Fax your question to the NASA Access Help Desk at 301–621–0134

- Telephone the NASA Access Help Desk at 301–621–0390

- Write to:
  NASA Access Help Desk
  NASA Center for AeroSpace Information
  7121 Standard Drive
  Hanover, MD 21076

NASA/CR—2000-210672

Mixing and NOx Emission Calculations of Confined Reacting Jet Flows in Cylindrical and Annular Ducts

Victor L. Oechsle and Christopher H. Connor
Allison Engine Company, Indianapolis, Indiana

Prepared under Contract NAS3–25950, Task Order 1

National Aeronautics and
Space Administration

Glenn Research Center

December 2000

Acknowledgments

This work was supported by NASA Contract NAS3–25950, Task Order #1.

Document Availability Change Notice

This document was published in December 2000 with an EAR restriction.
It was changed April 2003 to Unclassified/Unlimited per DAA modified February 10, 2003.

Per the STI Program Office and Code I at Headquarters,
you may modify copies in your possession. The restriction notice
on the cover, title page, and report documentation page, should be
boldly crossed out and the above statement printed clearly above or below it.

Note that at the time of research, the NASA Lewis Research Center
was undergoing a name change to the
NASA John H. Glenn Research Center at Lewis Field.
Both names may appear in this report.

Available from

NASA Center for Aerospace Information
7121 Standard Drive
Hanover, MD 21076

National Technical Information Service
5285 Port Royal Road
Springfield, VA 22100

Available electronically at http://gltrs.grc.nasa.gov

Table of Contents

Nomenclature

A	area
AN	annular mixer abbreviation
AN-Stag	annular mixer geometry with staggered orifice configuration inner/outer wall
A_m	duct cross-sectional area, also A_{tot}, in^2
ACd	also A_j, effective orifice area, in^2
Ar	area ratio (jet/mainstream) = A_j/A_m = ACd/A_m
AMIX	area weighted overall T or ϕ deviation from stoichiometry, Eq 6
B	area determined half width of the distribution function
CIR	circular mixer abbreviation
d	diameter of the orifice, inch
Do	outer diameter of the mixer, inch
DR	density ratio (jet/mainstream)
DP/P	total pressure loss across the mixing wall, %
EINOx	global NOx EI
f	non-dimensional equivalence ratio, Eq 5
f/a	fuel to air ratio
HO	configuration nomenclature (hole-optimization)
j	radial vector direction
J	momentum-flux ratio (jet/mainstream) = M^2/DR, also $(MR)^2/[(DR)(A_j/A_m)^2]$
k	tangential vector direction
L	orifice length, inch (longest dimension of the slot)
m_{tot}	overall mixer mass flowrate, lbm/sec = $m_{jet} + m_{main}$
M	mass flux ratio (jet/mainstream) = DR V_{jet} /U_{main}
MMIX	mass flow weighted overall T or ϕ deviation from equilibrium, Eq 7
MR	mass flowrate ratio (jet/mainstream)
P	total pressure, atm
Pen r/R	non-dimensional jet penetration from the outer wall of the mixer
R	radius of the mixing section, inch
r	radial distance from the centerline of the mixer, inch
S	orifice spacing in the circumferential direction, inch
T	temperature, R
T.E. x/R	orifice trailing edge axial location (for the circular mixer)
T.E. 2x/H	orifice trailing edge axial location (for the annular mixer)
u	local axial velocity, ft/sec
U_{main}	approach mainstream axial velocity, ft/sec
VR	velocity ratio (jet/mainstream) =V_{jet} / U_{main}
V_{jet}	radial velocity of the jet, ft/sec
W	orifice width, inch, (shortest dimension of the slot)
x	axial distance from the leading edge of the orifice, inch
ρ	fluid density, lbm/ft^3
ϕ	equivalence ratio $(f/a)_{local}$ / $(f/a)_{stoi}$

Subscripts

equil	equilibrium
j	jet
LZ	lean-zone
m	mainstream, also (main)
RZ	rich-zone
stoi	stoichiometric

Introduction

The design and development of gas turbine engines for the aeropropulsion and ground based power generation systems has been directed towards decreasing the gaseous emissions without adversely affecting the system performance. The environmental effects of carbon monoxide (CO), oxides of nitrogen (NOx), and unburned hydrocarbon fuels have been investigated extensively for many years and their potential hazards are increasingly becoming a more world wide sensitive issue. In specific, the effect of the NOx emissions on the environmental structure of our planet demands close attention due to the present ozone layer depletion discoveries.

The advancement in the gas turbine engine design has been channeled towards increasing both engine pressure ratio and rotor inlet temperature levels in order to increase the overall thermodynamic cycle efficiency thus reducing the specific fuel consumption. However, this effort has been adversely affecting both engine durability and gaseous emissions, especially that of NOx which is generally directly proportional to the cycle temperature in air breathing engines. The production of oxides of Nitrogen (generally classified into both NO and NO_2 gas emissions) are generally a function of the combustion system design, hot section temperature distribution, residence time, and localized fuel/air mixture. The NOx emission in a gas turbine engine can be divided into two main types: a) prompt NOx, which is generally associated with low temperature and fuel-rich mixtures and generally occurring early in the combustion typically near the fuel injector and primary zone of the combustion liner, and b) thermal NOx which is dominated with the available dissociated Oxygen atoms from the air mixed with the fuel. The thermal NOx is generally the highest NOx production in a typical gas turbine engine specifically in non-premixed diffusion flame combustion systems.

The development of an efficient and low-emission high speed civil transport combustion system demands increased insight in combustion chemical kinetics, efficient air/fuel mixture, and advanced materials and cooling techniques. The combustion liner cooling air flowrate significantly affects the combustion process by quenching the flame at localized regions near the wall thereby producing CO and also producing localized hot spots which increase the production of NOx. Current gas turbine combustion liner technology employs a single-stage combustion process in which both fuel and air are admitted into a controlled mixing chamber and are allowed to react. With the advent of higher temperature operating conditions, the reduction of NOx becomes a very difficult task to accomplish using single axial staged combustion. Therefore, alternative combustion methods are being explored by the main gas turbine engine manufacturers and other research organizations. Two of the main low NOx designs being developed are axially multistage combustion rich-burn/quick-mix/lean-burn (RQL), and lean premixed prevaporized (LPP). Both have advantages and disadvantages regarding operation range and hardware complexity.

In this report, the advantages and limitations of the RQL design are being explored by focusing on the performance of the quick-mix region where generally most of the thermal NOx is produced. The successful performance of the RQL combustor depends on a quick and efficient mixing of the rich zone combustion products with compressor discharge air to effectively reduce the overall and localized equivalence ratio from about 1.8 to about 0.5. This

process must be accomplished with a minimum transient time (at or near equivalence ratio of 1) where most of the NOx is produced due to the high resulting temperature levels and Oxygen availability.

An experimental and analytical effort (e.g. Bain, Smith, and Holdeman, 1992, 1993, and 1994; Doerr and Hennecke, 1993; Doerr, 1994; Doerr, Blomeyer, and Hennecke, 1995; Hatch, et al., 1992a and 1992b; Hatch, Sowa, and Samuelsen, 1994; Howe, et al., 1991; Kroll, et al., 1993; Kroll, Sowa, and Samuelsen, 1995; Liscinsky et al., 1992; Liscinsky, Vranos, and Lohmann, 1993; Liscinsky, True, and Holdeman, 1993, 1994, and 1995; Oechsle, Mongia, and Holdeman, 1992, 1993, and 1994; Oechsle, 1995; Oechsle and Holdeman, 1995; Smith, Talpallikar, and Holdeman, 1991; Sowa, et al., 1994); Talpallikar, et al., 1991; Vranos, et al., 1991; and Zhu and Lai, 1992) is underway to study and identify the critical design and flow parameters affecting the mixing effectiveness and its impact on NOx formation.

The overall scope of this program is to analyze several mixing configurations numerically and assess the major design parameters in order to apply this technology for the design of future RQL combustion systems for use in a high speed civil transport. This program is a 5 year NASA funded program in which over 100 different mixing configurations have been numerically analyzed spanning the domain of both non-reacting and reacting flowfields and both circular and annular mixing configurations.

In the first stage of the program, 21 different non-reacting cases were summarized using a circular mixing geometry. This study by Oechsle, Mongia, and Holdeman, (1992) indicates that mixing flowfield significantly depends of the operating conditions. Several orifice types and operating conditions were investigated in this study. The mixing uniformity of the flowfield also is significantly changed by the penetration of the jets. Large unmixed regions were found behind the orifice. This was a liability in a circular mixer design which tended to produce rich pockets of mixture and high quantities of NOx. The study in Oechsle, Mongia, and Holdeman, (1992) was performed in a purely non-reacting environment.

Following the 1992 study, a second study by Oechsle, Mongia, and Holdeman, (1993) was made to compare the predicted results with experimental data obtained by the University of California at Irvine by Hatch, et al. (1992a and b). This parallel numerical-experimental study allowed a detailed comparison of both methods to determine their strengths and weaknesses. The results show that the general trends are similar for the experimental and numerical data, however, mixedness was generally more developed in the experimental data and steeper gradients were more characteristic of the numerical results. These results also showed that the effect of orifice geometry on the mixing flowfield and jet penetration for the measured results compared favorably to the numerically obtained values. It was also established that the mixing flowfield in both the numerical and experimental results would be inherently different since the initial conditions for both are different. In the numerical simulation, the jet and mainstream mass injections are uniformly distributed throughout the entire injection area. Velocity, temperature, and mass fraction are uniform across the entire injection area. This was not obtained physically in the experimental setup. It is also important to consider that the inlet turbulence levels also significantly affect the mixing profile, and though these levels were not measured in the experimental setup, it is assumed that they are generally different than the standard values used in the numerical approach. Furthermore, more accurate comparisons of numerical and experimental results necessitate the need to clearly quantify and reproduce as much as possible

the initial conditions obtained in the experimental setup before duplicating them in the numerical model since it is believed that the reverse will be more difficult to accomplish.

In the following phase of the program, a comparison of the mixing flowfields in both reacting and non-reacting environments are shown in Oechsle, Mongia, and Holdeman, (1994). These results indicate good agreement in the conserved scalar fields in both reacting cases and non-reacting cases with similar orifice configurations and operating conditions. It was also evident from these results that the pockets of stoichiometric mixture near the outer wall behind the orifice were present in both reacting and non-reacting numerical calculations which verifies the results of the previous two studies. The statistical mixing non-uniformity parameters correlated with the observational data in predicting the best mixing configuration.

In the following study Oechsle, and Holdeman, (1995), eighteen different circular mixing configurations were analyzed in a fully reacting environment at actual engine altitude cruise operating condition. The results indicate that the mixing uniformity, as defined statistically, did not correlate with NOx production trends. The expected results indicates that better mixing of the mainstream flow and crossflow jets would yield an increase in temperature uniformity which consequently leads to lower NOx production. These expectations are however skewed by the way the mixing uniformity is quantified. In the above mentioned study, the mixing non-uniformity depends on the deviation from the equilibrium equivalence ratio value. This definition does not consider the deviation from the stoichiometric equivalence ratio value where most of the NOx is presumed to be produced. The results also indicate that the round orifices produce less NOx at low J conditions (J=25) and that slanted slots produce less NOx at higher J conditions (J=52, 80). Therefore, jet penetration which is significantly affected by the orifice shape has a strong impact on the NOx production.

In the present study, a 3-D numerical CFD code is used to predict the performance of an RQL mixing section. The mixing flowfield of several different mixer configurations are evaluated and compared with their corresponding NOx predictions. The objectives of this study are the following:

1) To compare the NOx production performance for both annular and circular mixing sections operating at similar conditions and with similar orifice geometries.

2) to vary the number of orifices per row in the circular mixer to minimize the NOx production for both round and slanted slot orifices at a given J condition, and

3) to understand the locations for high NOx production in both annular and circular mixing configurations.

Sixty different mixer configurations were analyzed with the 3-D numerical CFD code and the localized NOx production and overall mixer NOx production flowrate were calculated for each case. The NOx predictions were made by sub-dividing the overall mixing domain into smaller sectors. The local NOx value therefore represents the NOx production flowrate per unit volume (g of NOx per sec per m^3) since all the sectors which make the mixer domain are not sized equally. The mixer configurations include round holes and elongated slots with aspect ratio of L/W=4. Slots were modeled at both 0 degrees (aligned with the flow) and 67.5 degrees. The jet to mainstream momentum-flux ratio was maintained at 52 for all configurations.

Boundary conditions simulate the high speed civil transport gas turbine altitude cruise condition. An analysis was carried out to rank the mixer configurations with respect to both degree of mixing and NOx production. The mixing non-uniformity was redefined with respect to the stoichiometric equivalence ratio instead of the equilibrium value to investigate whether the mixing flowfield correlates with the NOx production.

Mathematical Model

3-D Flow Model

A production 3-D combustor code, COM-3D (Bruce, Mongia, and Reynolds, 1979) is used that solves the turbulent reacting flow transport equations using the SIMPLE algorithm of Patankar and Spalding (Patankar, 1980). This program simulates turbulence by the two-equation k-ε model (Launder and Spalding, 1974), and combustion following vaporization is determined by a four-step chemical reaction model based on Arrhenius and modified eddy breakup concepts. The transport equations for all dependent variables are of the following form as shown in Eq-1:

$$div\left[\rho_r u\xi - \left(\frac{\mu_{eff}}{P_r}\right) grad(\xi)\right] = S_\xi \tag{1}$$

where ρ_r is the mixture density, u is the velocity, μ_{eff} is the effective turbulent viscosity, P_r is the effective Prandtl/Schmidt number, and S_ξ is the source term for the variable ξ. The following variables are computed by COM-3D: 1) axial, radial, and swirl velocity components; 2) specific enthalpy and temperature; 3) turbulence kinetic energy and dissipation rate; 4) unburned fuel, CO, H_2, intermediate fuel, and composite fuel mass fractions; and 5) fuel spray trajectory and evaporation rate.

The computational effort is significantly reduced by modeling a sector of the mixing section comprising a single orifice (or dual, generally opposed, orifices as applied to the annular mixing configurations). Therefore, the shape of the sector was dependent on the number of orifices equally spaced in the circumferential direction. Periodic boundary conditions were applied in the circumferential direction. No-slip and adiabatic boundary conditions were applied at the outer and inner walls defining the mixing section. Zero-gradient boundary conditions were applied at the center axis as applied to the circular mixers only. Axial gradients at the exit boundary condition were assumed zero.

NOx model

The NOx model described herein was developed by Rizk and Mongia (1993). Because NOx formation in the combustion liner is significantly affected by the details of the front end of the RQL and the subsequent admittance of air into the various downstream zones, the combustion liner needs to be divided into a number of regions for modeling purposes. The hybrid modeling technique therefore consists of using the 3-D simulation results obtained with COM-3D such as gas flowrate, flow averaged temperature, fuel/air ratio, in addition to the turbulence characteristics to accurately describe the flow nuances affecting the NOx production.

The NOx model is subdivided into three main zones: rich zone, mixing zone and lean zone. Each of these zones exhibit significantly different characteristics as to their role in the NOx production in an RQL combustion liner. Lefebvre (1984) shows that the exhaust concentration of NOx can be calculated in terms of mean time in the combustion zone, chemical reaction rates, and mixing rates. Mellor (1976) describes a model that combines a number of perfectly stirred reactors and uses finite-rate mechanisms to calculate NOx. Furthermore, Fletcher and Heywood (1971) modeled the combustor primary zone as a partially stirred reactor burning gaseous fuel over a distribution about the primary zone equivalence ratio, a lateral mixing reactor, and a plug flow reactor. Based on these studies it is clear that NOx production characteristics in an RQL combustor required a detailed model of the mixing flow phenomena along with detailed description of the chemical kinetics in the flame reaction zone. The model used in this study subdivides the RQL combustor into the following zones: 1) rich zone made up of two parallel reactors: a stoichiometric reactor to account for the combustion at near-stoichiometric conditions and a rich zone feed. 2) Mixer air is admitted consecutively into the quench zone to form plug flow reactor, and 3) dilution air is admitted into the dilution zone to form a secondary plug flow reactor similar to that of the quench zone. To provide an accurate estimate of the trends of formation and reduction of NOx, the detailed reaction model developed by Westbrook and Pitz (1984), was combined with extended Zeldovich mechanisms for NOx. The detailed description of the mixing zone model will follow. Both rich and lean zone design is categoric at this stage and assumptions about the modeling of these two are made as follows:

1) The input flow field entering the quench zone is assumed to be fully reacted and in equilibrium. The species mole fractions for (CO, CO_2, H_2O, and H_2) were determined based on the given rich-zone equivalence ratio at chemical equilibrium at the prescribed operating conditions using JP-5 for the typical fuel properties. This assumption may not be totally realistic in an actual operating RQL rich section since more CO and unburned hydrocarbon emissions are expected as compared to this simplified rich zone model. The additional emissions are also expected to affect the mixing zone reaction prompted by the mixture of the rich zone products with additional air. However, since the rich-zone performance is not within the scope of this study, the assumed simplified rich-zone model (achieving chemical equilibrium) is a reasonable initial condition towards analyzing the reaction in the mixing zone. In addition, it provides a baseline initial condition which can be applied to all configurations equally since it is assumed that the rich zone and mixing zone performance are generally coupled and the variation of one may significantly affect the performance of the other. The four species used in the inlet mainstream condition correspond to the four-step chemical reaction used in COM-3D.

2) No expansion is assumed in the lean zone and no area contraction is applied to the mixing section. The RQL liner is usually designed with an area expansion downstream of the quench zone in order to increase the residence time to further oxidize the CO produced in the rich zone. In addition, no air is added in the lean zone downstream of the quench zone.

Based on these assumptions, the hybrid model was applied to the quench zone only.

Mixing zone model.

The kinetic scheme results for the quench zone reactor show that a substantial increase in NOx formation occurs as the residence time in the reactor is increased. The results obtained at a number of pressure levels and rich zone equivalence ratios have been correlated as follows:

$$NO_q\ (g/kg) = 1.57E7\ \tau_q^{nq} e^{\left\{\frac{-38,000}{T_q}\right\}} P^{0.2} \qquad (2)$$

T_q is the reaction temperature in the quench reactor, in K, and τ_q the residence time in the reactor in ms. The exponent nq is given in terms of the rich zone equivalence ratio ϕ_r as follows:

$$nq = 0.834\phi_r^{-0.36} \qquad (3)$$

The hybrid model consists in grouping the results obtained from a typical COM-3D grid with about 50,000 to 150,000 nodes into about 2,000 larger sub-volumes comprising of several computational nodes representing the entire mixing section of an RQL combustion liner. By this means, the reacting flow model results can be accurately represented and modeled using significantly less computational effort. For the NOx predictions only, the model of the quench zone extends to x/R= 2x/H = 5 since the domain beyond the quench zone was not considered to be a realistic lean zone model for the given correlations. This was implemented to prevent any unrealistic discontinuities in the predictions near the real interface between the quench and lean zones (x/R= 2x/H =1) where x is the downstream axial distance from the leading edge of the orifice and R is the mixer radius (for circular) and H is the annulus height (for annular).

Geometric Configuration

Two potential design considerations for the hot section component of the high speed civil transport engine are the circular and annular RQL combustion liners. In a typical RQL combustion liner, the rich zone, quench zone, and lean zones are axially inter-connected with an area contraction in the mixing section to speed up mixing by increasing the mainstream momentum flux. The configuration details of the mixing configurations follow. The details of each of the 60 configurations are shown in Tables-1 and 2.

Circular mixer description

The mixing section was modeled as a constant cross-sectional area throughout the axial direction with a single row of equally spaced orifices in the outer wall. The outer wall diameter is 3 inches (0.076 m) and the axial length of the mixing section extended from x/R=-1.4 to x/R=6. Sufficient axial distance was provided both upstream and downstream of the orifice to minimize the impact of the inlet and exit boundary conditions on the calculated flow structure in the primary domain of interest which is (0≤x/R≤1). The downstream limit (x/R=1) of the quench zone was arbitrarily defined to be x/R=1.

Annular mixer description

Two different annular mixers were modeled to investigate the effect of channel height on the mixing flowfield and NOx production:

a) A large channel mixer with an annulus height (H) equal to the circular mixer diameter where the inner and outer diameter dimensions are 13 and 19 inch respectively (0.330 m and 0.483 m). The inner and outer walls have the same size, number, and shape orifices. The overall mixing domain of the computation extends from 2x/H=-3 to 2x/H=6. This configuration was modeled to compare the effect of jet penetration of the circular and annular cases with a physically the same characteristic channel height dimension.

b) The analysis was also made with a small channel height (H) equal the circular mixer radius R = 1.5 inches (0.038 m). The inner and outer diameter dimensions of the mixer are 13 and 16 inches respectively (0.330 m and 0.406 m). The inner and outer walls have the same size, number, and shape orifices. The overall mixing domain of the computation extends from 2x/H=-4 to 2x/H=12. The short H annular mixer was modeled to investigate the effect of severe over-penetration on the mixing flowfield and NOx production.

In order to make a valid comparison between the circular and its corresponding annular mixer, it became essential to first duplicate the cross-sectional area of the circular mixer modeled sector in the annular configuration. For this purpose, the cross-sectional area of two equal (1-hole) sectors in the circular geometry (corresponding to the opposing orifices) are duplicated in the annular configuration. The total number of orifices in the annular mixer cases were determined by this constraint and the physical outer and inner wall dimensions mentioned earlier.

Note that based on the constraints imposed above, both the circular and annular cases with the same orifice shapes will yield the same hole size for a constant operating condition. Orifice Cd is assumed to be 0.7 throughout the entire study. The description of the orifice types and mixer configurations for all 60 configurations analyzed herein are as shown in Tables-1 and 2. Note that the actual number of holes per row are detailed separately from the equivalent number of holes. The equivalent number of holes is used to compare both annular and circular mixing configurations and is defined as the number of orifices per row per equivalent sector cross-sectional area as shown in Eq-4.

$$N_{eq} = \frac{N_c\left(Do_a^{\,2} - Di_a^{\,2}\right)}{2\left(Do_c^{\,2}\right)} \qquad (4)$$

where, N_{eq} = the equivalent number of annular orifices, N_c is the number of orifices in a circular can, Do_a and Di_a are the outer and inner annulus radii of the annular mixing configuration, and Do_c is the outer diameter of the circular mixer.

The equivalent sector is that given by the cross-sectional area of 2 opposing orifices in the circular mixer. In the circular mixer, the actual and equivalent number of holes is the same, however, for the annular mixer, the equivalent number of holes is significantly reduced since the

overall area of the annulus is larger than that of the circular mixer. In other words, the equivalent number of holes indicates how many orifices in the annular configurations will it take to equal 2 opposing orifices in the circular mixer. Also note that the calculated equivalent number of orifices is per wall, recognizing that both inner and outer walls in the annular configuration have the same number of orifices. The equivalent number of orifices for all configurations are shown in Tables-1 and 2. Note that in all of the annular configurations except for three different configurations, the orifice arrangement for the annular mixer are directly opposing orifices. The orifices in both the inner and outer walls for HO-34, 40, and 41 are in a staggered arrangement.

The computational domain was discretized into 50,000 to 150,000 finite control volumes arranged with about 70 to 120 nodes in the axial direction, and 30 to 40 nodes in both the radial and tangential directions. The grid was denser near the orifice to resolve the high velocity and temperature and equivalence ratio gradients resulting from the inlet of the crossflow jet. An orthogonal view of a typical grid arrangements for both circular and annular mixer types are shown in Figures-1 and 2. The grid is configured to allow smooth progressive volume change between adjacent control volumes to help speed up the convergence of the solution. In the 3-D numerical model, a secondary grid (staggered grid) is interpolated from that shown in Figures-1 and 2 to obtain the boundaries upon which the vector quantities are acting. In other words, the staggered grid becomes the control surfaces of the micro control volumes that constitute the inner volume of the mixing section.

A total of 60 circular and slanted slot orifice configurations were analyzed as shown in Tables-1 and 2. For the circular configurations, the blockage is defined as the circumferential projection of the orifice divided by the spacing between the orifice centers. The T.E. x/R is the non-dimensional axial location of the trailing edge of the orifice with respect to its leading edge (x/R=0). For the annular configurations, the blockage is defined as the circumferential projection of the orifice divided by the spacing between the orifice centers evaluated at the mid-area radius. The mid-area radius is the radius location that equally splits the cross-sectional area in 2. The orifice trailing edge non-dimensional parameter as applied to the annular configuration is T.E. 2x/H where the H is the annulus height. Both the blockage and the trailing edge nondimensional parameters are shown in Tables-1 and 2.

In this study, the following parameters were kept constant throughout this analysis. The control of these parameters is essential for a valid comparison of both mixing non-uniformity and NOx production between the appropriate configurations.

1) rich zone equivalence ratio $\phi_{RZ} = 1.80$
2) lean zone equivalence ratio $\phi_{LZ} = 0.416$
3) overall mixer pressure = 203 psia (14.1 atm)
4) jet temperature = 1710 R (950 K)
5) mainstream temperature = 3895 R (2164 K), from the chemical equilibrium code (CEC) developed by NASA
6) mixer diameter = 3 inch (0.076 m) (circular)
7) Di=13 inch (0.330 m) and Do = 16 inch (0.406 m) for the small annular mixer
8) Di=13 inch (0.330 m) and Do = 19 inch (0.482 m) for the large annular mixer
9) jet to mainstream mass flow rate MR = 2.96
10) jet to mainstream density ratio DR = 2.28

11) jet to mainstream momentum-flux ratio (J) = 52
12) overall mixer total pressure loss = 2.69%

The following were allowed to vary:

1) orifice blockage and T.E. x/R values depending on the orifice shape and orientation
2) number of orifices per row
3) orifice shape

Modeling specifications

The species mole fractions, temperature, and velocity profiles exiting the rich zone and entering the mixer were assumed to be uniform across the inlet cross-section of the mixing section. The air jet flow was characterized by a radial, uniform flow across the orifice effective area. COM-3D is not a body conforming code therefore accurate modeling of the orifice shape was obtained by a stair-stepping approximation using 80 to 300 control surfaces. This number of nodes/orifice allowed accurate modeling of both round and slot geometries. The assumption of uniform mass injection/area for the orifice air entry is applied in the mathematical model in all the configurations. The turbulence kinetic energy of the mainstream and jet flows were 0.3% of the square of the mean velocities. The turbulence length scales of the mainstream flow were 2% of the mixer diameter, and the turbulence length scale of the jet was of the order of the orifice diameter. The results from COM-3D were post processed into about 2000 sub-volumes, about 20 in the axial direction, 10 in the radial, and 10 in the circumferential direction. This input was used to generate the NOx predictions based on the flow characteristics.

A typical numerical solution took about 500 iterations for full reacting flow convergence with overall mass flow residuals of 0.05% of the total mixing section mass flowrate. All solutions were obtained using the Cray C-90 and a typically converged solution took about 2 hrs of CPU time.

Result representation

The temperature, local NOx, and normalized equivalence ratio plots are also shown in the figures in Appendix-A for all 60 configurations described in this report. The 3-D perspective of these plots places the observer downstream of the mixer looking upstream at the sector of the mixer. Note that configurations with many orifices per row tend to produce very thin single-orifice sectors. When this occurs, several sectors are plotted adjacent to each other in order to better illustrate the flow field (see Figure-A58). Five different radial-tangential planes have been chosen at x/R = 2x/H = 0.08, 0.25, 0.5, 0.75, and 1.0 showing the flow development and NOx production, mixing flowfield, and reaction temperature throughout the mixing section. The axial direction is plotted vertically and the flow moves from bottom towards the top.

To the left of each plot in Appendix-A is the temperature development in K. Nine different contours are represented in this plot ranging from 900K to 2500K.

The middle plot in Appendix-A figures is the localized NOx production in log(gr of NOx / {sec m^3}). The contour scale ranges from -4 to 4 and the shades indicate that the red contours are locations of the highest NOx production and consequently the blue indicates the lowest NOx production regions.

The parameter (f) defined in Eq-5, applied to the equivalence ratio scalar quantity (ϕ), is plotted to the far right in all figures in Appendix-A. Note that the equivalence ratio is a conserved scalar. The value of (f) varies from 0 to 1, where 0 (blue) is the value of the unmixed jet equivalence ratio and 1 (red) is the value of the mainstream flow equivalence ratio. Note that f = 1-θ, where θ is as defined previously (Holdeman, 1993) and used elsewhere also. Also note that the definition of (f) does not apply to the temperature distribution in the reacting flow solutions since the temperature in some areas of the mixing region rise above that of the incoming mainstream flow due to the chemical reaction of the rich-zone exit composition. The equilibrium (f) value was calculated in a purely adiabatic system at any location downstream of the jet injection.

$$f = \frac{\phi_{jk} - \phi_{jet}}{\phi_{main} - \phi_{jet}} \tag{5}$$

Results and Discussion

The mixing performance for all configurations analyzed in this study were ultimately evaluated at x/R = 2x/H =1. The flow mixing non-uniformity throughout the mixer volume ($0 \leq$ x/R = 2x/H $\leq$ 1) is also quantified since complex shear structures are present in the flow field near the jet entry region.

Two different methods were used to analyze the numerical results: observational analysis and statistical analysis. Both of these are described in detail below.

Observational analysis

Temperature, equivalence ratio, and NOx production field solutions were analyzed qualitatively using the figures shown in Appendix-A. Mixing non-uniformity is clearly shown by the variation in the color distribution in both temperature and equivalence ratio distribution contours. The temperature plots indicate locations, especially behind the orifice, where the reaction between the mainstream and jet flow produce the expected temperature rise. The NOx plots in Appendix-A show the critical NOx production locations. Note that the normalized equilibrium equivalence ratio for all configurations is 0.253. Similarly, the equilibrium temperature for all configurations is 1598K.

Statistical analysis

The statistical analysis involves the detailed characterization of the mixing flowfield using several different techniques. These techniques characterize the mixing non-uniformity only. Three different statistical methods are reported in this report and are shown in the figures in Appendix-B:

a) The performance of the mixing section at the radial-tangential planes at x/R=1 and 2x/H were quantified using an area weighted planar deviation parameter (AMIX) given by Eq-6. The deviation used in AMIX is calculated relative to the stoichiometric value of f which equals 0.556 for all configurations. The stoichiometric value is used as a reference because most NOx is produced in the rich regions of the flame. A large AMIX value indicates a more uniformly distributed flow and lower NOx production tendency. It is also important to note that AMIX does not correct for the bias introduced in the region of the mixer where the air is being injected through the orifice. However, AMIX is only evaluated at the exit of the mixer x/R= 2x/H =1 and this plane is downstream of the air injection in almost all configurations summarized in this report. Exceptions to this are configurations HO-19, 59, and 60 which have a T.E. 2x/H larger than 1.0 (see Tables-1 and 2). The area-weighted non-uniformity results are shown in Tables-3 and 4 in configuration nomenclature order and in Tables-5 and 6 sorted in order of mixer type. The AMIX is shown as a function of mixer axial location in the top plot in the figures in Appendix-B.

$$AMIX = \left[\frac{1}{A_{tot}} \sum_{jk} A_{jk} \left[\frac{\phi_{jk} - \phi_{stoich}}{\phi_{main} - \phi_{jet}} \right]^2 \right]^{\frac{1}{2}} \tag{6}$$

b) The mass flow weighted planar deviation parameter MMIX (also evaluated at x/R=1 or 2x/H) as defined in Eq-7 is also used to evaluate the mixing region. This parameter is similar to the area weighted parameter in Eq-6, with the added density and velocity weighting terms. MMIX parameters for all configurations are shown in Tables-3, 4, 5 and 6. As with the AMIX definition, large MMIX values correspond to better mixing and lower NOx production tendency. Axial profiles of MMIX are shown in the top plot in the figures in Appendix-B.

$$MMIX = \left[\frac{1}{\dot{M}_{tot}} \sum_{jk} A_{jk} \rho_{jk} u_{jk} \left[\frac{\phi_{jk} - \phi_{stoich}}{\phi_{main} - \phi_{jet}} \right]^2 \right]^{\frac{1}{2}} \tag{7}$$

c) The flow field was also evaluated by calculating a numerical volume integration NVI parameter for each mixing section ($0 \le x/R \le 1$ or $0 \le 2x/H \le 1$) as shown in Eq-8.

$$NVI = Volume\ Fraction/bin = \frac{\sum_{f_{l_i}}^{f_{h_i}} Volume_{ijk}}{\sum_{f_{jet}}^{f_{main}} Volume_{ijk}} \quad (8)$$

The NVI parameter allows analysis of the entire flow field and is more descriptive of the overall flow phenomena in the mixing section as compared to a planar deviation analysis shown in Eqs-6 and 7. This NVI analysis was only performed on the equivalence ratio distribution. The entire range of the normalized parameter f (from 0 to 1) was sub-divided into 200 equal size bins and the volume of the computational control volumes corresponding to the value of (f) at a certain bin size (f_i to $f_{i+\Delta f}$) was integrated as shown in Figure-3. The integrated volume in each bin was normalized based on the entire analyzed mixer volume, thus obtaining the normalized volume fraction. The volume fraction for each bin was plotted as a histogram as a function of f. In addition, the incremental partial volume per bin was integrated from f = 0 to 1 and the cumulative volume fraction was obtained for all the 60 analyzed configurations as shown in Figures 4 and 5. If the histogram is integrated from f=0 to f=1, the value of the cumulative volume fraction will be 1 since the overall volume itself is also normalized to 1.

The shape of the volume fraction histogram was also characterized by the definition of B(+) and B(-). The value of B(+) is the "area determined" distribution half width above f_{stoich} such that the integrated area under the histogram above f_{stoich} is 1/2 that of the overall histogram area above f_{stoich}. The same applies to B(-) for the area below f_{stoich}. The definitions of B(+) and B(-) are shown pictorially in Figure-3. The lowest NOx tendency yields highest B(+) and B(-) indicating that most of the flowfield within the mixing volume is either too rich or too lean to produce significant amount of NOx. The histogram shape value SUM-B is defined as the sum of B(+) and B(-). The shape of the volume histograms for all 60 configurations are shown in the bottom plot in the figures in Appendix-B.

Effect of the change in the number of orifices/row on jet penetration

In this comparison it is important to reiterate that the comparison is made without changing the overall ACd of the row of orifices and that the variation of the number was accomplished by changing the size of the orifice to keep the same row ACd. This was necessary in order to keep the jet-to-mainstream mass-flow ratio constant for all configurations. In addition, the shape of the orifices, whether round or slot, was preserved and the hole became smaller for a larger number or orifices. It is also important to note that for certain annular configurations, a maximum number of orifices is associated with the case and this means that the web between the orifices in the circumferential direction becomes zero.

Jet penetration as shown in Tables-3, 4, 5 and 6 is defined from the outer wall of the mixer in both annular and circular mixers. The jet penetration is expressed as a non-dimensional

quantity r/R for the circular configurations and 2r/H for the annular configurations. The jet penetration is also calculated by plotting the normalized equivalence ratio as a function of radius along the axial-radial plane through the center of the orifice. The jet penetration is therefore evaluated at x/R=1 (circular) or 2x/H (annular) at the radial location where the value of f is minimum thereby indicating the location of the center core of the jet.

The variation in the jet penetration for both annular and circular mixers are shown in Figures-4 and 5 respectively. The abscissa value in both plots is the equivalent number of orifices which has been defined previously in Eq-4. These figures also show the difference in the jet penetration as a function of orifice shape as a parameter. In addition, Figure-5 indicates the effect of the change in annulus height on the jet penetration. . The results indicate the jets have penetrated to the center of the mixer in almost all cases of the small annulus height mixers with the round orifices (labeled as 16ANN-RO, which indicates 16 inch Do, annular mixer with round holes). The 16ANN-SS results however indicate moderate decrease in jet penetration with the increase in number of orifices. Note that the SS indicates the 67.5° slanted slot L/W=4 orifice type. The large annulus mixer 19ANN-AS and 19ANN-RO results for the aligned slot L/W=4 and round orifices respectively indicate also moderate decrease in jet penetration with increasing number of orifices. Note that the AS nomenclature is used for the flow aligned slot L/W=4. The trends shown in Figure-4 are expected, especially for the difference between the slanted slot and round holes for the same mixer type. The slanted slot has been shown previously by Oechsle, Mongia, and Holdeman, 1992, 1993, and 1994, to have lower jet penetration due to the transfer of the radial momentum to circumferential recirculation as the jet penetrates into a circular mixer. The same phenomena is shown herein for annular mixers as well. Note that the jet penetration for the staggered hole arrangement are not plotted in Figure-4 since the definition of the jet penetration does not hold when the jets penetrate beyond the mid-plane of the annular mixer.

The results in Figure-5 for the circular mixers also show the expected trends for the AS, RO, and SS orifices (flow aligned slot L/W=4, round, and 67.5° slanted slot L/W=4) respectively. The decrease in jet penetration with increase in orifice number is weaker for the strongest penetrating configuration (the aligned slot) as compared to the weakest (the slanted slot). These results are confirmed by other studies in the literature. It is however important to note that the orifices in the circular mixer have much more difficulty penetrating to the center core as compared to the annular cases. For the cases where the jets in the circular mixer penetrate to the center core (which is a singular axis in the flow field), the mainstream flow produces great resistance. This however is not shown in the annular mixers since there is no singularity at the center of the mixer and therefore the jets can more readily penetrate completely to the center as shown in Figure-4 with values of jet penetration equals 1.

Effect of the change in number of orifices/row on AMIX and MMIX

The AMIX variations as a function of the equivalent number of orifices per row are shown in Figures-6 and 7 for the annular and circular mixers respectively. Reiterating that the large value of AMIX has a lower NOx production potential, the results in Figure-6 show that the orifices with high jet penetration such as the 16ANN-RO, and the 16ANN-RO-STAG have minimum AMIX at 22 eq holes/row. However, orifices with lower jet penetration such as the 19ANN-RO, 19ANN-SS, and 19ANN-AS minimized AMIX at much lower eq number of holes (about 8). This same trend appears to be similar in Figure-7 results for the annular mixer type.

The orifices producing stronger penetration seem to have minimized AMIX at higher number of orifices per row (8, 12, and 18) for the SS, RO, AS respectively.

The MMIX variations as a function of the equivalent number of orifices per row are shown in Figures-8 and 9 for the annular and circular mixers respectively. The results appear to be similar to the AMIX results. Note that the a small MMIX indicate a greater tendency to produce NOx in the mixing section. The orifices that penetrate to the center core as the number of holes is decreased tend to have a lower MMIX at a higher number of equivalent holes per row (for the cases shown herein, about 20 to 30 eq holes/row). Configurations with shallow penetration and fewer holes have higher values of MMIX (see Figures-8 and 9). It is also evident from the Figure-10 that the jet penetration for minimum AMIX value is about 0.7 to 0.8 for the annular mixers while being about 0.6 or less for the circular mixers. The correlating trends between the MMIX parameter and the jet penetration (shown in Figure-11) are also similar to that of the AMIX case for both the annular and circular mixers.

Effect of the change in number of orifices/row on SUM-B

SUM-B variations as a function of the equivalent number of orifices per row are shown in Figures-12 and 13 for the annular and circular mixers respectively for mixer domain of $0<x/R<1$ or $0<2x/H<1$. It is important to reiterate that the largest values of SUM-B tend to produce less NOx. The results indicate that in both annular and circular mixers, as the number of orifices is increased, the value of SUM-B also increases for all orifice shapes. These results are expected since, although the values are normalized for the unit volume in the mixing section, as the volume sample decreases, the likelihood to encounter larger gradients in the flow also increases. This also indicates that mixing uniformity degrades as the volume decreases which appears to be common for all configurations with large number of orifices per row. These results support the results shown in Oechsle and Holdeman (1995) that volume is essential for adequate mixing. Therefore it is expected that the SUM-B will increase for a reduced number of orifices. The results shown in Figure-14 indicate good correlation between the SUM-B parameter and the jet penetration for the annular and circular mixers. Decreasing SUM-B appears to be prevalent for all configurations exhibiting stronger penetration. Note that the 16ANN-RO data values in Figure14a appear not to follow this trend. This is expected since all these cases are over-penetrating to the core of the mixer. The results in Figure-14 indicate that as the jet penetrates to the core, a larger fraction of the flow field with a fuel concentration approaching the stoichiometric value increases, thereby resulting in a tendency to produce more NOx. It is important to note that although the volume fraction histogram defines the partial volume in the mixer with a specific f value near the stoichiometric value, this parameter is not a function of the residence time which is an important factor in the NOx production. Therefore the correlation between SUM-B and NOx reduction should carry the assumption that the flow field mean velocity is generally constant in the axial direction. This, of course, may not be applicable in some cases, especially in flow fields with large recirculation vortices where pockets of the mixture appear to reside longer at a certain value of f due to the transient time within the recirculation eddy.

Effect of the change in number of orifices/row on mixer NOx production

In this comparison, the NOx cumulative concentration is calculated up to the exit boundary of the mixing section. As mentioned previously, the exit boundary for the circular mixer is $x/R=1$ and for the annular mixer is $2x/H$. The NOx concentration (CUM NOx) in ppm is

accumulated throughout the mixing section, including any NOx formed upstream of the x/R = 2x/H=0 inlet boundary. This is important since the jet flow in many of the over-penetrating mixing configurations tend to recirculate upstream of the x=0 boundary mixer and mix with the mainstream flow. When this occurs, temperature rise is expected in the region upstream of the designated mixer inlet and thus NOx is formed. It is also important to note that although a designated exit boundary has been imposed in this study, additional mixing and reaction can occur beyond this limit, therefore producing NOx that is not accounted in the CUM-NOx value described above. Therefore, a second NOx parameter is defined (Global EINOx) which is the NOx emission index for the entire computational domain. This parameter is considered valuable since it accounts for the NOx that is produced downstream of the mixer up to a value of x/R = 2x/H = 6. Note that the sample length of the mixer is the same for both the circular and annular mixers. This is essential since NOx is significantly dependent on the residence time. It is also assumed that this length is sufficient to allow full reaction of the available dissociated Oxygen atoms enough to assume that no NOx will be produced further downstream. It is therefore believed that the global EINOx is a more descriptive value of the NOx production in a mixing region.

The effect of the variation of the number of holes on the CUMNOx is plotted in Figures-15 and 16 for the annular and circular mixers respectively. The results indicate no simple relationship between the NOx production in the mixer as the number of equivalent holes in increased in the range analyzed. It appears that the NOx production is somehow dependent on the jet penetration. The results shown previously indicated increase in the number of orifices resulted in a decrease in jet penetration for constant MR, J, and DR. It is also recognized that once the jet penetration has reached the core, further reduction in the number of orifices could have secondary effects on the mixing and NOx production. The results shown in Figure-17 indicate that there are multiple values of the jet penetration where NOx production is low. It is therefore apparent that there is no unique correlation between the NOx production in the mixing section (CUM NOx) with jet penetration. However, differences in the behavior between circular and annular mixers as shown in Figure-17a and b indicate that possible change in the trends from over-penetration to under-penetration could possibly cause different NOx production trends as well.

The effect of the variation of the number of holes on the Global EINOx value is plotted in Figures-18 and 19 for the annular and circular mixers respectively. Although there does not appear to be a simple relation between the overall NOx production and increasing number of equivalent orifices, there is however a possible qualitative explanation for the trend. All of the orifices in all of the mixer types indicate the same general trend in the NOx production as the number of holes is changed. These results indicate that jet penetration is definitely a strong factor in the NOx production. If the jet penetrates too much, the jet flow will be assimilated into the mixer flow in the center leaving a largely poorly unmixed region behind the orifice where NOx is produced. Similarly, if the jet penetration is low, a poorly mixed region will be created near the core of the mixer. To understand the trends shown in Figures 18 and 19, the observer must follow the trend from the under-penetrated side (moving in the abscissa from the right to left) as the number of equivalent orifices per row is continuously decreased. The trends will be described in detail below in three phases:

Phase-a) As the number of orifices is decreased, the jet penetration increases (see Figures-4 and 5) slowly towards the optimum level and, the NOx production decreases to its lowest

value. The cases that show this trend are the 19ANN-AS at 18 equivalent holes per row in Figure-18 and all the trends shown in Figure-19 for the circular mixer at 30, 20 and 10 holes/row for the AS, RO, and SS hole shapes respectively. It is interesting to note that the minimum NOx is attained for these configurations at jet penetration between 0.4 and 0.55.

Phase-b) When optimum jet penetration is reached, a further decrease in the number of orifices per row increases the jet penetration and resulting in increased NOx. Cases 19ANN-AS clearly indicate this trend in Figure-18 and for the CAN-AS and CAN-RO (ranges from 30 to 16 holes/row) and (20 to 10 holes/row) respectively shown in Figure-19. The NOx production in phase-b generally increases as the jet penetration increases beyond the optimum value. Note that the NOx production peaks in this phase, however, this peak may or may not correlate with the jet over-penetration to the center core as shown in Figures-4 and 5. However, it is evident that further increase in the jet penetration beyond the high NOx peak in phase-b, actually lowers the NOx production.

Phase-c) This is the final phase of the trend. When a reduction in the number of orifices produces further increase in jet penetration, two things may happen: 1) the jet may have already penetrated to the center core in which case it cannot go any further, or 2) the jet is still approaching the center core. It is apparent that with either of these cases, the increase in the jet penetration produces a decrease in NOx formation. The decrease in NOx formation is primarily aided by secondary mixing phenomena that has been previously neglected due to the small effect it has during phases a and b. For example, the annular configuration benefits from this over-penetration by forming vortices in the circumferential direction caused by the collision of the opposing jets. However, in the circular mixer, this can not occur since the volume in the center core of the mixer is a singular point. Nevertheless, further mixing is aided in the circular mixer, especially in the region behind the orifice. In this region, the upstream recirculating flow created by the colliding jets re-enters the mixer usually behind the orifice since the jet flow is occupying the center core. The effect of the grossly over-penetrated cases is shown schematically in Figure-20.

The illustration of the three phases in two different orifice shapes and mixer types are shown in Figure-21a. The other configurations not mentioned in these three phases only exhibit part of the full trend just described. The reason for this is that in many cases, the maximum number of orifices was reached and no further orifices could possibly be fit in the annular configurations. This was the case with 16ANN-SS, 16ANN-RO, 19ANN-RO. The other cases were not investigated due to time constraints. Also it is important to note that the value of the number of orifices for minimized NOx formation is different for different orifice shapes and mixer types. This means that the number of required orifices to produced the lowest NOx is generally higher for a round hole or aligned slot which generally have stronger jet penetration. In similar manner, weaker penetration orifice configuration such as the slanted slot will require fewer number of holes to obtain an optimum design.

It is difficult to access whether optimum number of orifices was found for all the orifice configurations, especially since not all three phases of the trend are shown for some of the cases. However configurations such as the 19ANN-AS, 16ANN-SS, and all the circular mixer orifices indicate that generally the lowest NOx attainable form either the annular or circular mixers is about 2 NOx EI and the overall variation of NOx is about 7 times the minimum. Therefore an

optimization study is recommended for any RQL mixer design since it has the potential of having a significant NOx reduction at a given operating condition.

The plots shown in Figure-21a also indicate that the comparison between the annular and circular mixers indicate similar trends as mentioned above. All three phases of the trend are shown for the aligned slot L/W=4. However, the trends are shifted with respect to each other. The annular configuration shows the trend shifted towards lower equivalent number of orifices per row as compared to the circular results. It is important to note that in this comparison the physical dimension between the opposing orifices is the same (3 inches) for both the circular and annular mixers. It is also anticipated that in this comparison (where J, MR, and DR are constant), similar jet penetrations are expected for the same orifice shapes. However, the jet penetration into the circular geometry is inherently different compared to that of the annular case. This is probably the main reason for the shift in the trends in Figure-21a. Also note that the lowest NOx was over 50% less in the annular case as opposed to the circular mixer for a given orifice shape.

If the comparison is made for a given mixer geometry type with different orifice shapes as shown in Figure-21b, similar trends are found. The difference in the jet penetration for the round orifices as opposed to the slanted slot are significant (see Figure-4) for the annular configuration. However, the trends shown in this figure are not complete as the ones shown in Figure-21a. Most of the trend for the 16ANN-RO (16 inch Do annular configuration with the round orifice) over-penetrated throughout the entire analyzed range from 4 to 30 equivalent number of orifices, therefore the portion of the trend shown is the phase-c part with a small part of phase-b. The 16ANN-SS however, due to the shallower jet penetration, exhibits the phase-a from 12 to 20 eq holes/row, phase-b between 8 to 12, and phase-c below 8 eq holes/row. The significant shift in the trends for the round to the slanted slot are again explained by the difference in the jet penetration as a function of J and MR. Note that for a given mixer, the variation of orifice shape (round to slanted slot, see Figure-21b) appears not to have significantly affected the minimum NOx value (EI=4). This means that if the designer has the freedom to vary the number of orifices per row in a given design, any orifice shape will probably be adequate in obtaining an optimum low NOx value.

Similar trends are shown for the different orifices in the circular mixer in Figure-19. Both the round hole and the flow aligned L/W=4 slot have complete trends exhibiting the three phases in the shown spectrum. The 67.5° slanted slot L/W=4, however, has the lowest jet penetration of all three orifice shapes plotted in Figure-19 and therefore has an incomplete trend with part of phase-c missing. Note that the shift in the trends for all three orifices moves to the left for orifices with lower jet penetration as a function of J and MR.

Correlation between the mixing parameters and NOx production

The results between the correlation of the global NOx EI and the different mixing non-uniformity parameters are shown in Figures-22, 23, and 24 for the phase-b results only. The phase-b results were chosen for several reasons, including the fact that most of the data points are within this regime. It is believed that all three phases will have different correlation factors, therefore only one is chosen in this comparison. The results show definite trends in the NOx formation with change in the mixing non-uniformity as expected. Note that in all plots in Figures-22 through 24, the NOx production decreases with increasing mixing non-uniformity

parameters (AMIX, MMIX, and SUM-B). As the AMIX, MMIX, and SUM-B parameter increase, the flow field in the mixing region is more stratified away from the stoichiometric value and therefore has less tendency to produce NOx. The best correlation was found to be the SUM-B value. This is not surprising since this parameter considers the NOx production throughout the entire mixer as opposed to the AMIX and MMIX values which only consider the region downstream of the jet injection. Also note that Figure-22, 23 and 24 indicate that the orifice shape is a variable to be considered in the correlation since it significantly affects the jet penetration.

Conclusions

1) The jet penetration is significantly dependent on the mixer geometry whether a circular or annular configuration. The mixing flowfield and NOx production are different in the circular and annular mixers. Significant NOx production was shown in the region behind the orifices in the circular and annular mixers at locations beyond x/R=1 for configurations with deep jet penetration. The cases with shallow penetration tend to produce NOx near the center core of the mixer. Optimum jet penetration minimizes the NOx production in these two regions. NOx production in the shear layer between the jet and the mainstream flow will generally be present and difficult to eliminate.

2) The statistical parameters AMIX, MMIX, and SUM-B appear to correlate better with the NOx production when the stoichiometric reference value is used instead of the equilibrium value.

3) The NOx production variation as a function of the equivalent number of orifices was found to have a common trend development for all orifice configurations and mixer types. The trend has been divided into three phases which cover the range between over-penetration, optimal penetration, and under-penetration. Each phase has an associated NOx trend as a function of the variation of number of orifices. Minimum NOx formation was found in the interface between phase-a and phase-b which coincides with the optimum jet penetration. Optimum penetration was between 40 to 60% of the characteristic dimension between the outer wall and the center of the mixer. The variation of this optimum penetration was surprisingly low between different orifice configurations and mixer types.

4) The comparison of the performance of the aligned slot L/W=4 in both circular and annular mixing configurations for constant J, MR, DR, and orifice ACd/row indicate that the annular mixers produce significantly lower NOx as compared to the circular counterpart. However no measurable difference was found in the lowest NOx production for the round orifice and the 67.5°slanted slot L/W=4 when both are used in an annular mixer. This also indicates that if the designer has the freedom to vary the number of orifices/row in a given mixer design, any orifice shape will probably be adequate to obtain a low NOx production value. This statement is however qualified by the fact that the jet penetration is crucial and that there is a minimum number of orifices tare required to achieve the optimum jet penetration.

References

Bain, D.B., Smith, C.E., and Holdeman, J.D. (1992), "CFD Mixing Analysis of Jets Injected from Straight and Slanted Slots into Confined Crossflow in Rectangular Ducts," AIAA paper No. 92-3087. (Also NASA TM 105699).

Bain, D.B., Smith, C.E., and Holdeman, J.D. (1993), "Parametric CFD Analysis of Jet Mixing into Confined Crossflow in Rectangular Ducts," accepted for publication in Journal of Propulsion and Power (see also AIAA-93-2044 and NASA TM 106179).

Bain, D.B., Smith, C.E., and Holdeman, J.D. (1994), "CFD Assessment of Orifice Aspect Ratio and Mass Flow Ratio on Jet Mixing in Rectangular Ducts," Journal of Propulsion and Power, Vol 11, No.3, Sept-Oct 1995, pp 885-893 (see also AIAA Paper No. 94-0218 and NASA TM 106434).

Bruce, T.W., Mongia, H.C., and Reynolds, R.S. (1979), "Combustion design criteria validation,", (USARTL-TR78- 55A, B, and C).

Doerr, Th., and Hennecke, D.K. (1993), "The Mixing Process in the Quenching Zone of the Rich-Lean-Combustion Concept," AGARD-PEP 81st Symposium of Fuels and Combustion Technology for Advanced Aircraft Engines.

Doerr, Th. (1994), "Ein Beitrag zur Reduzierung des Stickoxydaussto Bess von Gasturbinen-brennkammem - Die Optimumierung des Mischunsprozesses der Fett-Mager-Stufenverbrennung. University of Darmstadt, Germany.

Doerr, Th., Bloymeyer, M., and Hennecke, D.K. (1995), " Optimization of Multiple Jet Mixing With Confined Crossflow," ASME paper 95-GT-313.

Hatch, M.S., Sowa, W.A., Samuelsen, G.S., and Holdeman, J.D. (1992a), "Jet Mixing Into a Heated Cross Flow in a Cylindrical Duct: Influence of Geometry and Flow Variations," Journal of Propulsion and Power, Vol 11, No.3, May-June 1995, pp. 393-402 (see also AIAA-92-0773 and NASA TM 105390).

Hatch, M.S., Sowa, W.A., Samuelsen, G.S., and Holdeman, J.D. (1992b), "Influence of Geometry and Flow Variations on NO Formation in the Quick Mixer of a Staged Combustor," accepted for publication in Journal of Engineering for Gas Turbines and Power (see also NASA TM 105639).

Hatch, M.S., Sowa, W.A., and Samuelsen, G.S. (1994), "Influence of Geometry and Flow Variation on Jet Mixing and Nox Formation in a Model Staged Combustor with Eight Orifices," NASA Contractors Report 194473. (Controlled Distribution to February 1996).

Holdeman, J.D., "Mixing of Multiple Jets with a Confined Subsonic Crossflow (1993)," Prog. Energy Combust. Sci., (1993), Vol 19, pp 31-70. (Also see AIAA Paper No. 91-2458 and NASA TM 104412).

Howe, G.W., Li, Z., Shih, T.I.-P., and Nguyen, H.L. (1991), "Simulation of mixing in the quick quench region of a rich burn - quick quench mix - lean burn combustor," AIAA Paper No. 91-0410.

Kroll, J.T., Sowa, W.A., Samuelsen, G.S., and Holdeman, J.D. (1993), "Optimization of Circular Orifice Jets Mixing into a Heated Crossflow in a Cylindrical Duct," AIAA Paper No. 93-0249.

Kroll, J.T., Sowa, W.A., and Samuelsen, G.S. (1993), "Optimization of Orifice Geometry for Crossflow Mixing in a Cylindrical Duct," UCICL-ARTR-93-4, University of California, Irvine. (Controlled Distribution)

Launder, B.E., and Spalding, D.B. (1972), "Lectures in Mathematical Models of Turbulence," Academic Press Inc. (London) LTD.

Lefebvre, A.H. (1984), "Fuel Effects on Gas Turbine Combustion-Liner Temperature, Pattern Factor, and Pollutant Emissions," AIAA Journal of Aircraft, Vol 21, No. 11, pp 887-98.

Liscinsky, D.S., True, B., Vranos, A., and Holdeman, J.D. (1992), "Experimental Study of Cross-Stream Mixing in a Rectangular Ducts," AIAA Paper No. 92-3090. (Also NASA TM 106194).

Liscinsky, D.S., True, B., and Holdeman, J.D. (1993), "Experimental Investigation of Crossflow Jet Mixing in a Rectangular Duct." AIAA Paper No. 93-2037. (Also NASA TM 106152).

Liscinsky, D.S., Vranos, A., and Lohmann, R.P. (1993), "Experimental Study of Cross Flow Mixing in Cylindrical and Rectangular Ducts," NASA Contractors Report 187141.

Liscinsky, D.S., True, B., and Holdeman, J.D. (1994), "Mixing Characteristics of Directly Opposed Rows of Jets Injected Normal to a Crossflow in a Rectangular Duct," AIAA Paper No. 94-0217. (Also NASA TM 106477).

Liscinsky, D.S., True, B., and Holdeman, J.D. (1995), "Crossflow Mixing of Noncircular Jets," accepted for publication in Journal of Propulsion and Power (see also AIAA-95-0732 and NASA TM 106865).

Oechsle, V.L., Mongia, H.C., and Holdeman, J.D. (1992), "A Parametric Numerical Study of Mixing in a Cylindrical Duct," AIAA Paper No. 92-3088. (Also NASA TM 105695).

Oechsle, V.L., Mongia, H.C., and Holdeman, J.D. (1993), "An Analytical Study of Jet Mixing in a Cylindrical Duct," AIAA Paper No. 93-2043. (Also NASA TM 106181).

Oechsle, V.L., Mongia, H.C., and Holdeman, J.D. (1994), "Comparison of the Mixing Calculations of Reacting and Nonreacting Flows in a Cylindrical Duct," AIAA Paper No. 94-0865. (Also NASA RM 106435).

Oechsle, V.L. and Holdeman, J.D. (1995), "Numerical Mixing Calculations of Confined Reacting Jet Flows in a Cylindrical Duct," AIAA Paper No. 95-0733. (Also NASA TM 106736).

Oechsle, V.L. (1995), " Mixing and NOx Emission Calculations of Confined Reacting Jet Flows in a Cylindrical Duct," Allison Engine Company. (LERD)

Patankar,S.V. (1980), "Numerical Heat Transfer and Fluid Flows," Hemisphere, Washington D.C.

Rizk, N.K., Mongia, H.C. (1993), "Three-Dimensional NO_X Model for Rich/Lean Combustor," AIAA Paper No. 93-0251.

Shaw, R.J. (1991), "Engine Technology Challenges for a 21st Century High Civil Speed Transport," AIAA 10th International Symposium on Air Breathing Engines. (Also NASA TM 104361).

Smith, C.E., Talpallikar, M.V., and Holdeman, J.D. (1991), "A CFD Study of Jet Mixing in Reduced Flow Areas for Lower Combustion Emissions," AIAA Paper No. 91-2460. (Also NASA TM 104411).

Sowa, W.A., Kroll, J.T., Samuelsen, G.S., and Holdeman, J.D. (1994), "Optimization of Orifice Geometry for Cross-FLow Mixing in a Cylindrical Duct," AIAA Paper No. 94-0219. (Also NASA TM 106436).

Talpallikar, M.V., Smith, C.E., Lai, M.C., and Holdeman, J.D. (1992), "CFD Analysis of Jet Mixing in Low NO_X Flametube Combustors," Journal of Engineering for Gas Turbines and Power, Vol No. 114, pp 416, (see also ASME Papaer No. 91-GT-217 and NASA TM 104466).

Zhu, G. and Lai, M.-C. (1995), "A Parametric Study of the Penetration and Mixing of Radial Jets in Necked-Down Cylindrical Crossflow," Journal of propulsion and Power, Vol 11, No.2, March-April 1995, pp 252-260, (see also AIAA Paper No. 92-3091).

HO #	# Holes /wall	# eq Holes /wall	Orifice Shape /wall	Mixer Type	Diameter Outer inch	Diameter Inner inch	Angle deg	Orifice L or D inch	Orifice Width inch	Blockage	T.E. x/R 2x/H
1	6	6	SLOT	Circular	3		67.5	1.164	0.291	0.685	0.297
2	8	8	SLOT	Circular	3		67.5	1.008	0.252	0.790	0.257
3	10	10	SLOT	Circular	3		67.5	0.902	0.226	0.884	0.230
4	12	12	SLOT	Circular	3		67.5	0.823	0.206	0.968	0.210
5	14	14	SLOT	Circular	3		67.5	0.762	0.191	1.046	0.194
6	6	6	ROUND	Circular	3			0.639		0.407	0.426
7	8	8	ROUND	Circular	3			0.553		0.470	0.369
8	10	10	ROUND	Circular	3			0.495		0.525	0.330
9	12	12	ROUND	Circular	3			0.452		0.575	0.301
10	14	14	ROUND	Circular	3			0.418		0.621	0.279
11	29	6	ROUND	Annular	16	13		0.639		0.405	0.852
12	39	8	ROUND	Annular	16	13		0.551		0.465	0.735
13	48	10	ROUND	Annular	16	13		0.497		0.524	0.662
14	58	12	ROUND	Annular	16	13		0.452		0.572	0.602
15	68	14	ROUND	Annular	16	13		0.417		0.616	0.556
16	16	16	ROUND	Circular	3			0.391		0.664	0.261
17	18	18	ROUND	Circular	3			0.369		0.704	0.246
18	20	20	ROUND	Circular	3			0.35		0.743	0.233
19	19	4	ROUND	Annular	16	13		0.789		0.333	1.052
20	29	6	SLOT	Annular	16	13	67.5	1.164	0.291	0.681	0.594
21	39	8	SLOT	Annular	16	13	67.5	1.004	0.251	0.783	0.512
22	48	10	SLOT	Annular	16	13	67.5	0.905	0.226	0.882	0.462
23	58	12	SLOT	Annular	16	13	67.5	0.823	0.206	0.963	0.420
24	68	14	SLOT	Annular	16	13	67.5	0.76	0.190	1.037	0.388
25	77	16	ROUND	Annular	16	13		0.392		0.662	0.523
26	87	18	ROUND	Annular	16	13		0.369		0.700	0.492
27	97	20	ROUND	Annular	16	13		0.349		0.737	0.466
28	106	22	ROUND	Annular	16	13		0.334		0.776	0.446
29	116	24	ROUND	Annular	16	13		0.319		0.809	0.426
30	77	16	SLOT	Annular	16	13		0.714	0.179	1.114	0.364

Table-1. Configuration description for cases HO-1 through HO-30

HO #	# Holes /wall	# eq Holes /wall	Orifice Shape /wall	Mixer Type	Diameter Outer inch	Diameter Inner inch	Angle deg	Orifice L or D inch	Orifice Width inch	Blockage	T.E. x/R 2x/H
31	87	18	SLOT	Annular	16	13	67.5	0.672	0.168	1.179	0.343
32	97	20	SLOT	Annular	16	13	67.5	0.636	0.159	1.240	0.325
33	145	30	ROUND	Annular	16	13		0.286		0.904	0.381
34	68	14	ROUND	Ann-Stag	16	13		0.417		0.616	0.556
35	16	16	SLOT	Circular	3		67.5	0.713	0.178	1.118	0.182
36	18	18	SLOT	Circular	3		67.5	0.672	0.168	1.186	0.171
37	20	20	SLOT	Circular	3		67.5	0.638	0.160	1.251	0.163
38	24	24	ROUND	Circular	3			0.319		0.813	0.213
39	64	6	ROUND	Annular	19	13		0.639		0.804	0.426
40	21	2	ROUND	Annular	19	13		1.115		0.468	0.744
41	106	22	ROUND	Ann-Stag	16	13		0.334		0.776	0.446
42	145	30	ROUND	Ann-Stag	16	13		0.286		0.904	0.381
43	64	6	SLOT	Annular	19	13		1.164	0.291	0.366	0.776
44	6	6	SLOT	Circular	3			1.164	0.291	0.185	0.776
45	277	26	SLOT	Annular	19	13		0.56	0.140	0.763	0.373
46	26	26	SLOT	Circular	3			0.56	0.140	0.386	0.373
47	107	10	SLOT	Annular	19	13		0.9	0.225	0.472	0.600
48	149	14	SLOT	Annular	19	13		0.764	0.191	0.561	0.509
49	192	18	SLOT	Annular	16	13		0.672	0.168	0.634	0.448
50	235	22	SLOT	Annular	16	13		0.608	0.152	0.701	0.405
51	10	10	SLOT	Circular	3			0.9	0.225	0.239	0.600
52	14	14	SLOT	Circular	3			0.76	0.190	0.282	0.507
53	18	18	SLOT	Circular	3			0.672	0.168	0.321	0.448
54	22	22	SLOT	Circular	3			0.608	0.152	0.355	0.405
55	30	30	SLOT	Circular	3			0.52	0.130	0.414	0.347
56	34	34	SLOT	Circular	3			0.488	0.122	0.440	0.325
57	38	38	SLOT	Circular	3			0.464	0.116	0.468	0.309
58	299	28	SLOT	Annular	19	13		0.54	0.135	0.792	0.360
59	21	2	SLOT	Annular	19	13		2.032	0.508	0.213	1.355
60	11	1	SLOT	Annular	19	13		2.808	0.702	0.147	1.872

Table-2. Configuration description for cases HO-31 through HO-60

24	14	AN	slt slot	0.742	0.41	0.443	0.853	0.407	0.394	28	3.8	16	0.57	1.037	0.388
25	16	AN	round	0.767	0.33	0.404	0.734	0.336	0.388	35.6	6.5	16	1	0.662	0.523
26	18	AN	round	0.77	0.4	0.356	0.756	0.332	0.384	33.8	7.1	16	1	0.700	0.492
27	20	AN	round	0.77	0.365	0.386	0.751	0.32	0.377	15.1	7.2	16	1	0.737	0.466
28	22	AN	round	0.78	0.357	0.386	0.743	0.32	0.376	15.1	9.2	16	1	0.776	0.446
29	24	AN	round	0.784	0.357	0.386	0.743	0.324	0.373	15.4	9.2	16	1	0.809	0.426
30	16	AN	slt slot	0.743	0.4	0.466	0.866	0.422	0.406	28.7	4.3	16	0.45	1.114	0.364

Table-3. Mixing uniformity and NOx production results for the cases HO-1 through 30

HO	#eq holes	Mixer Type	Hole type	Cum Vol @ f stoi	B(+)	B(-)	SUM-B	AMIX	MMIX	Cumul NOx, ppm	EINOx	Do inch	Pen r/R from Do	Block	T.E. x/R T.E. 2x/H
31	18	AN	slt slot	0.772	0.365	0.477	0.842	0.427	0.41	31.5	4.5	16	0.39	1.179	0.343
32	20	AN	slt slot	0.77	0.356	0.483	0.839	0.431	0.413	29.6	3.9	16	0.33	1.240	0.325
33	30	AN	round	0.777	0.352	0.43	0.782	0.361	0.368	15.5	7.1	16	0.91	0.904	0.381
34	14	AN-Stag	round	0.73	0.339	0.422	0.761	0.343	0.391	26.6	3.6	16	n/a	0.616	0.556
35	16	CIR	slt slot	0.824	0.378	0.512	0.89	0.445	0.417	30.7	7.5	3	0.289	1.118	0.182
36	18	CIR	slt slot	0.821	0.37	0.514	0.884	0.446	0.405	32.9	7.5	3	0.224	5.270	0.171
37	20	CIR	slt slot	0.821	0.4	0.513	0.913	0.451	0.41	34.1	9.2	3	0.244	1.251	0.163
38	24	CIR	round	0.816	0.387	0.399	0.786	0.383	0.39	25.1	7.9	3	0.482	0.813	0.213
39	6	AN	round	0.794	0.343	0.395	0.738	0.337	0.375	62.8	14.4	19	0.85	0.804	0.426
40	2	AN	round	0.802	0.233	0.43	0.663	0.35	0.395	36	7.3	19	1	0.468	0.744
41	22	AN-Stag	round	0.779	0.383	0.386	0.769	0.327	0.373	41.6	5.8	16	n/a	0.776	0.446
42	30	AN-Stag	round	0.709	0.339	0.433	0.772	0.353	0.352	39.8	9.5	16	n/a	0.904	0.381
43	6	AN	alg slot	0.706	0.339	0.413	0.752	0.347	0.394	47.5	9.6	19	1	0.366	0.776
44	6	CIR	alg slot	0.876	0.199	0.425	0.624	0.351	0.371	45.1	5.97	3	0.9	0.185	0.776
45	26	AN	alg slot	0.768	0.368	0.505	0.873	0.455	0.438	14.7	3.4	19	0.4	0.763	0.373
46	26	CIR	alg slot	0.797	0.409	0.377	0.786	0.345	0.381	37.7	7.1	3	0.49	0.386	0.373
47	10	AN	alg slot	0.732	0.432	0.39	0.822	0.347	0.373	46.2	5.3	19	0.76	0.472	0.600
48	14	AN	alg slot	0.748	0.379	0.474	0.853	0.425	0.423	16.8	2.52	19	0.6	0.561	0.509
49	18	AN	alg slot	0.756	0.331	0.51	0.841	0.453	0.423	14.6	1.6	19	0.5	0.634	0.448
50	22	AN	alg slot	0.758	0.326	0.5	0.826	0.449	0.431	9.9	2.4	19	0.39	0.701	0.405
51	10	CIR	alg slot	0.89	0.19	0.406	0.596	0.357	0.356	44.5	6.4	3	0.82	0.239	0.600
52	14	CIR	alg slot	0.87	0.181	0.364	0.545	0.333	0.335	65	10.7	3	0.67	0.282	0.507
53	18	CIR	alg slot	0.803	0.277	0.351	0.628	0.324	0.344	49.7	8.8	3	0.6	0.321	0.448
54	22	CIR	alg slot	0.794	0.41	0.364	0.774	0.334	0.367	49.1	8.07	3	0.54	0.355	0.405
55	30	CIR	alg slot	0.788	0.423	0.392	0.815	0.364	0.399	38.5	4.76	3	0.46	0.414	0.347
56	34	CIR	alg slot	0.791	0.432	0.403	0.835	0.372	0.404	35.8	6.33	3	0.44	0.440	0.325
57	38	CIR	alg slot	0.795	0.413	0.404	0.817	0.375	0.41	40.1	10.1	3	0.44	0.468	0.309
58	28	AN	alg slot	0.756	0.352	0.506	0.858	0.453	0.43	40.9	10.6	19	0.44	0.792	0.360
59	2	AN	alg slot	0.765	0.243	0.399	0.642	0.398	0.444	49.2	5.51	19	1	0.213	1.355
60	1	AN	alg slot	0.724	0.216	0.368	0.584	0.379	0.443	34.93	5.57	19	1	0.147	1.872

Table-4. Mixing uniformity and NOx production results for the cases HO-31 through 60

HO	#eq	Mixer	Hole	Cum Vol	B(+)	B(-)	SUM-B	AMIX	MMIX	Cumul	EINOx	Do	Pen r/R	Blockage	T.E. x/R
	holes	Type	type	@ f stoi						NOx, ppm	Global	inch	from Do		T.E. 2x/H
60	1	AN	alg slot	0.724	0.216	0.368	0.584	0.379	0.443	34.93	5.57	19	1	0.147	1.872
59	2	AN	alg slot	0.765	0.243	0.399	0.642	0.398	0.444	49.2	5.51	19	1	0.213	1.355
43	6	AN	alg slot	0.706	0.339	0.413	0.752	0.347	0.394	47.5	9.6	19	1	0.366	0.776
47	10	AN	alg slot	0.732	0.432	0.39	0.822	0.347	0.373	46.2	5.3	19	0.76	0.472	0.600
48	14	AN	alg slot	0.748	0.379	0.474	0.853	0.425	0.423	16.8	2.52	19	0.6	0.561	0.509
49	18	AN	alg slot	0.756	0.331	0.51	0.841	0.453	0.423	14.6	1.6	19	0.5	0.634	0.448
50	22	AN	alg slot	0.758	0.326	0.5	0.826	0.449	0.431	9.9	2.4	19	0.39	0.701	0.405
45	26	AN	alg slot	0.768	0.368	0.505	0.873	0.455	0.438	14.7	3.4	19	0.4	0.763	0.373
58	28	AN	alg slot	0.756	0.352	0.506	0.858	0.453	0.43	40.9	10.6	19	0.44	0.792	0.360
19	4	AN	round	0.799	0.15	0.412	0.562	0.399	0.453	26.8	6.5	16	1	0.333	1.052
11	6	AN	round	0.789	0.181	0.43	0.611	0.356	0.404	24.3	4	16	1	0.405	0.852
12	8	AN	round	0.772	0.247	0.426	0.673	0.352	0.4	26.9	5.3	16	1	0.465	0.735
13	10	AN	round	0.762	0.269	0.421	0.69	0.345	0.393	28.4	5.1	16	1	0.524	0.662
14	12	AN	round	0.782	0.229	0.413	0.642	0.342	0.392	33.2	5.6	16	1	0.572	0.602
15	14	AN	round	0.759	0.264	0.412	0.676	0.34	0.391	33.5	5.8	16	1	0.616	0.556
25	16	AN	round	0.767	0.33	0.404	0.734	0.336	0.388	35.6	6.5	16	1	0.662	0.523
26	18	AN	round	0.77	0.4	0.356	0.756	0.332	0.384	33.8	7.1	16	1	0.700	0.492
27	20	AN	round	0.77	0.365	0.386	0.751	0.32	0.377	15.1	7.2	16	1	0.737	0.466
28	22	AN	round	0.78	0.357	0.386	0.743	0.32	0.376	15.1	9.2	16	1	0.776	0.446
29	24	AN	round	0.784	0.357	0.386	0.743	0.324	0.373	15.4	9.2	16	1	0.809	0.426
33	30	AN	round	0.777	0.352	0.43	0.782	0.361	0.368	15.5	7.1	16	0.91	0.904	0.381
40	2	AN	round	0.802	0.233	0.43	0.663	0.35	0.395	36	7.3	19	1	0.468	0.744
39	6	AN	round	0.794	0.343	0.395	0.738	0.337	0.375	62.8	14.4	19	0.85	0.804	0.426
20	6	AN	slt slot	0.663	0.3	0.417	0.717	0.346	0.39	17.6	7	16	0.95	0.681	0.594
21	8	AN	slt slot	0.647	0.422	0.39	0.812	0.325	0.369	28.8	7.6	16	0.78	0.783	0.512
22	10	AN	slt slot	0.689	0.422	0.386	0.808	0.345	0.37	32.9	5.8	16	0.7	0.882	0.462
23	12	AN	slt slot	0.756	0.4	0.434	0.834	0.374	0.377	30.3	3.7	16	0.68	0.963	0.420
24	14	AN	slt slot	0.742	0.41	0.443	0.853	0.407	0.394	28	3.8	16	0.57	1.037	0.388
30	16	AN	slt slot	0.743	0.4	0.466	0.866	0.422	0.406	28.7	4.3	16	0.45	1.114	0.364
31	18	AN	slt slot	0.772	0.365	0.477	0.842	0.427	0.41	31.5	4.5	16	0.39	1.179	0.343
32	20	AN	slt slot	0.77	0.356	0.483	0.839	0.431	0.413	29.6	3.9	16	0.33	1.240	0.325
34	14	AN-Stag	round	0.73	0.339	0.422	0.761	0.343	0.391	26.6	3.6	16	n/a	0.616	0.556
41	22	AN-Stag	round	0.779	0.383	0.386	0.769	0.327	0.373	41.6	5.8	16	n/a	0.776	0.446
42	30	AN-Stag	round	0.709	0.339	0.433	0.772	0.353	0.352	39.8	9.5	16	n/a	0.904	0.381

Table-5. Mixing uniformity and NOx production results for the annular mixers

HO	#eq	Mixer	Hole	Cum Vol	B(+)	B(-)	SUM-B	AMIX	MMIX	Cumul	EINOx	Do	Pen r/R	Blockage	T.E. x/R
	holes	Type	type	@ f stoi						NOx, ppm	Global	inch	from Do		T.E. 2x/H
44	6	CIR	alg slot	0.876	0.199	0.425	0.624	0.351	0.371	45.1	5.97	3	0.9	0.185	0.776
51	10	CIR	alg slot	0.89	0.19	0.406	0.596	0.357	0.356	44.5	6.4	3	0.82	0.239	0.600
52	14	CIR	alg slot	0.87	0.181	0.364	0.545	0.333	0.335	65	10.7	3	0.67	0.282	0.507
53	18	CIR	alg slot	0.803	0.277	0.351	0.628	0.324	0.344	49.7	8.8	3	0.6	0.321	0.448
54	22	CIR	alg slot	0.794	0.41	0.364	0.774	0.334	0.367	49.1	8.07	3	0.54	0.355	0.405
46	26	CIR	alg slot	0.797	0.409	0.377	0.786	0.345	0.381	37.7	7.1	3	0.49	0.386	0.373
55	30	CIR	alg slot	0.788	0.423	0.392	0.815	0.364	0.399	38.5	4.76	3	0.46	0.414	0.347
56	34	CIR	alg slot	0.791	0.432	0.403	0.835	0.372	0.404	35.8	6.33	3	0.44	0.440	0.325
57	38	CIR	alg slot	0.795	0.413	0.404	0.817	0.375	0.41	40.1	10.1	3	0.44	0.468	0.309
6	6	CIR	round	0.8603	0.133	0.395	0.528	0.336	0.358	42.9	8	3	0.85	0.407	0.426
7	8	CIR	round	0.847	0.154	0.386	0.54	0.331	0.36	53.6	11.4	3	0.72	0.470	0.369
8	10	CIR	round	0.8405	0.172	0.369	0.541	0.319	0.362	51.7	12.6	3	0.66	0.525	0.330
9	12	CIR	round	0.852	0.309	0.351	0.66	0.315	0.351	57	8.2	3	0.6	0.575	0.301
10	14	CIR	round	0.861	0.383	0.342	0.725	0.319	0.355	52.2	5.9	3	0.594	0.621	0.279
16	16	CIR	round	0.852	0.37	0.347	0.717	0.318	0.362	37.9	4.7	3	0.556	0.664	0.261
17	18	CIR	round	0.8381	0.392	0.356	0.748	0.341	0.37	26.9	3.9	3	0.543	0.704	0.246
18	20	CIR	round	0.826	0.41	0.367	0.777	0.356	0.381	27	2.2	3	0.523	0.743	0.233
38	24	CIR	round	0.816	0.387	0.399	0.786	0.383	0.39	25.1	7.9	3	0.482	0.813	0.213
1	6	CIR	slt slot	0.742	0.326	0.364	0.69	0.321	0.368	37.1	5.3	3	0.69	0.685	0.297
2	8	CIR	slt slot	0.796	0.397	0.333	0.73	0.313	0.33	48.2	4.2	3	0.402	0.790	0.257
3	10	CIR	slt slot	0.811	0.4	0.375	0.775	0.372	0.368	25.7	3.2	3	0.386	0.884	0.230
4	12	CIR	slt slot	0.816	0.388	0.462	0.885	0.414	0.401	28.4	4.6	3	0.358	0.968	0.210
5	14	CIR	slt slot	0.813	0.383	0.487	0.87	0.431	0.413	32.7	6.3	3	0.31	1.046	0.194
35	16	CIR	slt slot	0.824	0.378	0.512	0.89	0.445	0.417	30.7	7.5	3	0.289	1.118	0.182
36	18	CIR	slt slot	0.821	0.37	0.514	0.884	0.446	0.405	32.9	7.5	3	0.224	5.270	0.171
37	20	CIR	slt slot	0.821	0.4	0.513	0.913	0.451	0.41	34.1	9.2	3	0.244	1.251	0.163

Table-6. Mixing uniformity and NOx production results for the circular mixer

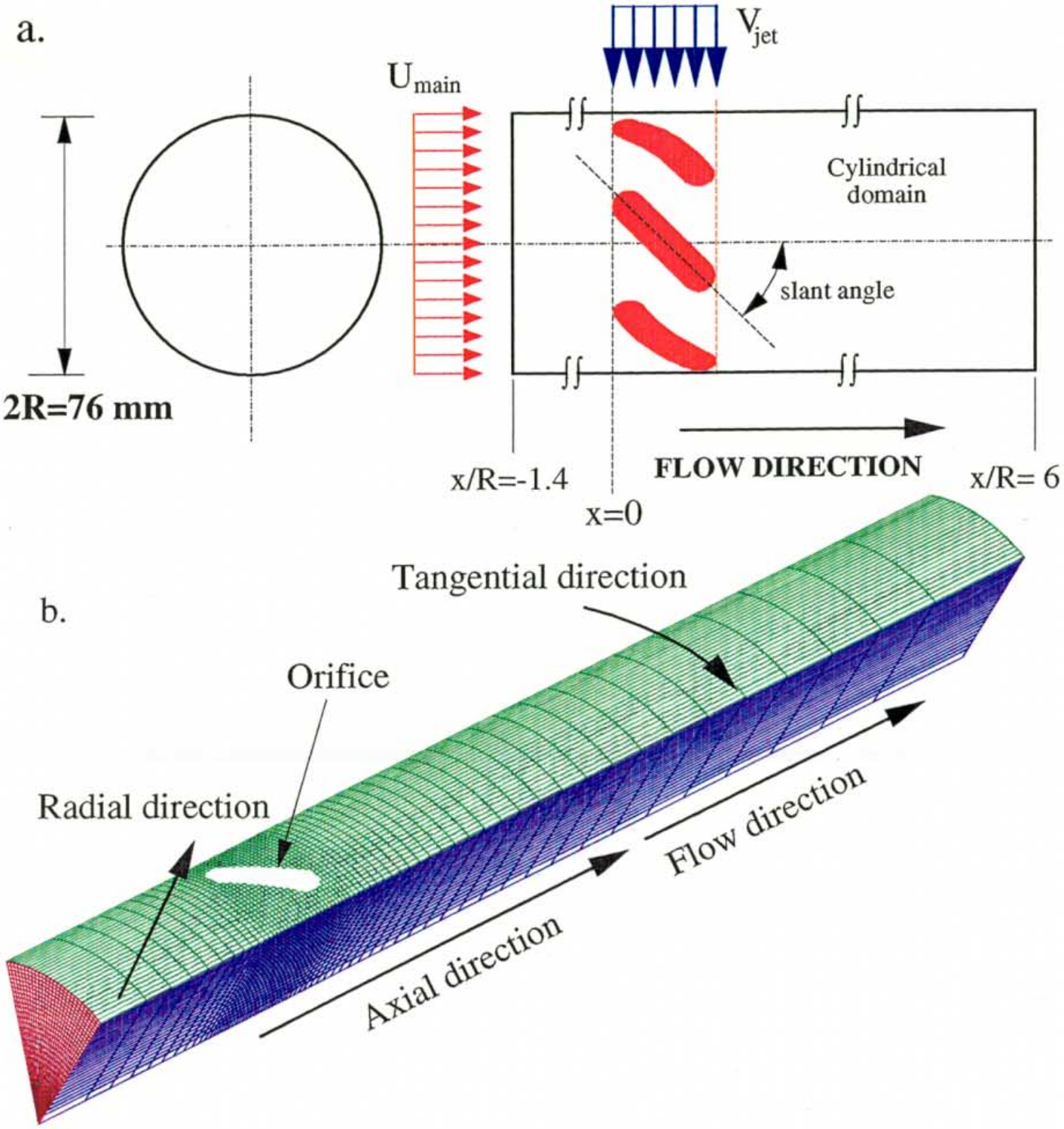

Figure-1. a) Geometric configuration of the mixing section, and
b) orthogonal view of the computational grid with a 45° slot

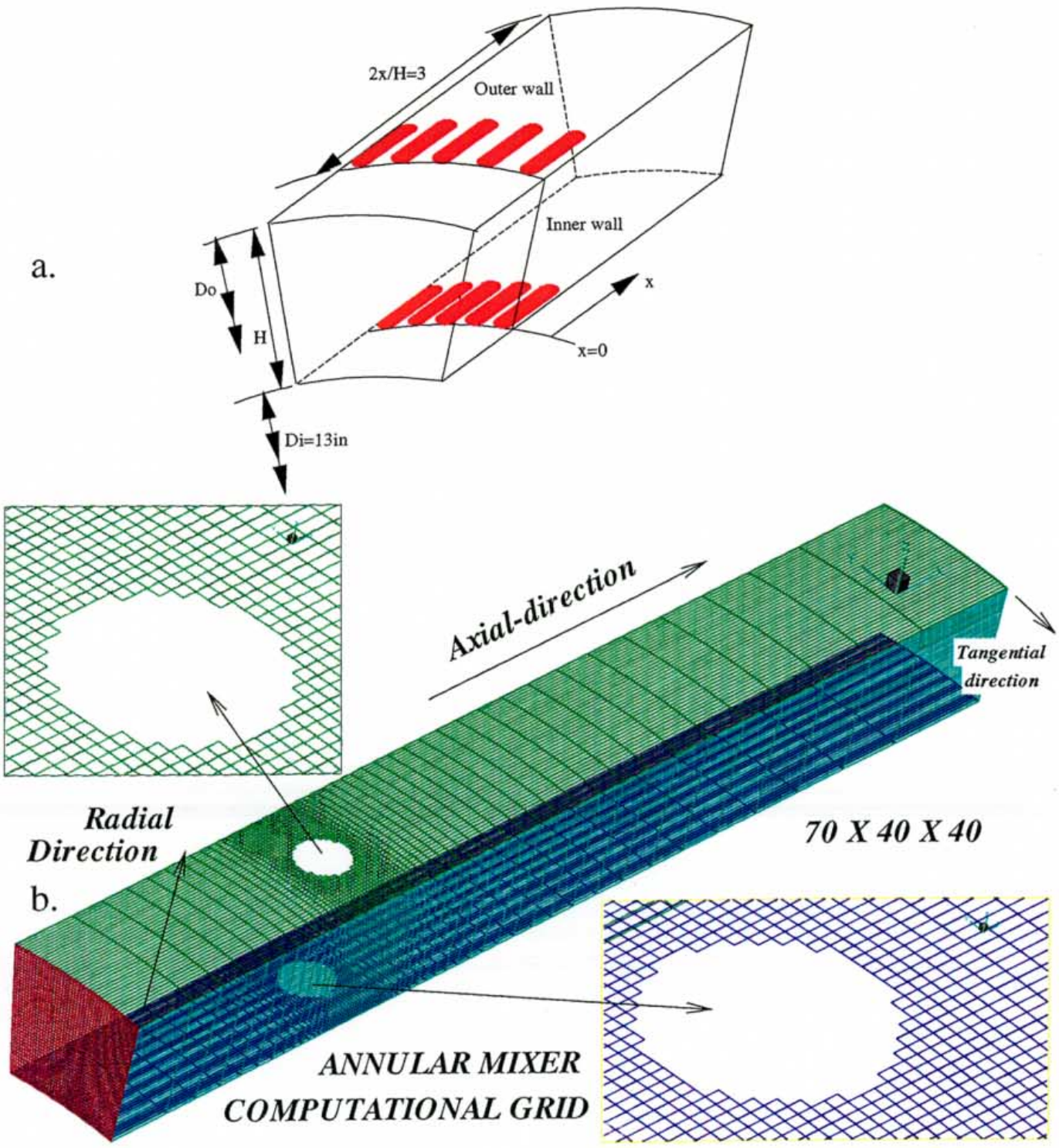

Figure-2. a) Geometric configuration of the typical annular section, and
b) orthogonal view of a single sector of the computational domain with round holes

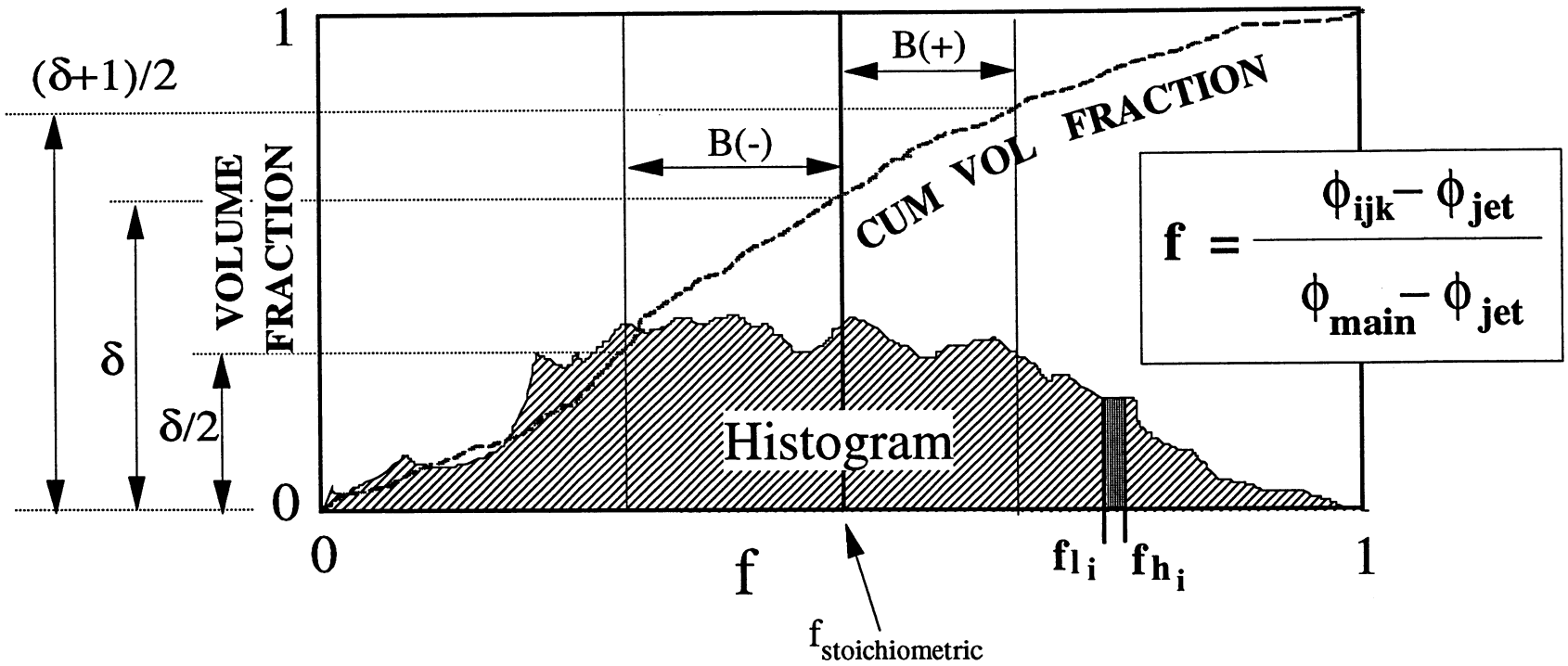

Figure-3. Description of the volume histogram statistical analysis for the mixing non-uniformity evaluation

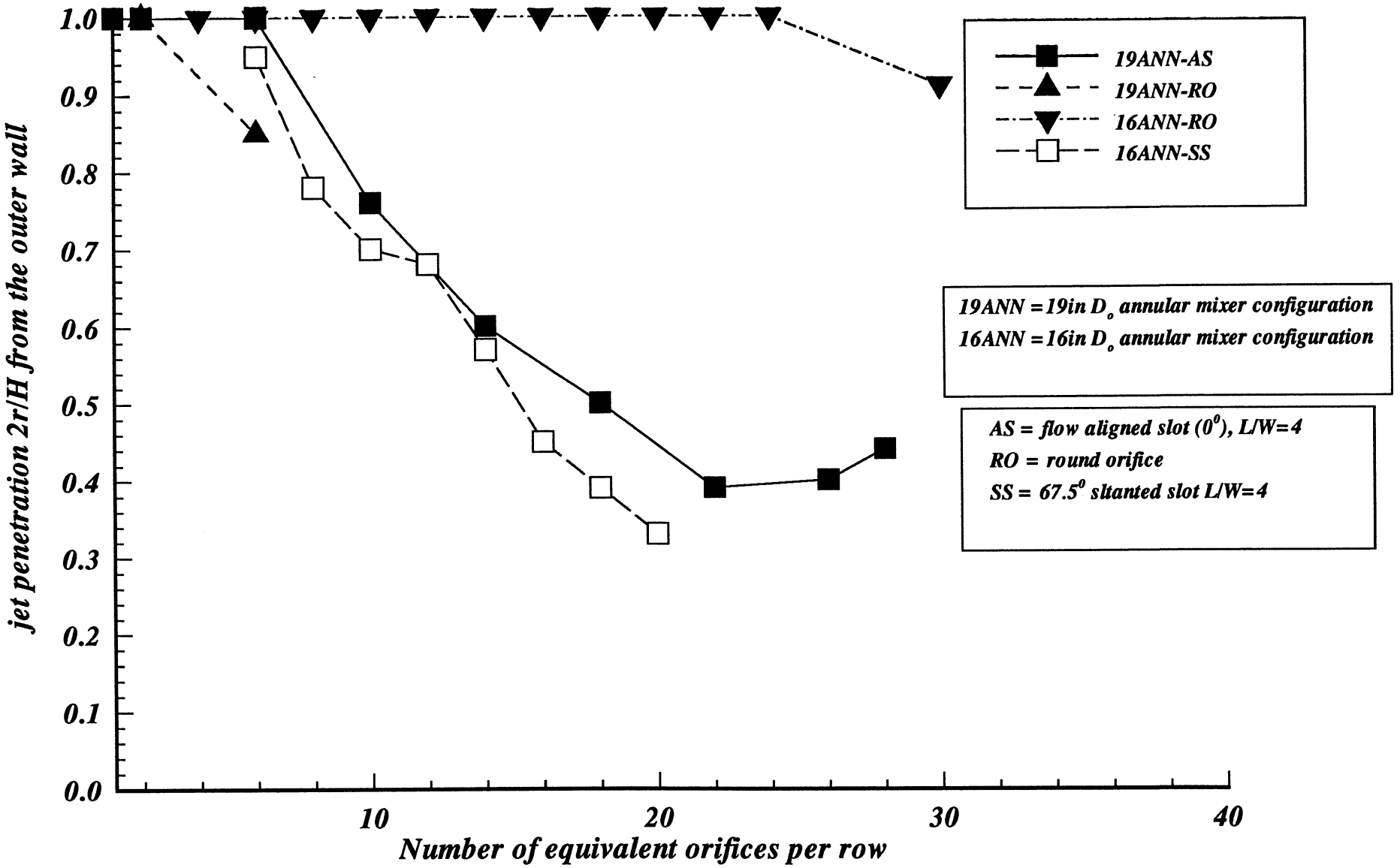

Figure-4. Effect of the variation of the number of orifices on the jet penetration for the annular mixers

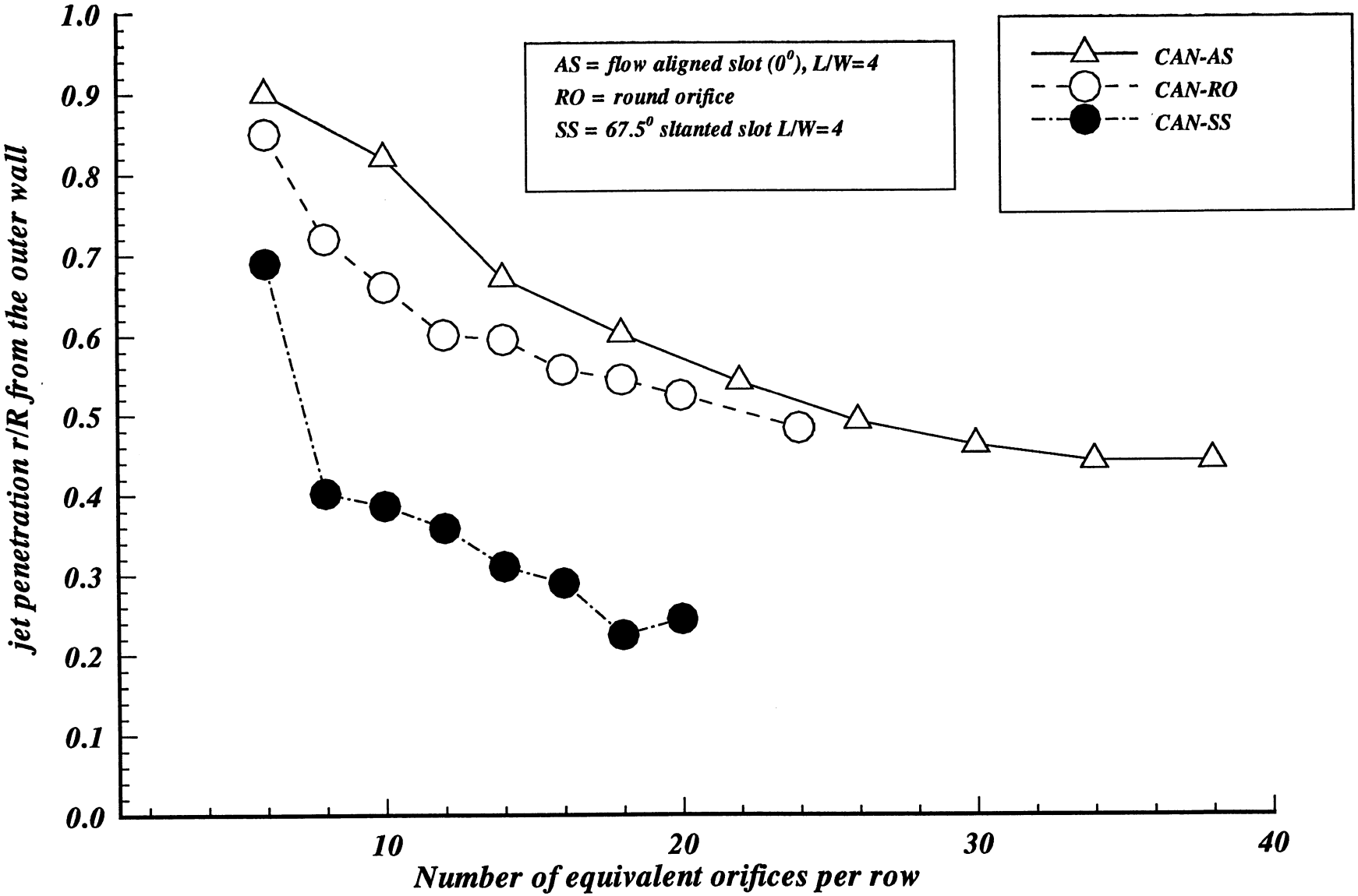

Figure-5. Effect of the variation of the number of orifices on the jet penetration for the circular mixers

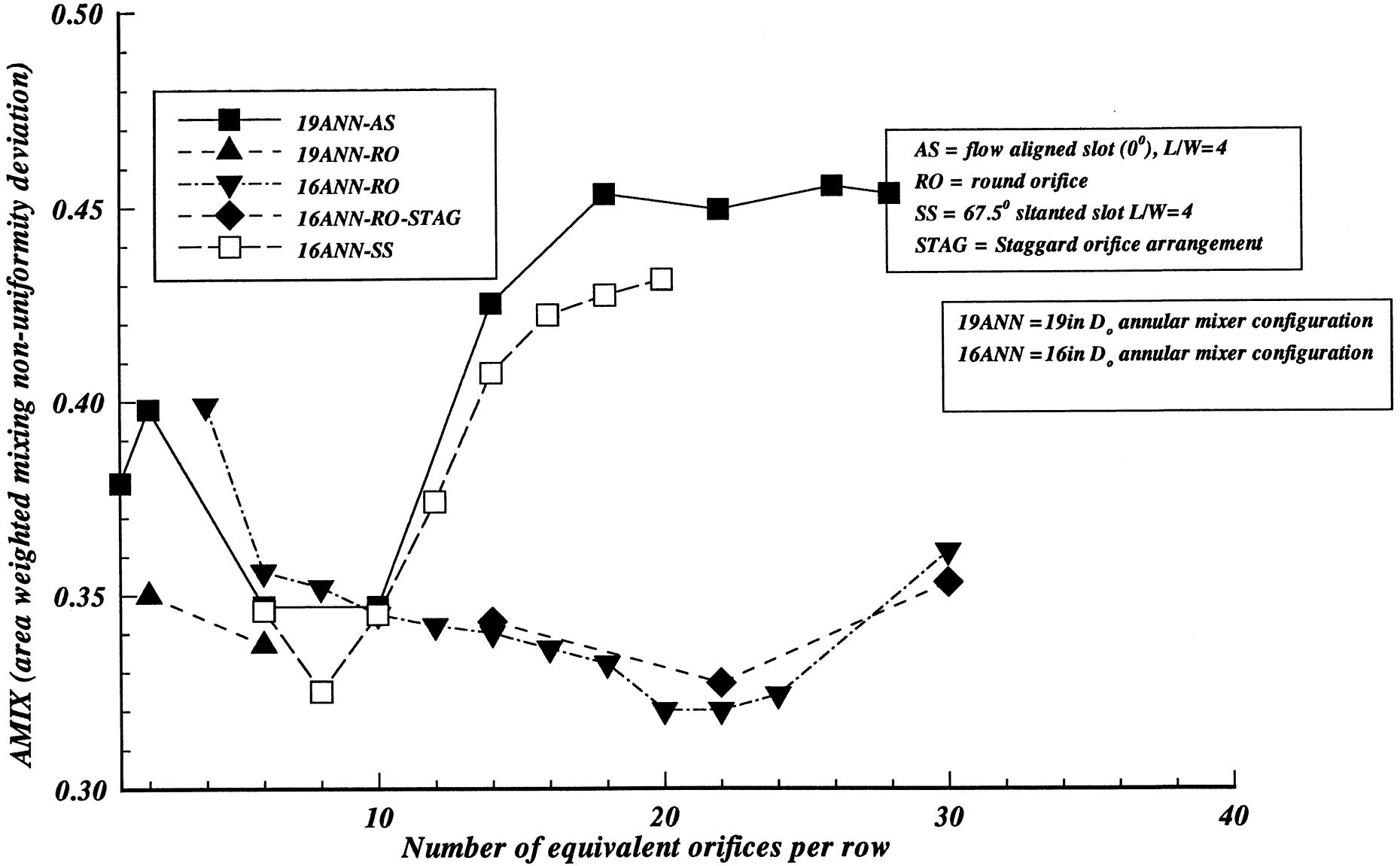

Figure-6. Effect of the variation of the number of orifices on the mixing non-uniformity AMIX for the annular mixers

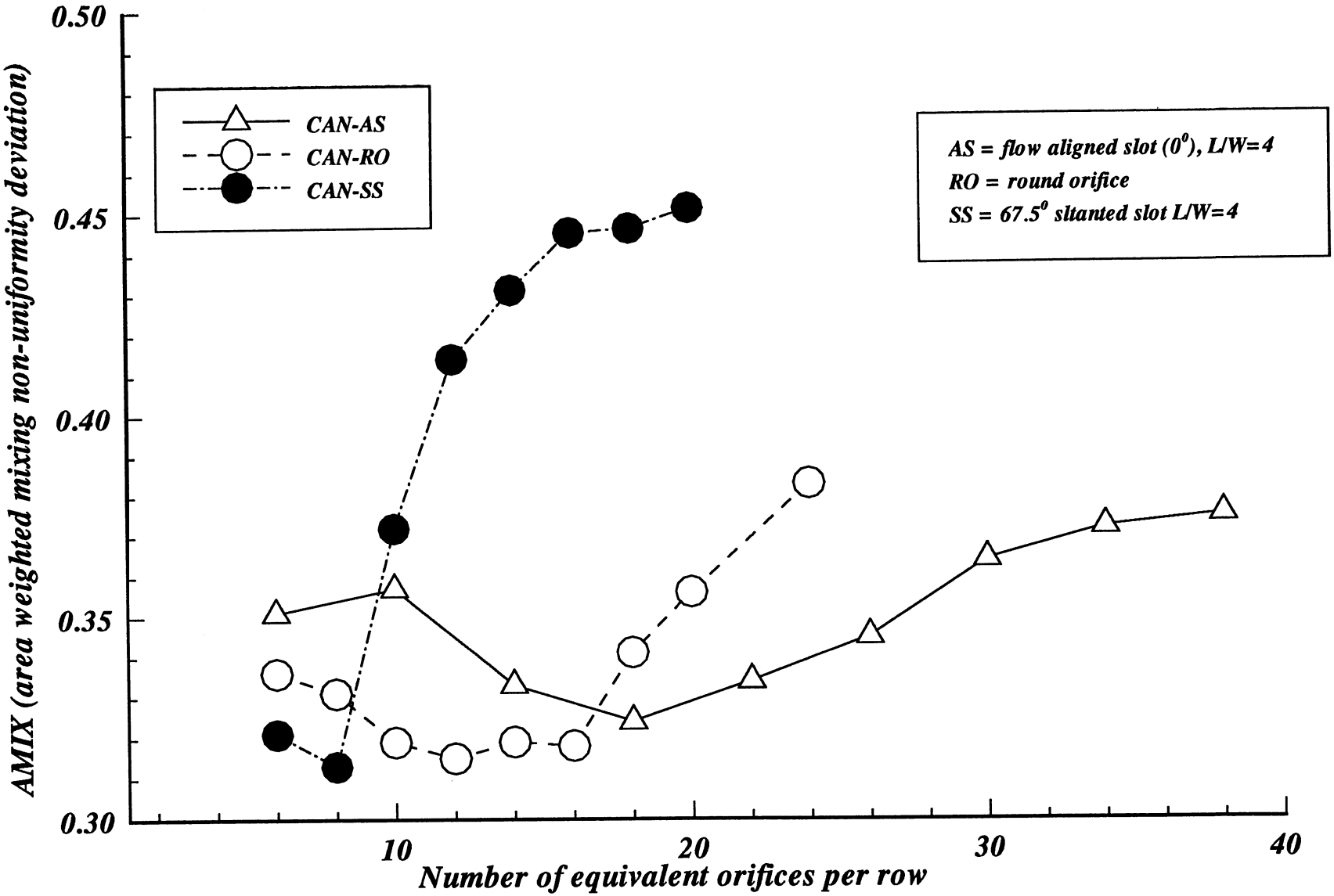

Figure-7. Effect of the variation of the number of orifices on the mixing non-uniformity AMIX for the circular mixer

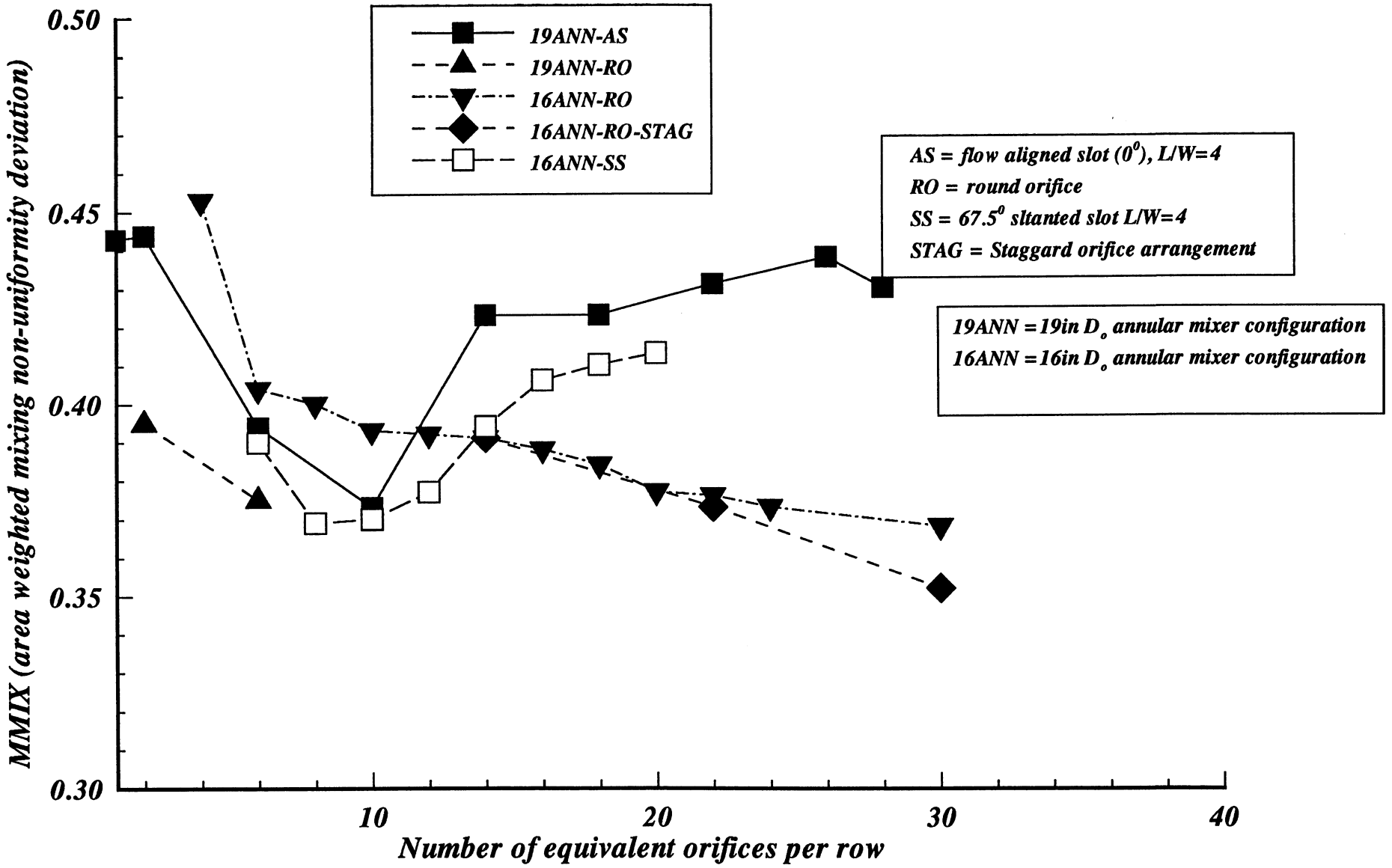

Figure-8. Effect of the variation of the number of orifices on the mixing non-uniformity MMIX for the annular mixers

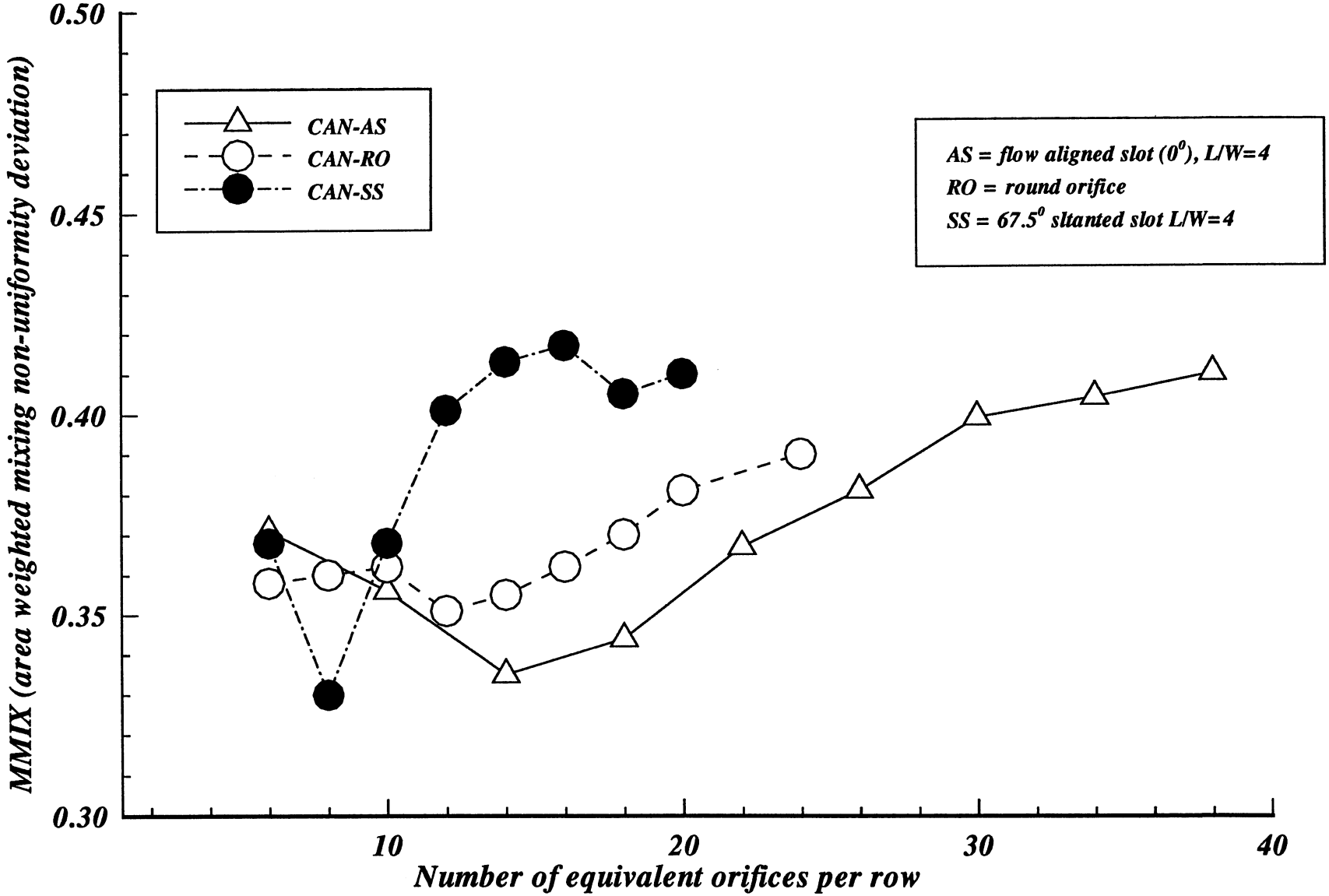

Figure-9. Effect of the variation of the number of orifices on the mixing non-uniformity MMIX for the circular mixer

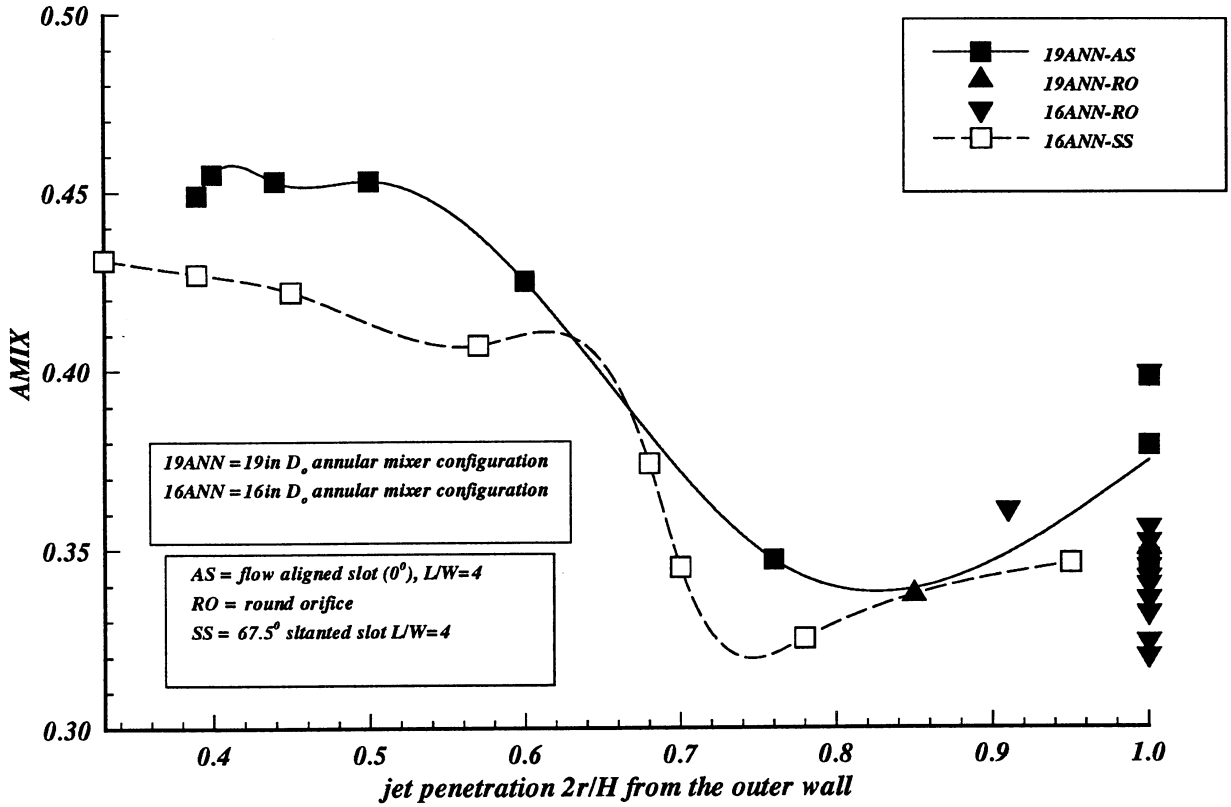

Figure-10a. Correlation between AMIX and jet penetration for the annular mixers

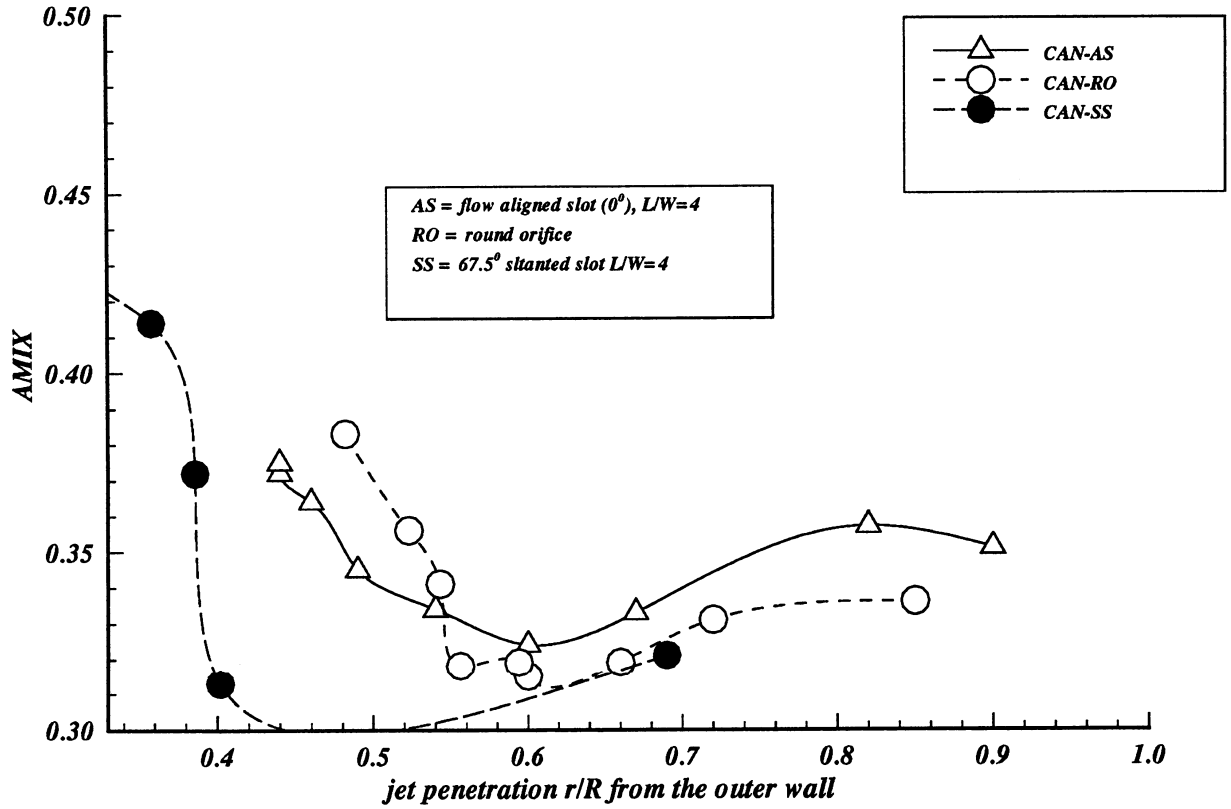

Figure-10b. Correlation between AMIX and jet penetration for the circular mixers

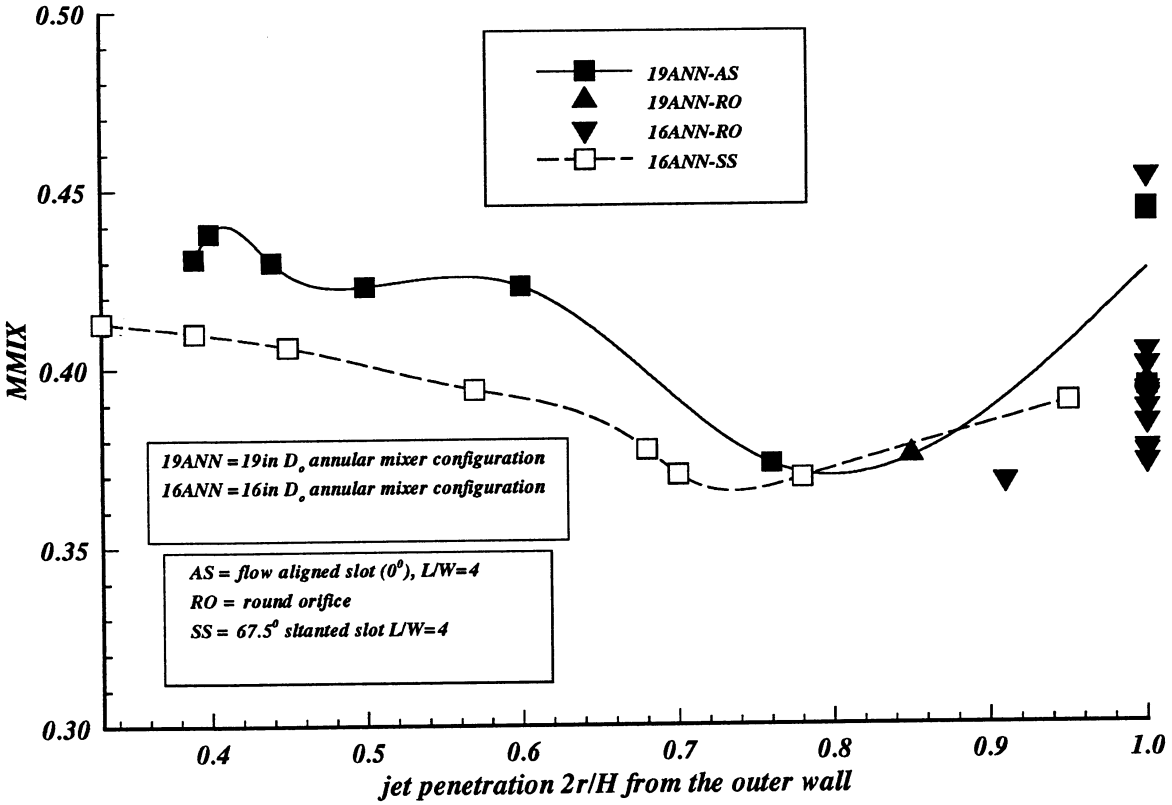

Figure-11a. Correlation between MMIX and jet penetration for the annular mixers

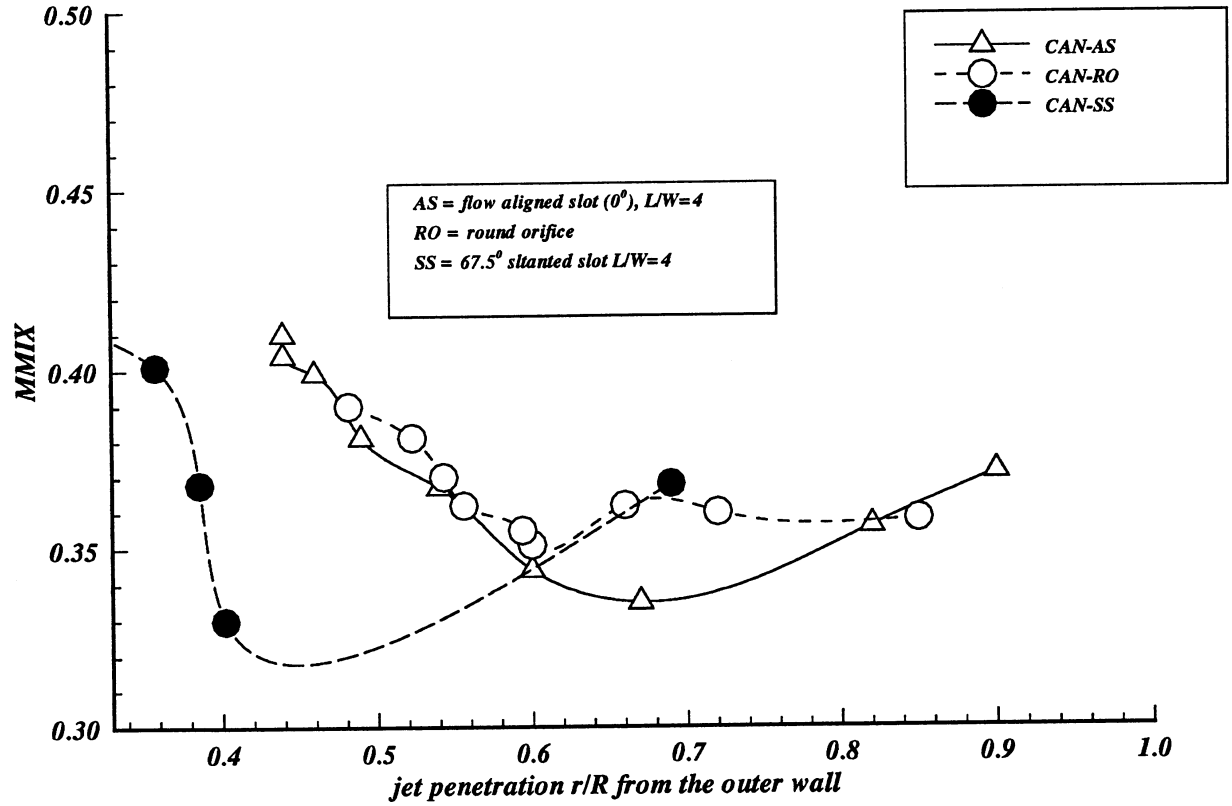

Figure-11b. Correlation between MMIX and jet penetration for the circular mixers

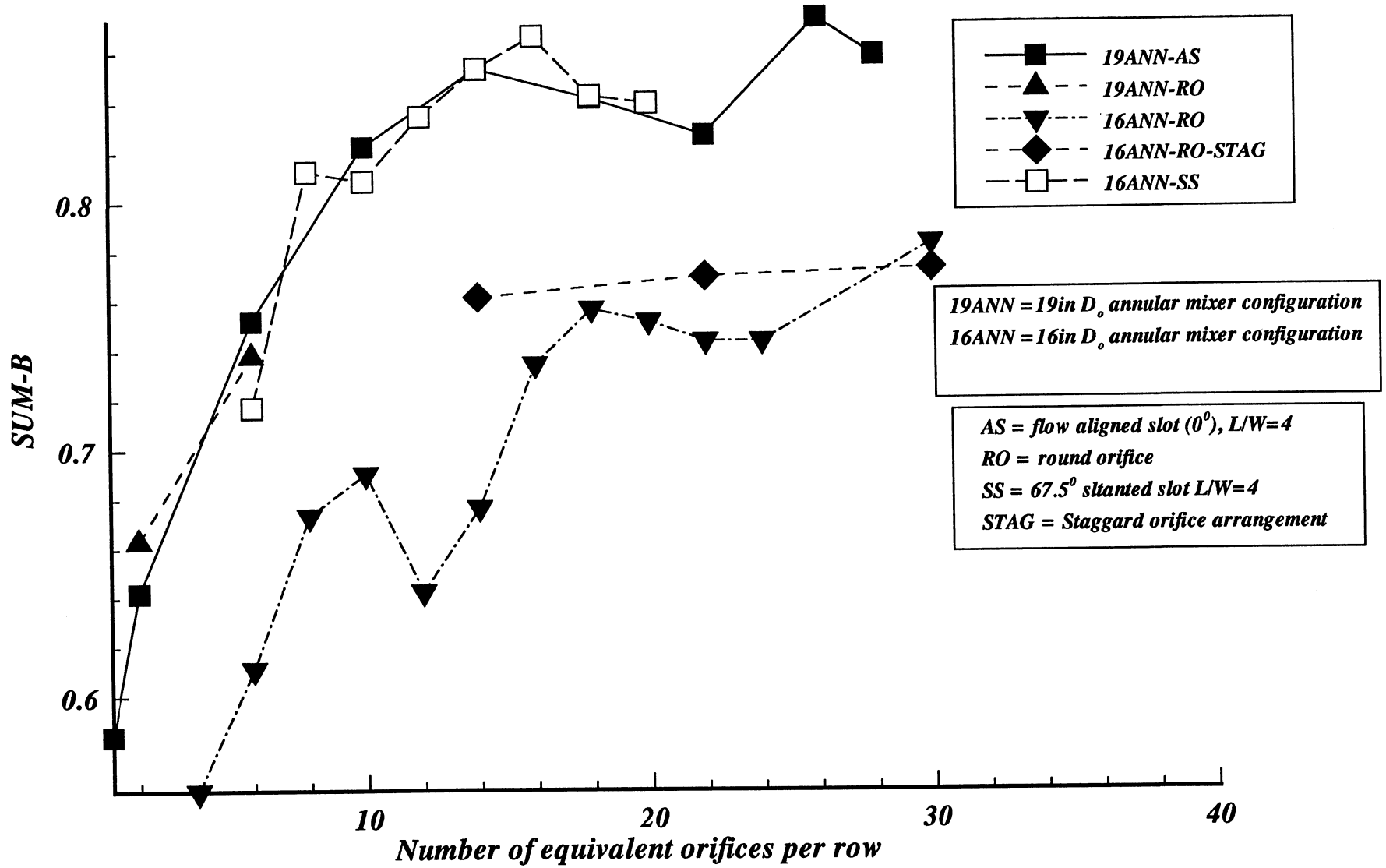

Figure-12. Effect of the variation of the number of orifices on themixing non-uniformity volume histogram shape for the annular mixers

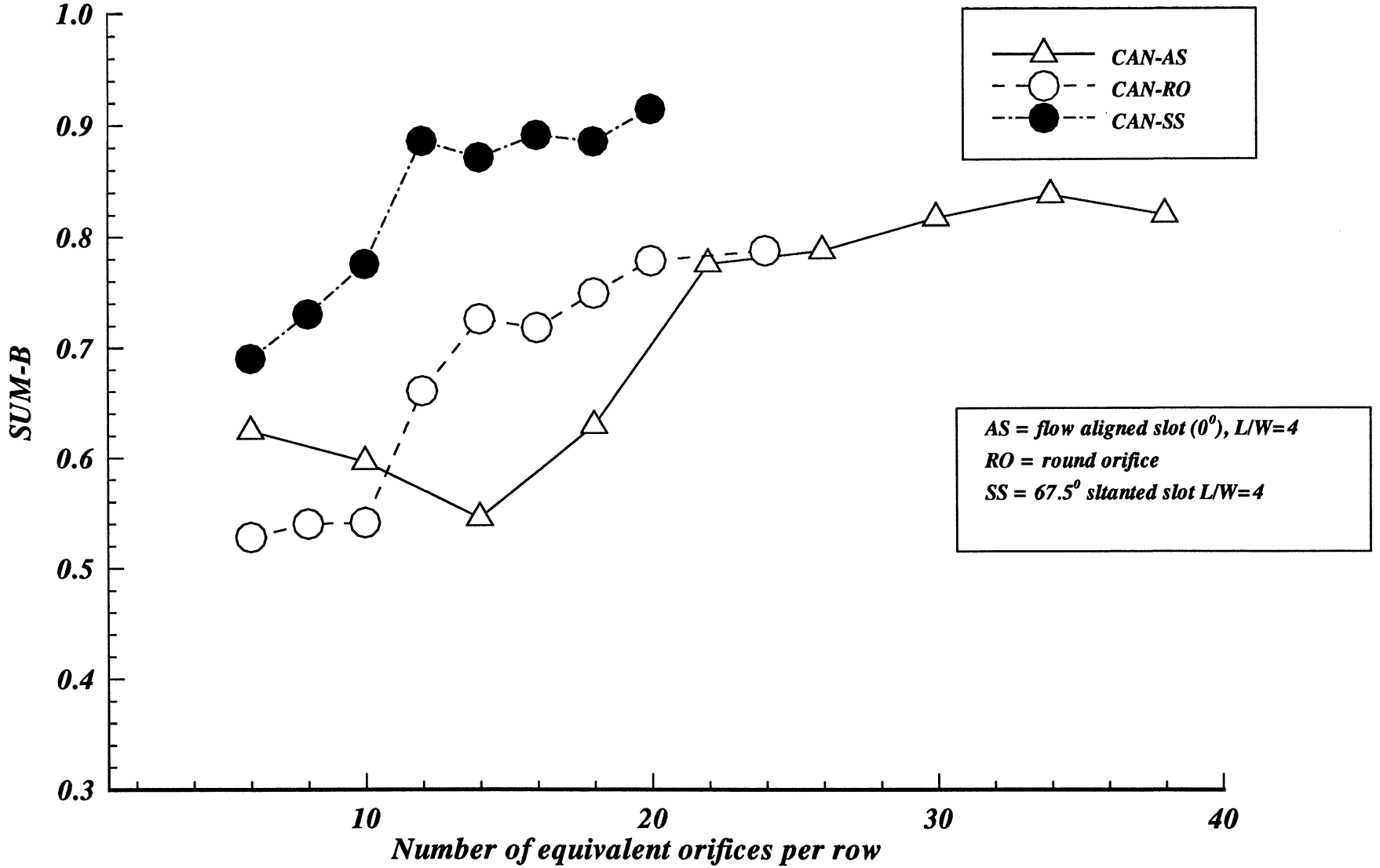

Figure-13. Effect of the variation of the number of orifices on themixing non-uniformity volume histogram shape for the circular mixers

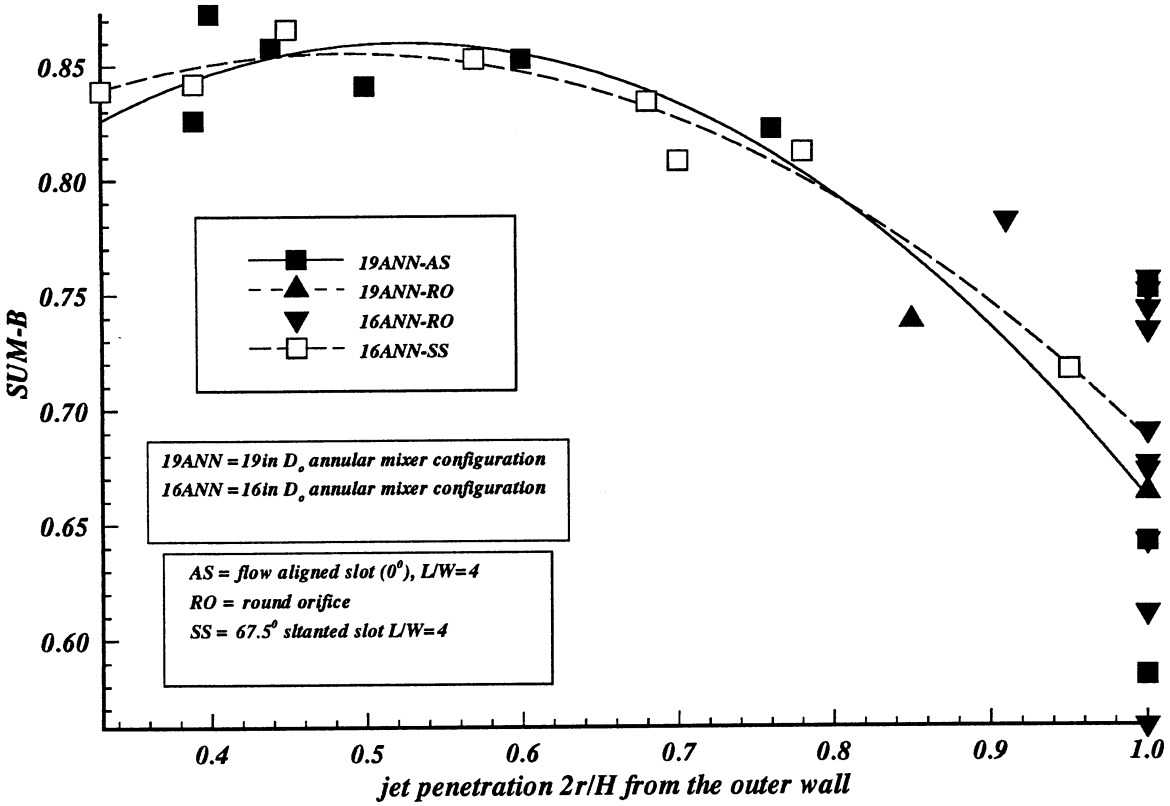

Figure-14a. Correlation between SUM-B and jet penetration for the annular mixers

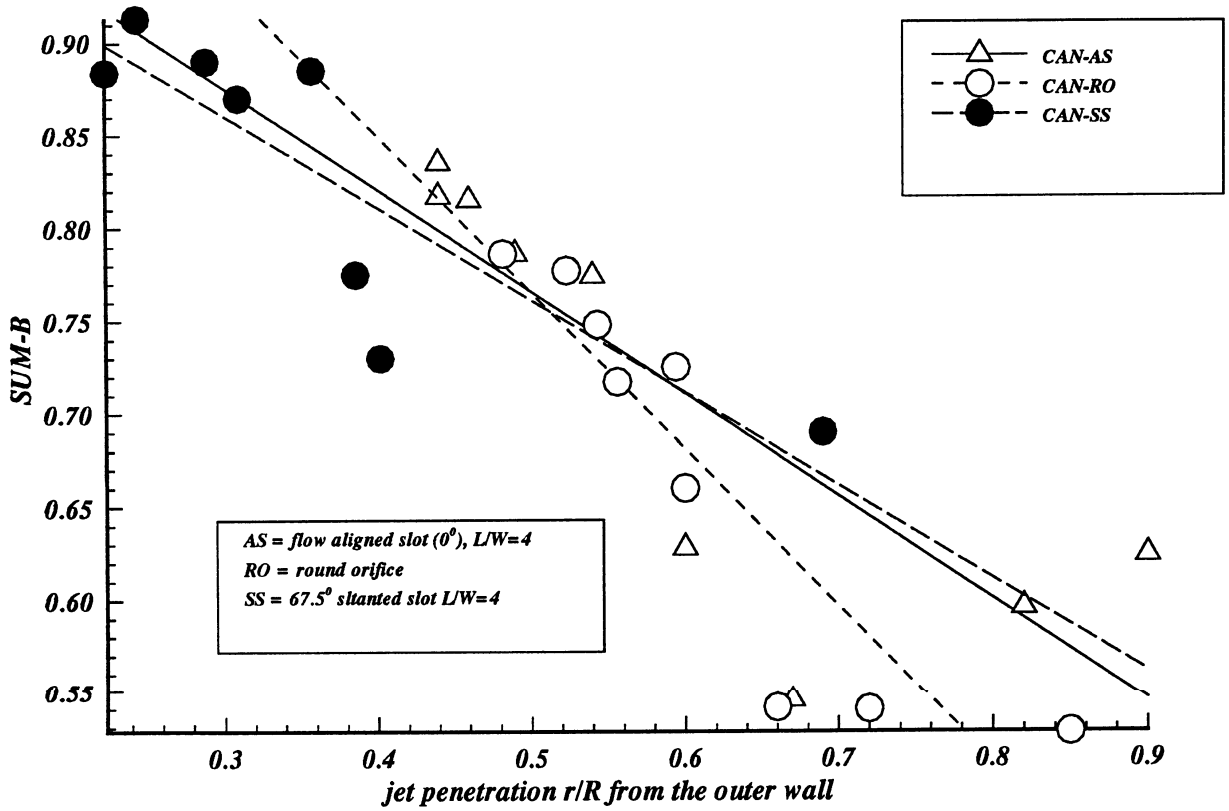

Figure-14b. Correlation between SUM-B and jet penetration for the circular mixer

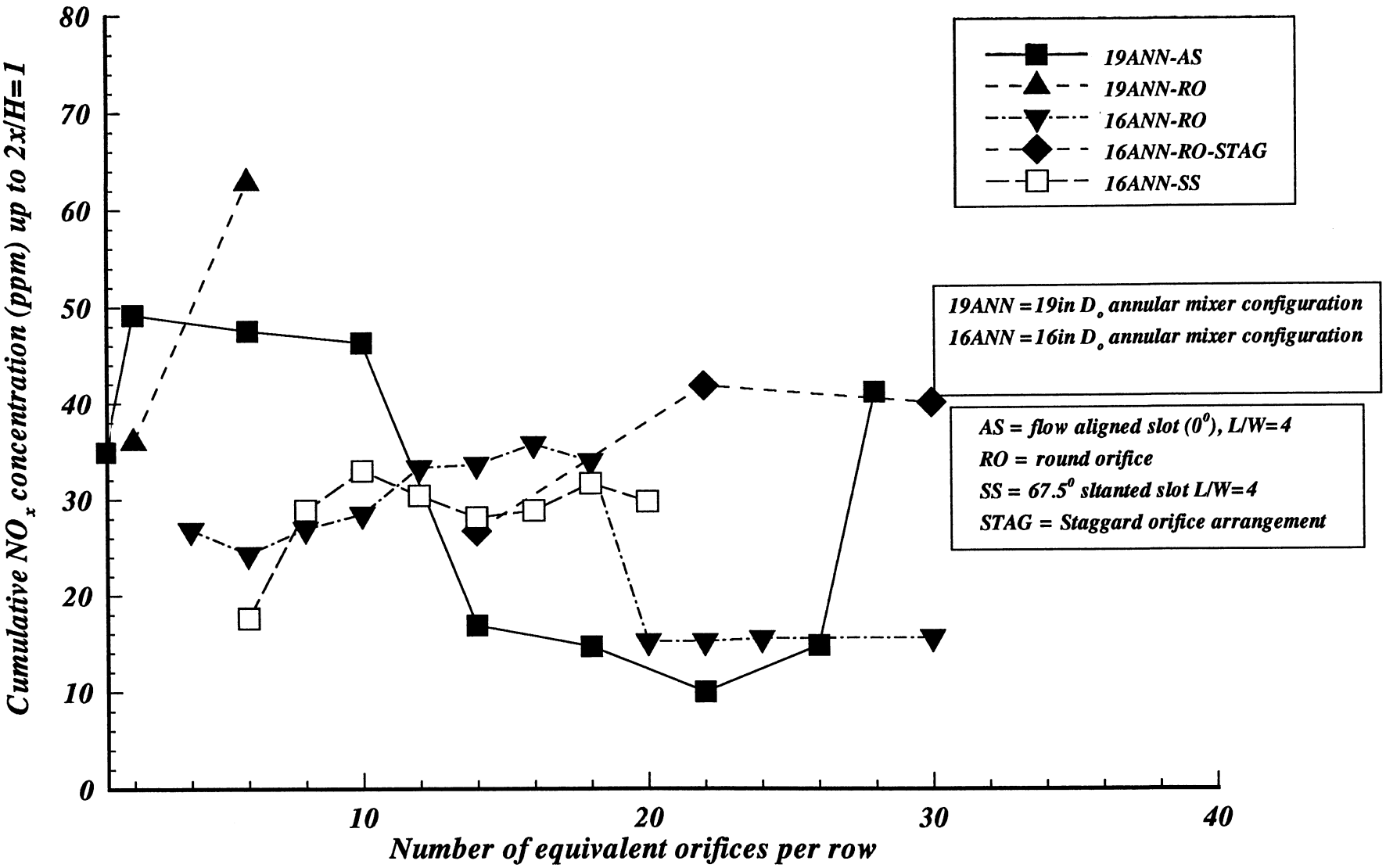

Figure-15. Effect of the variation of the number of orifices on the mixer NOx production for the annular mixers

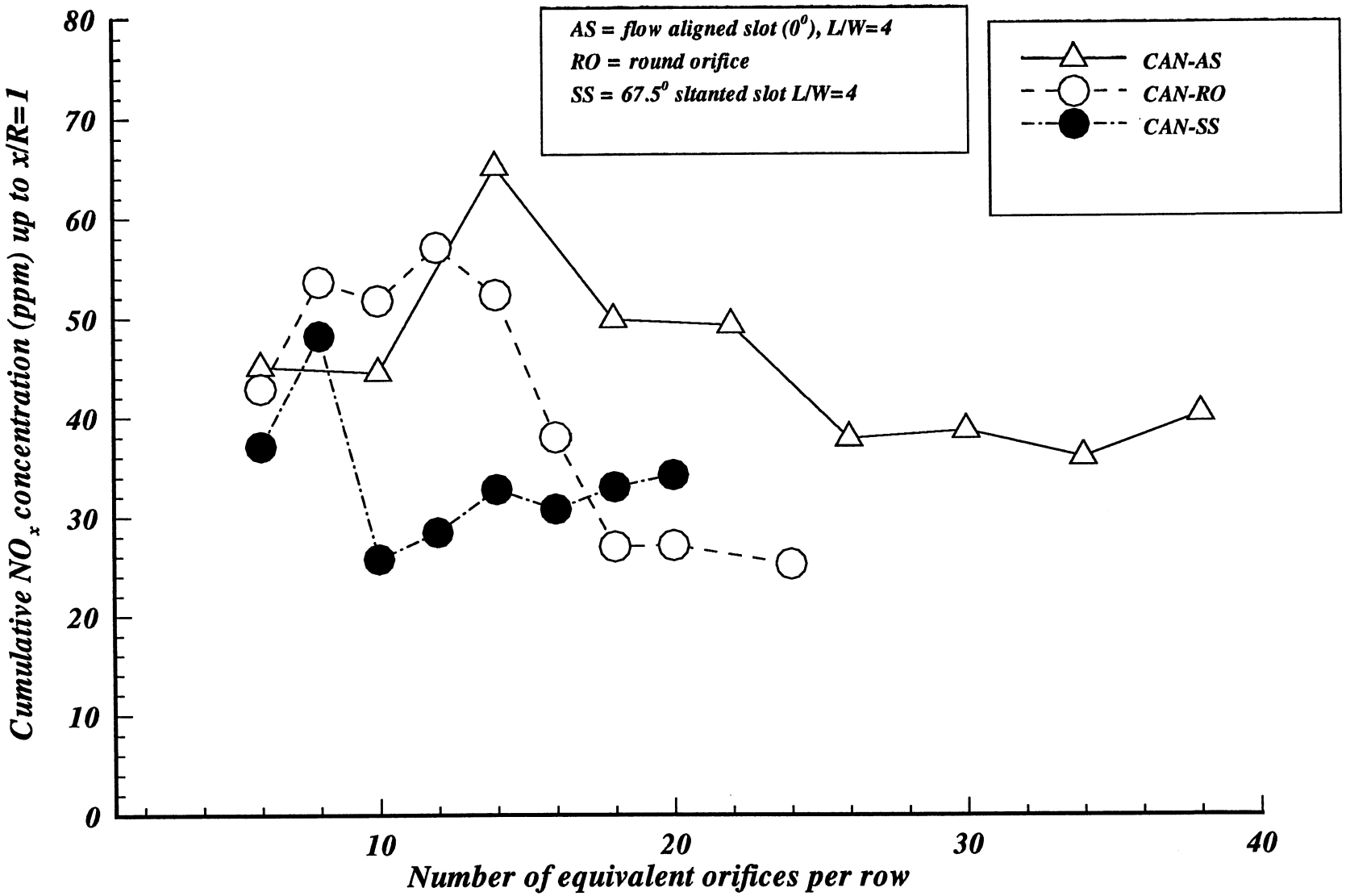

Figure-16. Effect of the variation of the number of orifices on the mixer NOx production for the circular mixers

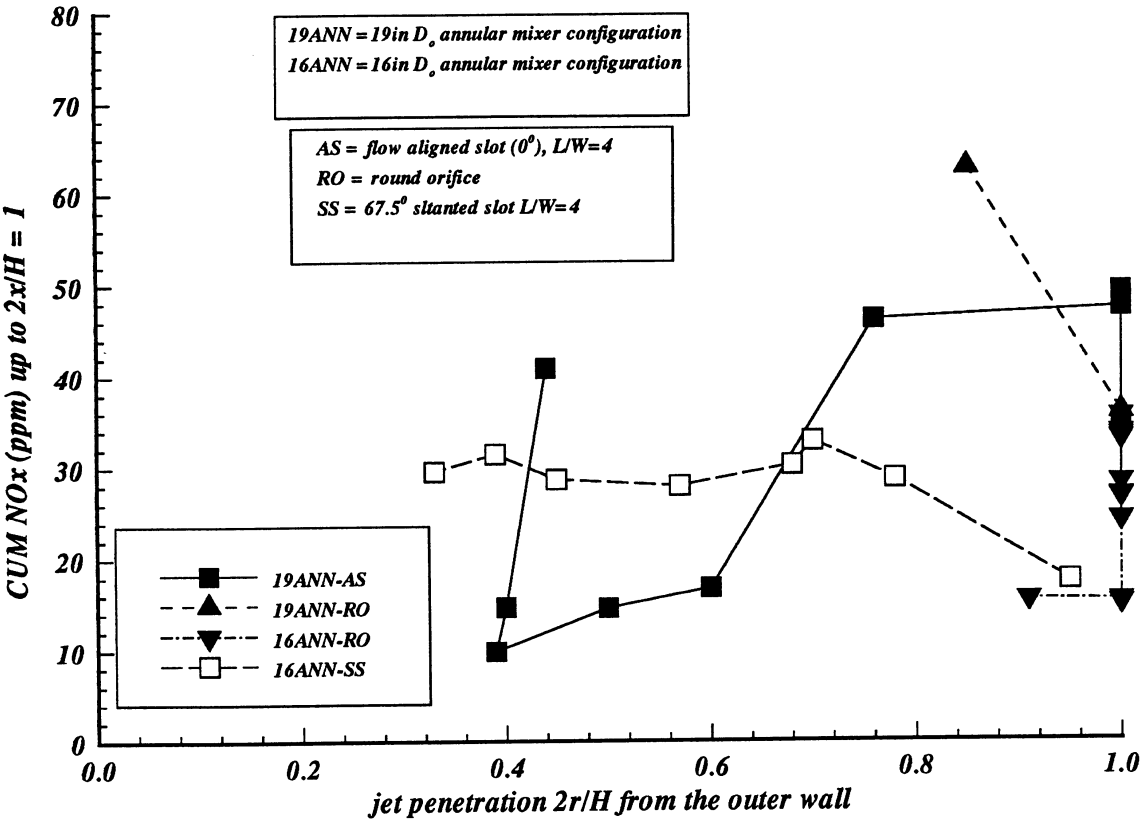

Figure-17a. Correlation between CUM-NOx and jet penetration for the annular mixers

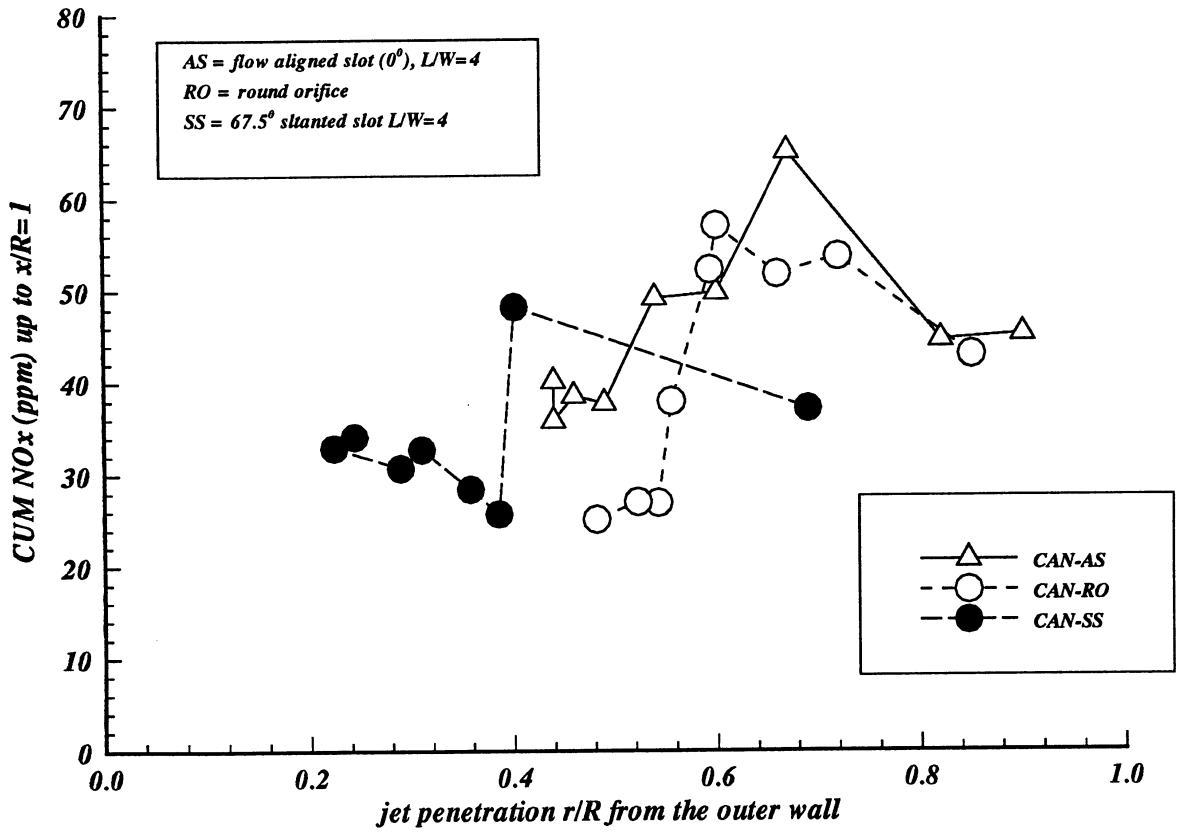

Figure-17b. Correlation between CUM NOx and jet penetration for the circular mixer

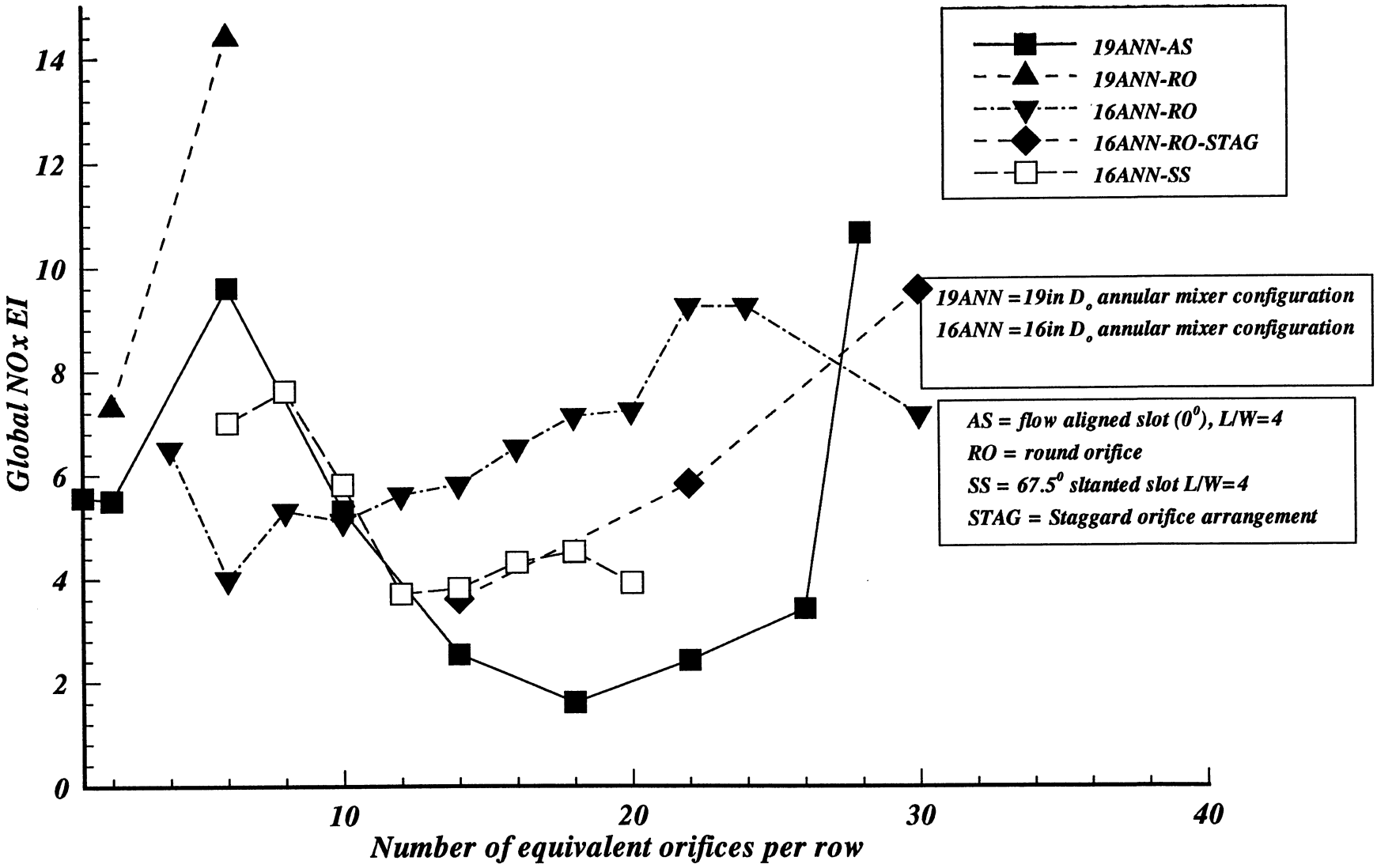

Figure-18. Effect of the variation of the number of orifices on the global NOx production for the annular mixers

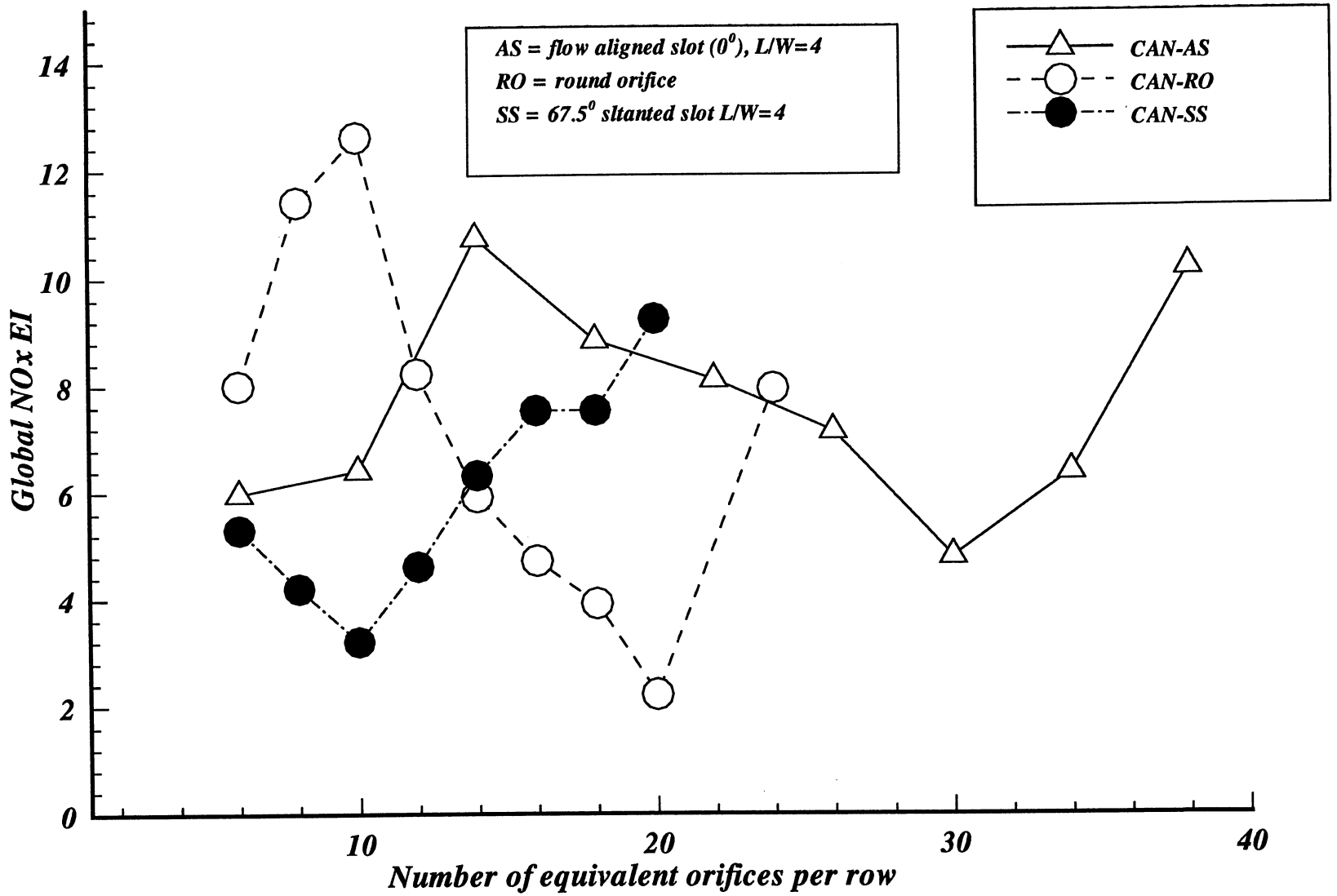

Figure-19. Effect of the variation of the number of orifices on the global NOx production for the circular mixers

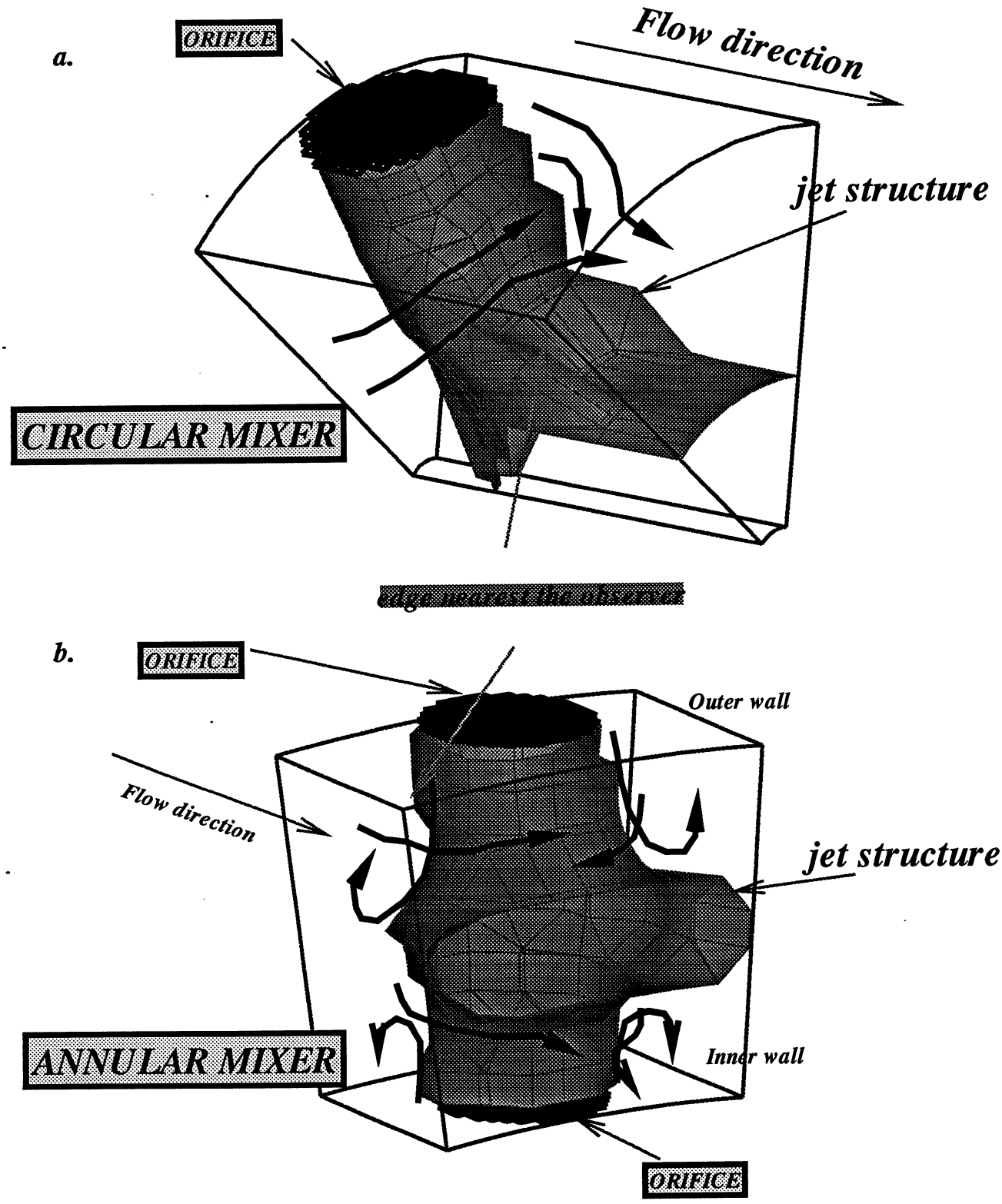

Figure-20. Mixing modes for the circular (a) and annular (b) mixer types with representative round orifices

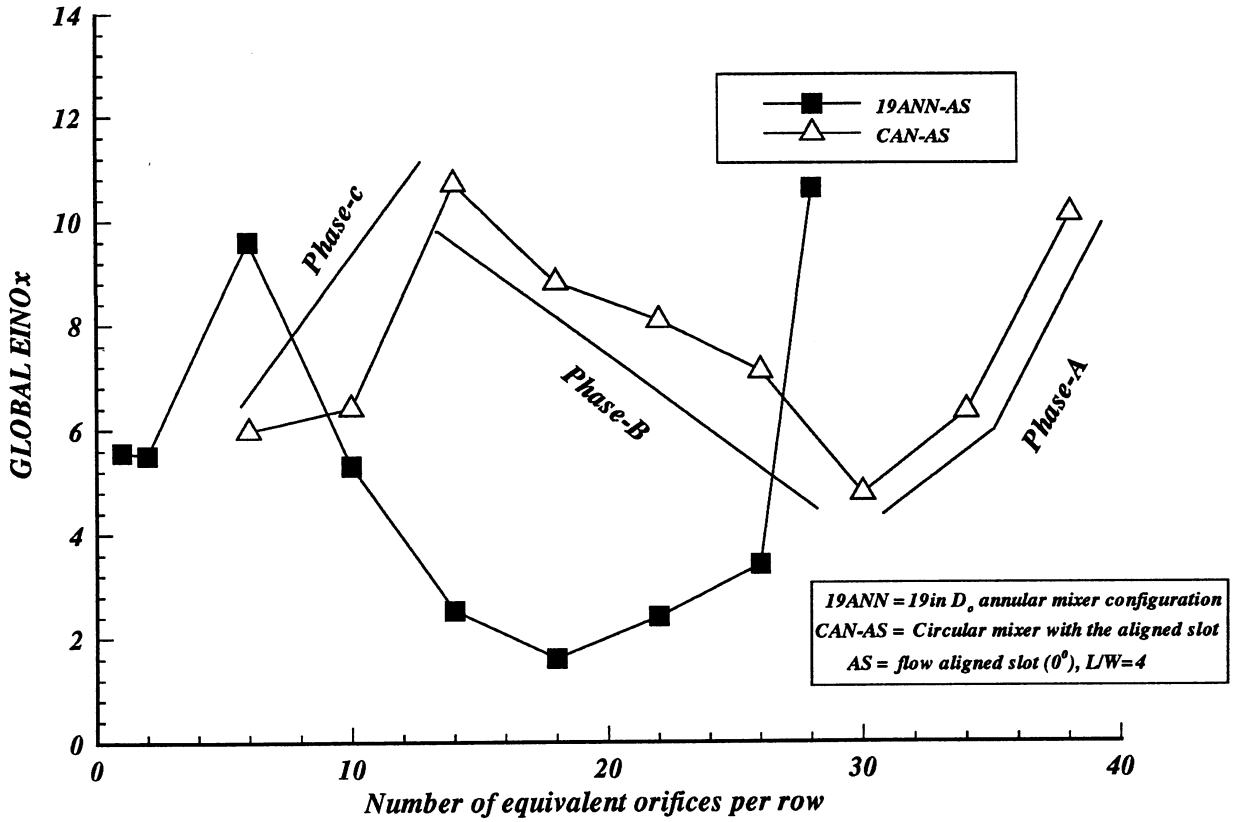

Figure-21a. Comparison between the performance of the annular and circular mixers with the aligned slot

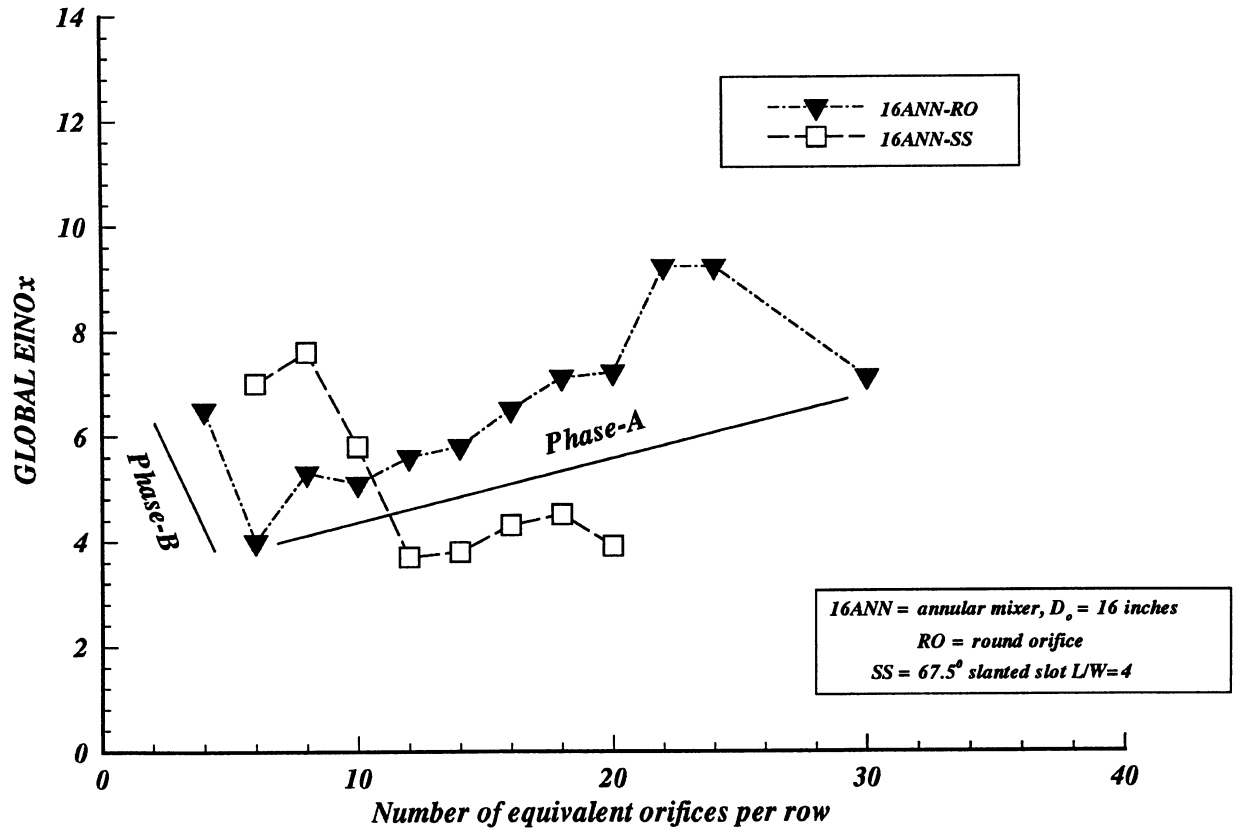

Figure-21b. Comparison between the performance of the annular mixer with round and slanted slot orifices

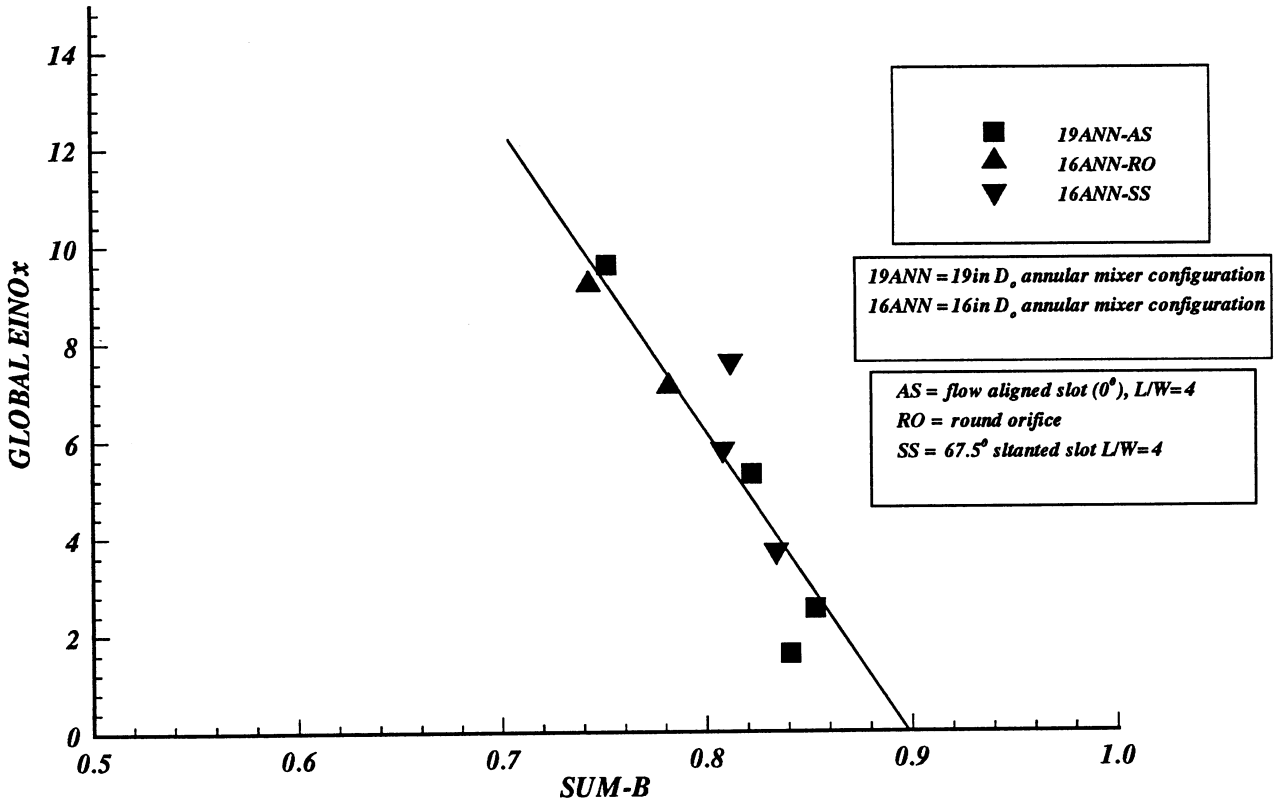

Figure-22a. Correlation between the NOx production and mixing non-uniformity (SUM-B) for the annular mixers (phase-b) trend

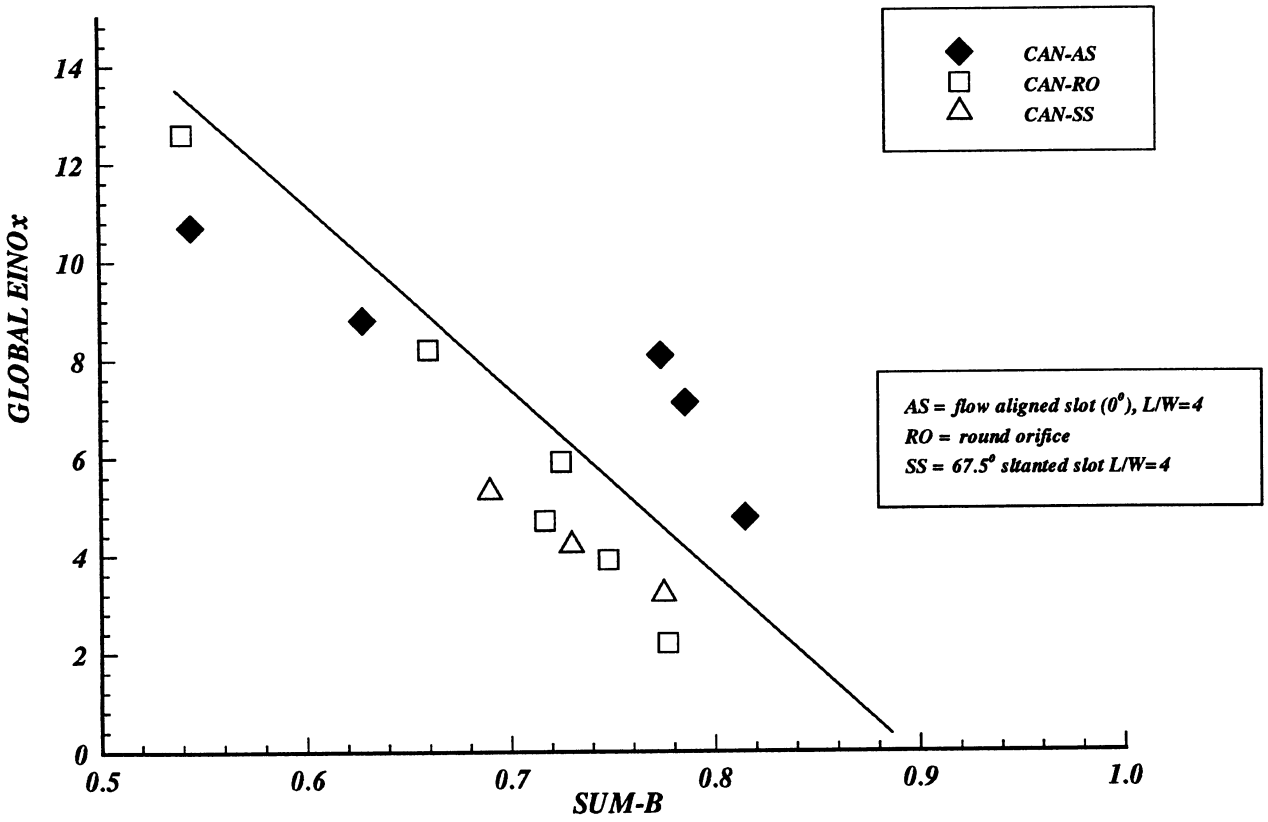

Figure-22b. Correlation between the NOx production and mixing non-uniformity (SUM-B) for the circular mixers (phase-b) trend

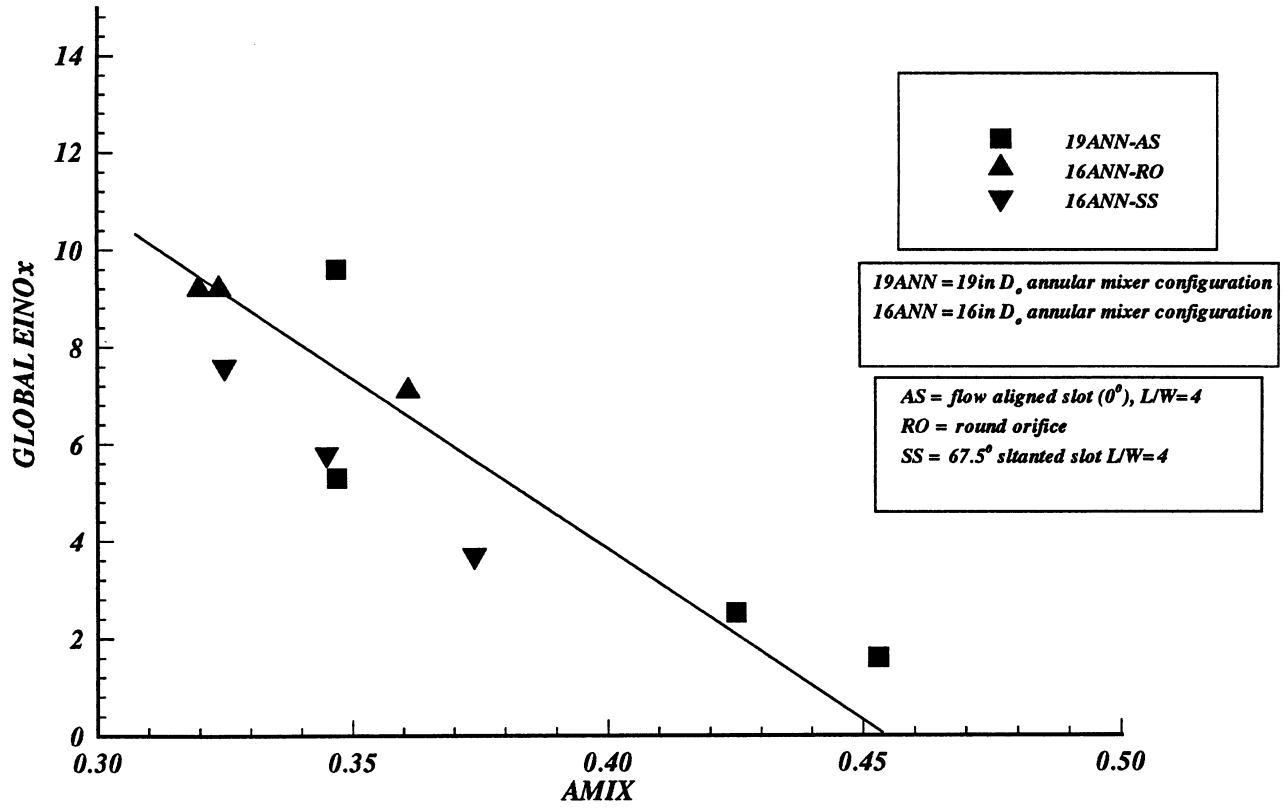

Figure-23a. Correlation between the NOx production and mixing non-uniformity (AMIX) for the annular mixers (phase-b) trend

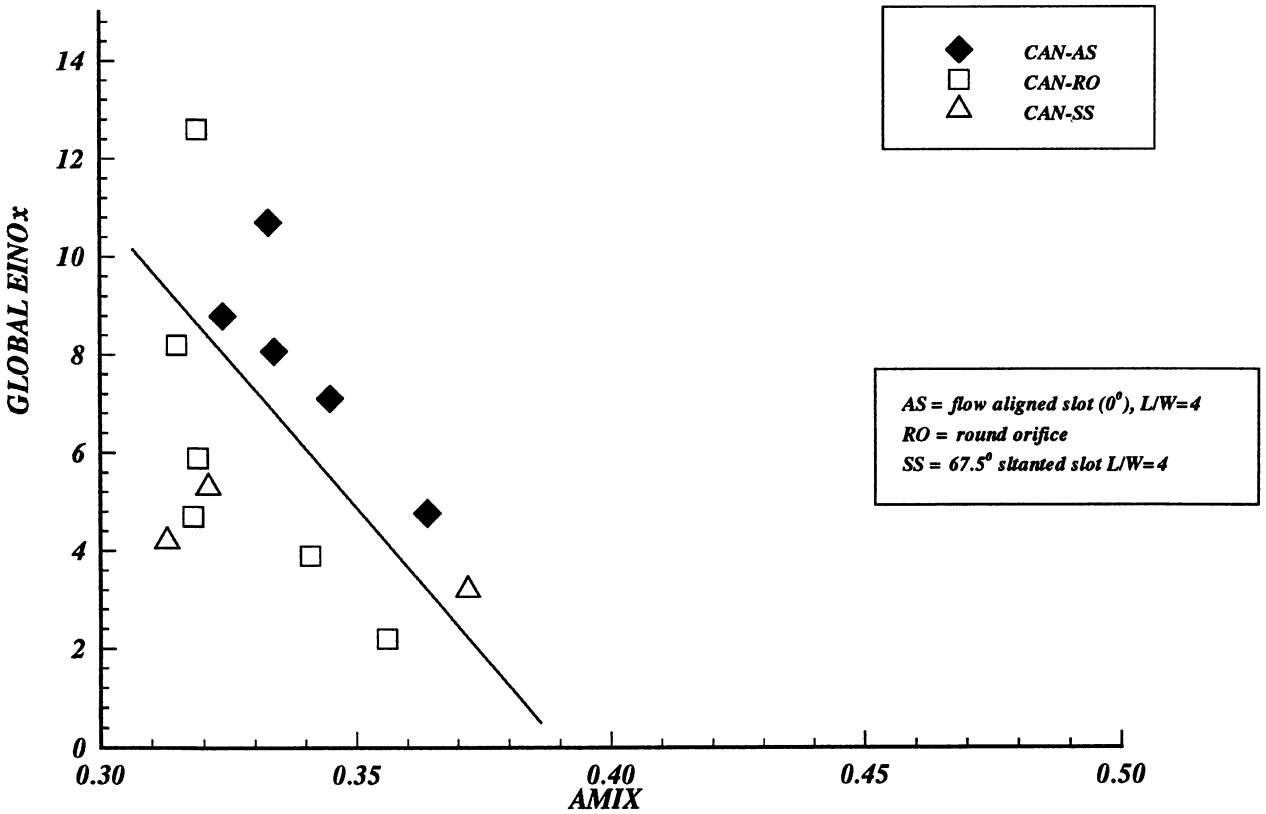

Figure-23b. Correlation between the NOx production and mixing non-uniformity (AMIX) for the circular mixers (phase-b) trend

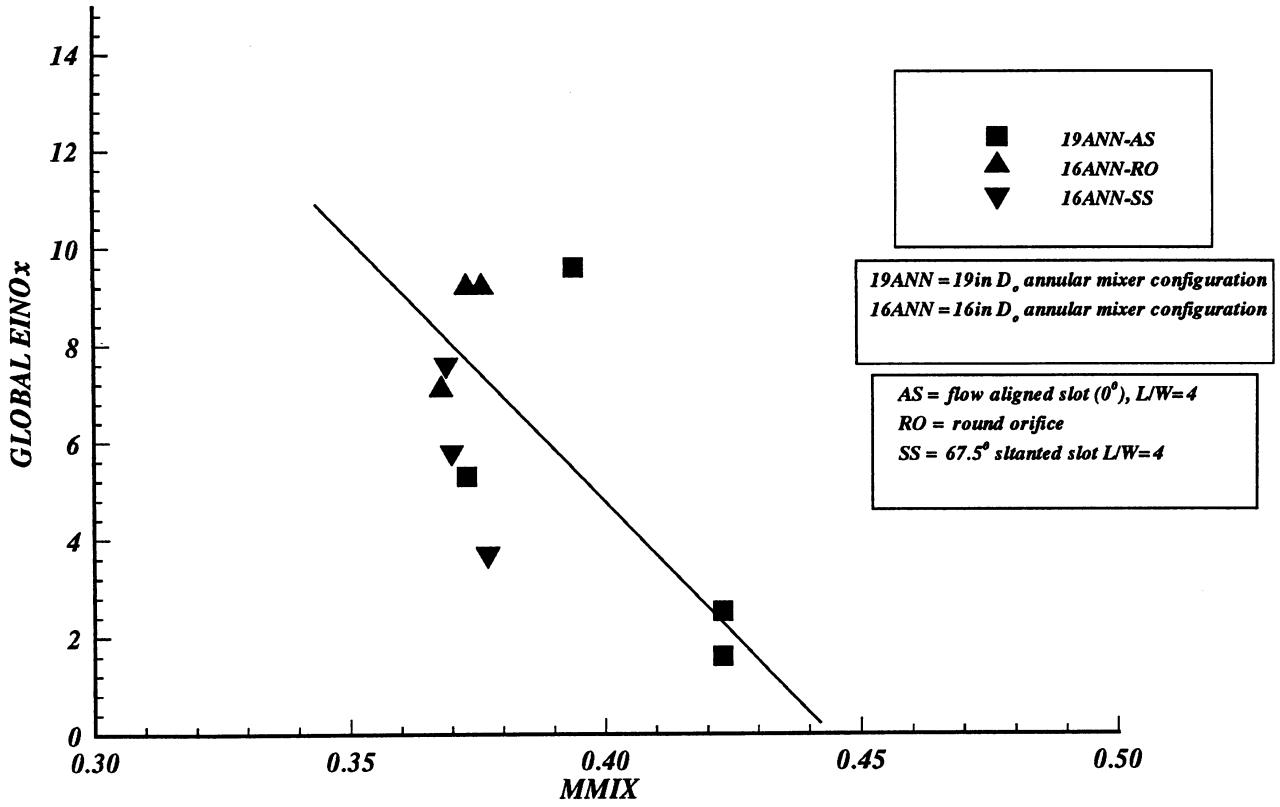

Figure-24a. Correlation between the NOx production and mixing non-uniformity (MMIX) for the annular mixers (phase-b) trend

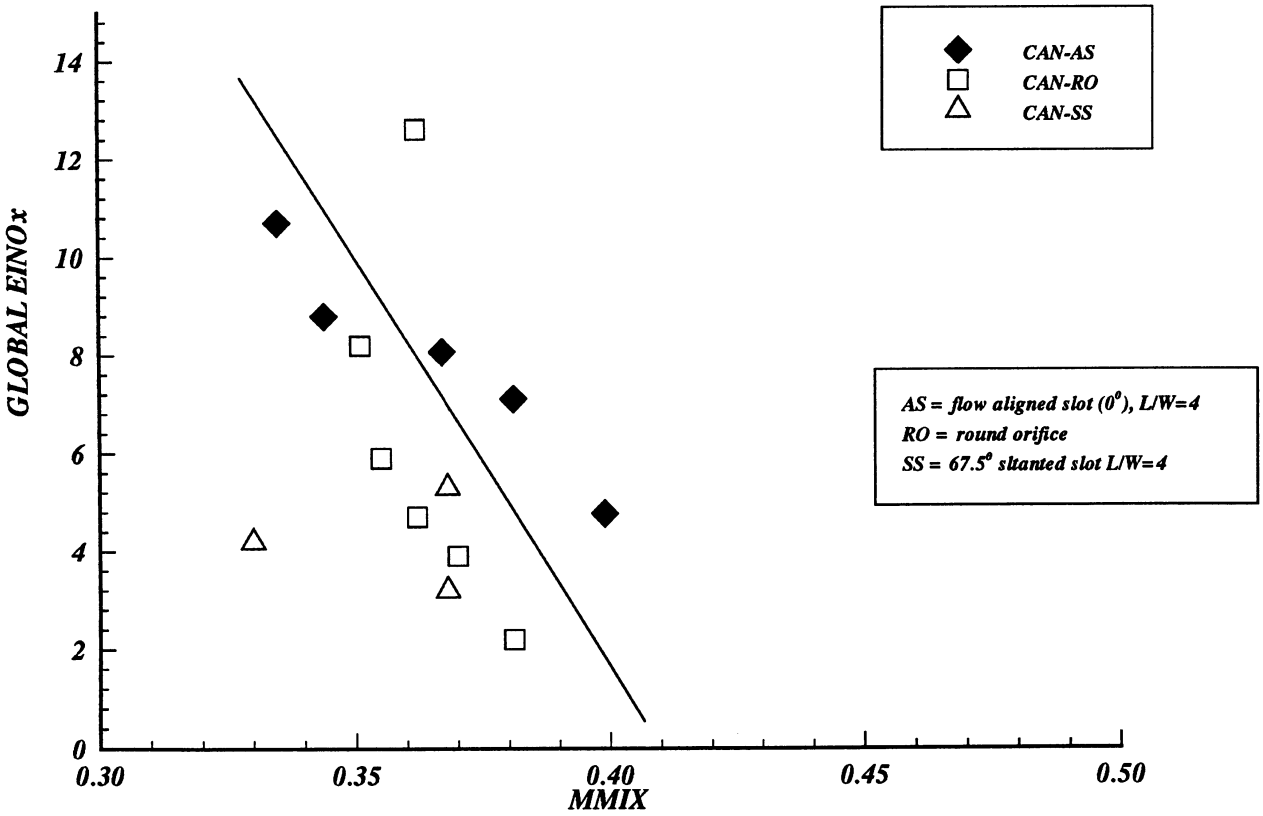

Figure-24b. Correlation between the NOx production and mixing non-uniformity (MMIX) for the circular mixers (phase-b) trend

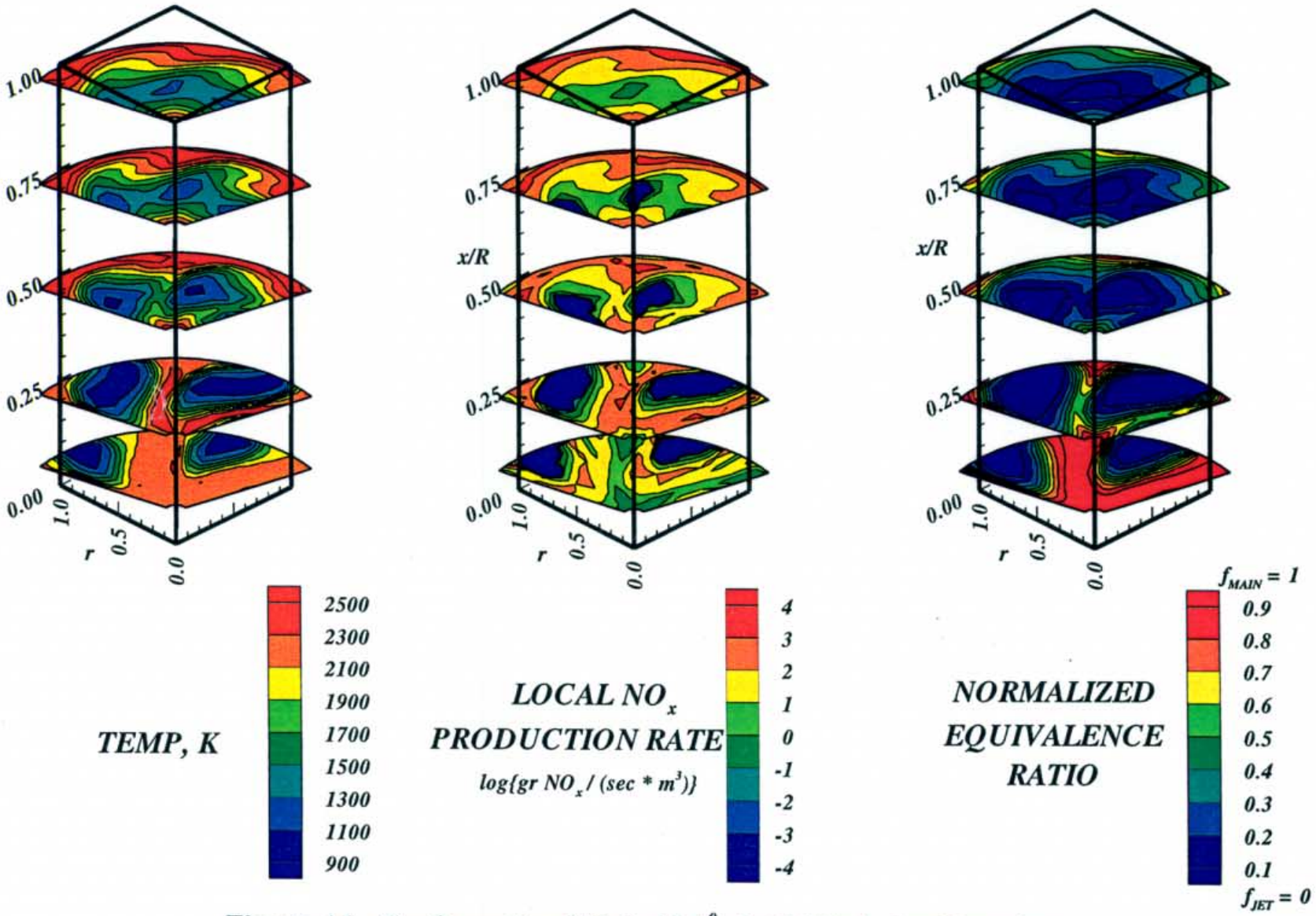

Figure-A1. Configuration HO-1, 67.5^0 slot L/W=4, 6 orifices /row
J=52.0, MR=2.96, DR=2.28, ϕ_{RZ} = 1.80, ϕ_{LZ} = 0.416 (2-adjacent sectors)

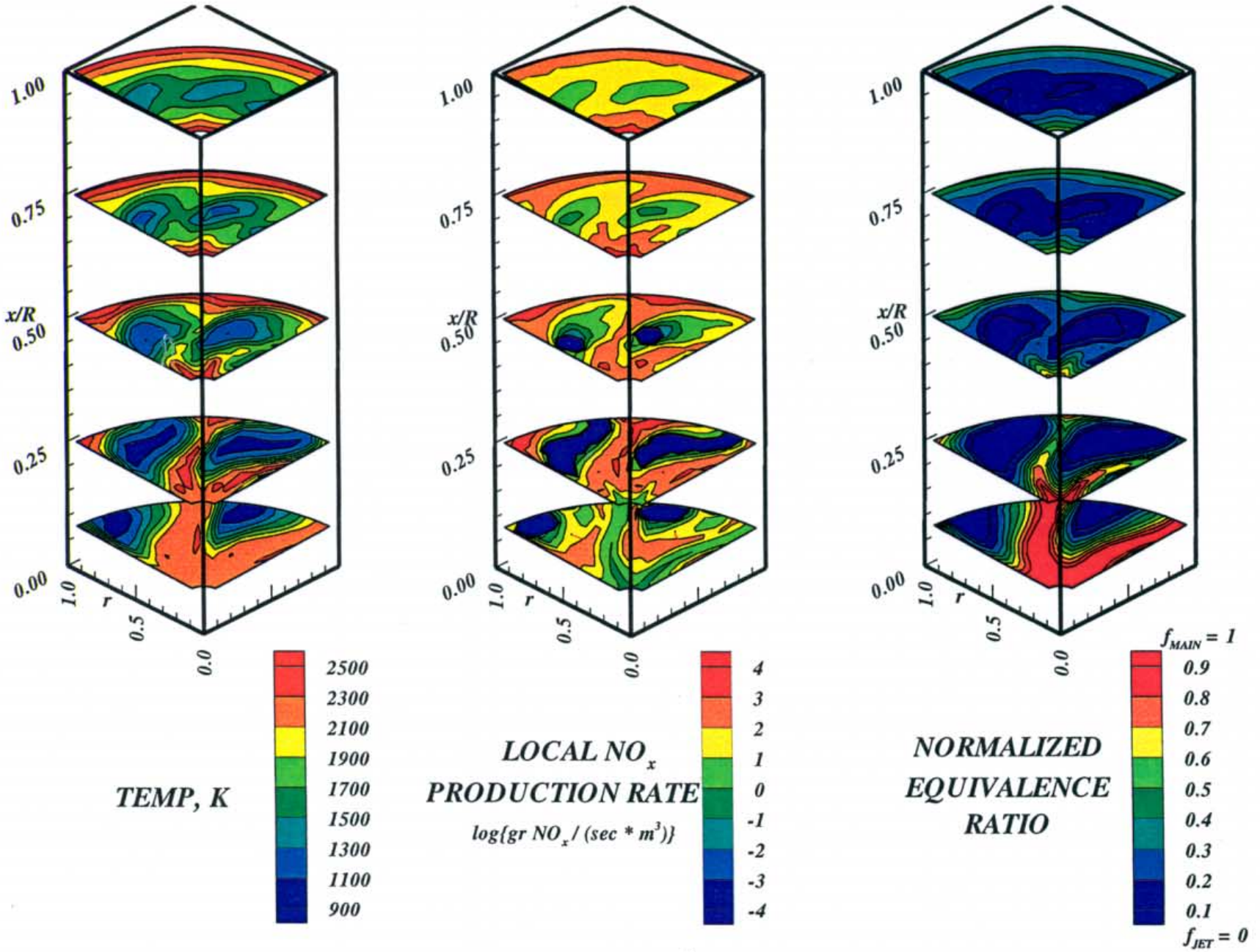

Figure-A2. Configuration HO-2, 67.5^0 slot L/W=4, 8 orifices /row

J=52.0, MR=2.96, DR=2.28, ϕ_{RZ} = 1.80, ϕ_{LZ} = 0.416 (2-adj acent sectors)

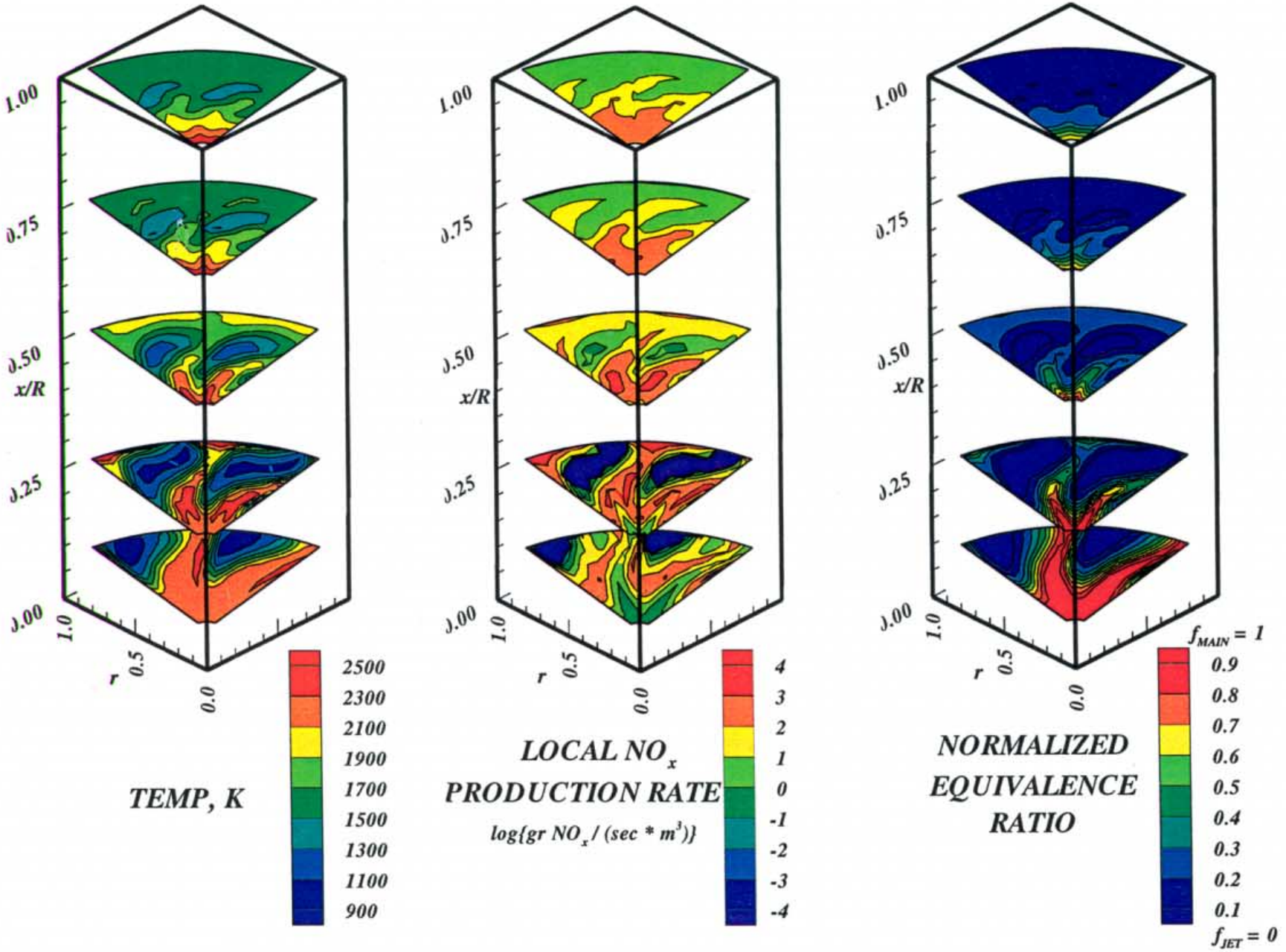

Figure-A3. Configuration HO-3, 67.5^0 slot L/W=4, 10 orifices /row

J=52.0, MR=2.96, DR=2.28, ϕ_{RZ} = 1.80, ϕ_{LZ} = 0.416 (2-adj acent sectors)

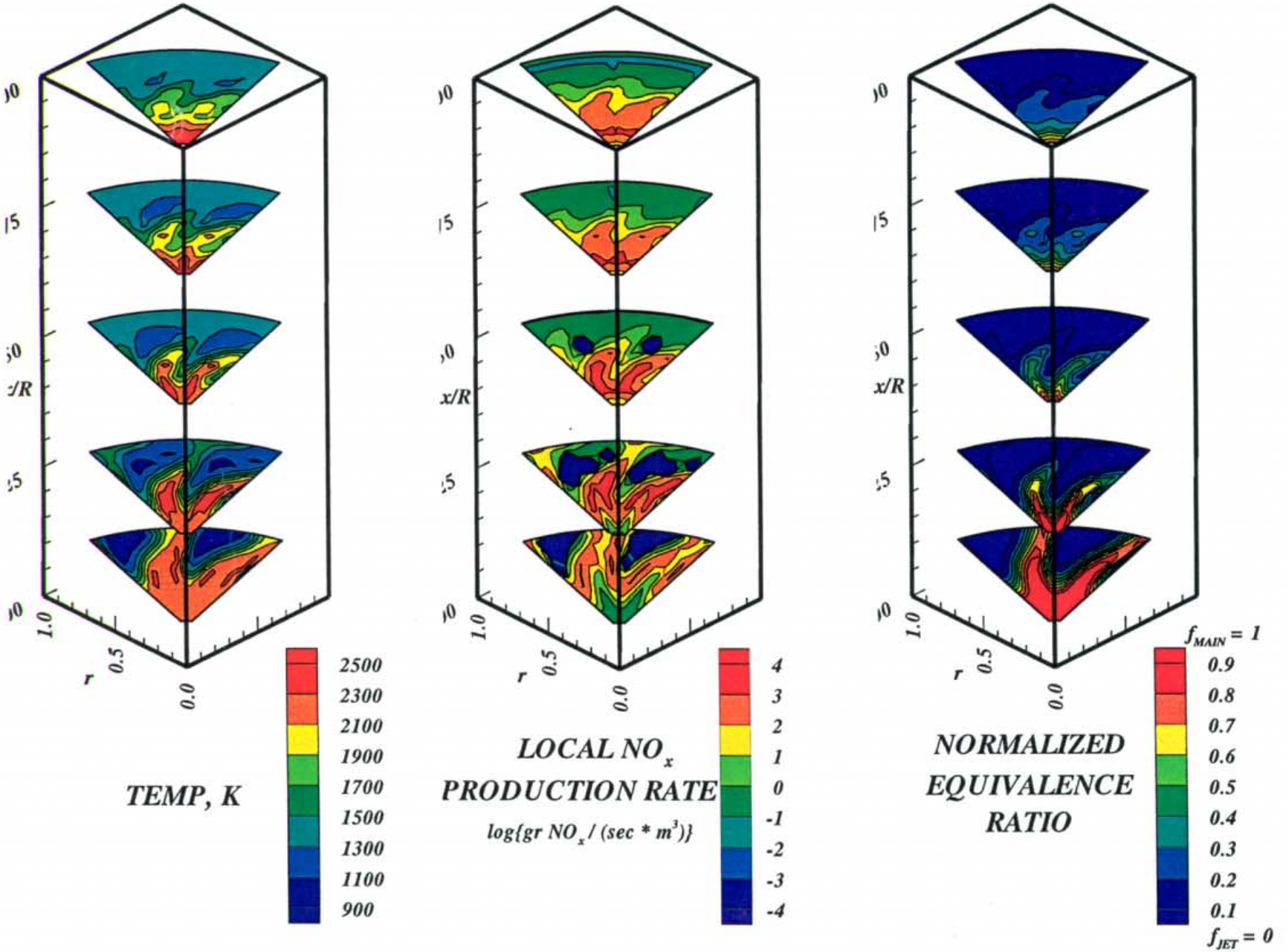

Figure-A4. Configuration HO-4, 67.5^0 slot L/W=4, 12 orifices /row
J=52.0, MR=2.96, DR=2.28, ϕ_{RZ} = 1.80, ϕ_{LZ} = 0.416 (2-adjacent sectors)

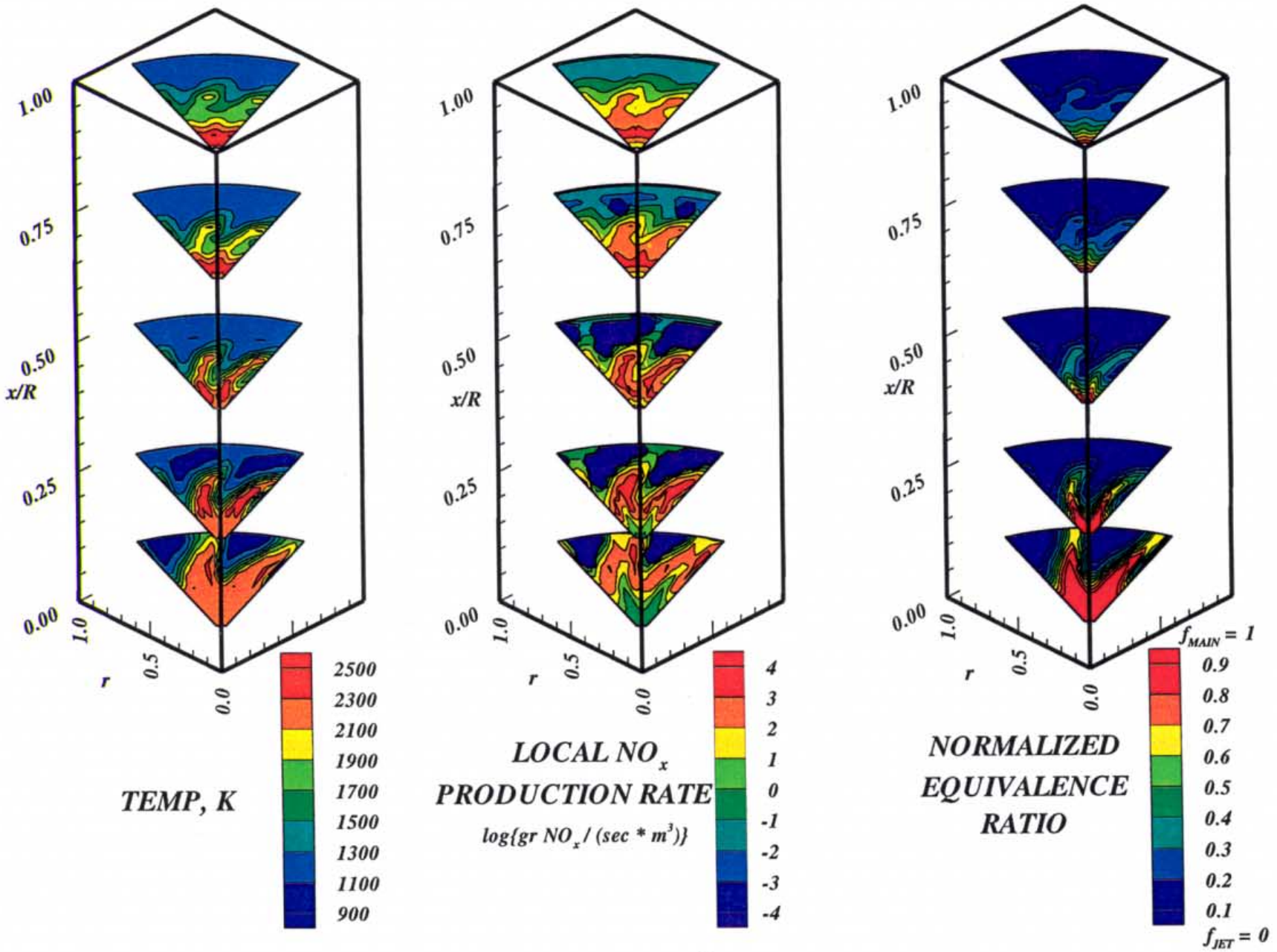

Figure-A5. Configuration HO-5, 67.5^0 slot L/W=4, 14 orifices /row
J=52.0, MR=2.96, DR=2.28, ϕ_{RZ} = 1.80, ϕ_{LZ} = 0.416 (2-adjacent sectors)

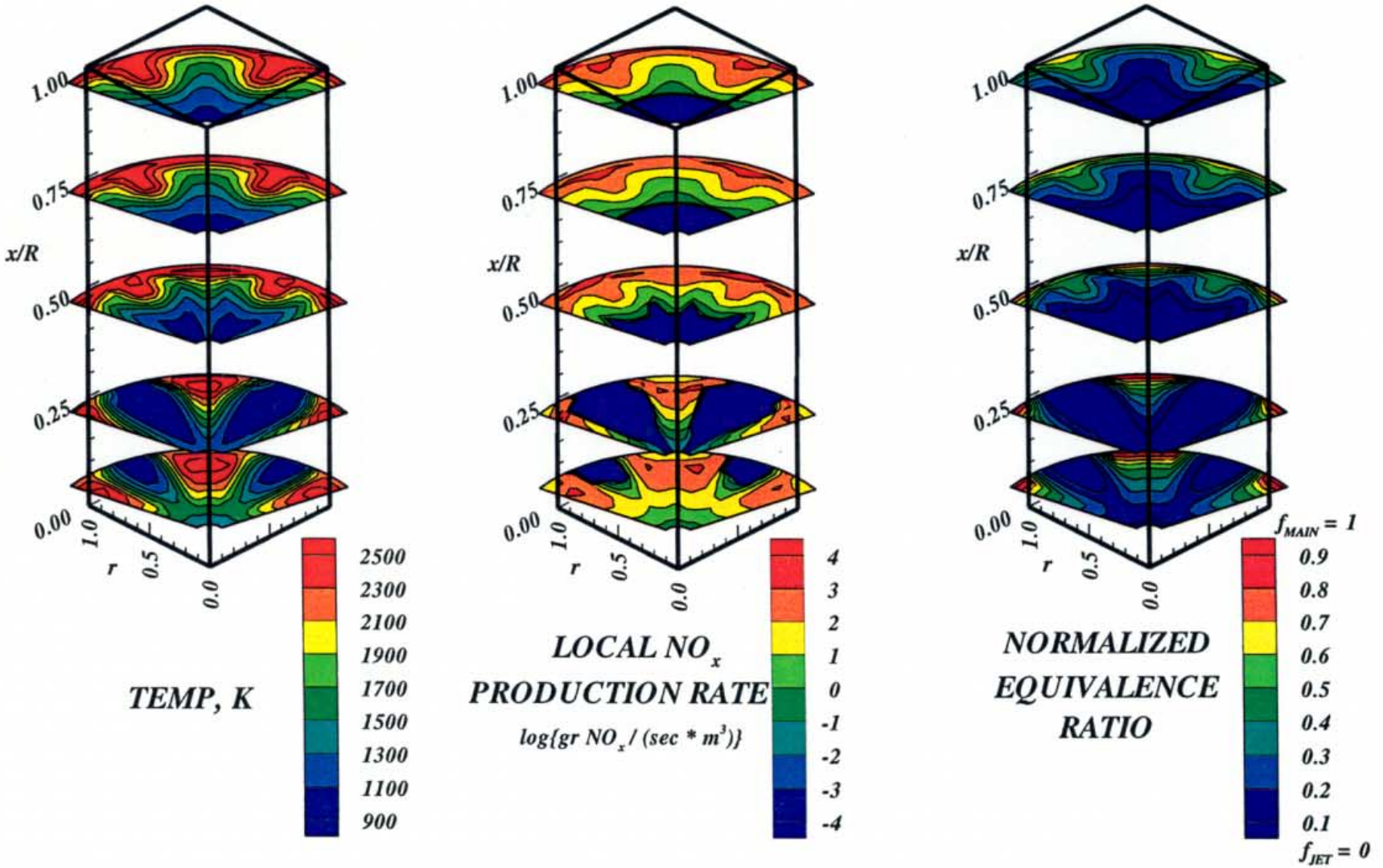

Figure-A6. Configuration HO-6, 6 round orifices /row

J=52.0, MR=2.96, DR=2.28, ϕ_{RZ} = 1.80, ϕ_{LZ} = 0.416 (2-adjacent sectors)

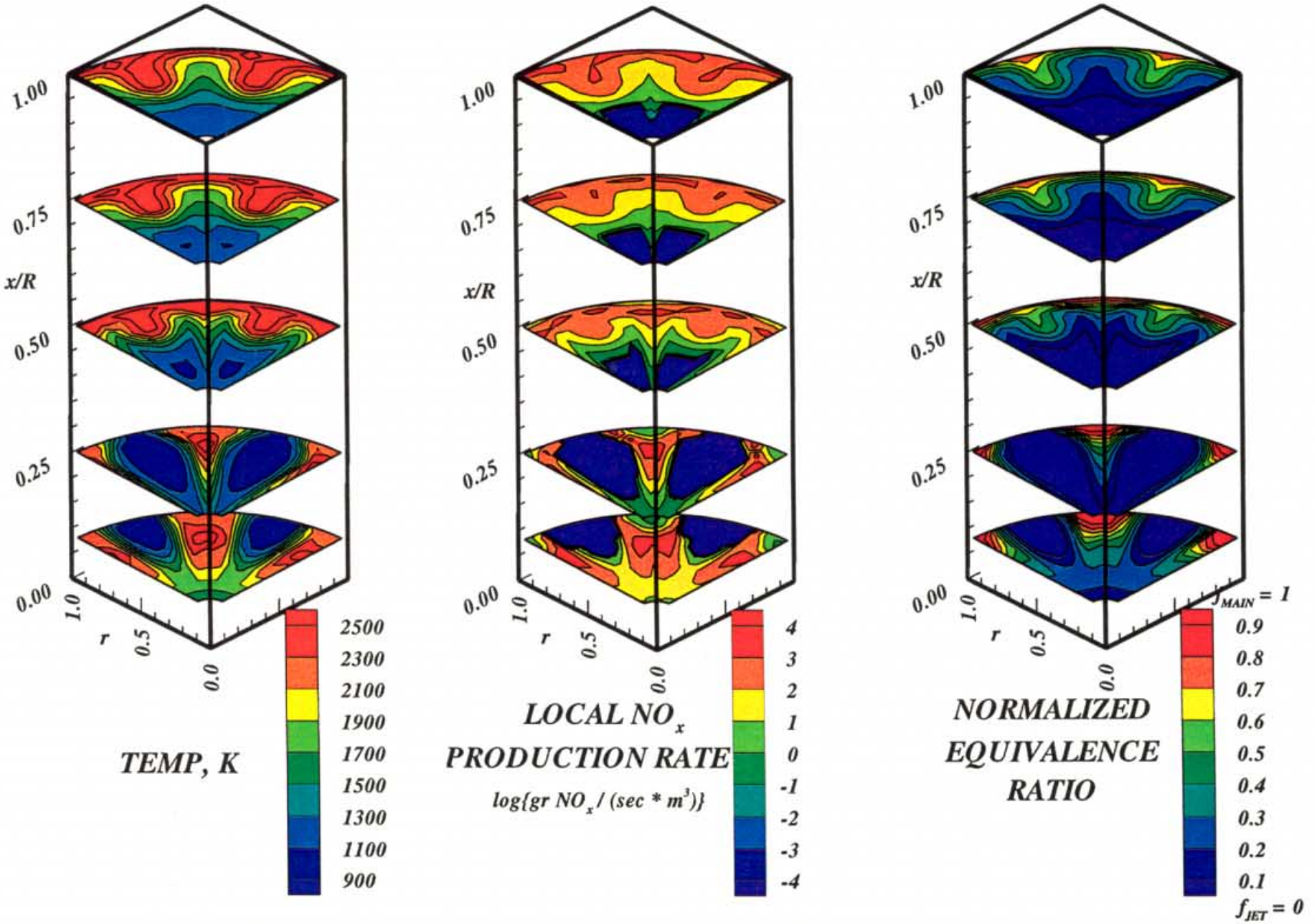

Figure-A7. Configuration HO-7, 8 round orifices /row

J=52.0, MR=2.96, DR=2.28, ϕ_{RZ} = 1.80, ϕ_{LZ} = 0.416 (2-adj acent sectors)

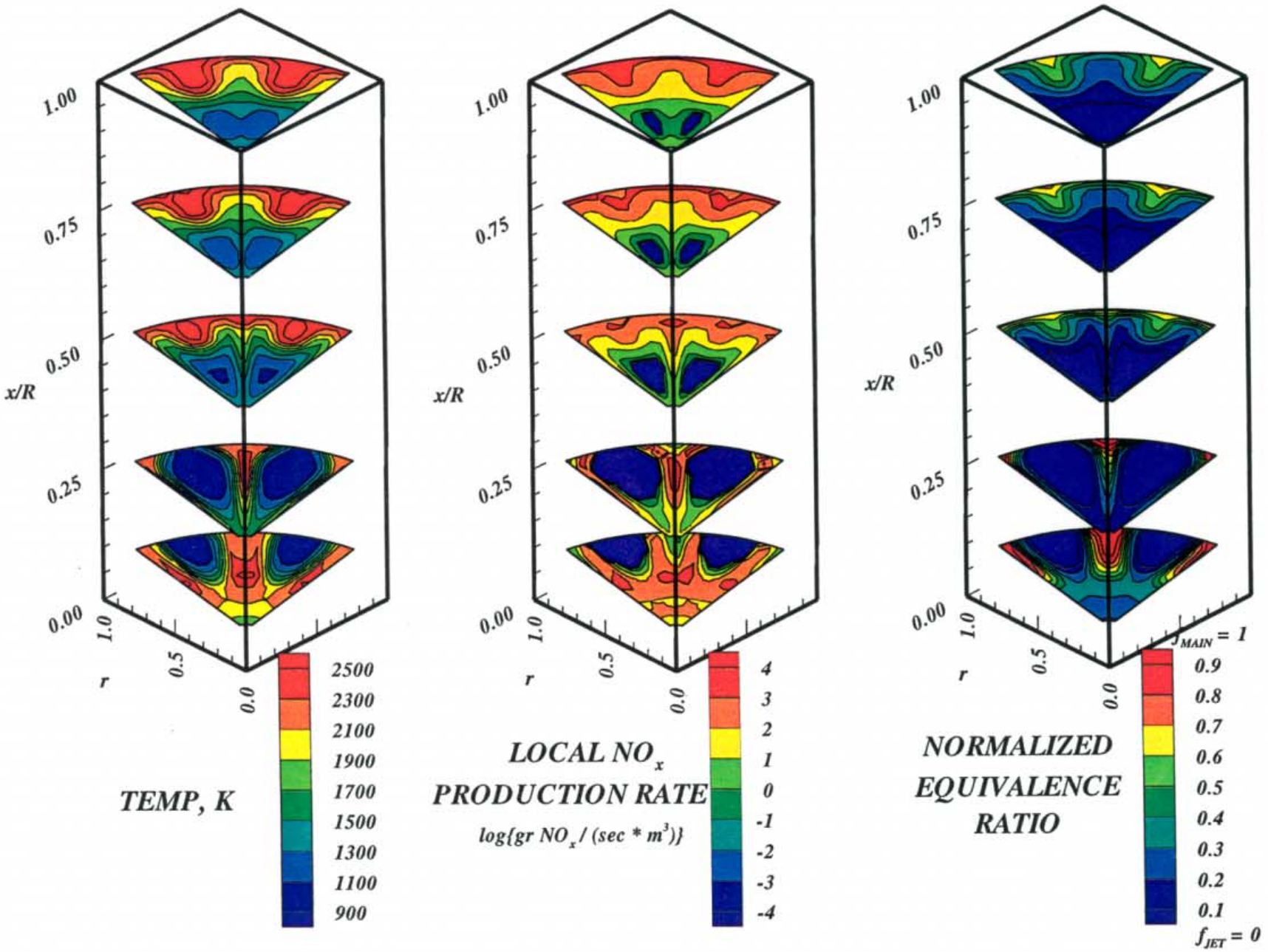

Figure-A8. Configuration HO-8, 10 round orifices /row

J=52.0, MR=2.96, DR=2.28, ϕ_{RZ} = 1.80, ϕ_{LZ} = 0.416 (2-adj acent sectors)

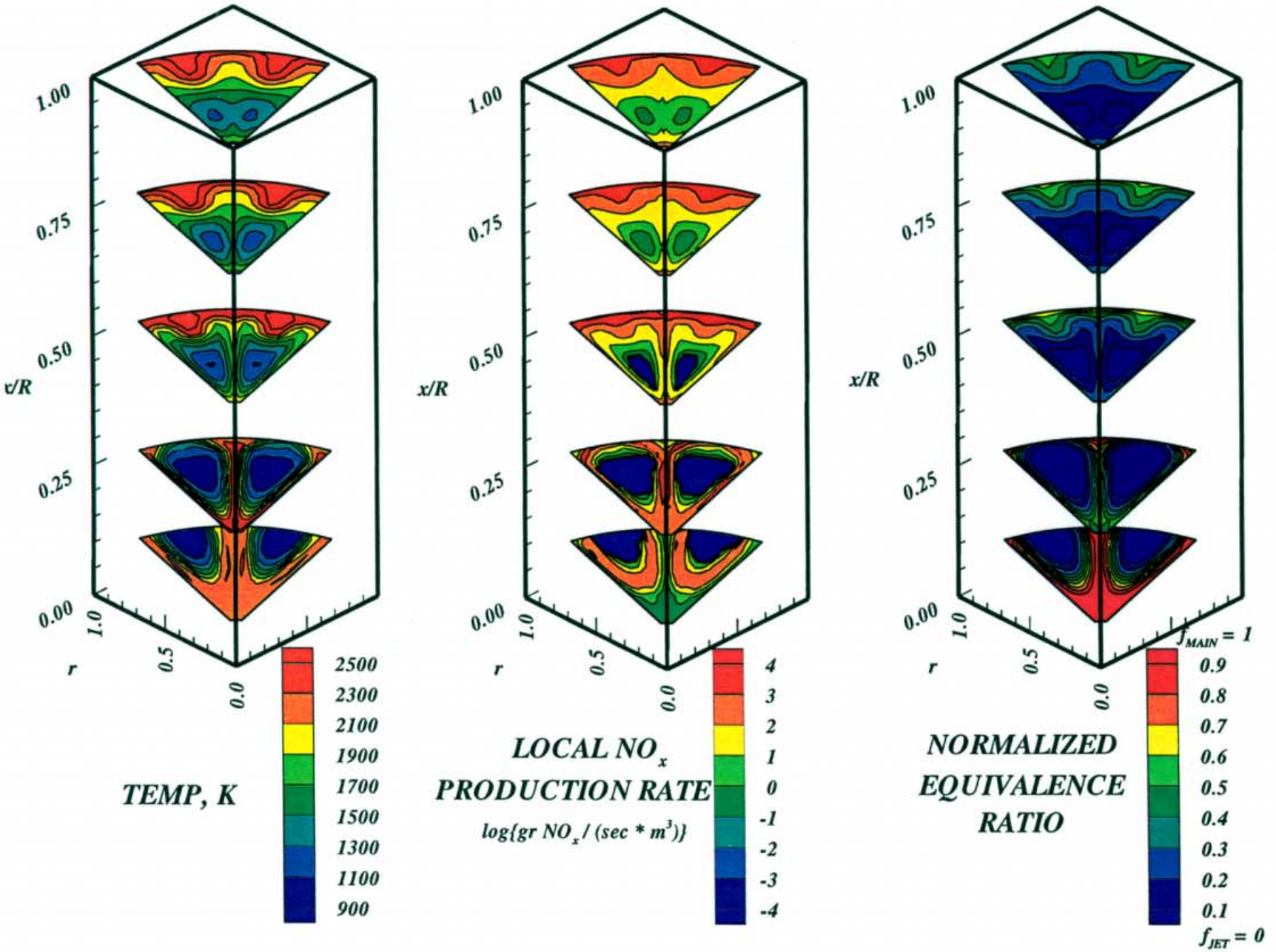

Figure-A9. Configuration HO-9, 12 round orifices /row

J=52.0, MR=2.96, DR=2.28, ϕ_{RZ} = 1.80, ϕ_{LZ} = 0.416 (2-adjacent sectors)

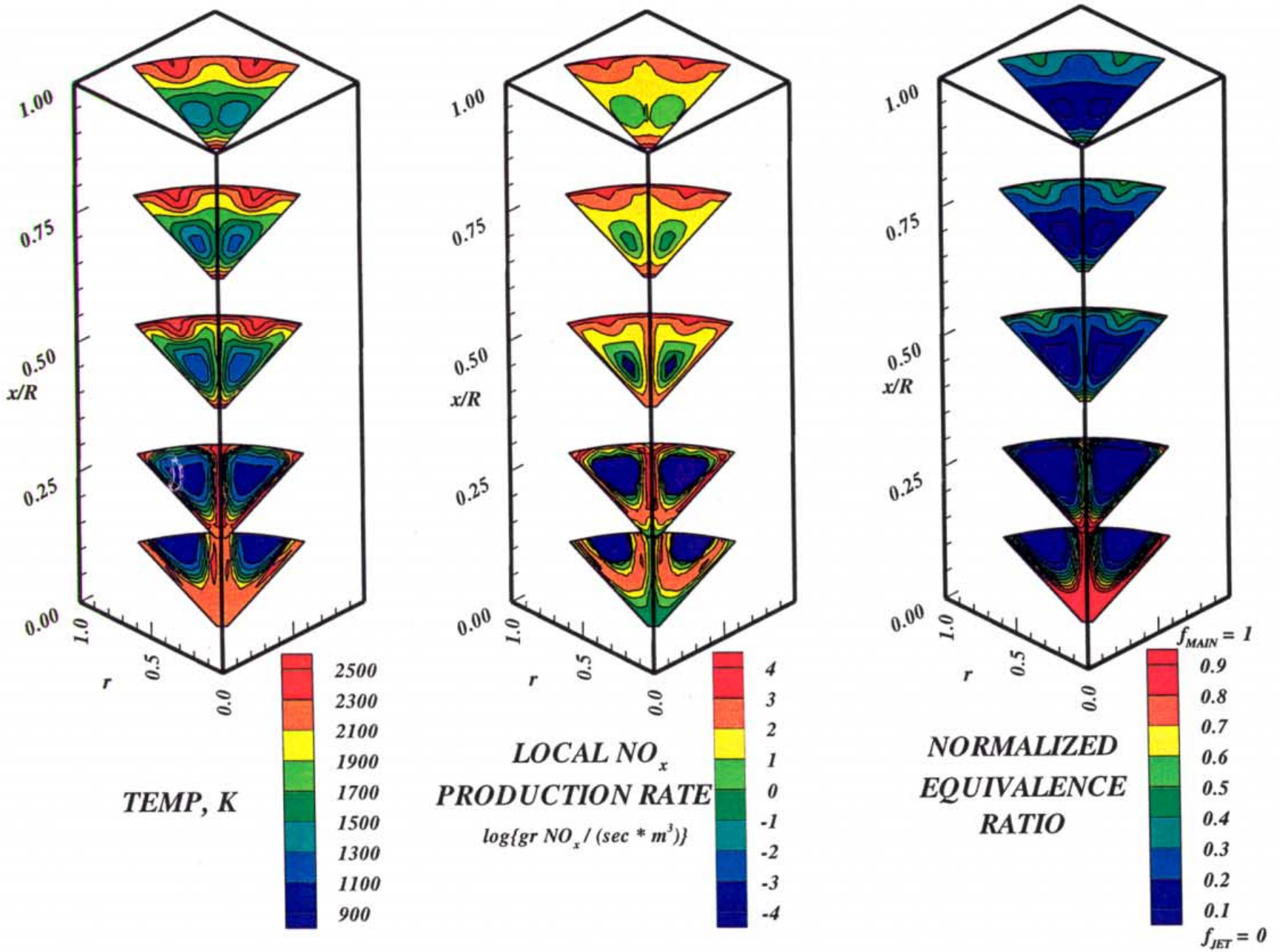

Figure-A10. Configuration HO-10, 14 round orifices /row

J=52.0, MR=2.96, DR=2.28, ϕ_{RZ} = 1.80, ϕ_{LZ} = 0.416 (2-adjacent sectors)

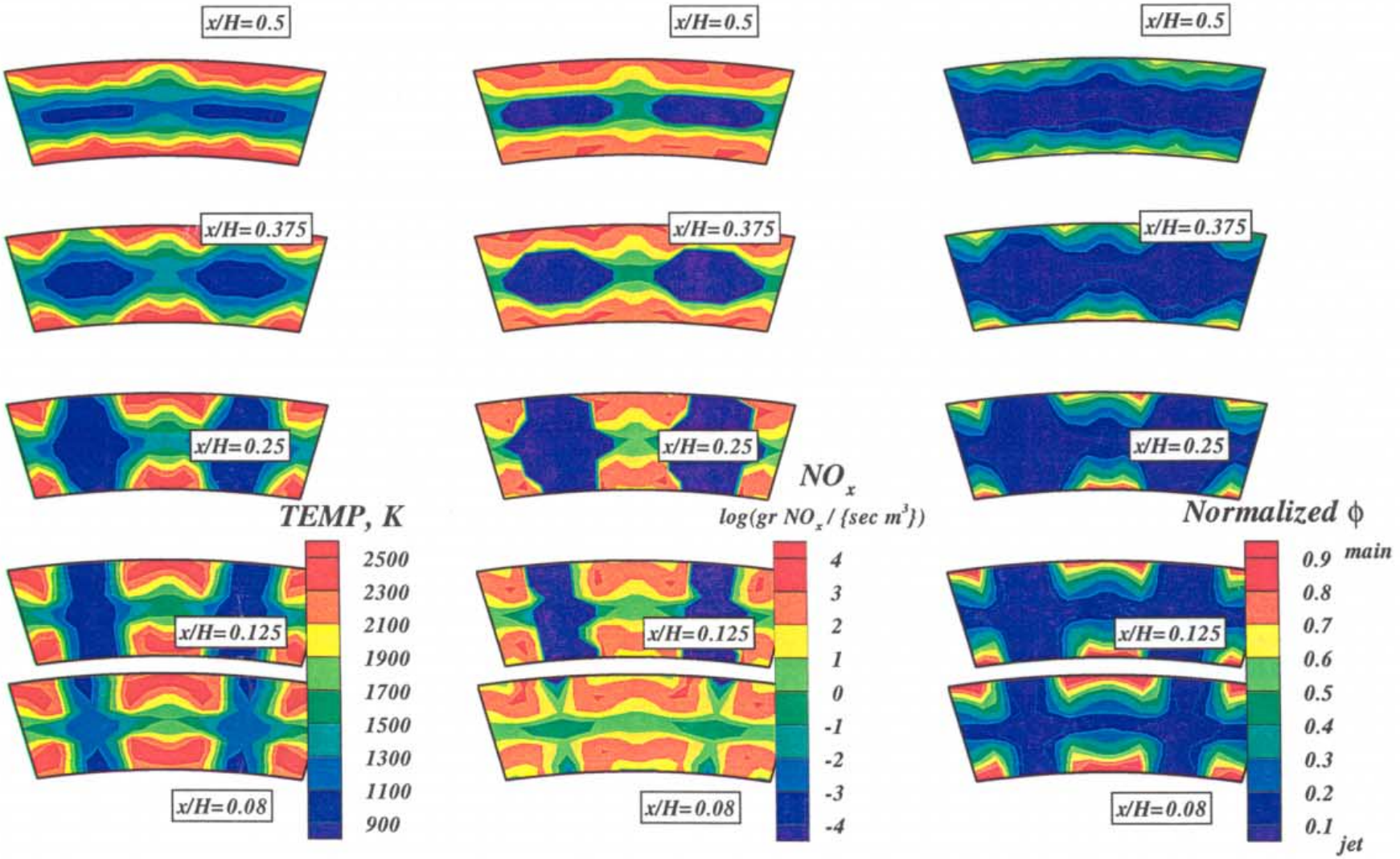

Figure-A11. Annular mixer configuration HO-11, 29 round holes per row (6 eq holes/row)
J=52.0, MR=2.96, DR=2.28, ϕ_{RZ}=1.80, ϕ_{LZ}=0.416 (2 sectors)

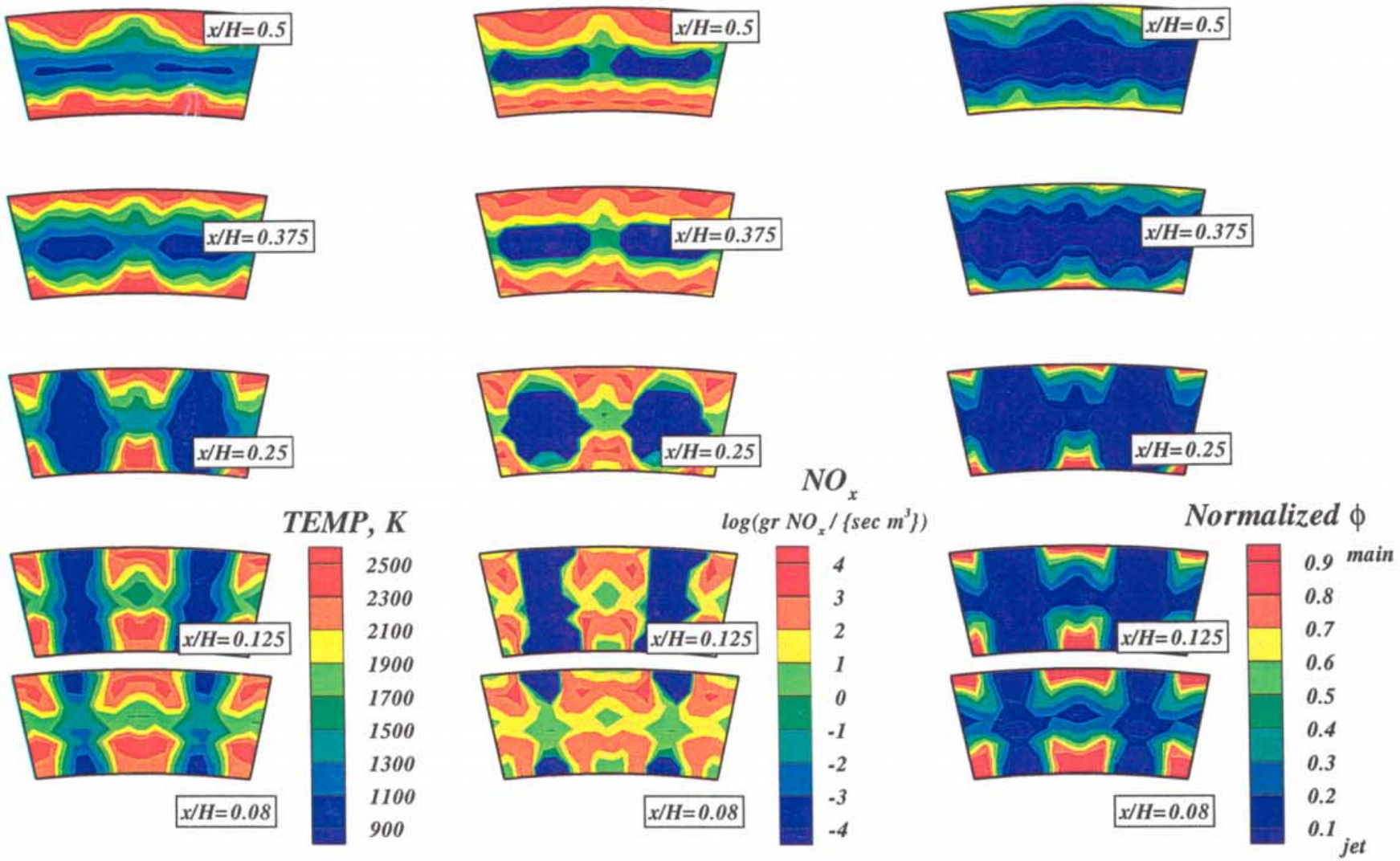

Figure-A12. Annular mixer configuration HO-12, 39 round holes per row (8 eq holes/row)
J=52.0, MR=2.96, DR=2.28, ϕ_{RZ}=1.80, ϕ_{LZ}=0.416 (2 sectors)

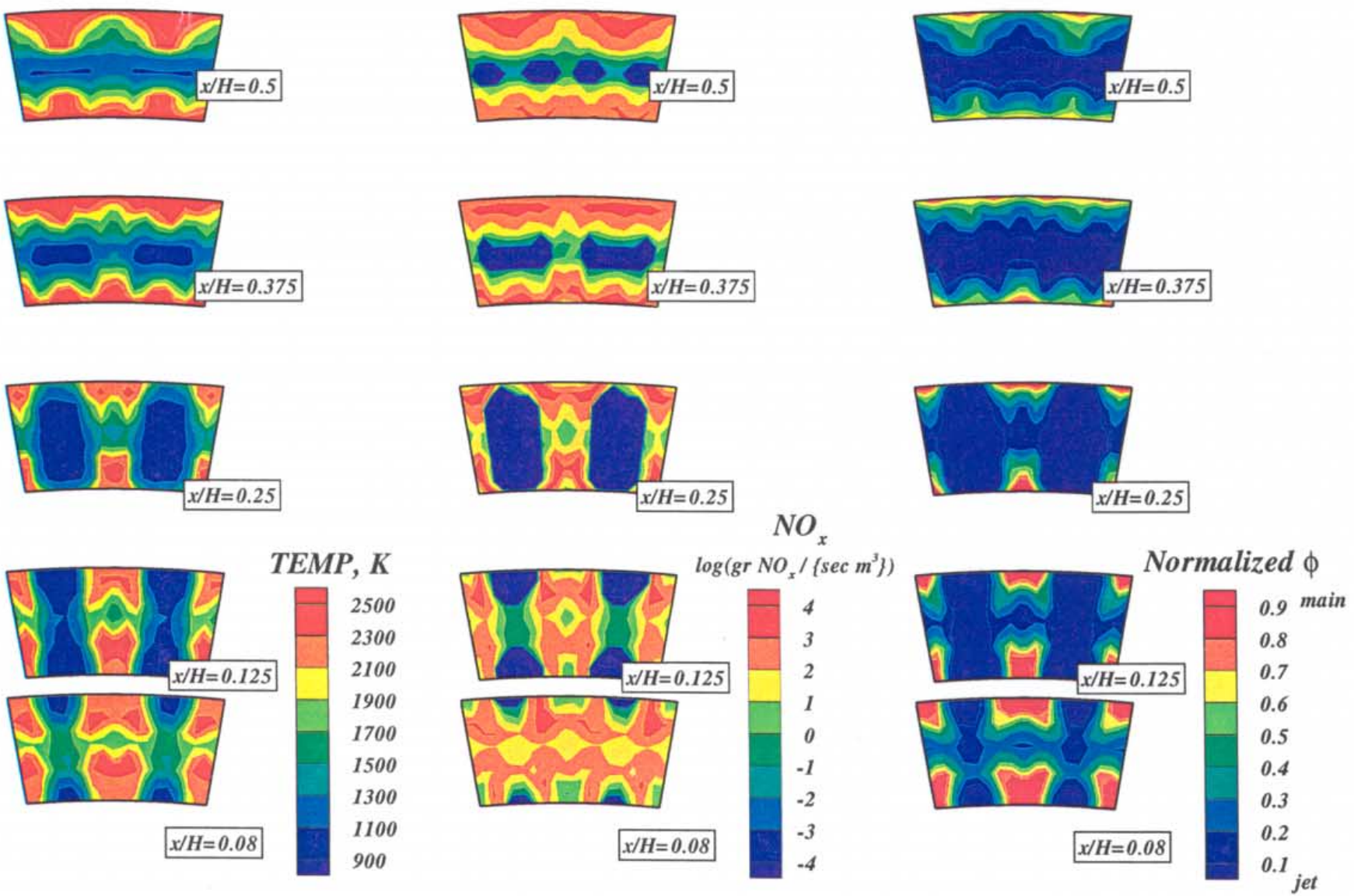

Figure-A13. Annular mixer configuration HO-13, 48 round holes per row (10 eq holes/row)
J=52.0, MR=2.96, DR=2.28, ϕ_{RZ}=1.80, ϕ_{LZ}=0.416 (2 sectors)

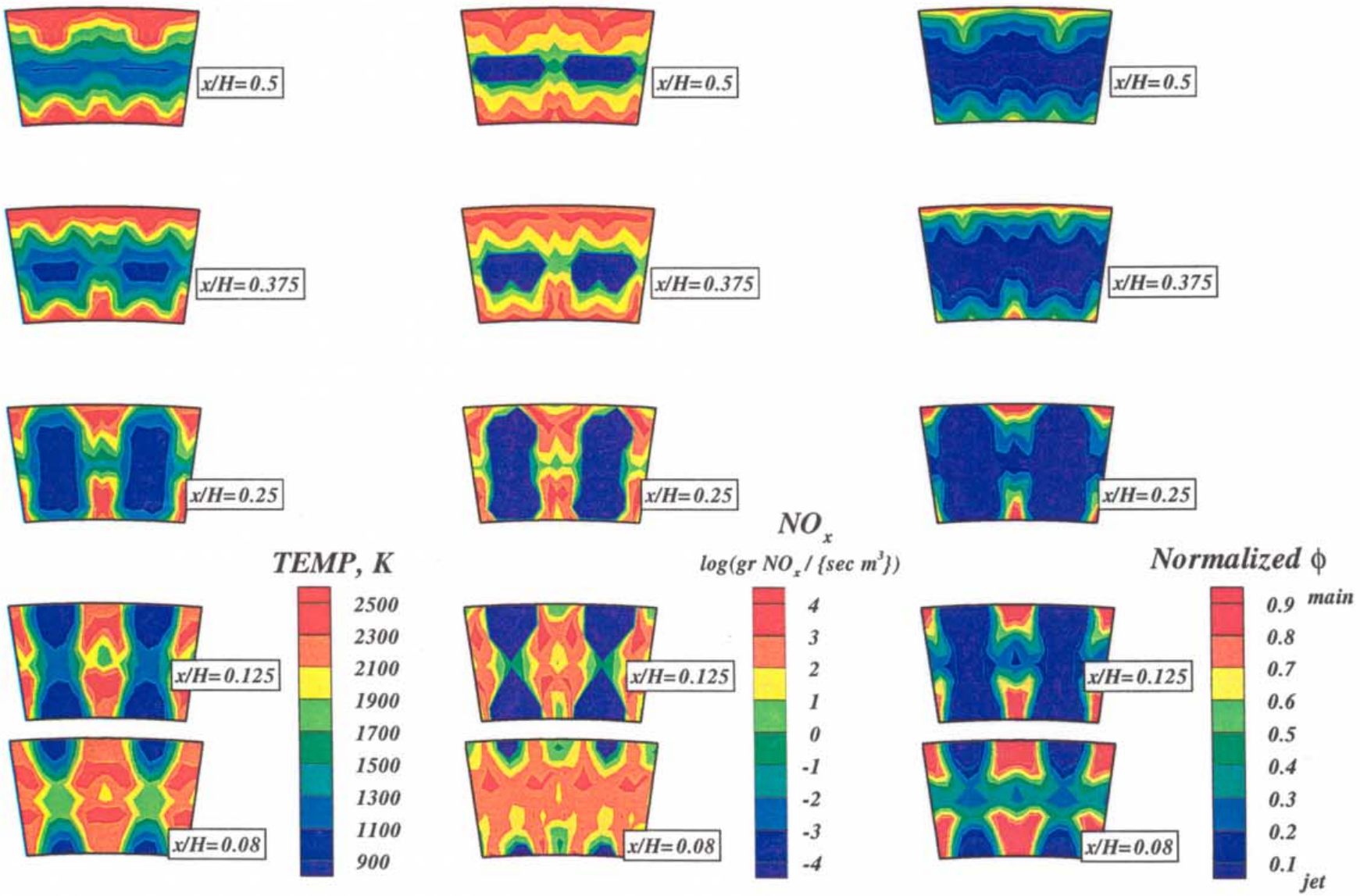

Figure-A14. Annular mixer configuration HO-14, 58 round holes per row (12 eq holes/row)
J=52.0, MR=2.96, DR=2.28, ϕ_{RZ}=1.80, ϕ_{LZ}=0.416 (2 sectors)

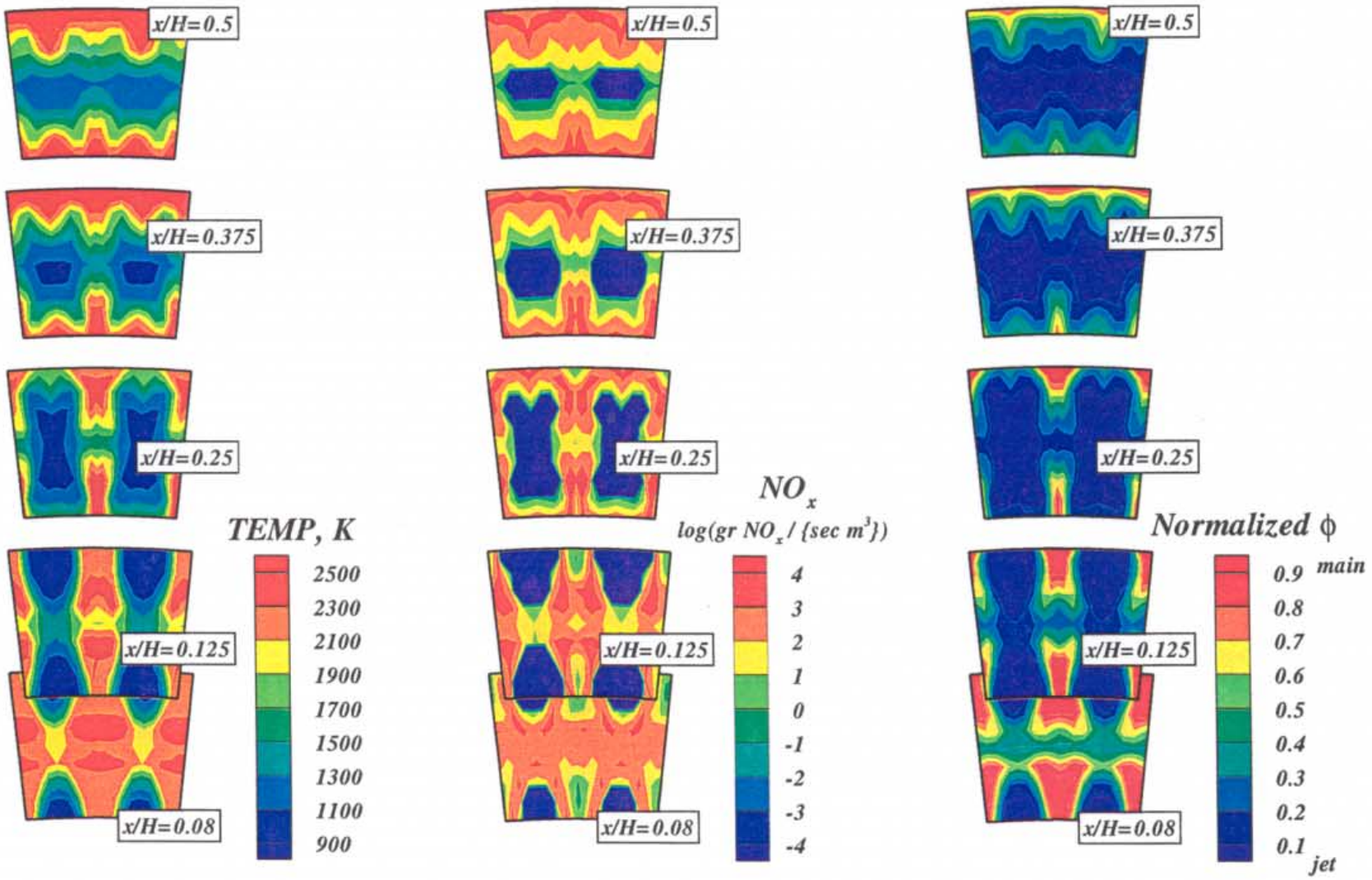

Figure-A15. Annular mixer configuration HO-15, 68 round holes per row (14 eq holes/row)
J=52.0, MR=2.96, DR=2.28, ϕ_{RZ}=1.80, ϕ_{LZ}=0.416 (2 sectors)

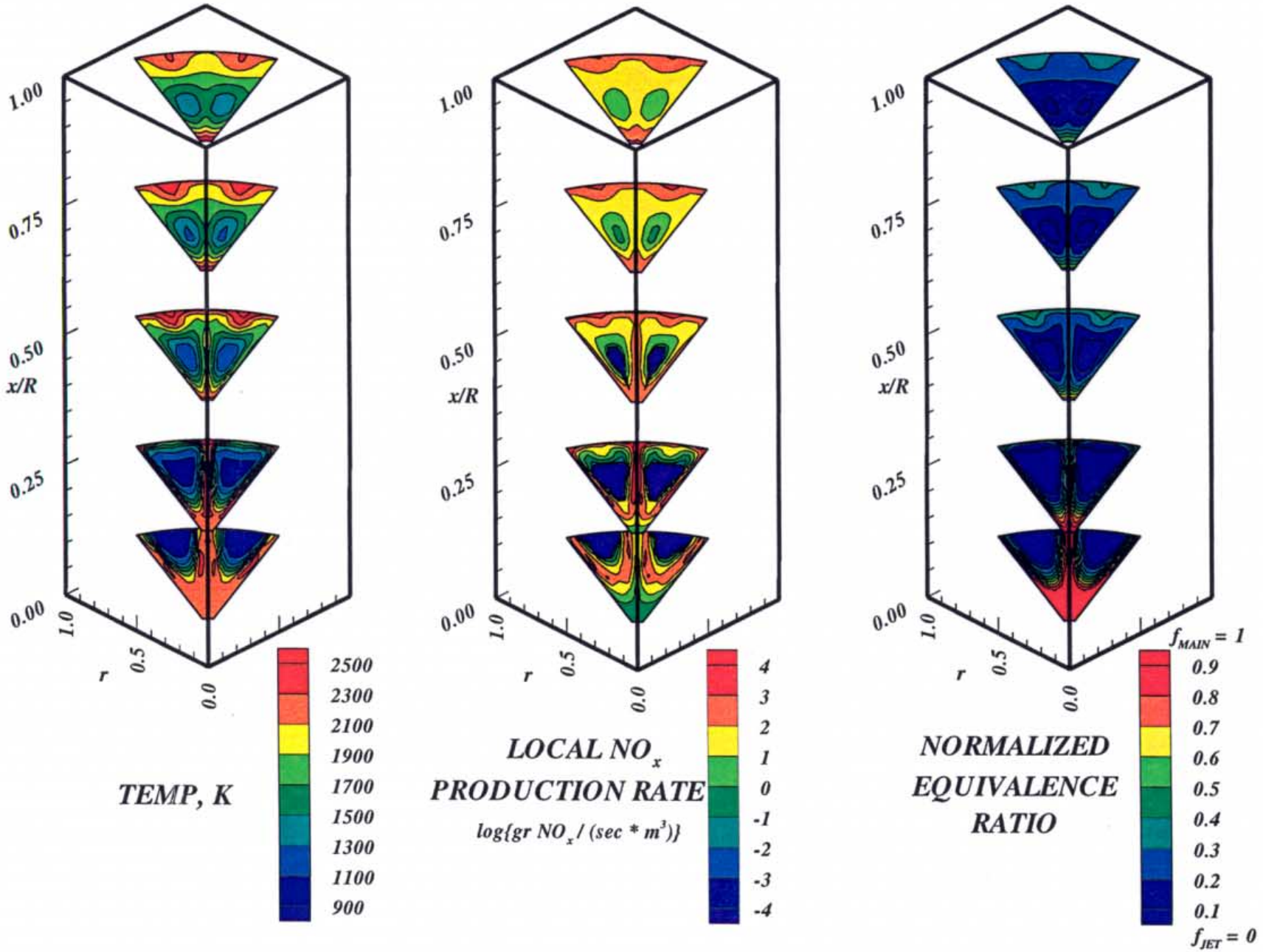

Figure-A16. Configuration HO-16, 16 round orifices /row

J=52.0, MR=2.96, DR=2.28, ϕ_{RZ} = 1.80, ϕ_{LZ} = 0.416 (2-adjacent sectors)

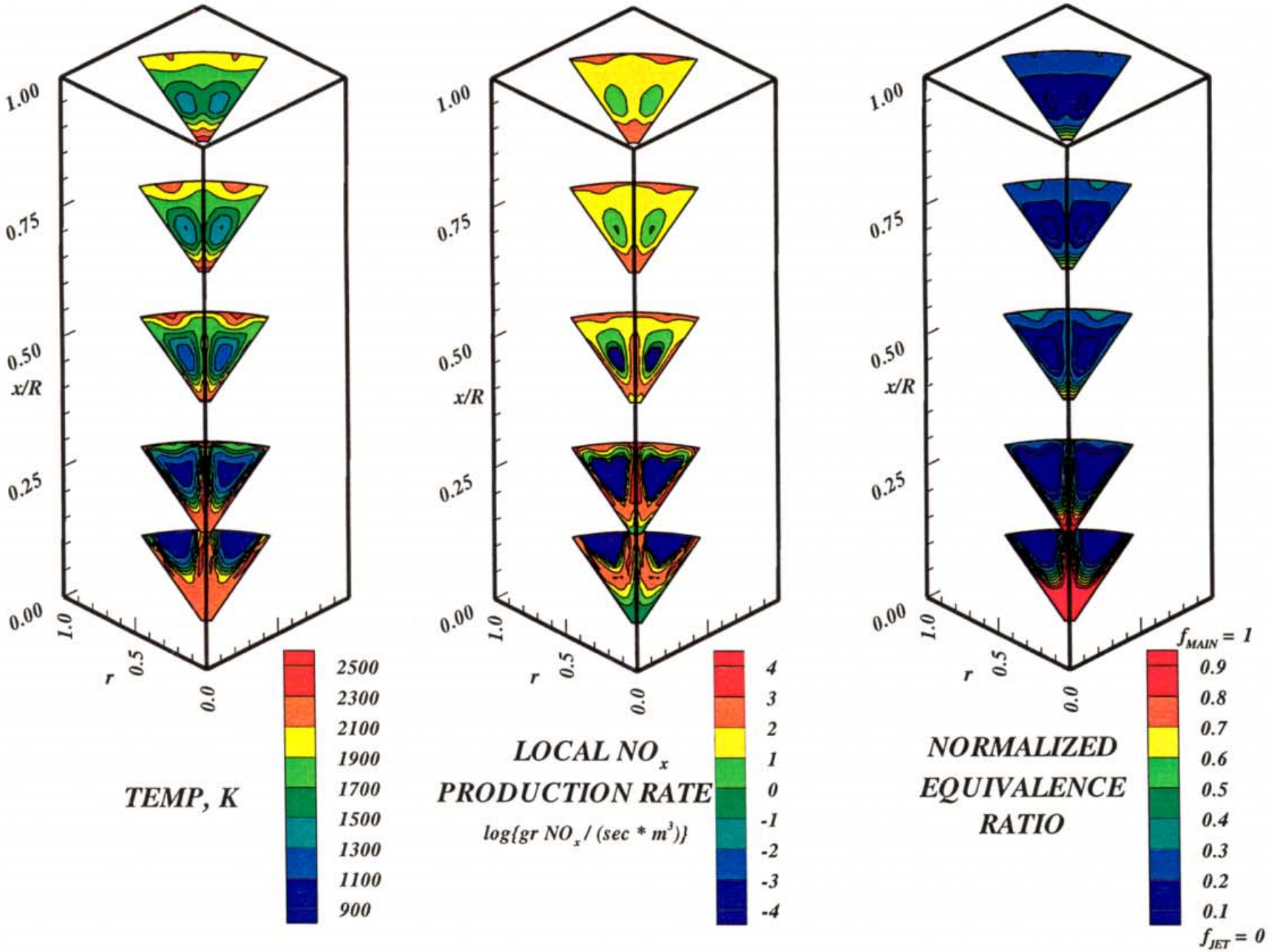

Figure-A17. Configuration HO-17, 18 round orifices /row

J=52.0, MR=2.96, DR=2.28, ϕ_{RZ} = 1.80, ϕ_{LZ} = 0.416 (2-adjacent sectors)

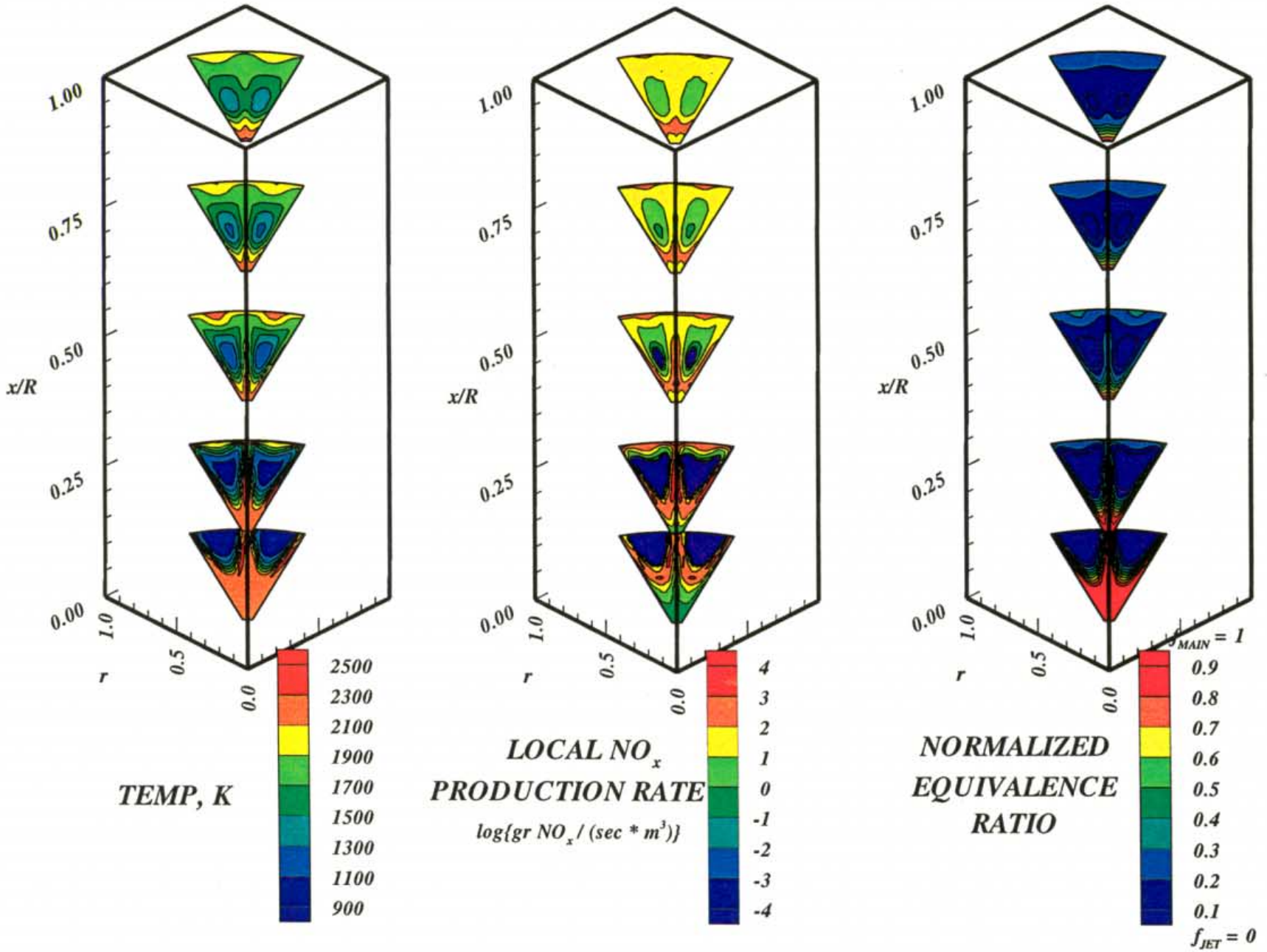

Figure-A18. Configuration HO-18, 20 round orifices /row

J=52.0, MR=2.96, DR=2.28, ϕ_{RZ} = 1.80, ϕ_{LZ} = 0.416 (2-adjacent sectors)

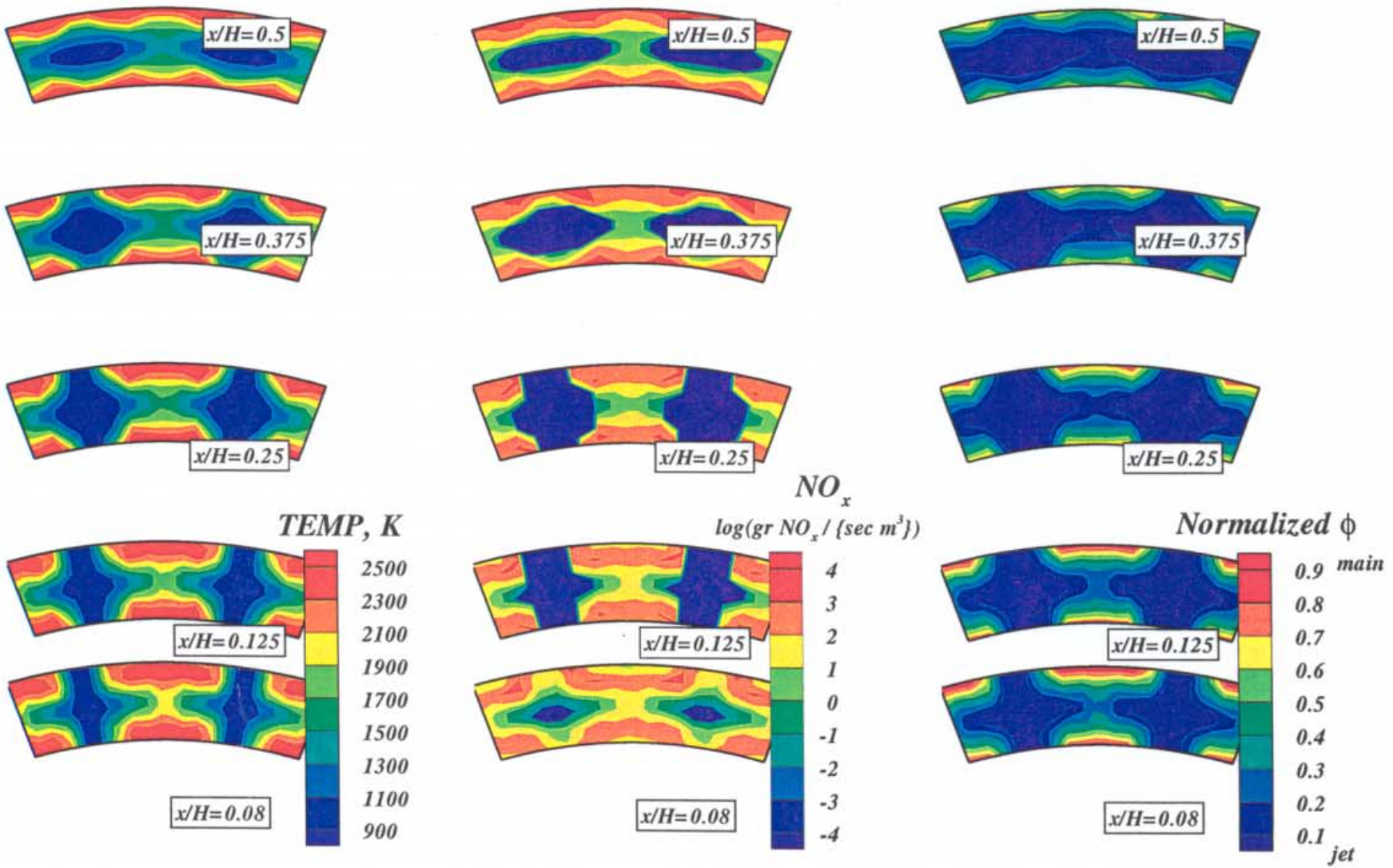

Figure-A19. Annular mixer configuration HO-19, 19 round holes per row (4 eq holes/row)
J=52.0, MR=2.96, DR=2.28, ϕ_{RZ}=1.80, ϕ_{LZ}=0.416 (2 sectors)

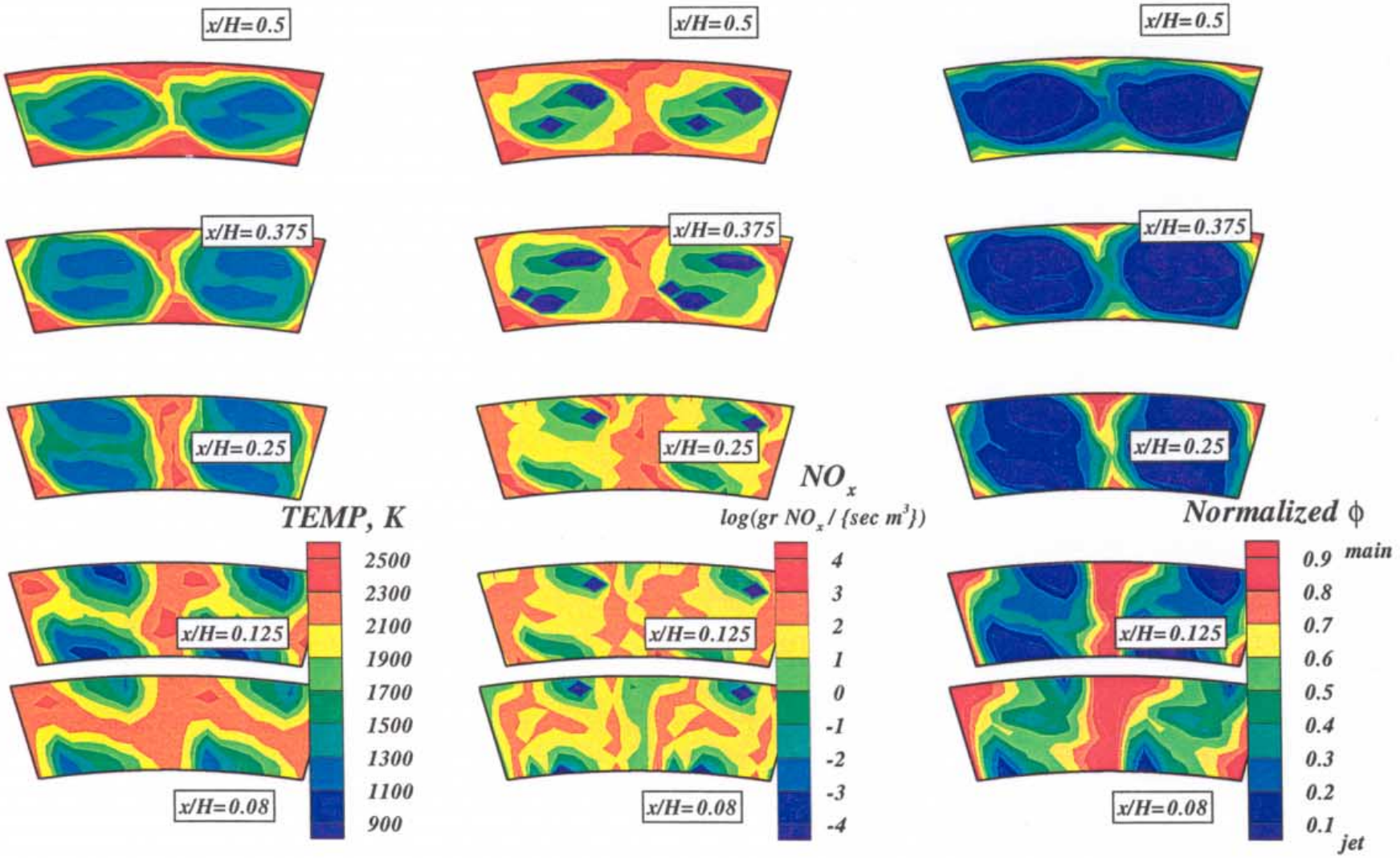

Figure-A20. Annular mixer configuration HO-20, 67.5^0 slanted slots L/W=4, 29 per row (6 eq holes/row)
J=52.0, MR=2.96, DR=2.28, ϕ_{RZ}=1.80, ϕ_{LZ}=0.416 (2 sectors)

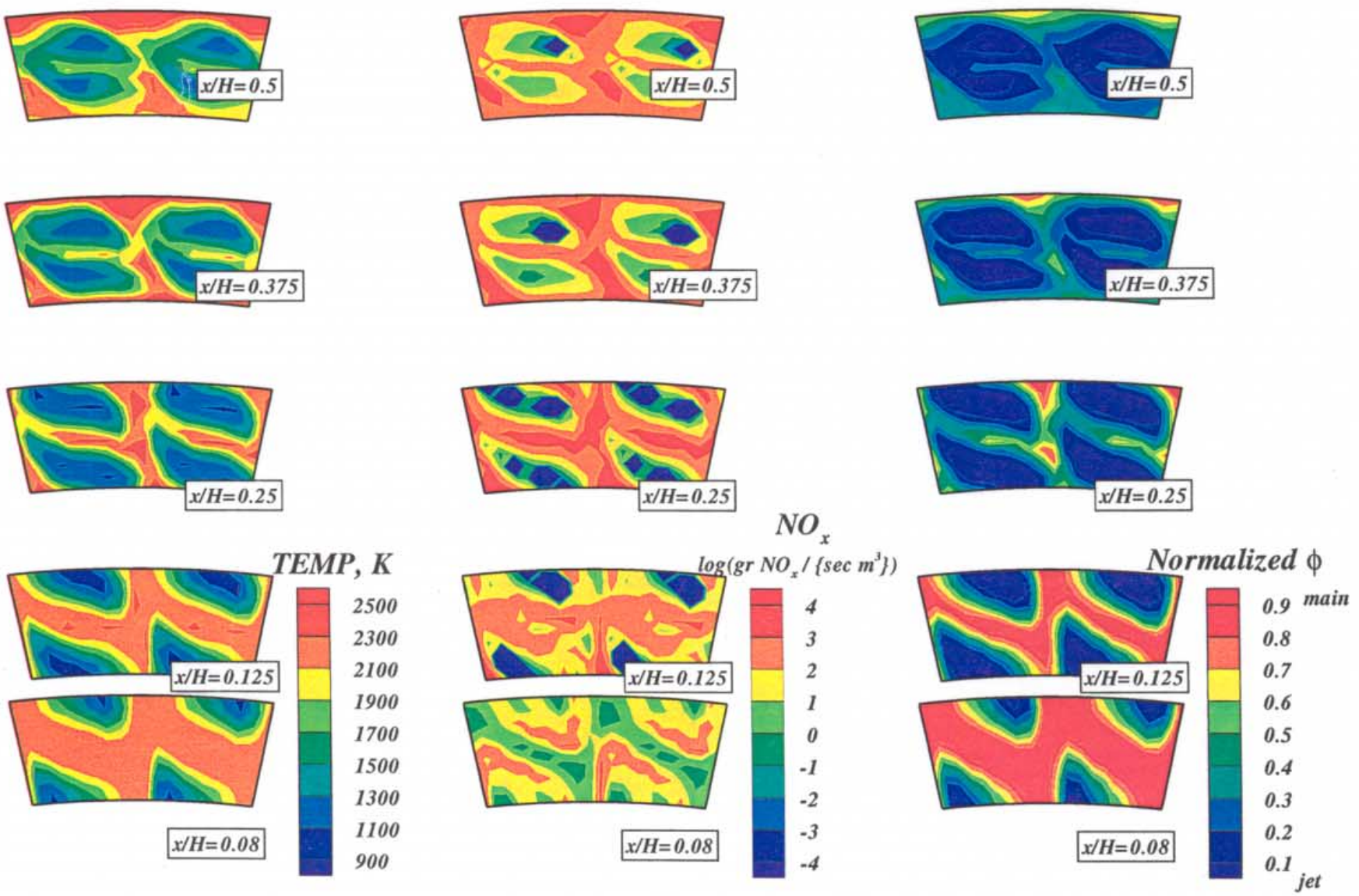

Figure-A21. Annular mixer configuration HO-21, 67.5^0 slanted slots L/W=4, 39 per row (8 eq holes/row)
J=52.0, MR=2.96, DR=2.28, ϕ_{RZ}=1.80, ϕ_{LZ}=0.416 (2 sectors)

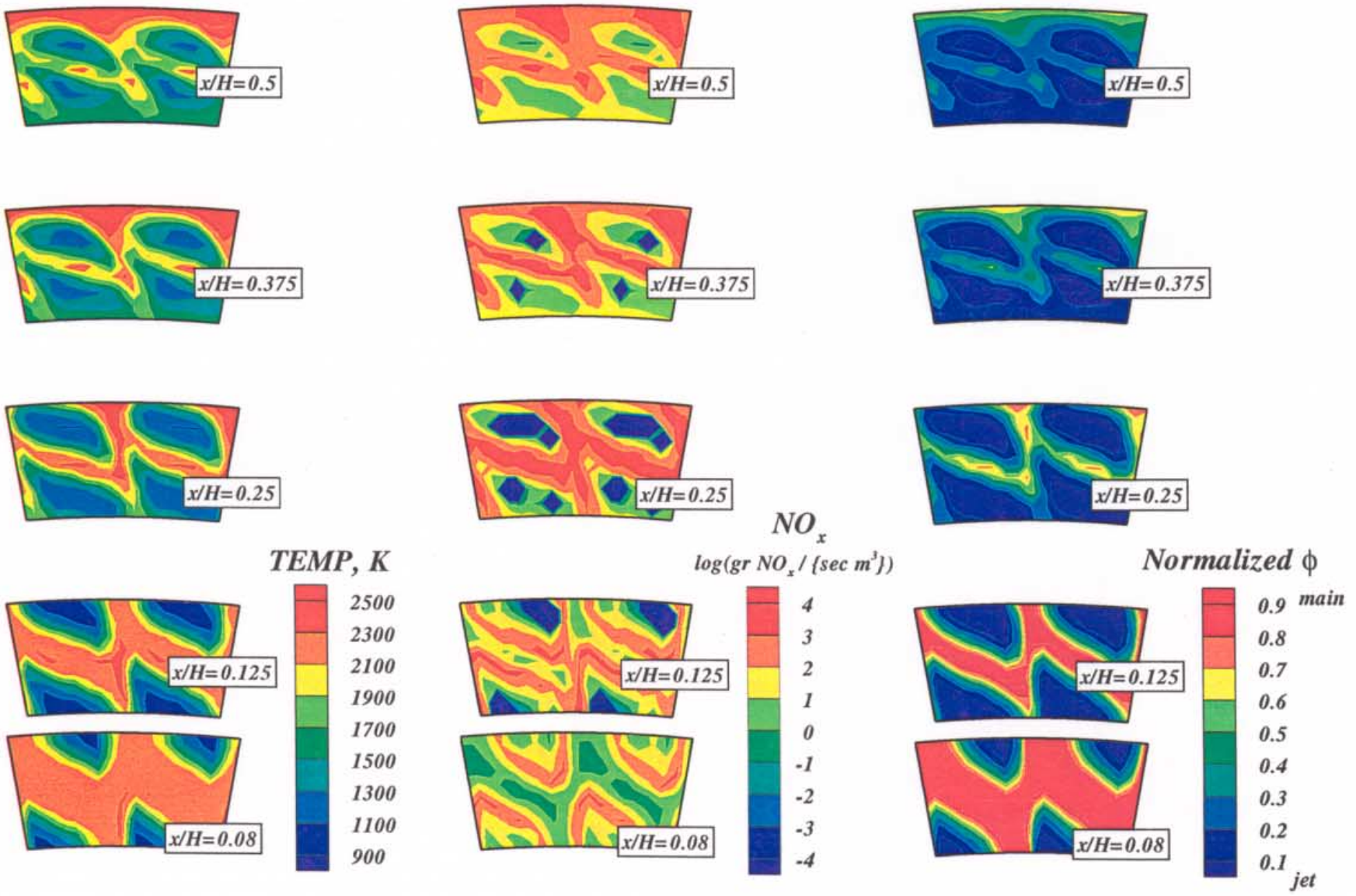

Figure-A22. Annular mixer configuration HO-22, 67.5^0 slanted slots L/W=4, 48 per row (10 eq holes/row) J=52.0, MR=2.96, DR=2.28, ϕ_{RZ}=1.80, ϕ_{LZ}=0.416 (2 sectors)

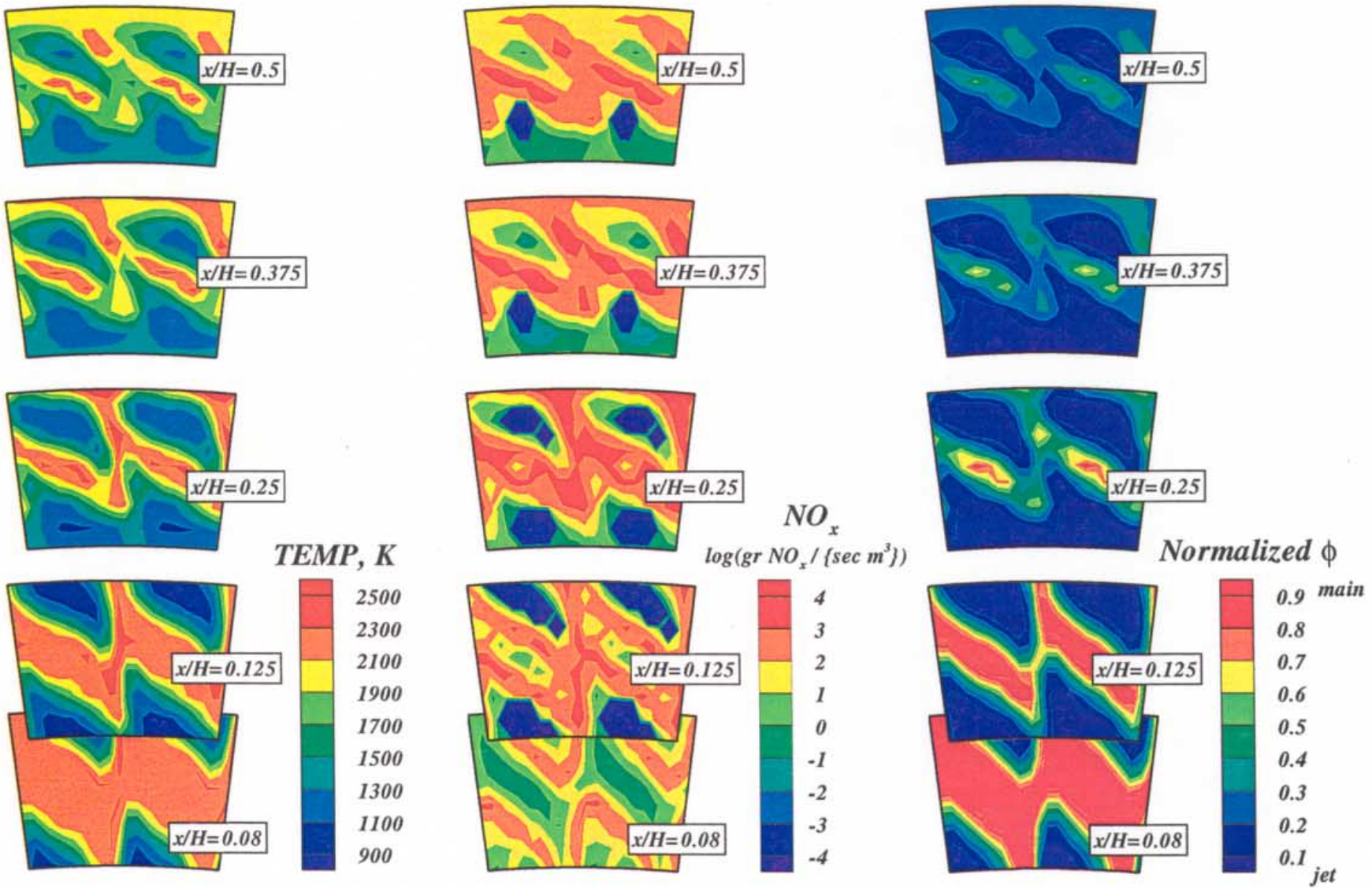

Figure-A23. Annular mixer configuration HO-23, 67.5^0 slanted slots L/W=4, 58 per row (12 eq holes/row) J=52.0, MR=2.96, DR=2.28, ϕ_{RZ}=1.80, ϕ_{LZ}=0.416 (2 sectors)

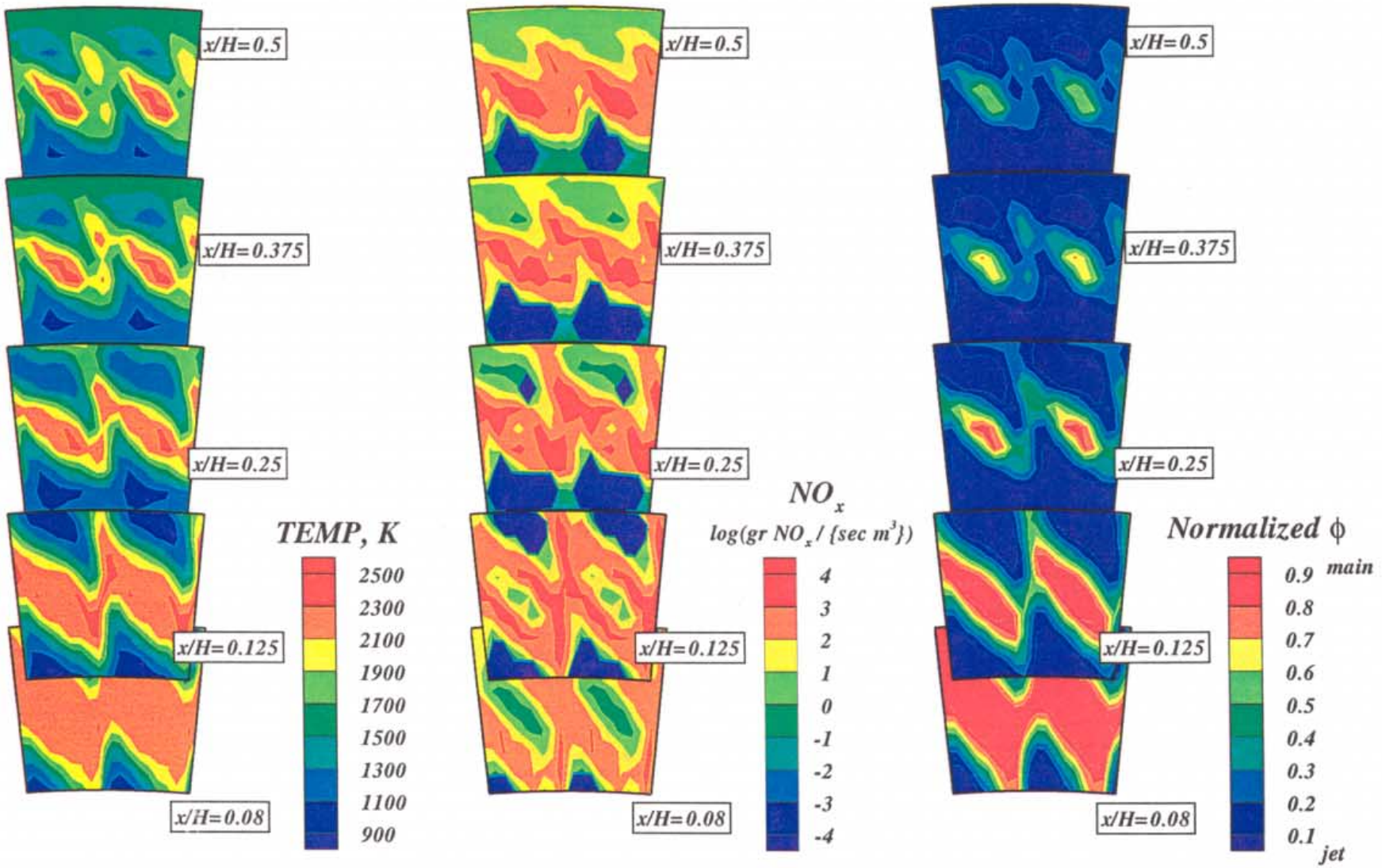

Figure-A24. Annular mixer configuration HO-24, 67.5^0 slanted slots L/W=4, 68 per row (14 eq holes/row) J=52.0, MR=2.96, DR=2.28, ϕ_{RZ}=1.80, ϕ_{LZ}=0.416 (2 sectors)

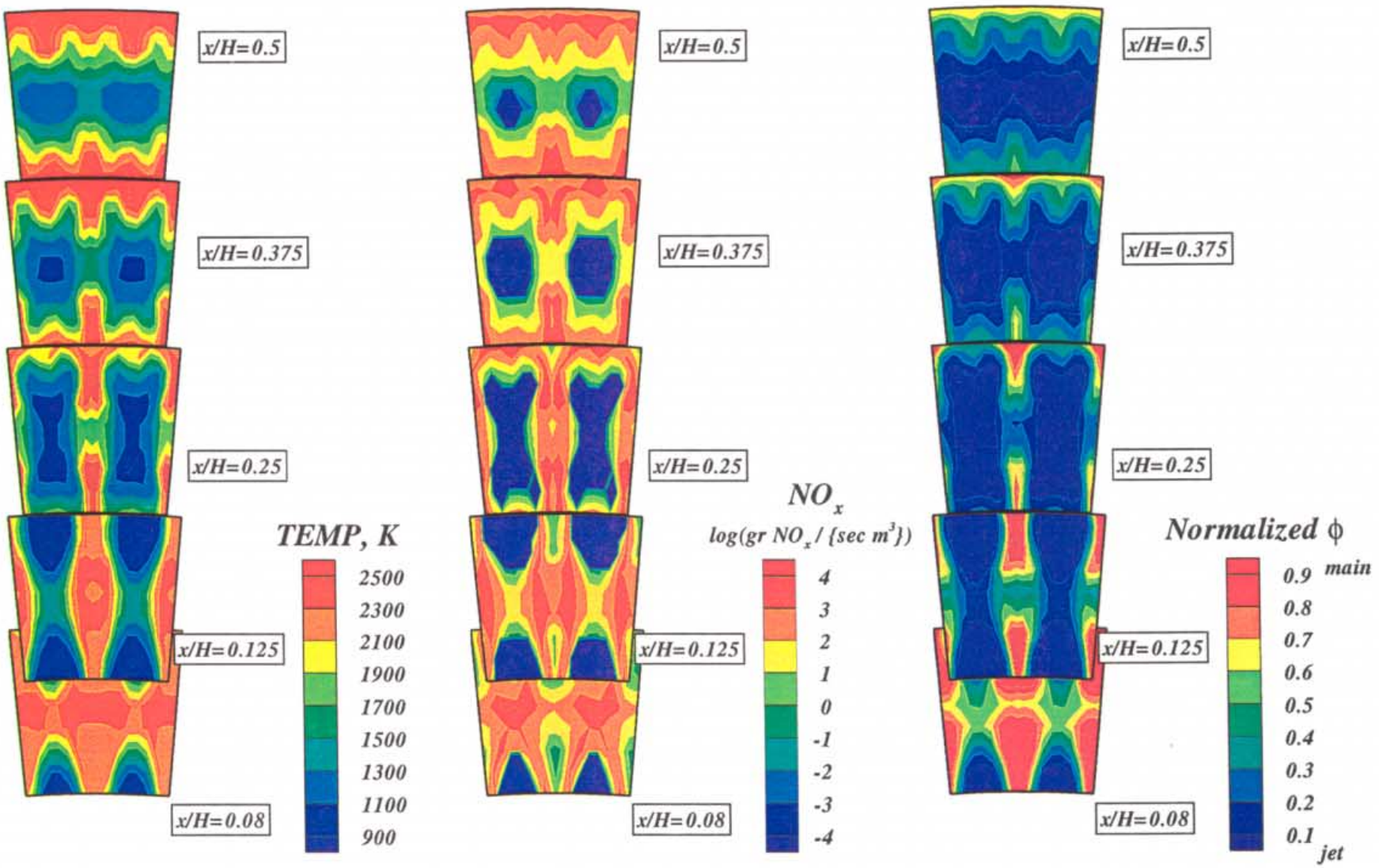

Figure-A25. Annular mixer configuration HO-25, 77 round holes per row (16 eq holes/row)
J=52.0, MR=2.96, DR=2.28, ϕ_{RZ}=1.80, ϕ_{LZ}=0.416 (2 sectors)

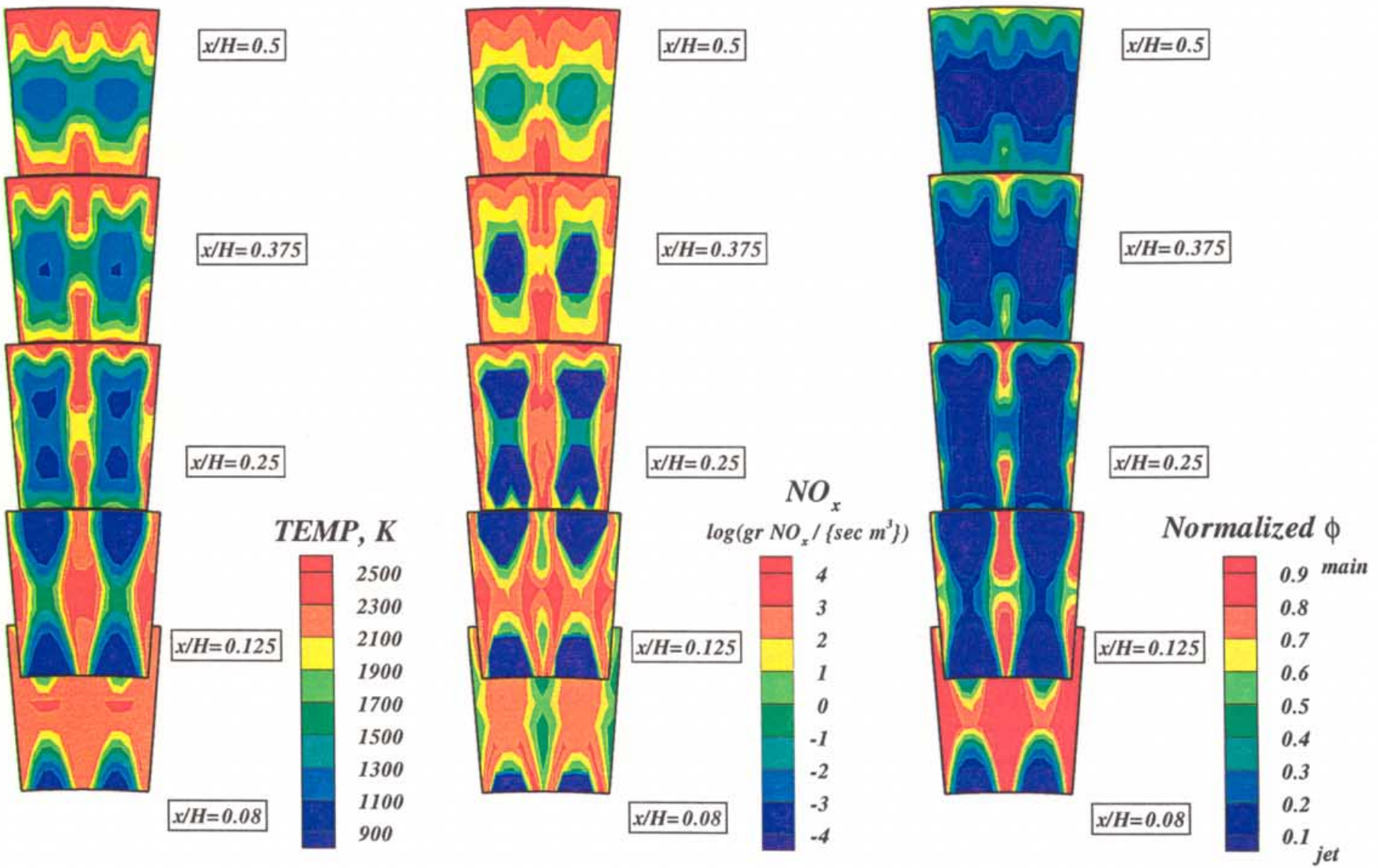

Figure-A26. Annular mixer configuration HO-26, 87 round holes per row (18 eq holes/row)
J=52.0, MR=2.96, DR=2.28, ϕ_{RZ}=1.80, ϕ_{LZ}=0.416 (2 sectors)

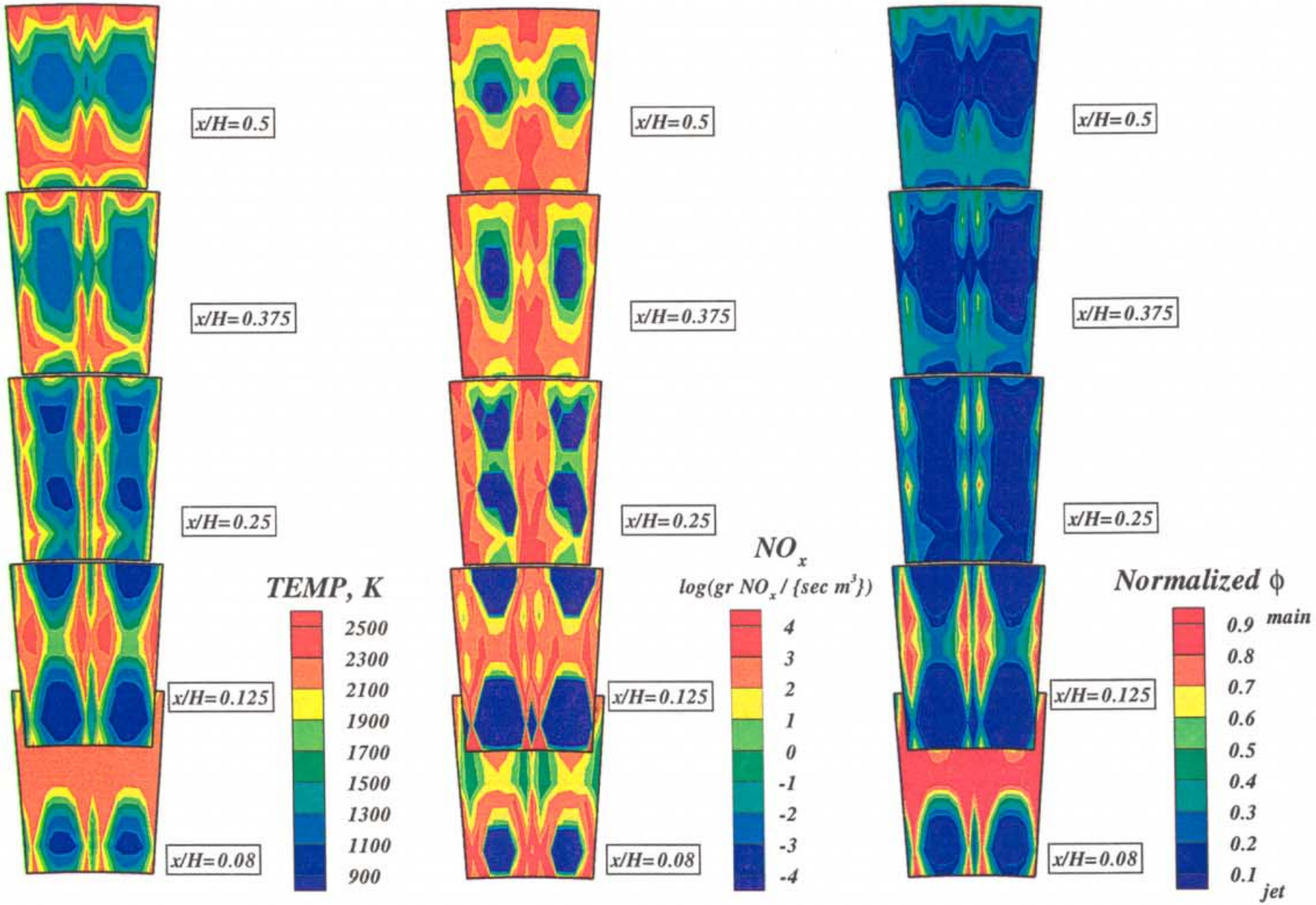

Figure-A27. Annular mixer configuration HO-27, 97 round holes per row (20 eq holes/row)
J=52.0, MR=2.96, DR=2.28, ϕ_{RZ}=1.80, ϕ_{LZ}=0.416 (2 sectors)

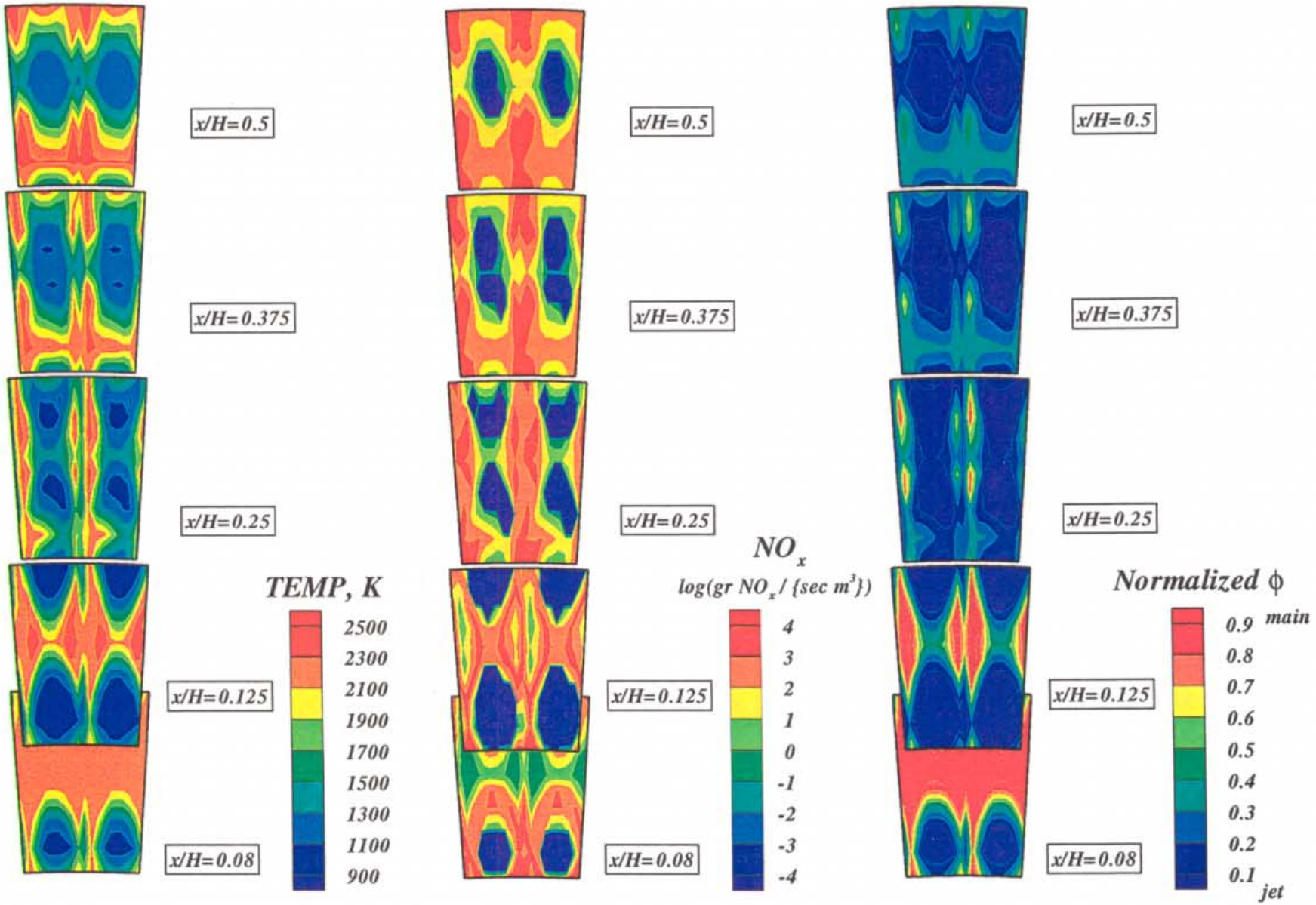

Figure-A28. Annular mixer configuration HO-28, 106 round holes per row (22 eq holes/row)
J=52.0, MR=2.96, DR=2.28, ϕ_{RZ}=1.80, ϕ_{LZ}=0.416 (2 sectors)

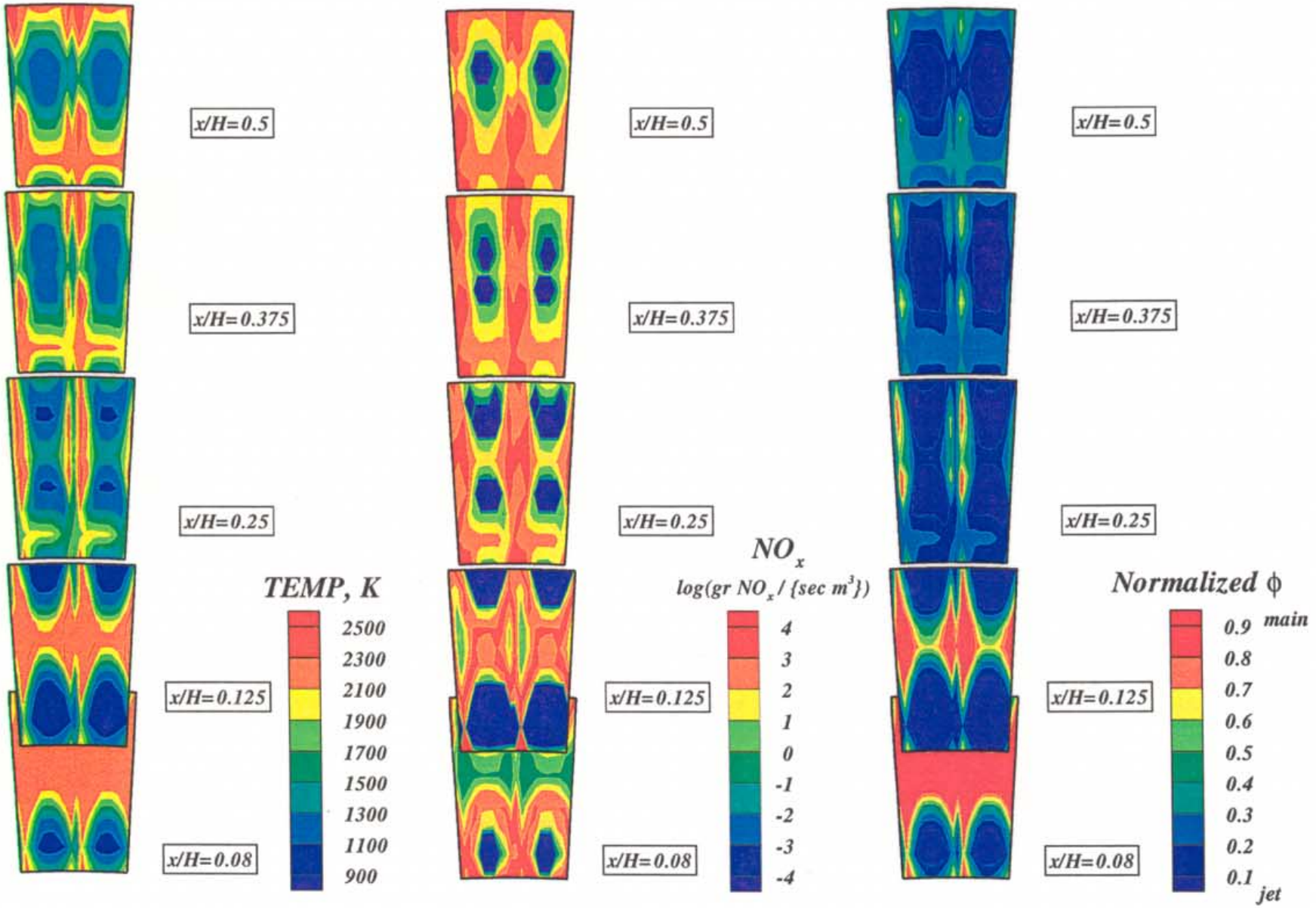

Figure-A29. Annular mixer configuration HO-29, 116 round holes per row (24 eq holes/row)
J=52.0, MR=2.96, DR=2.28, ϕ_{RZ}=1.80, ϕ_{LZ}=0.416 (2 sectors)

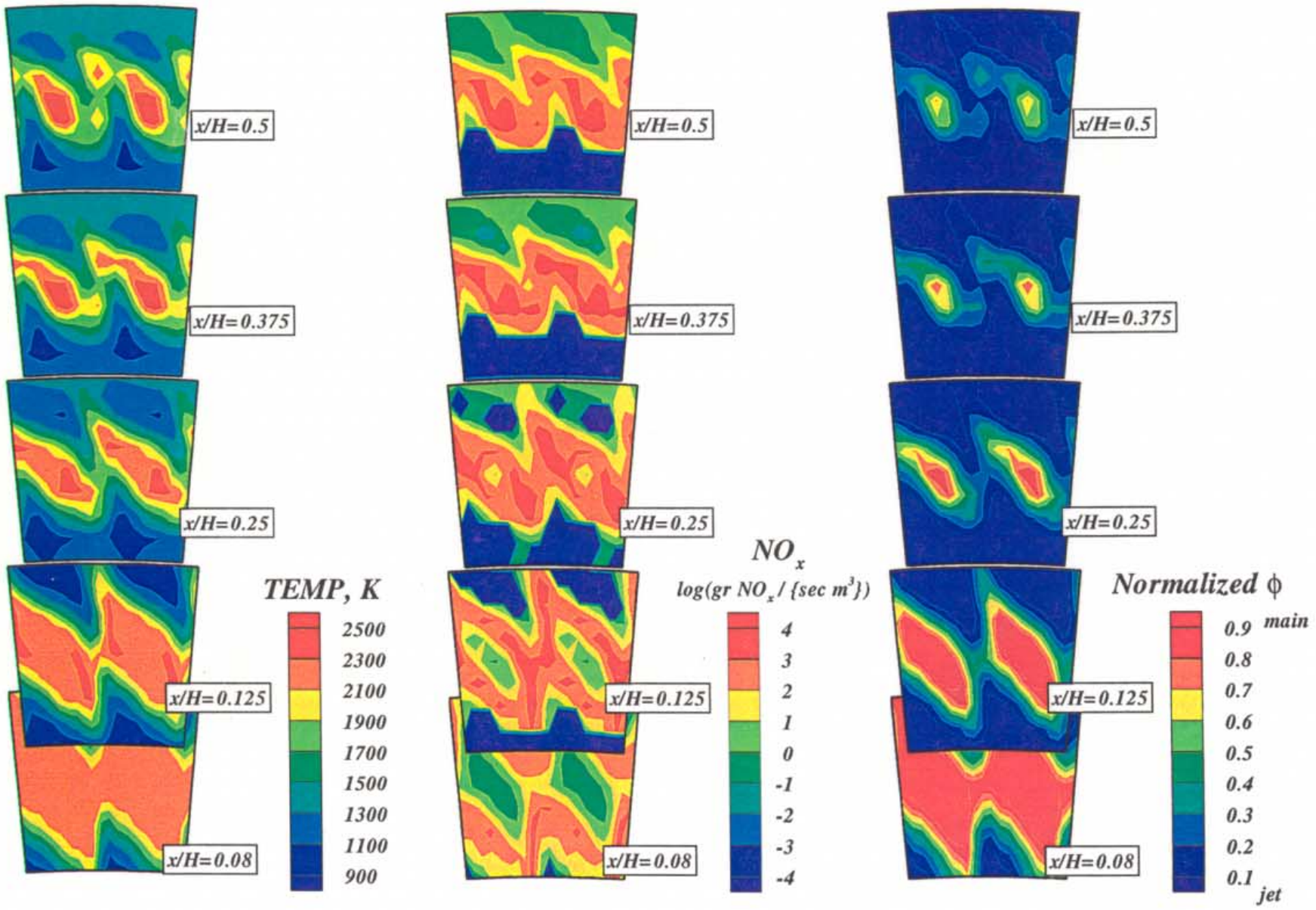

Figure-A30. Annular mixer configuration HO-30, 67.5^0 slanted slot, L/W=4, 77 per row (16 eq holes/row) J=52.0, MR=2.96, DR=2.28, ϕ_{RZ}=1.80, ϕ_{LZ}=0.416 (2 sectors)

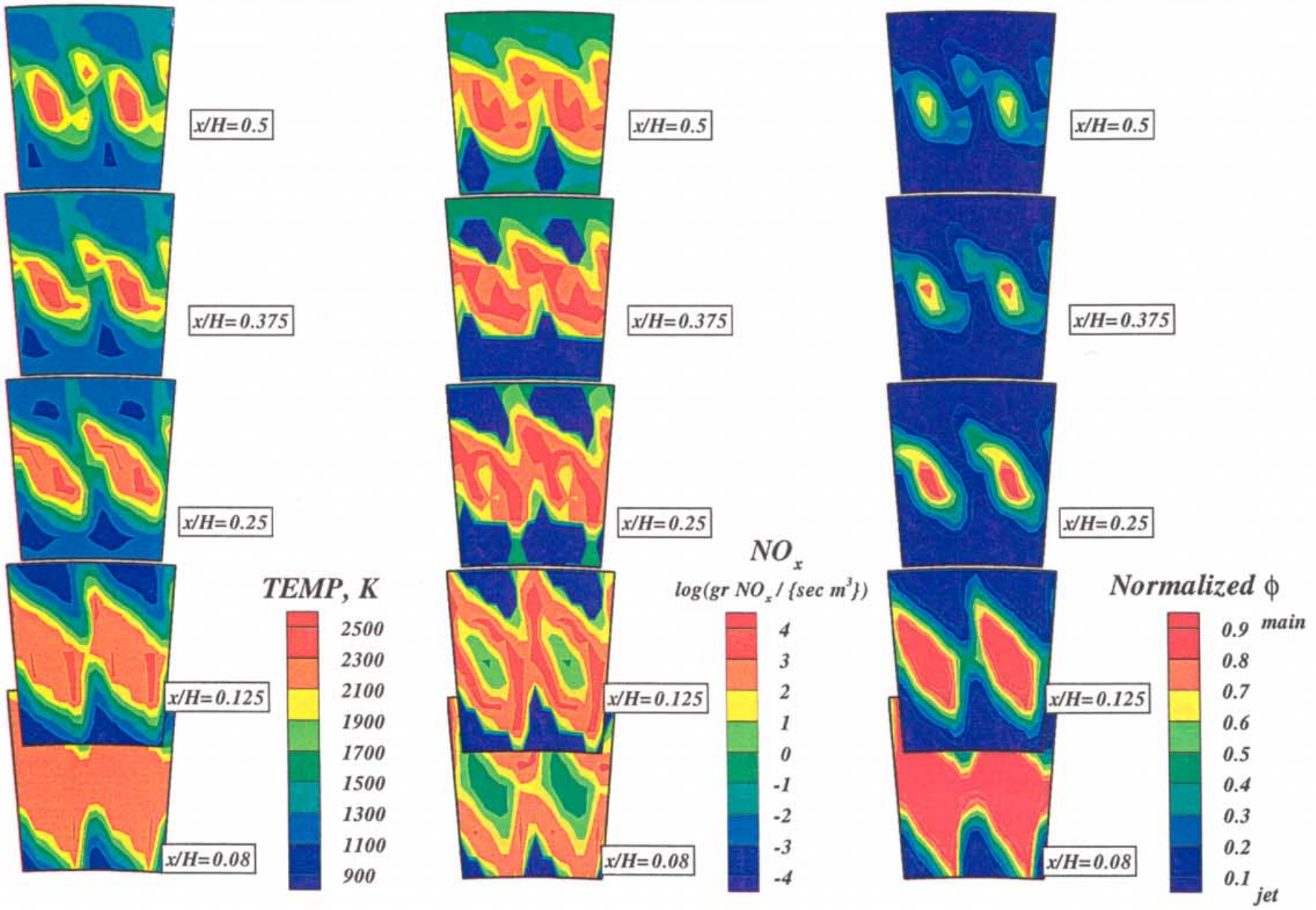

Figure-A31. Annular mixer configuration HO-31, 67.5^0 slanted slot, L/W=4, 87 per row (18 eq holes/row)
J=52.0, MR=2.96, DR=2.28, ϕ_{RZ}=1.80, ϕ_{LZ}=0.416 (2 sectors)

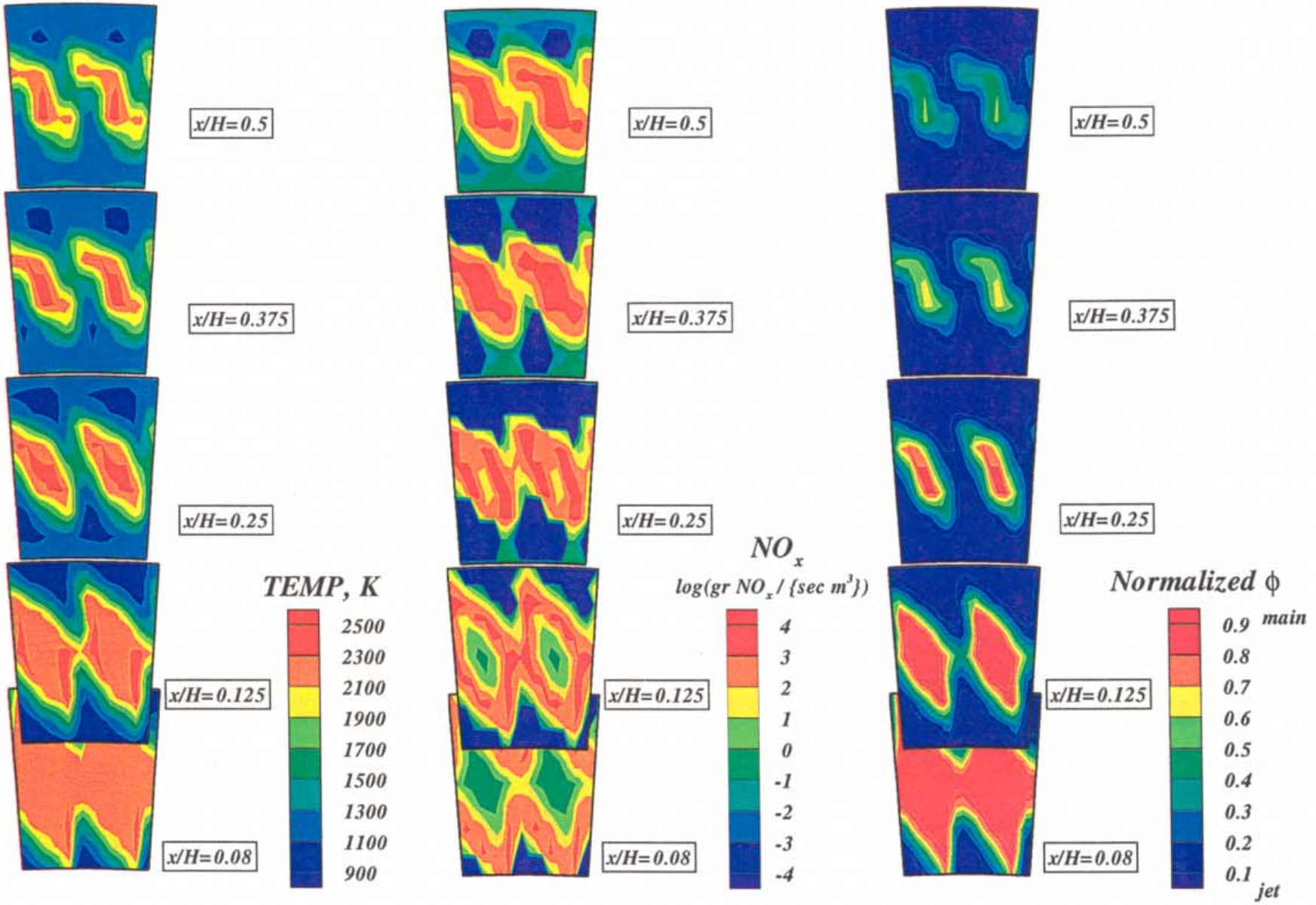

Figure-A32. Annular mixer configuration HO-32, 67.5^0 slanted slot, L/W=4, 97 per row (20 eq holes/row) J=52.0, MR=2.96, DR=2.28, ϕ_{RZ}=1.80, ϕ_{LZ}=0.416 (2 sectors)

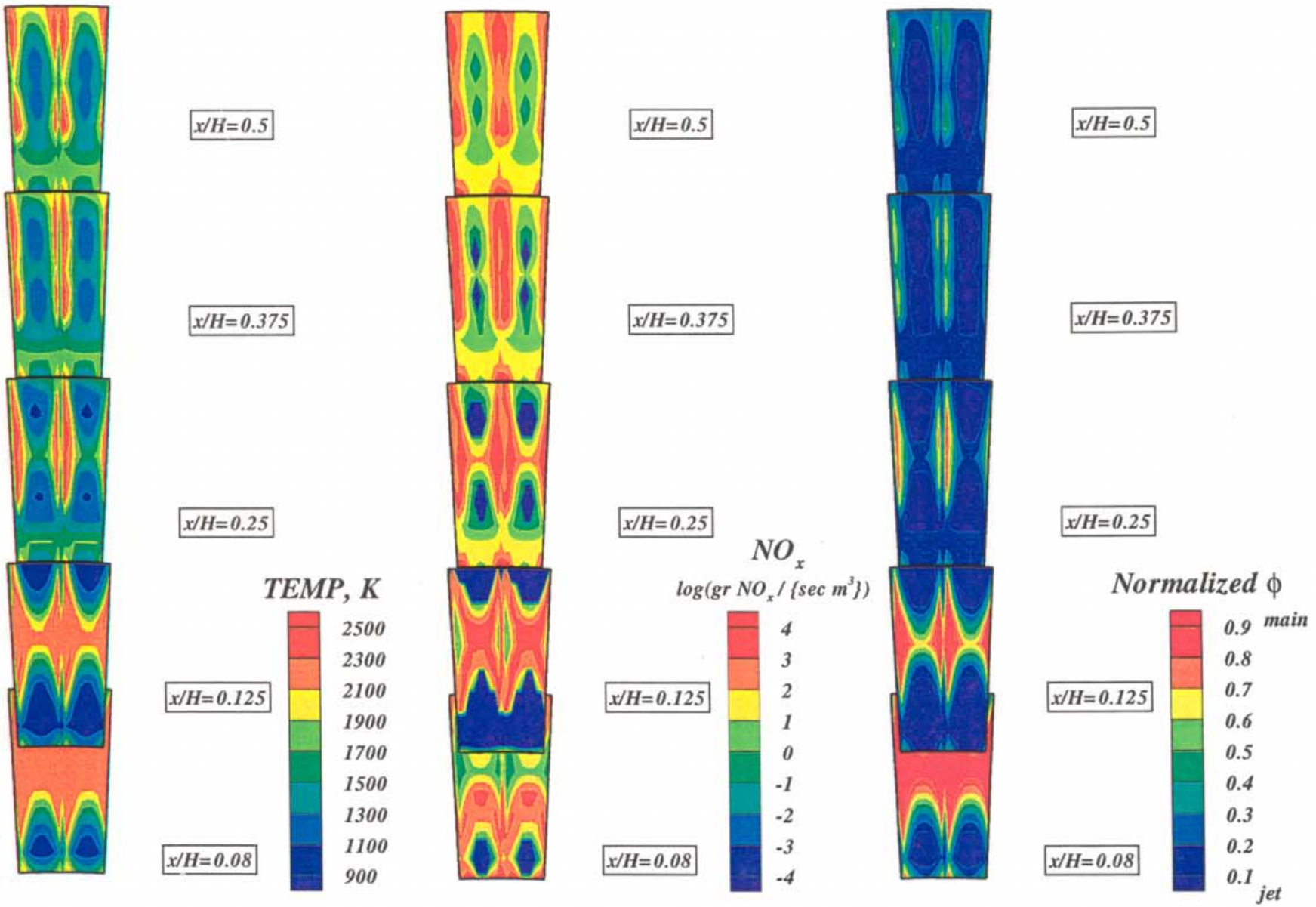

Figure-A33. Annular mixer configuration HO-33, 145 round holes per row (30 eq holes/row)
J=52.0, MR=2.96, DR=2.28, ϕ_{RZ}=1.80, ϕ_{LZ}=0.416 (2 sectors)

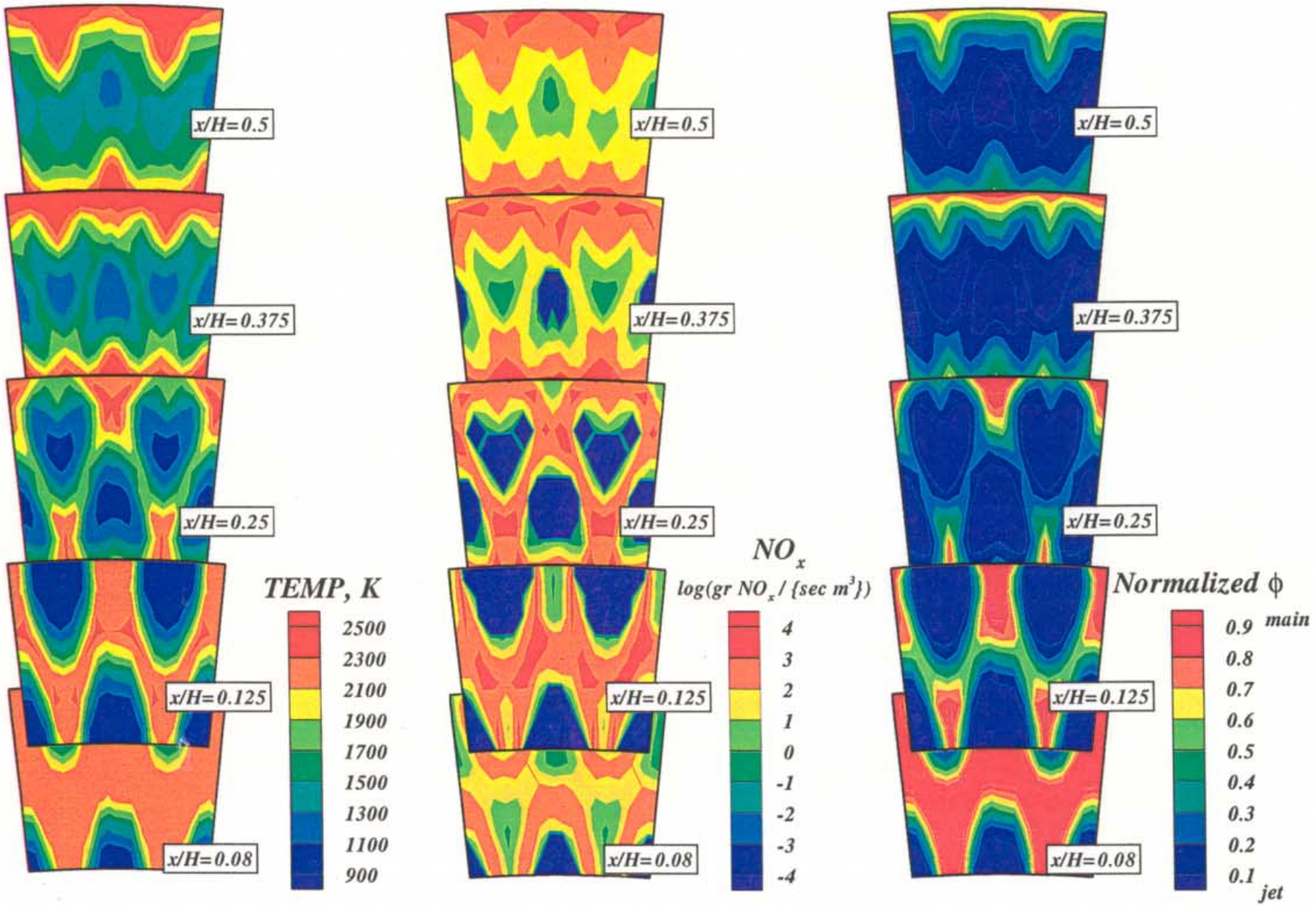

Figure-A34. Annular mixer configuration HO-34, 68 round holes per row (14 eq holes/row)
J=52.0, MR=2.96, DR=2.28, ϕ_{RZ}=1.80, ϕ_{LZ}=0.416 (2 sectors) [STAGGERED HOLE CONF]

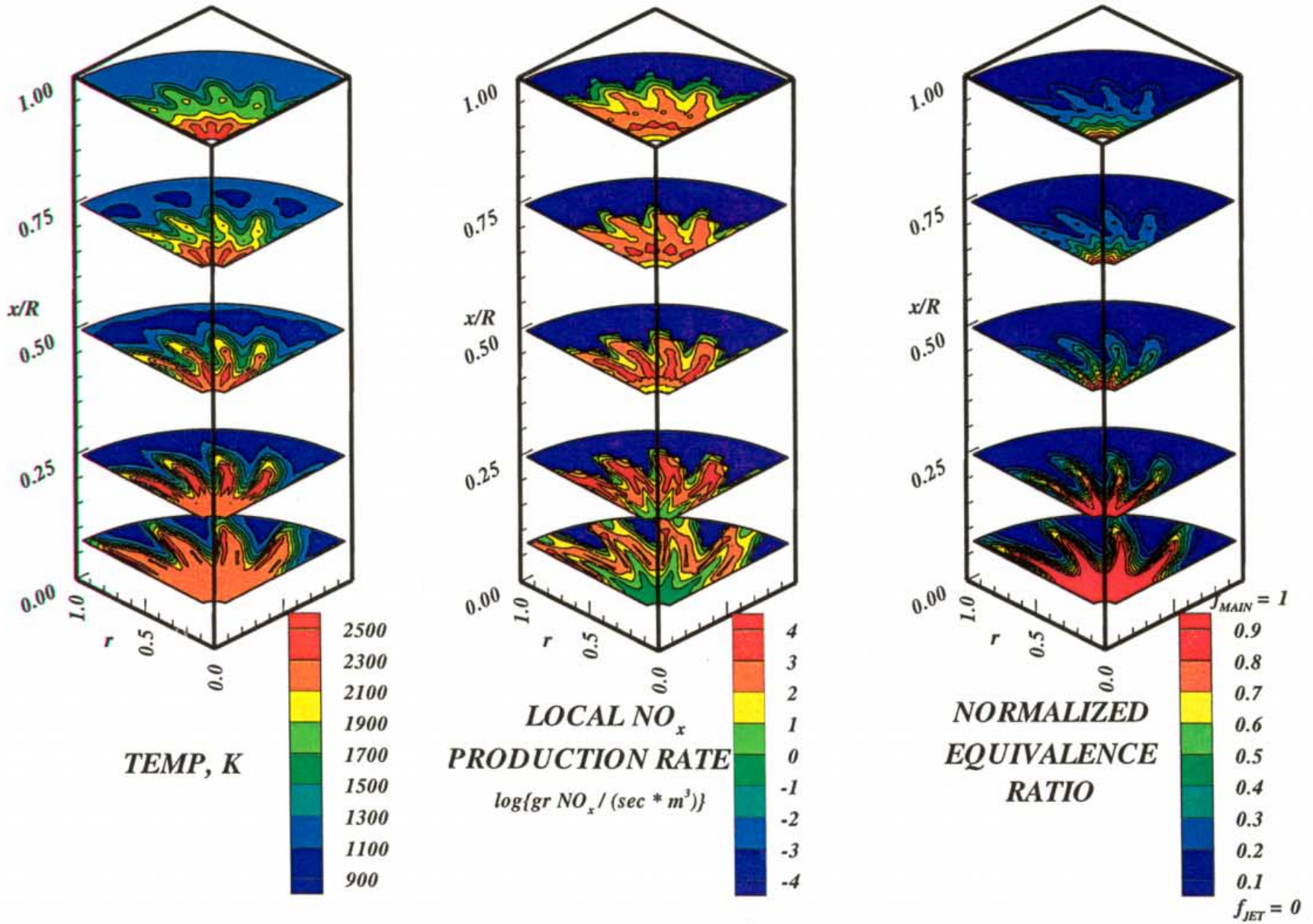

Figure-A35. Configuration HO-35, 67.5^0 slot L/W=4, 16 orifices /row
J=52.0, MR=2.96, DR=2.28, ϕ_{RZ} = 1.80, ϕ_{LZ} = 0.416 (4-adjacent sectors)

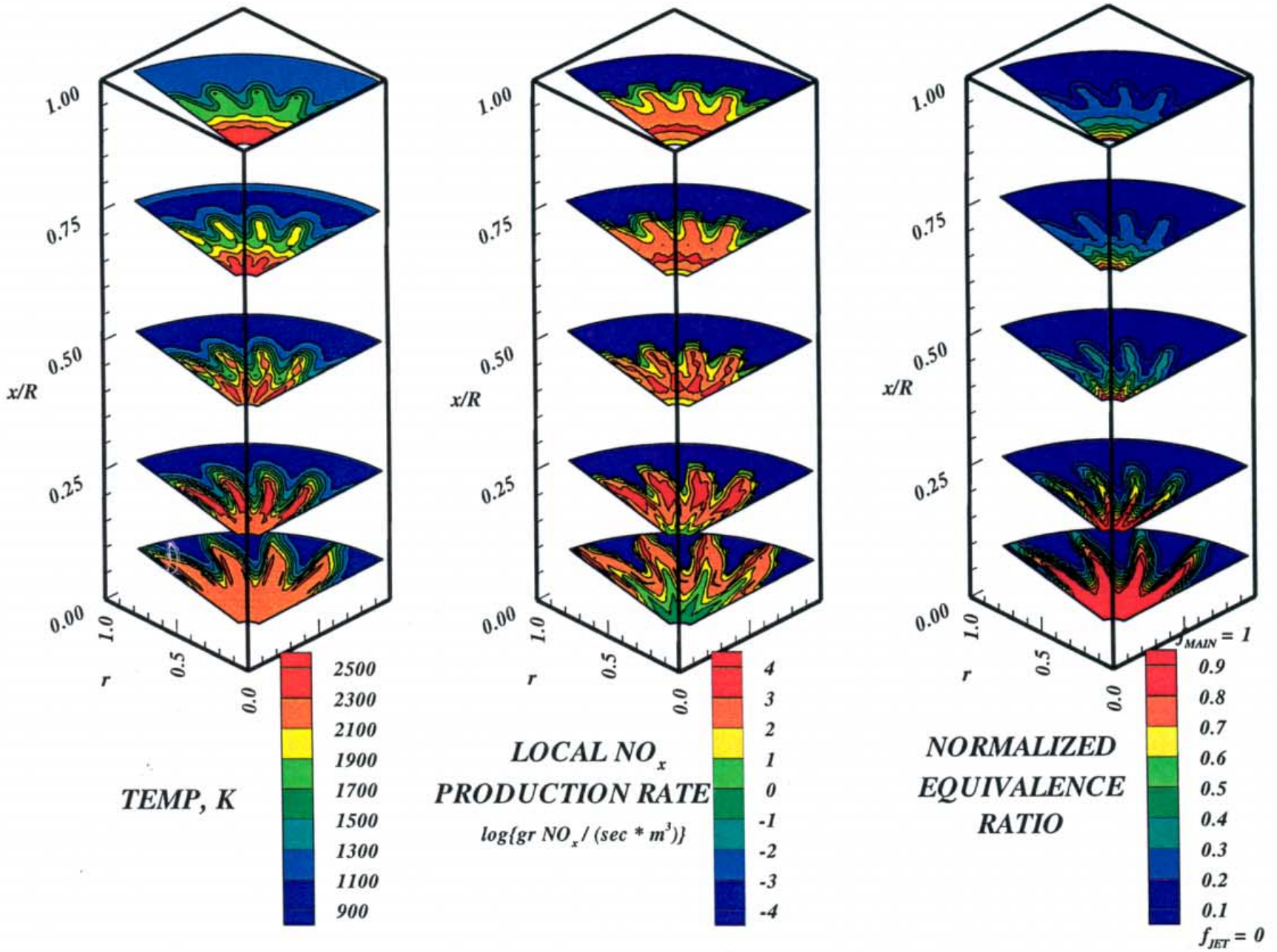

Figure-A36. Configuration HO-36, 67.5^0 slot L/W=4, 18 orifices /row
J=52.0, MR=2.96, DR=2.28, ϕ_{RZ} = 1.80, ϕ_{LZ} = 0.416 (4-adjacent sectors)

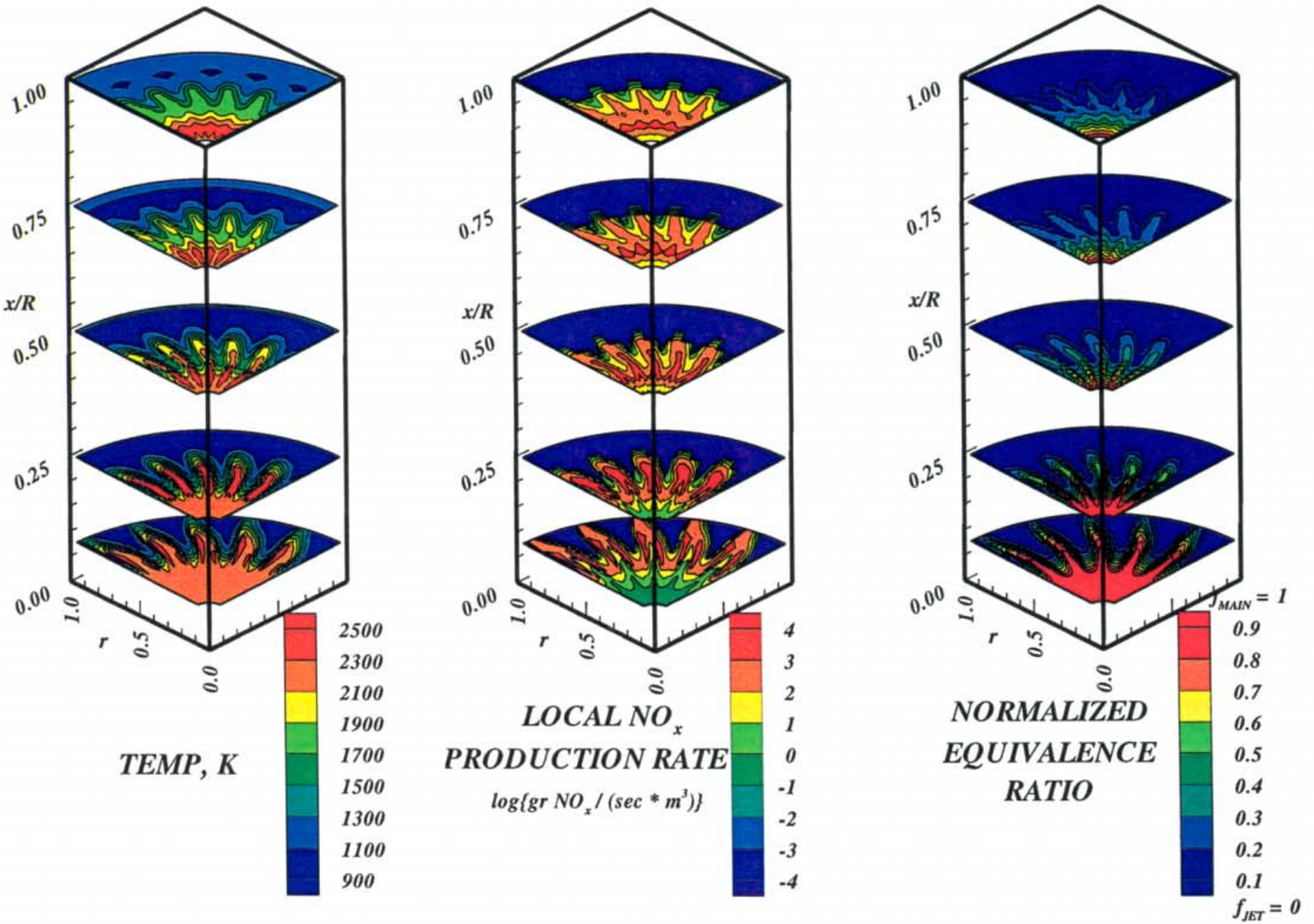

Figure-A37. Configuration HO-37, 67.5^0 slot L/W=4, 20 orifices /row
J=52.0, MR=2.96, DR=2.28, ϕ_{RZ} = 1.80, ϕ_{LZ} = 0.416 (5-adjacent sectors)

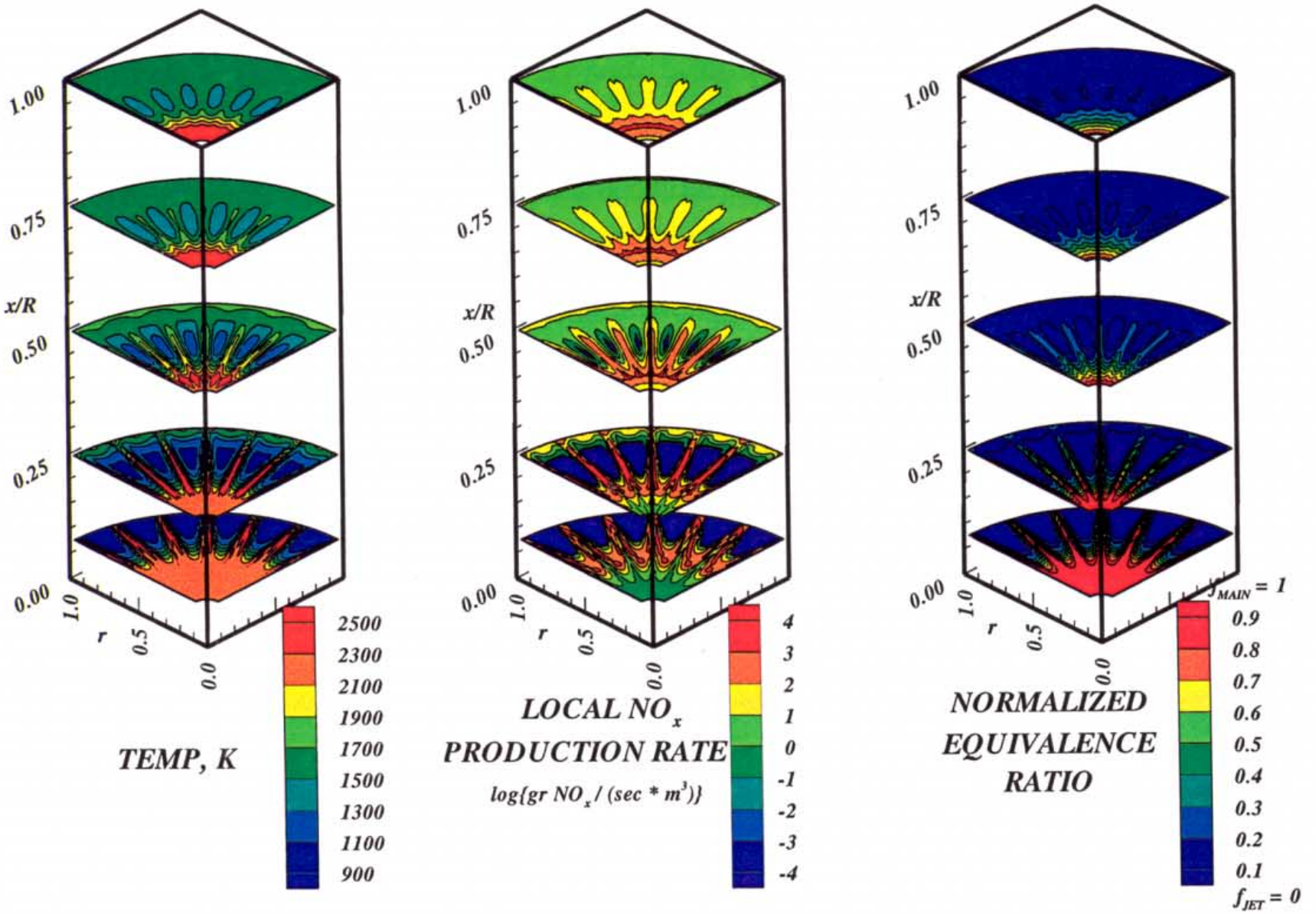

Figure-A38. Configuration HO-38, 24 round orifices /row

J=52.0, MR=2.96, DR=2.28, ϕ_{RZ} = 1.80, ϕ_{LZ} = 0.416 (6-adjacent sectors)

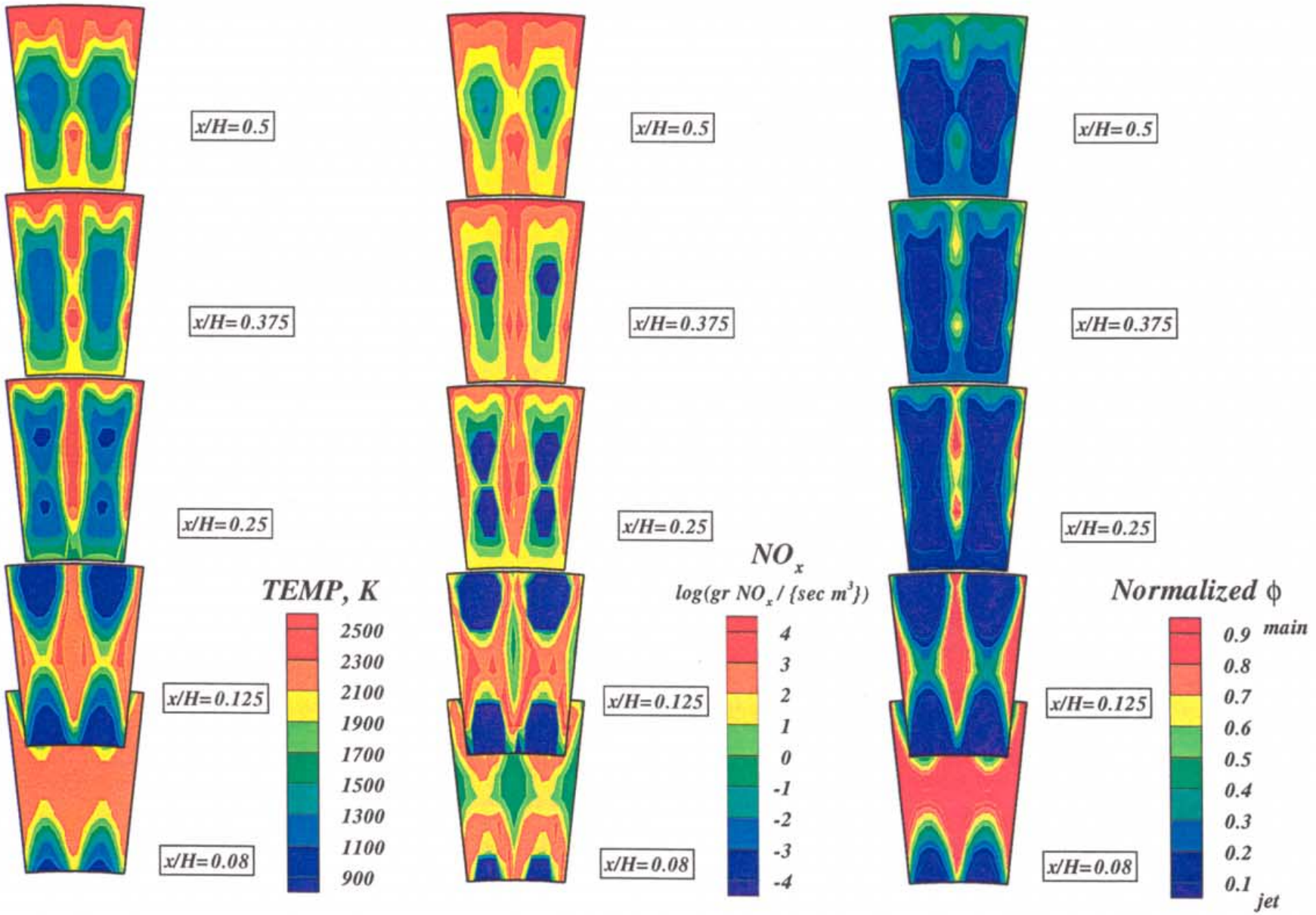

Figure-A39. Annular mixer configuration HO-39, 64 round holes per row (6 eq holes/row)
J=52.0, MR=2.96, DR=2.28, ϕ_{RZ}=1.80, ϕ_{LZ}=0.416 (2 sectors)

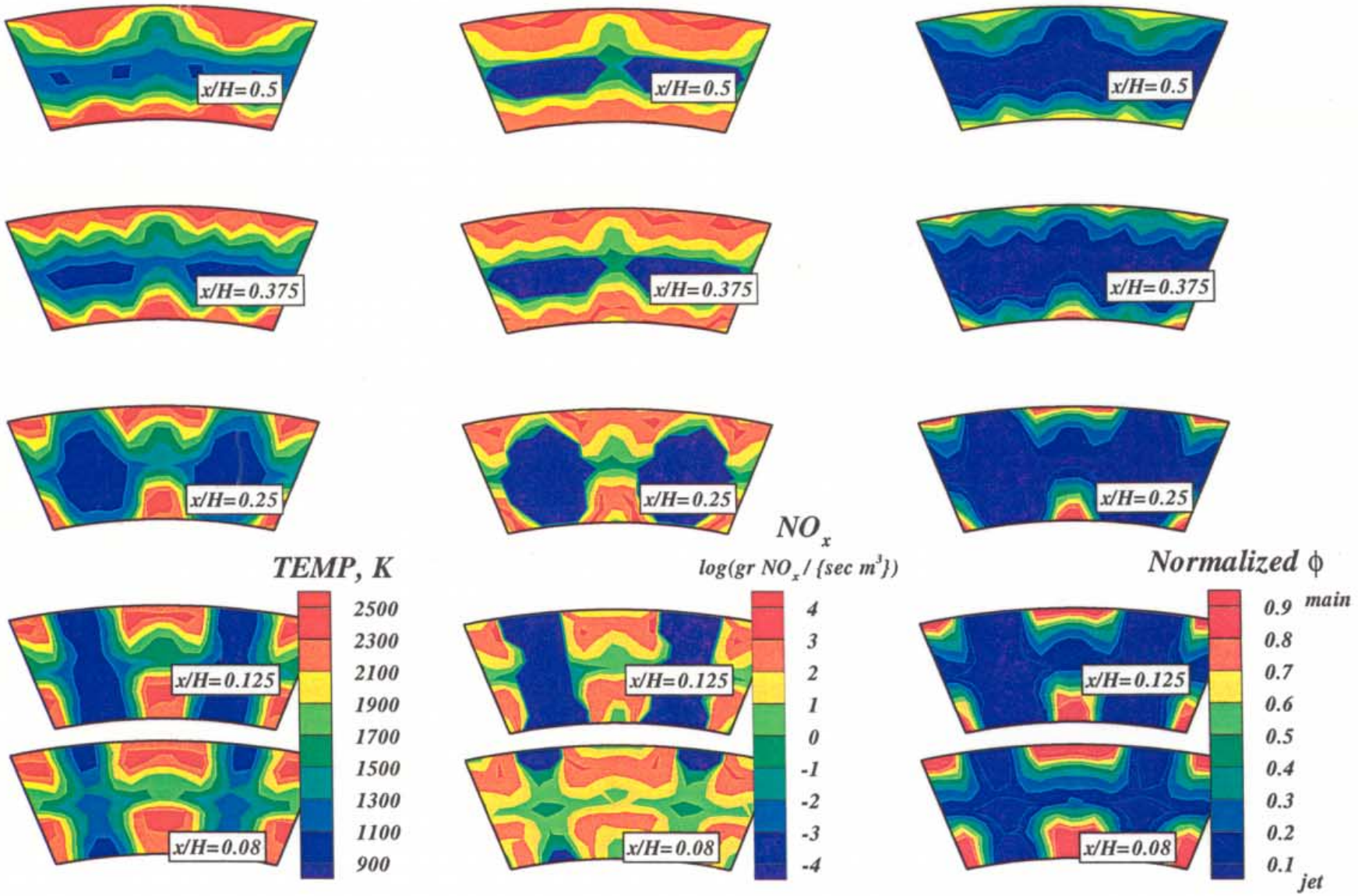

Figure-A40. Annular mixer configuration HO-40, 21 round holes per row (2 eq holes/row)
J=52.0, MR=2.96, DR=2.28, ϕ_{RZ}=1.80, ϕ_{LZ}=0.416 (2 sectors)

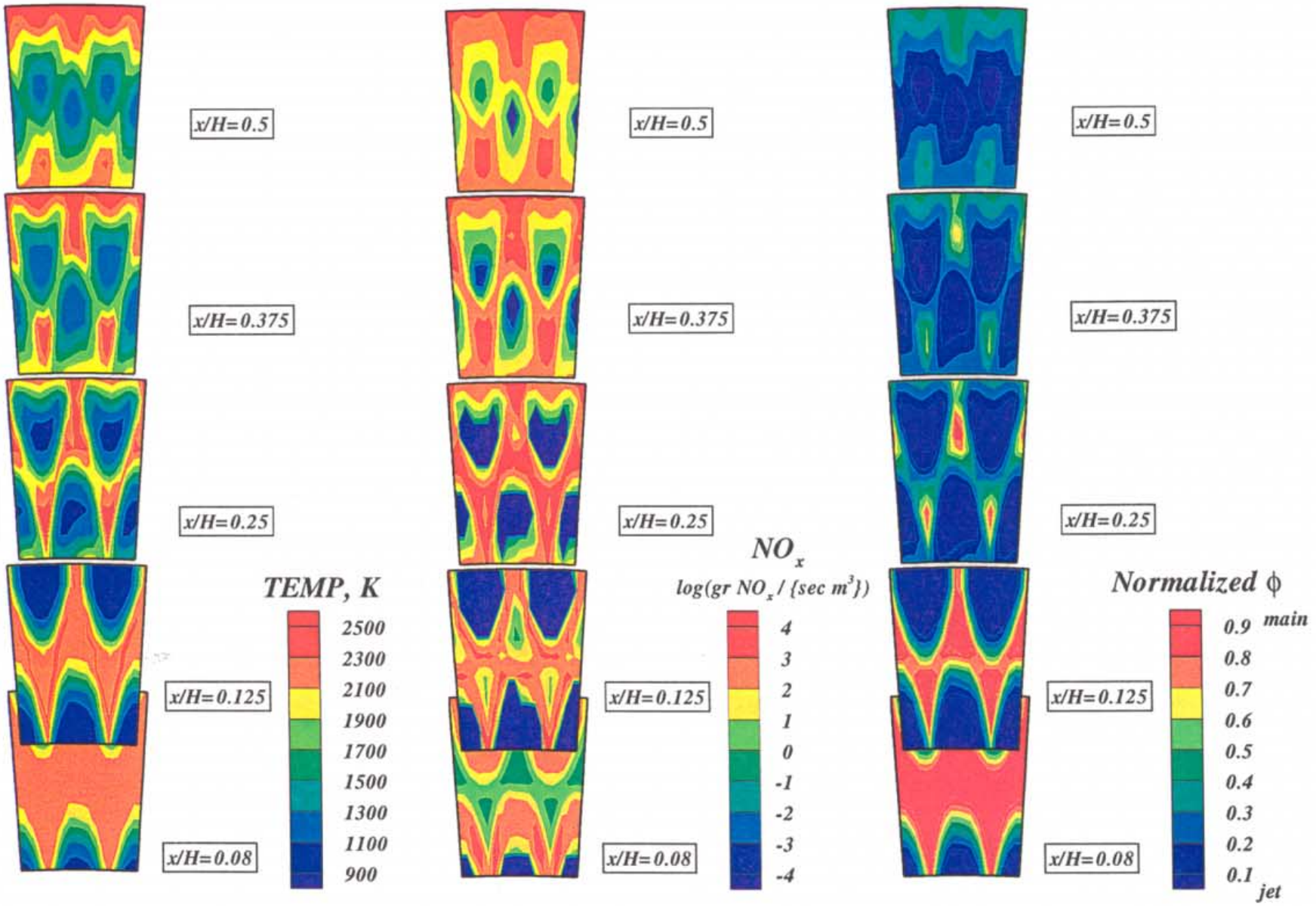

Figure-A41. Annular mixer configuration HO-41, 106 round holes per row (22 eq holes/row)
J=52.0, MR=2.96, DR=2.28, ϕ_{RZ}=1.80, ϕ_{LZ}=0.416 (2 sectors) [STAGGERED HOLE CONF]

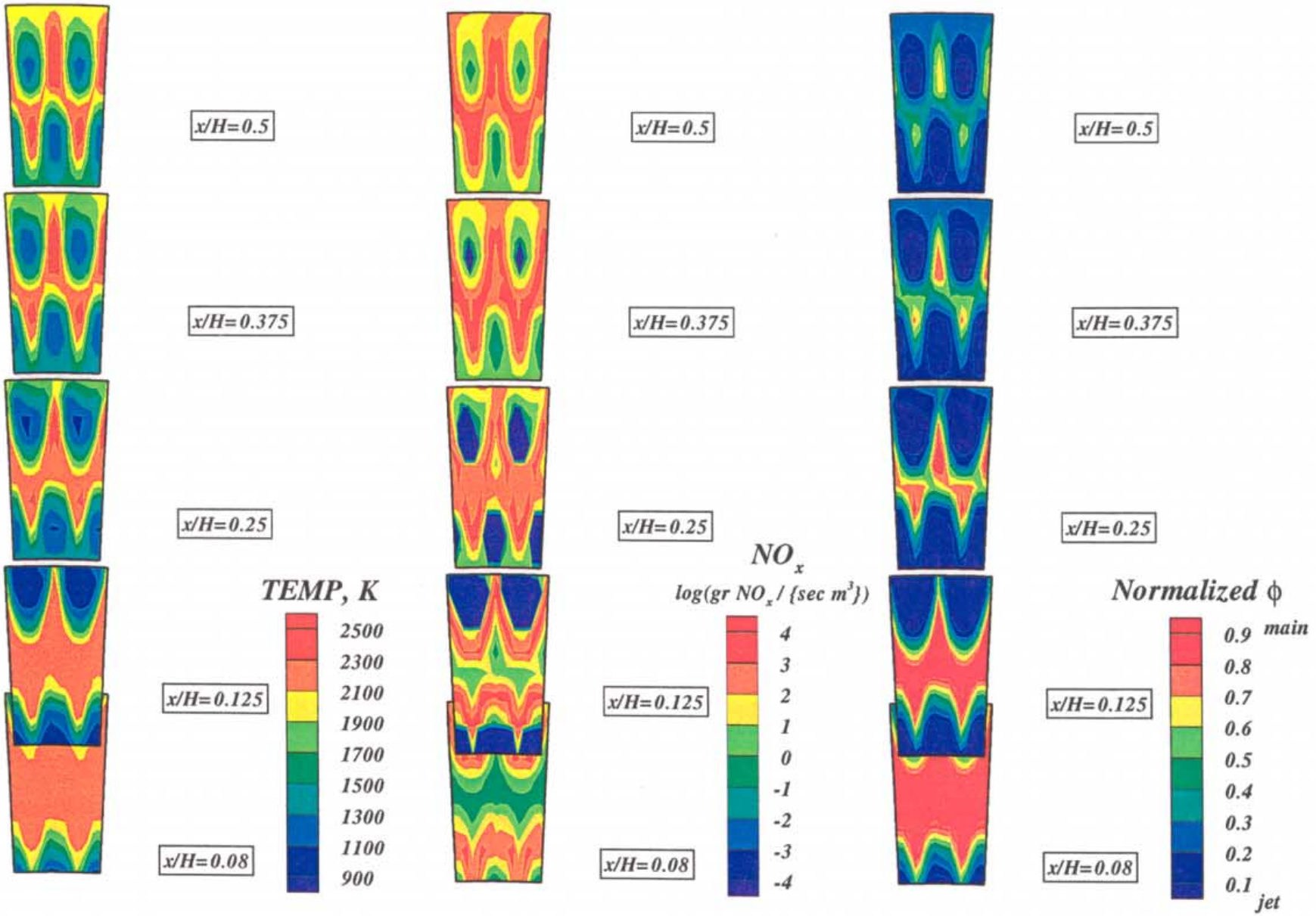

Figure-A42. Annular mixer configuration HO-42, 145 round holes per row (30 eq holes/row) J=52.0, MR=2.96, DR=2.28, ϕ_{RZ}=1.80, ϕ_{LZ}=0.416 (2 sectors) [STAGGERED HOLE CONF]

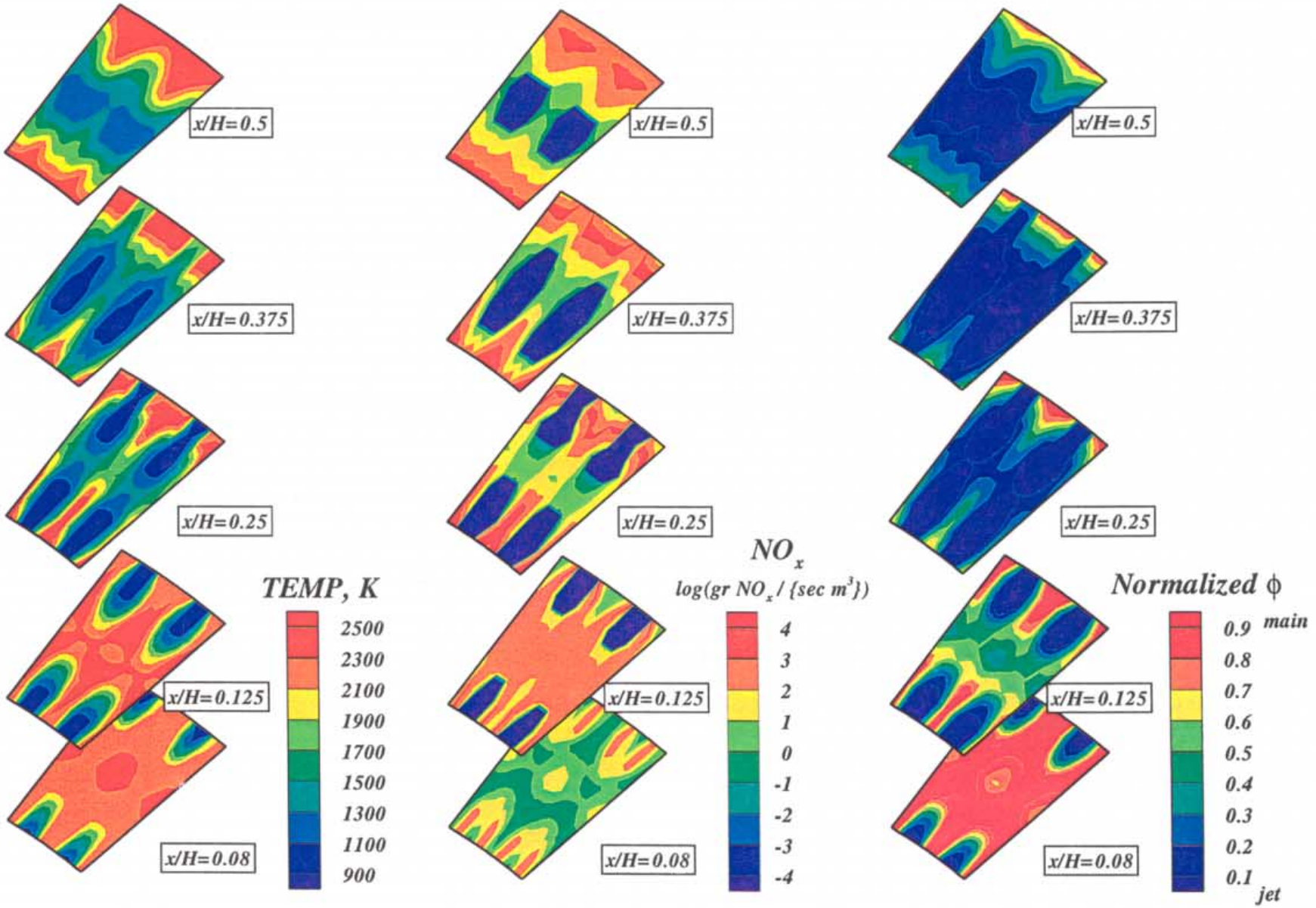

Figure-A43. Annular mixer configuration HO-43, flow aligned slot L/W=4, 64 per row (6 eq holes/row)
J=52.0, MR=2.96, DR=2.28, ϕ_{RZ}=1.80, ϕ_{LZ}=0.416 (2 sectors)

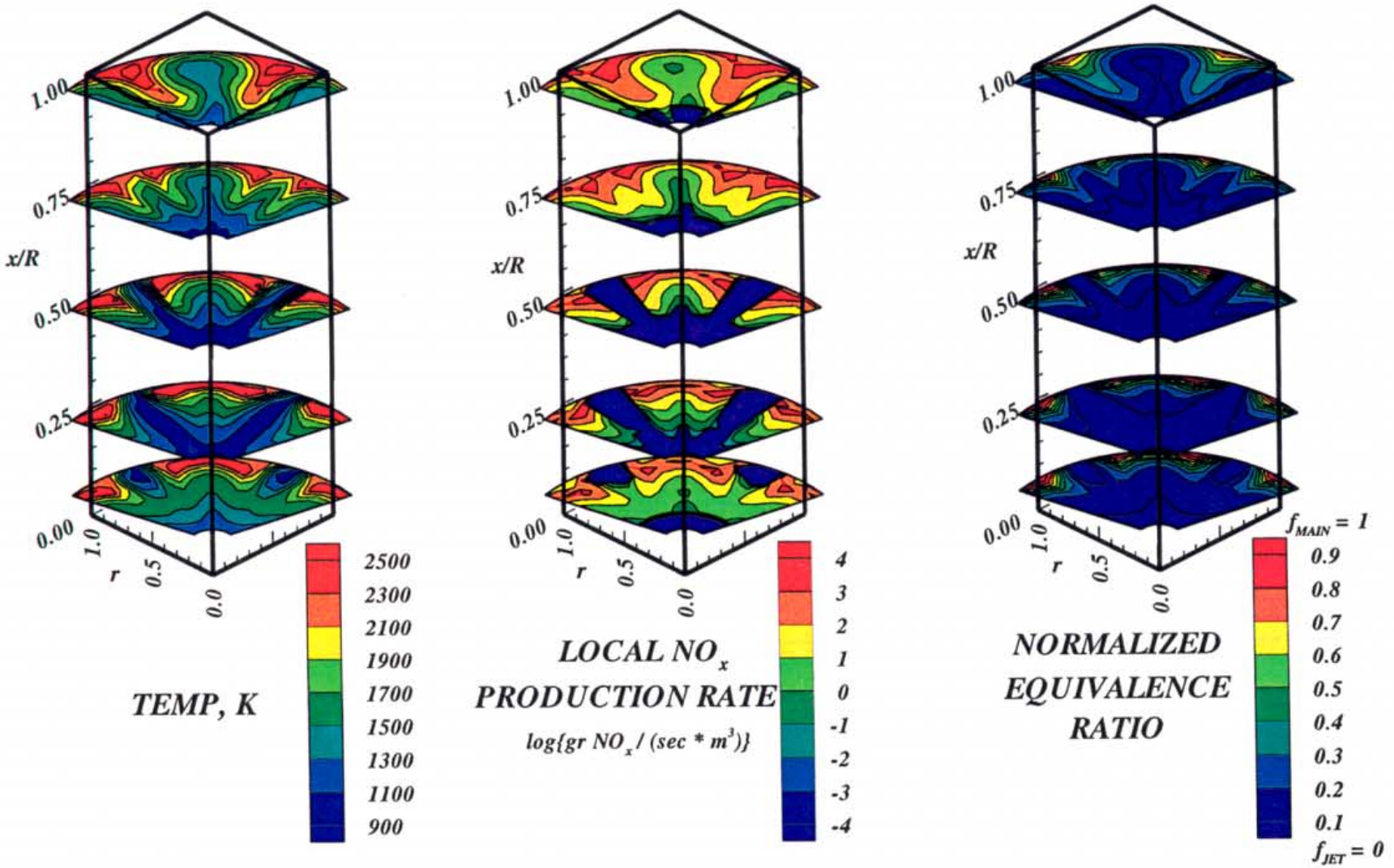

Figure-A44. Configuration HO-44, flow aligned slot L/W=4, 6 orifices /row

J=52.0, MR=2.96, DR=2.28, ϕ_{RZ} = 1.80, ϕ_{LZ} = 0.416 (2-adjacent sectors)

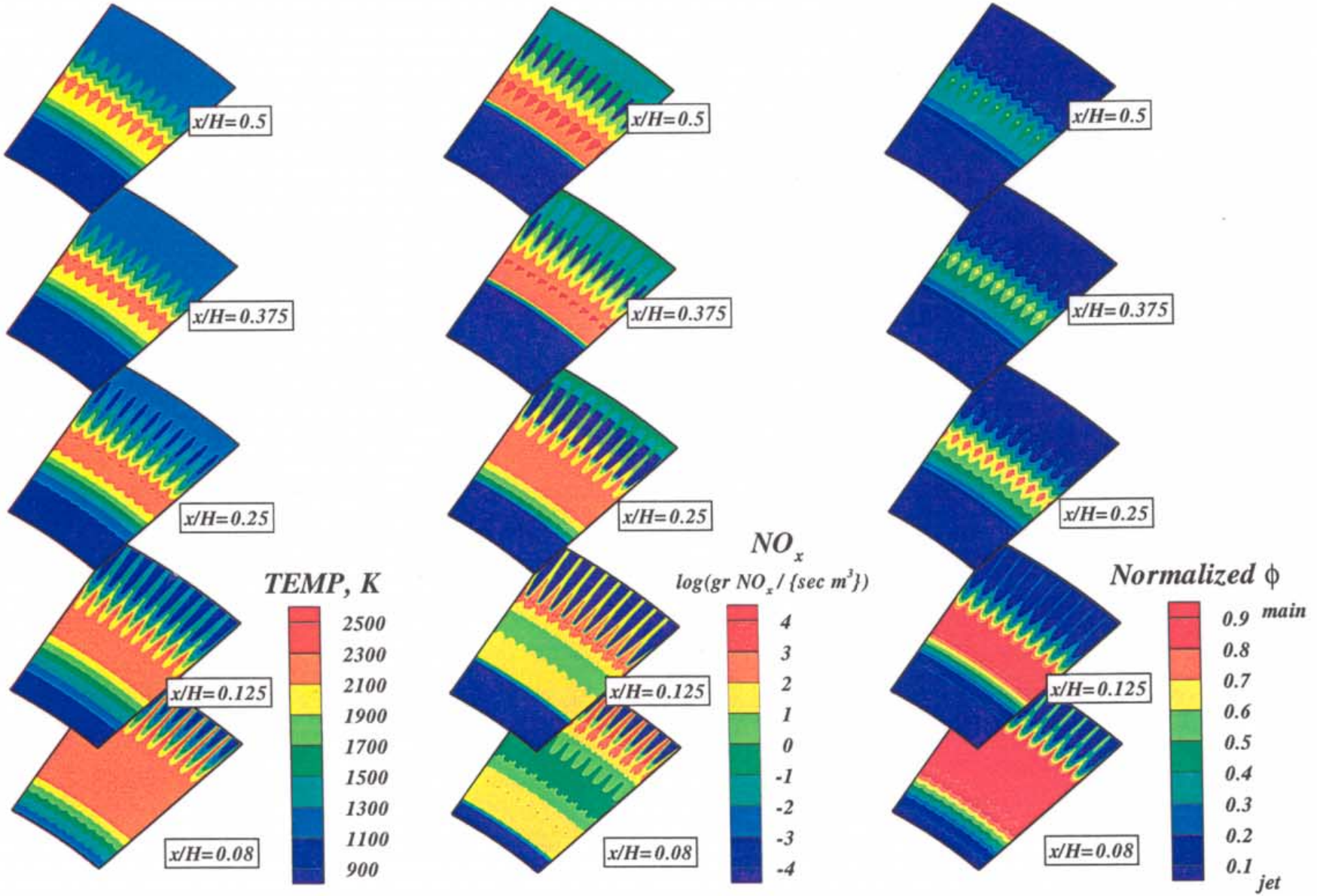

Figure-A45. Annular mixer configuration HO-45, flow aligned slot L/W=4, 277 per row (26 eq holes/row) J=52.0, MR=2.96, DR=2.28, ϕ_{RZ}=1.80, ϕ_{LZ}=0.416 (10 sectors)

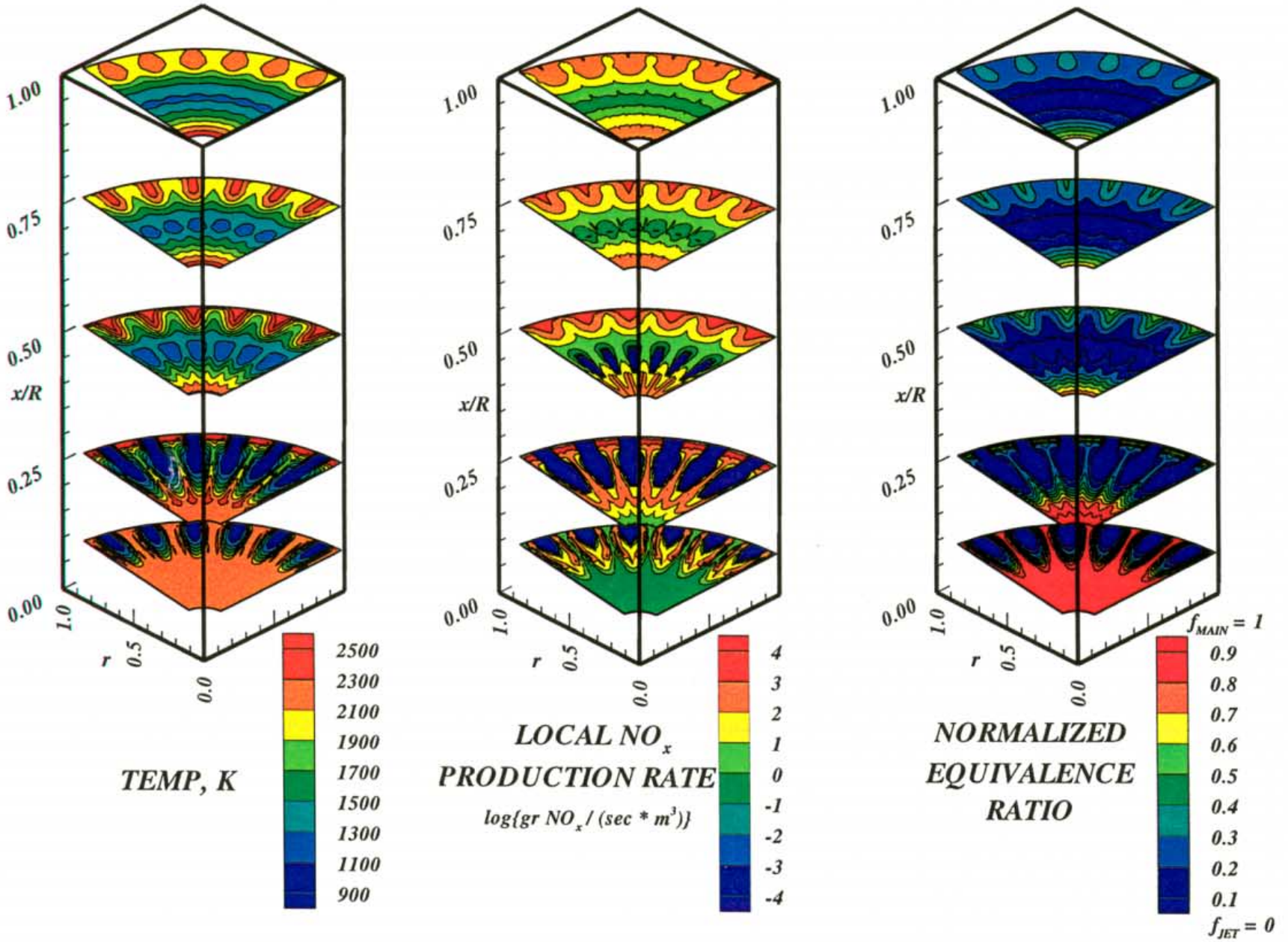

Figure-A46. Configuration HO-46, flow aligned slot L/W=4, 26 orifices /row
J=52.0, MR=2.96, DR=2.28, ϕ_{RZ} = 1.80, ϕ_{LZ} = 0.416 (6-adjacent sectors)

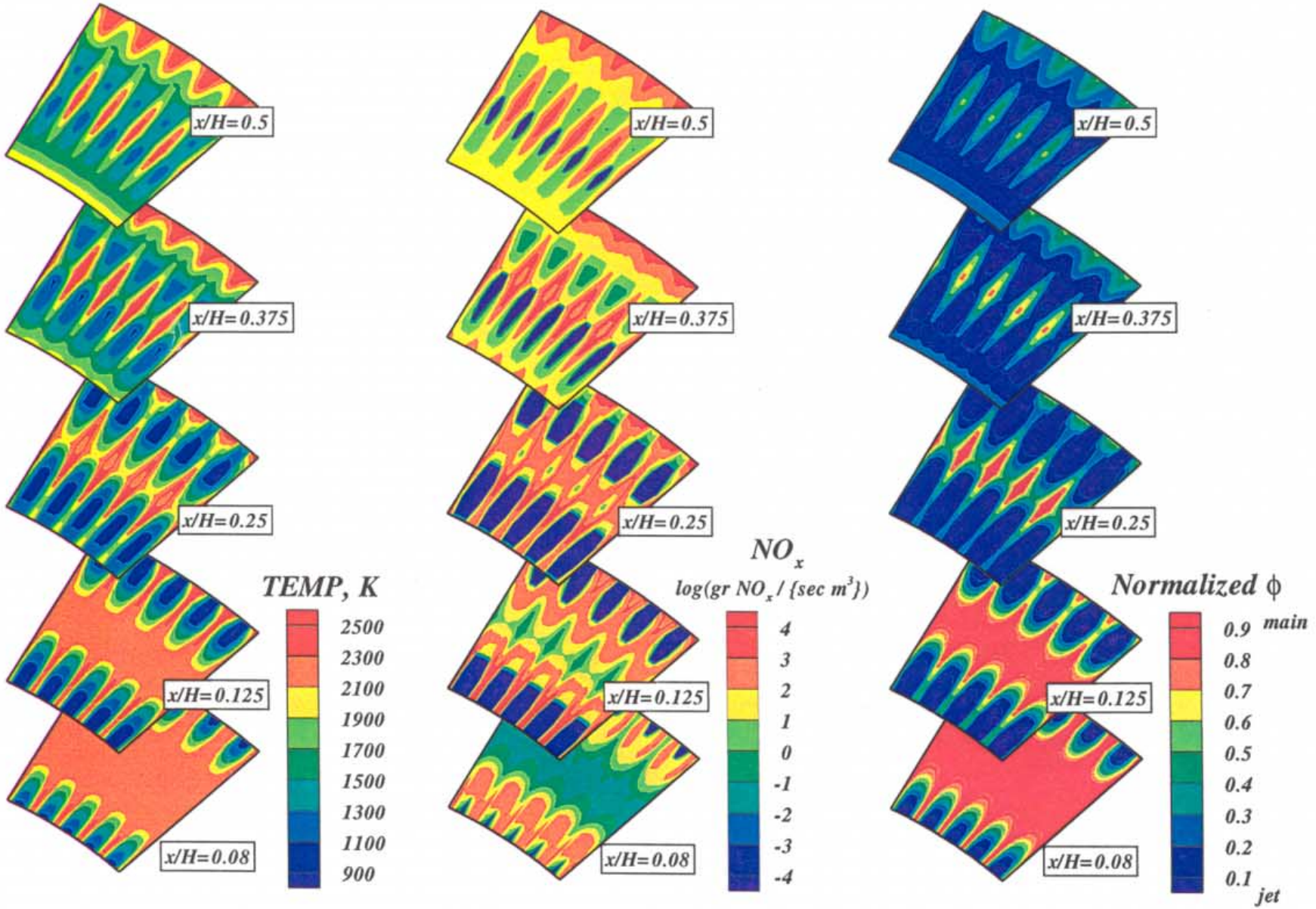

Figure-A47. Annular mixer configuration HO-47, flow aligned slot L/W=4, 107 per row (10 eq holes/row)
J=52.0, MR=2.96, DR=2.28, ϕ_{RZ}=1.80, ϕ_{LZ}=0.416 (5 sectors)

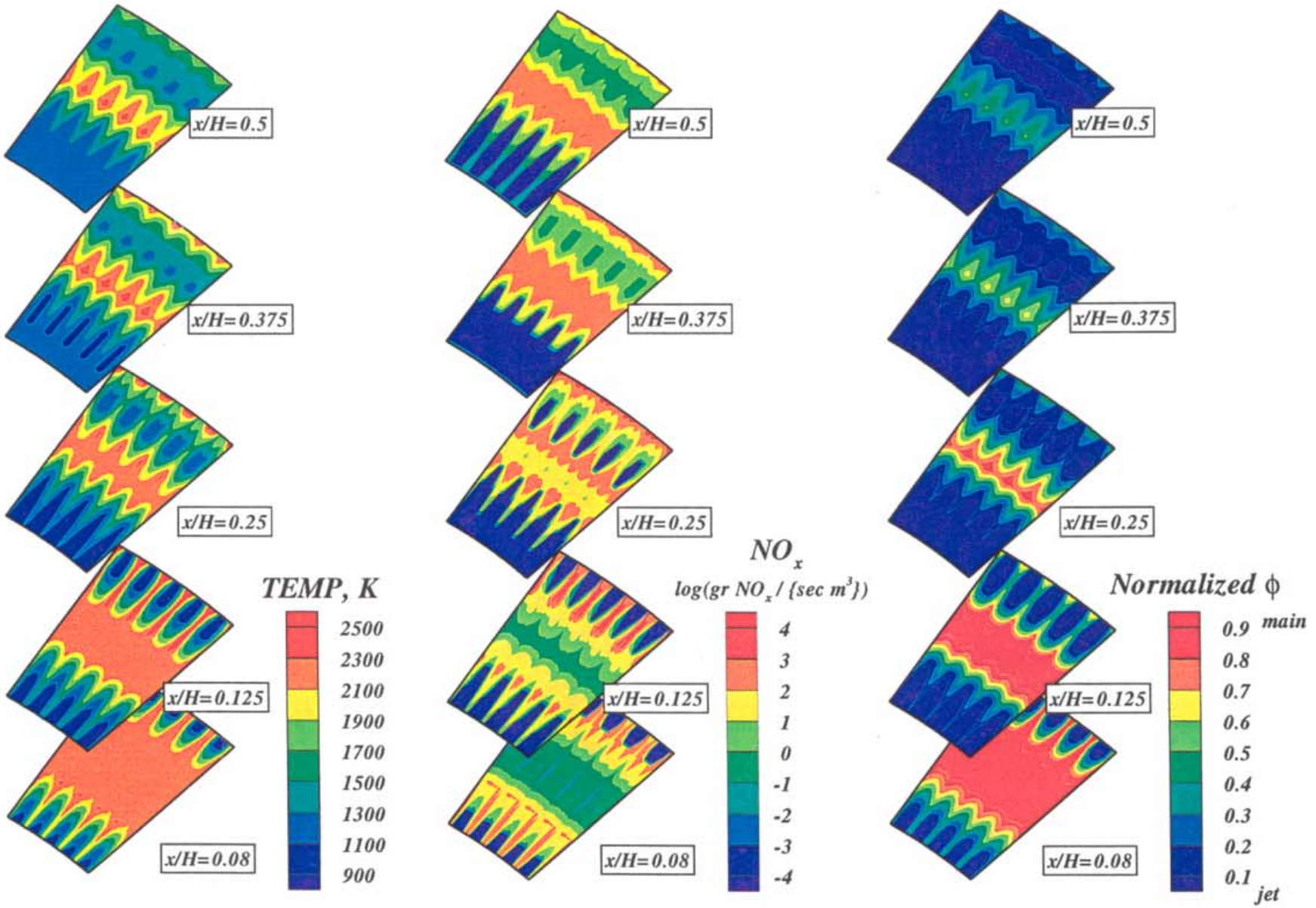

Figure-A48. Annular mixer configuration HO-48, flow aligned slot L/W=4, 149 per row (14 eq holes/row) J=52.0, MR=2.96, DR=2.28, ϕ_{RZ}=1.80, ϕ_{LZ}=0.416 (5 sectors)

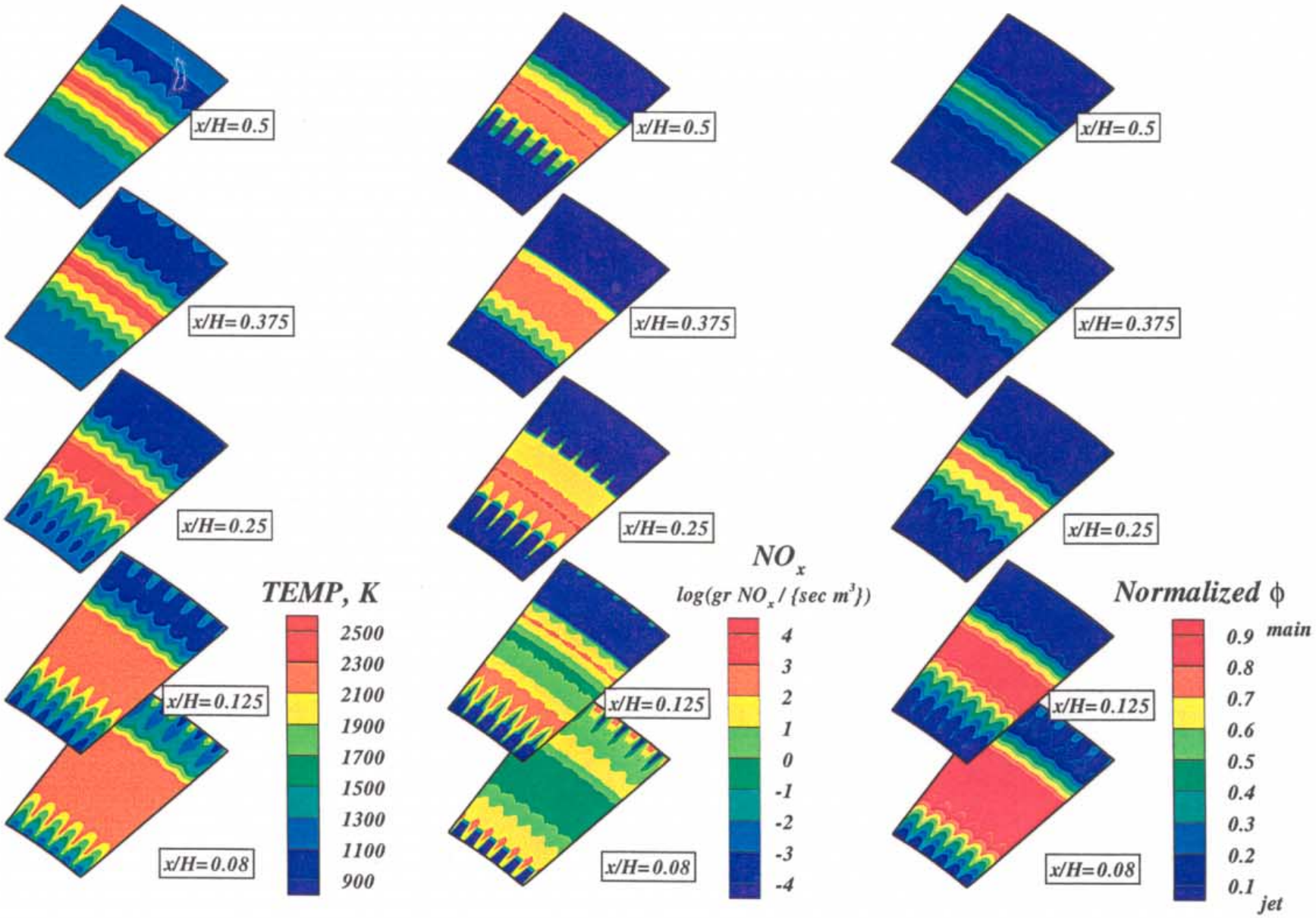

Figure-A49. Annular mixer configuration HO-49, flow aligned slot L/W=4, 192 per row (18 eq holes/row)
J=52.0, MR=2.96, DR=2.28, ϕ_{RZ}=1.80, ϕ_{LZ}=0.416 (6 sectors)

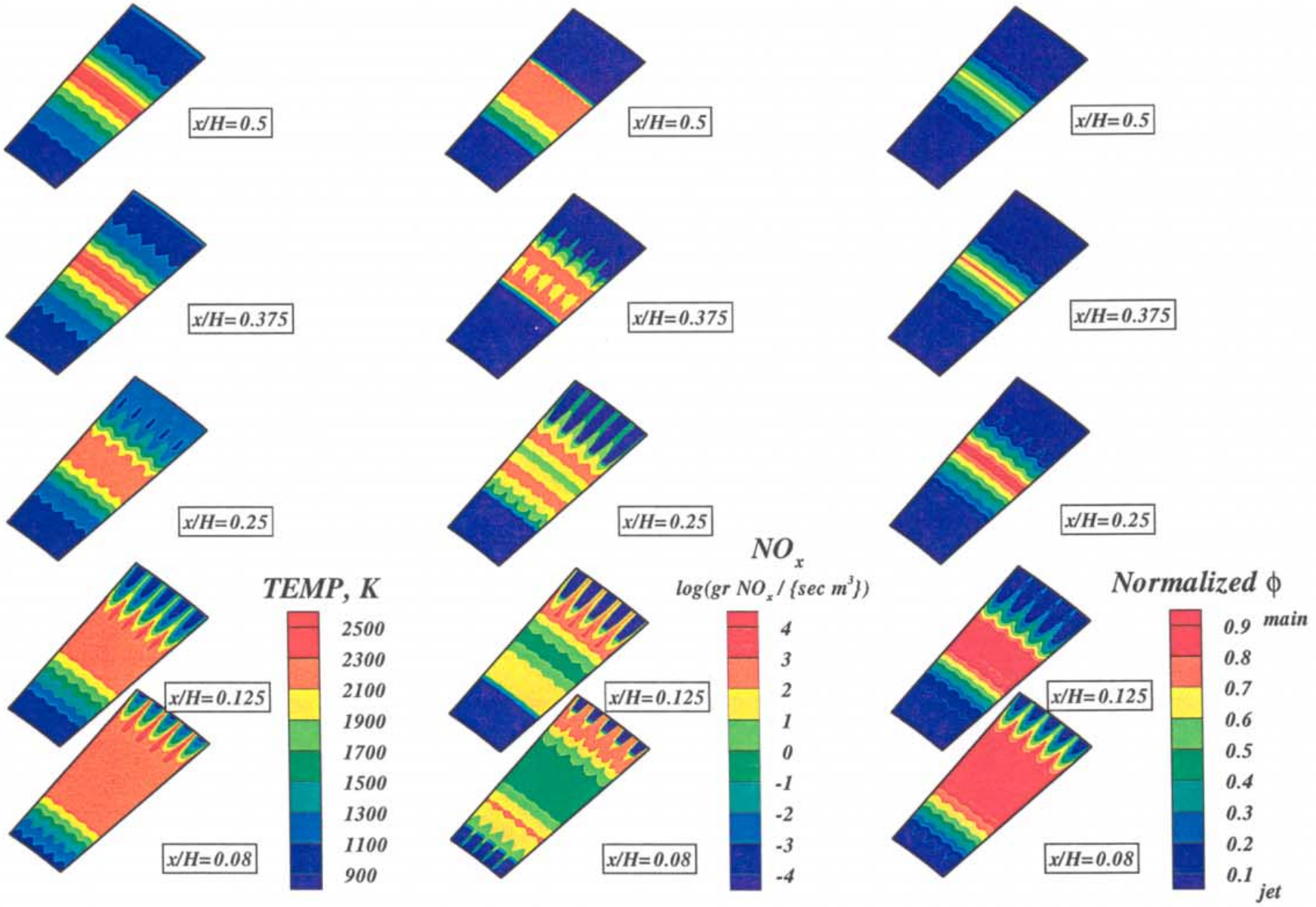

Figure-A50. Annular mixer configuration HO-50, flow aligned slot L/W=4, 235 per row (22 eq holes/row) J=52.0, MR=2.96, DR=2.28, ϕ_{RZ}=1.80, ϕ_{LZ}=0.416 (5 sectors)

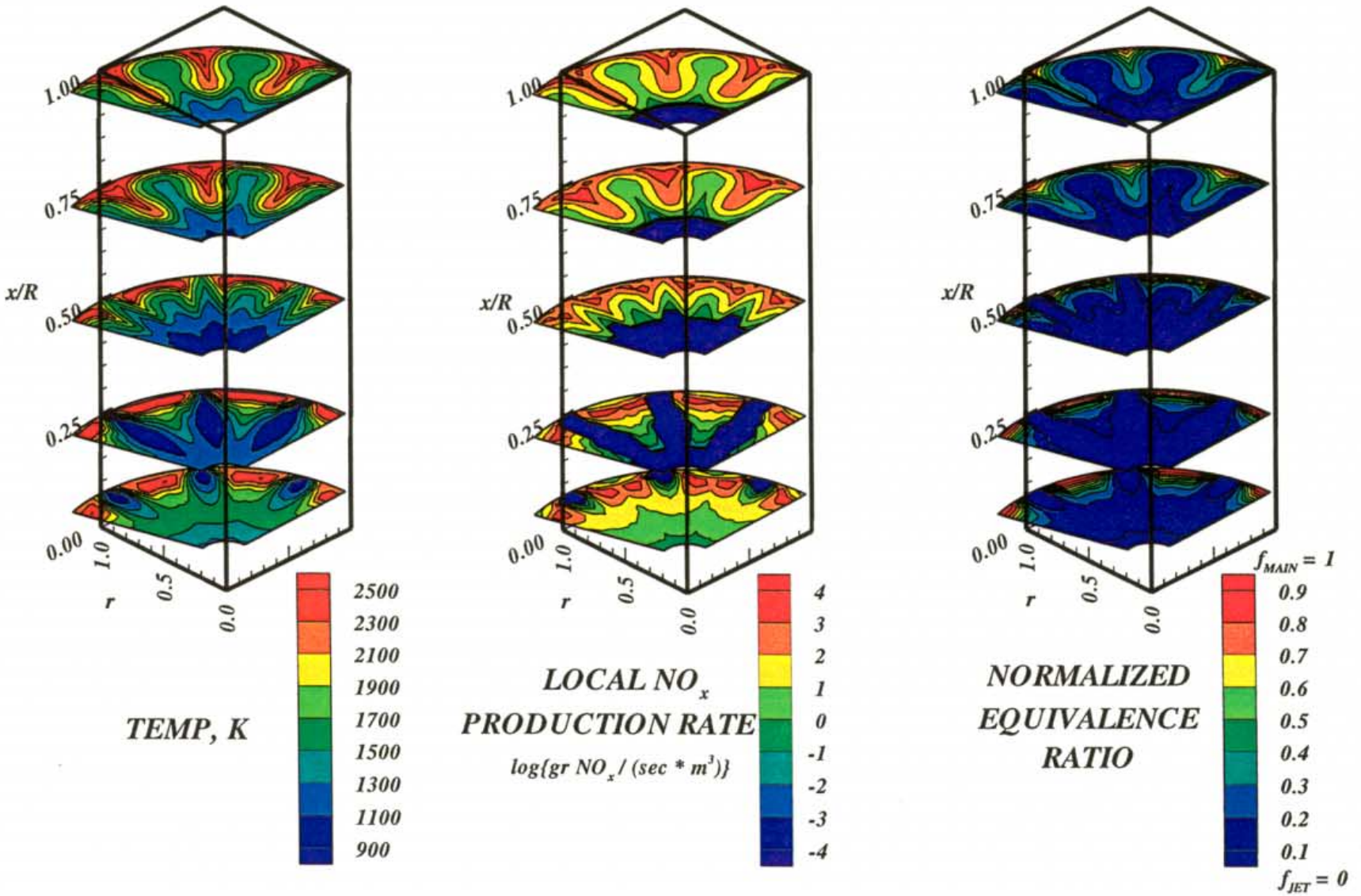

Figure-A51. Configuration HO-51, flow aligned slot L/W=4, 10 orifices /row
J=52.0, MR=2.96, DR=2.28, ϕ_{RZ} = 1.80, ϕ_{LZ} = 0.416 (3-adjacent sectors)

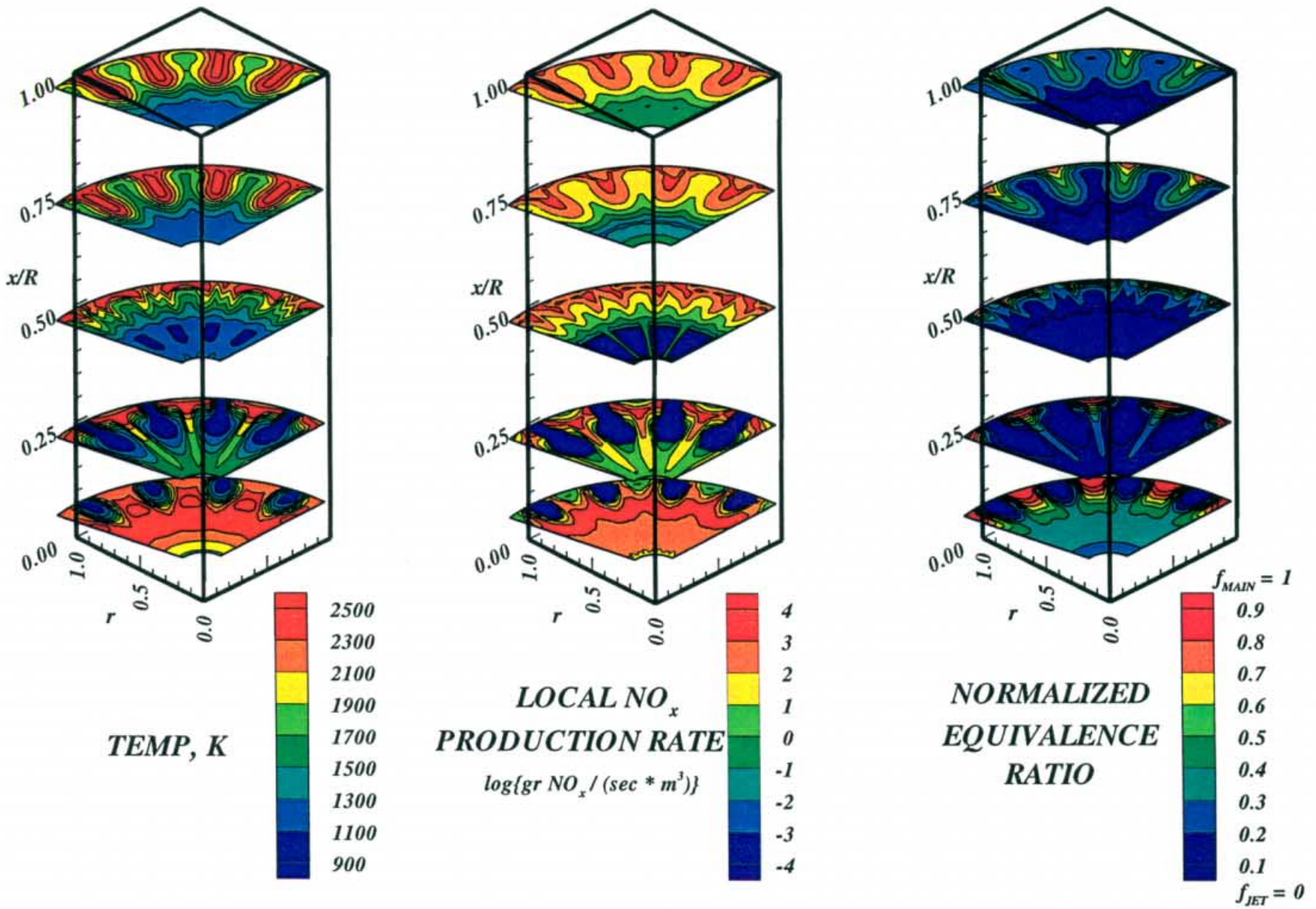

Figure-A52. Configuration HO-52, flow aligned slot L/W=4, 14 orifices /row
J=52.0, MR=2.96, DR=2.28, ϕ_{RZ} = 1.80, ϕ_{LZ} = 0.416 (4-adjacent sectors)

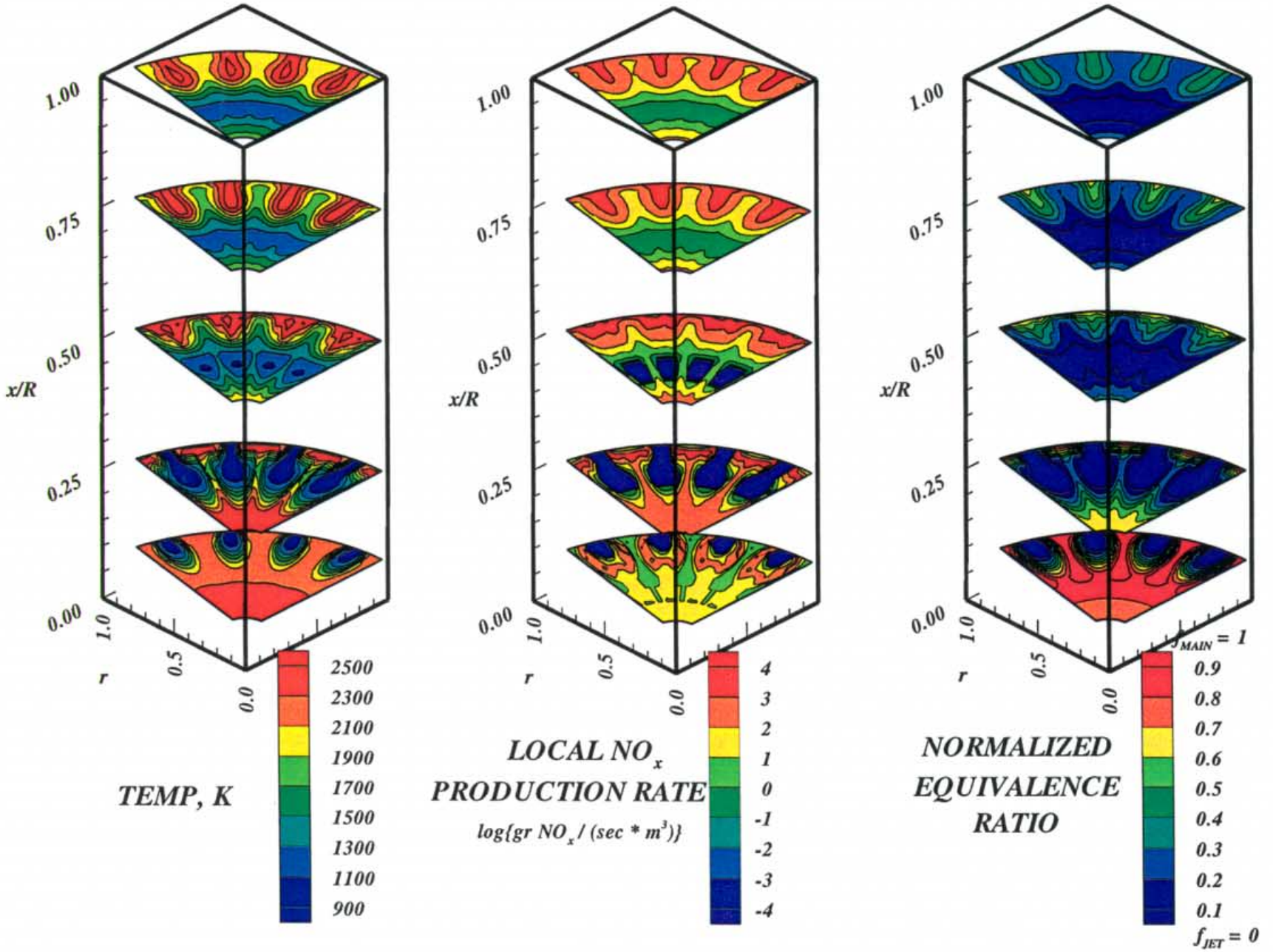

Figure-A53. Configuration HO-53, flow aligned slot L/W=4, 18 orifices /row
J=52.0, MR=2.96, DR=2.28, ϕ_{RZ} = 1.80, ϕ_{LZ} = 0.416 (4-adjacent sectors)

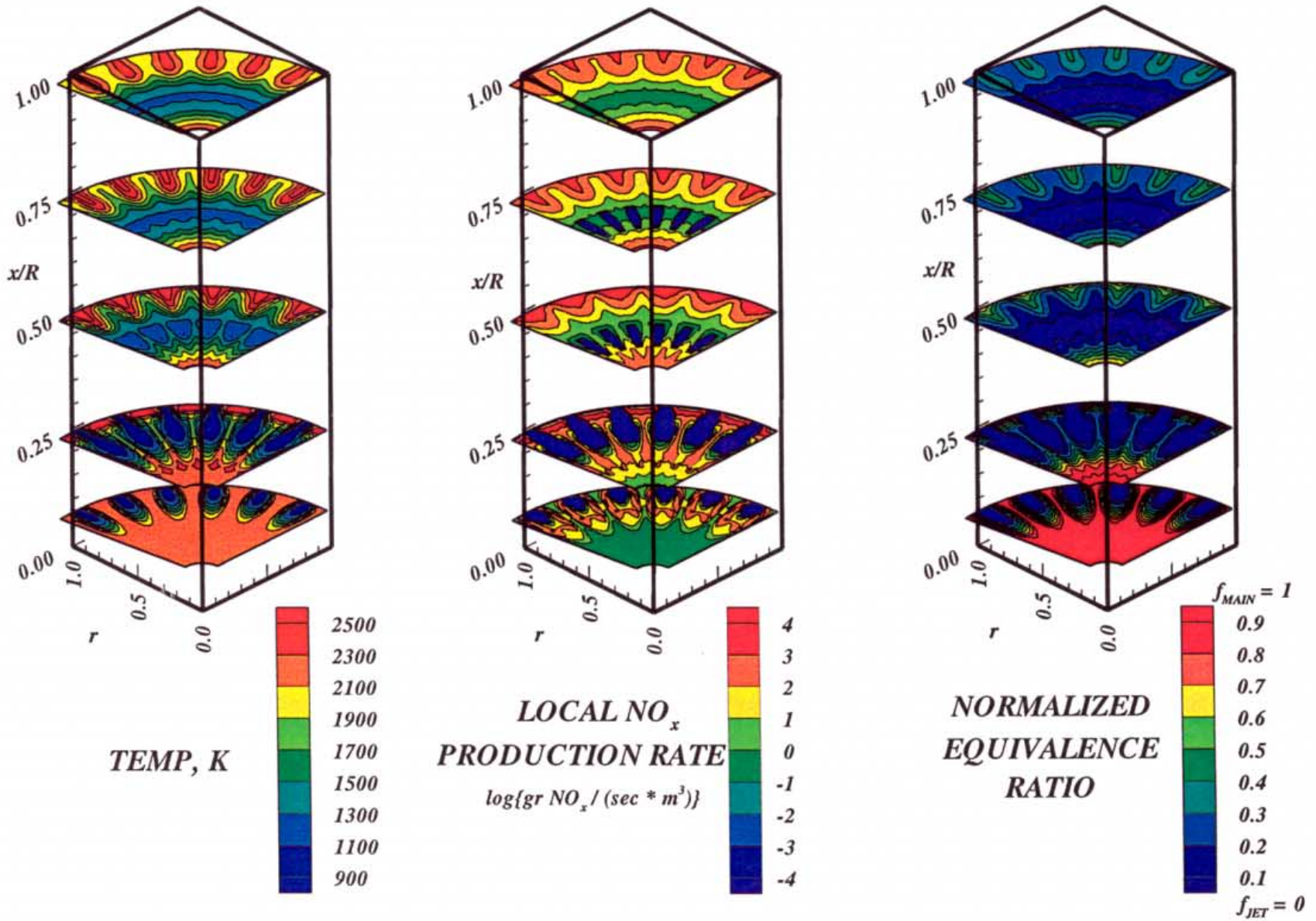

Figure-A54. Configuration HO-54, flow aligned slot L/W=4, 22 orifices /row
J=52.0, MR=2.96, DR=2.28, ϕ_{RZ} = 1.80, ϕ_{LZ} = 0.416 (6-adjacent sectors)

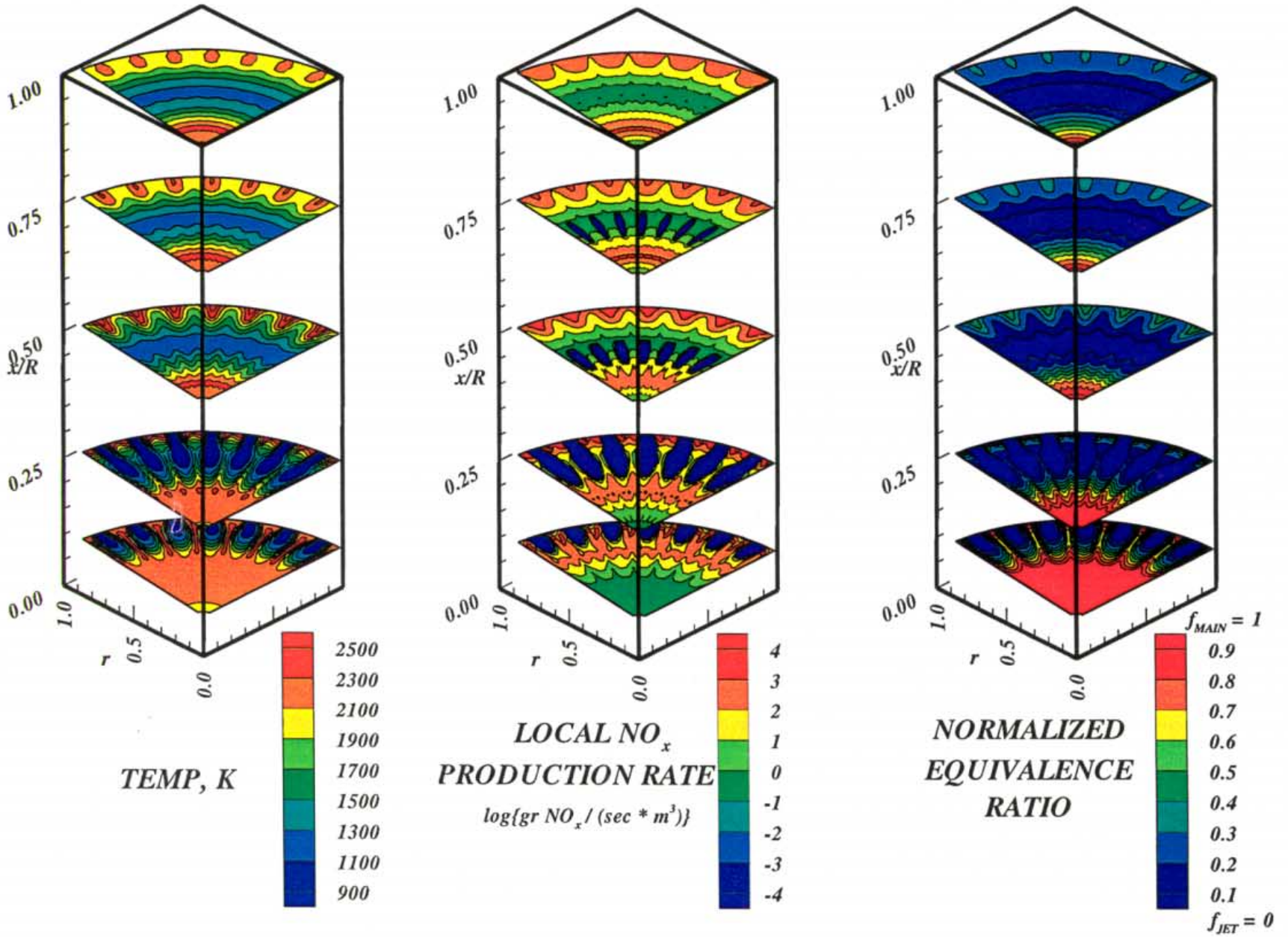

Figure-A55. Configuration HO-55, flow aligned slot L/W=4, 30 orifices /row
J=52.0, MR=2.96, DR=2.28, ϕ_{RZ} = 1.80, ϕ_{LZ} = 0.416 (7-adjacent sectors)

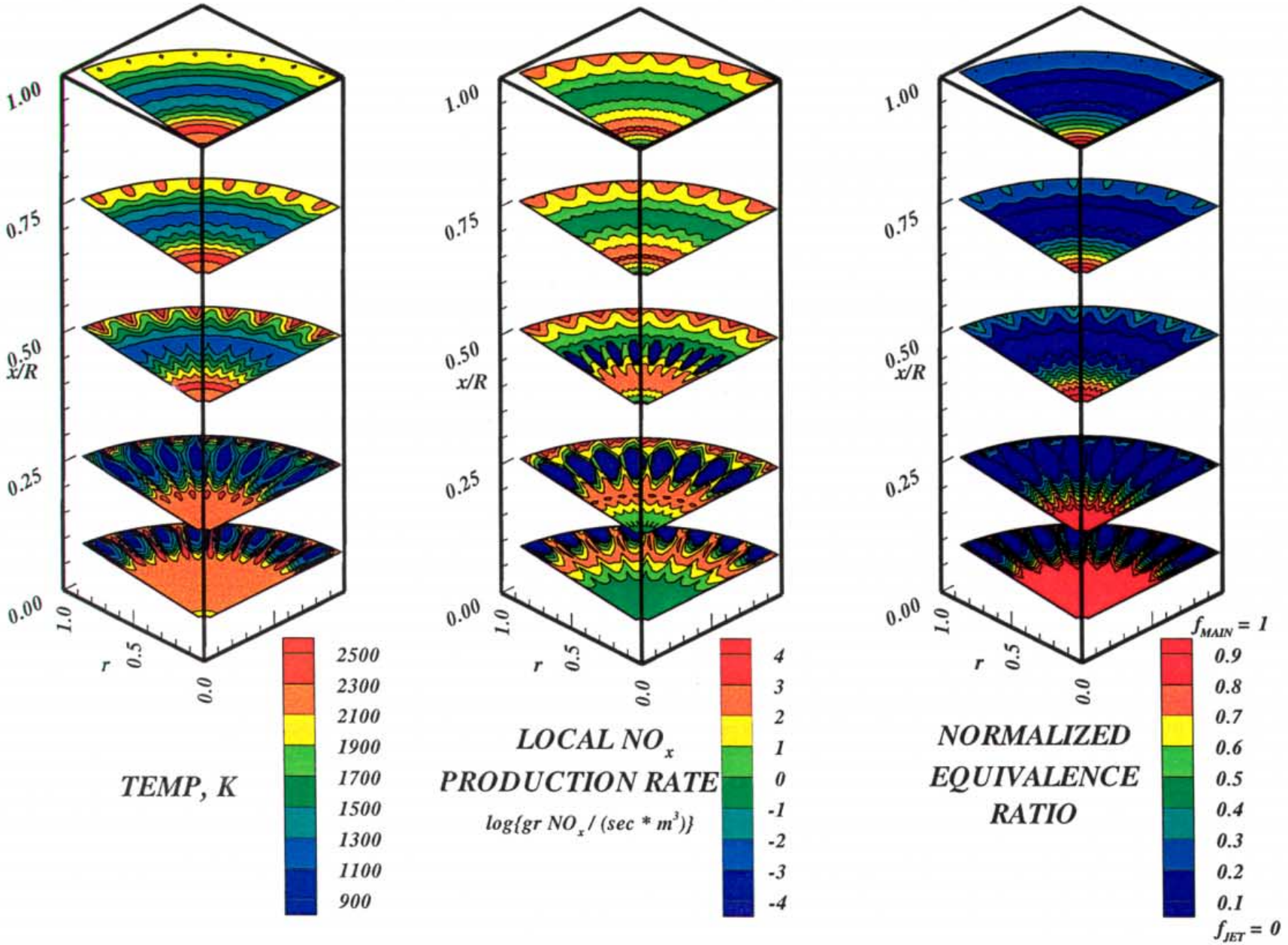

Figure-A56. Configuration HO-56, flow aligned slot L/W=4, 34 orifices /row
J=52.0, MR=2.96, DR=2.28, ϕ_{RZ} = 1.80, ϕ_{LZ} = 0.416 (8-adjacent sectors)

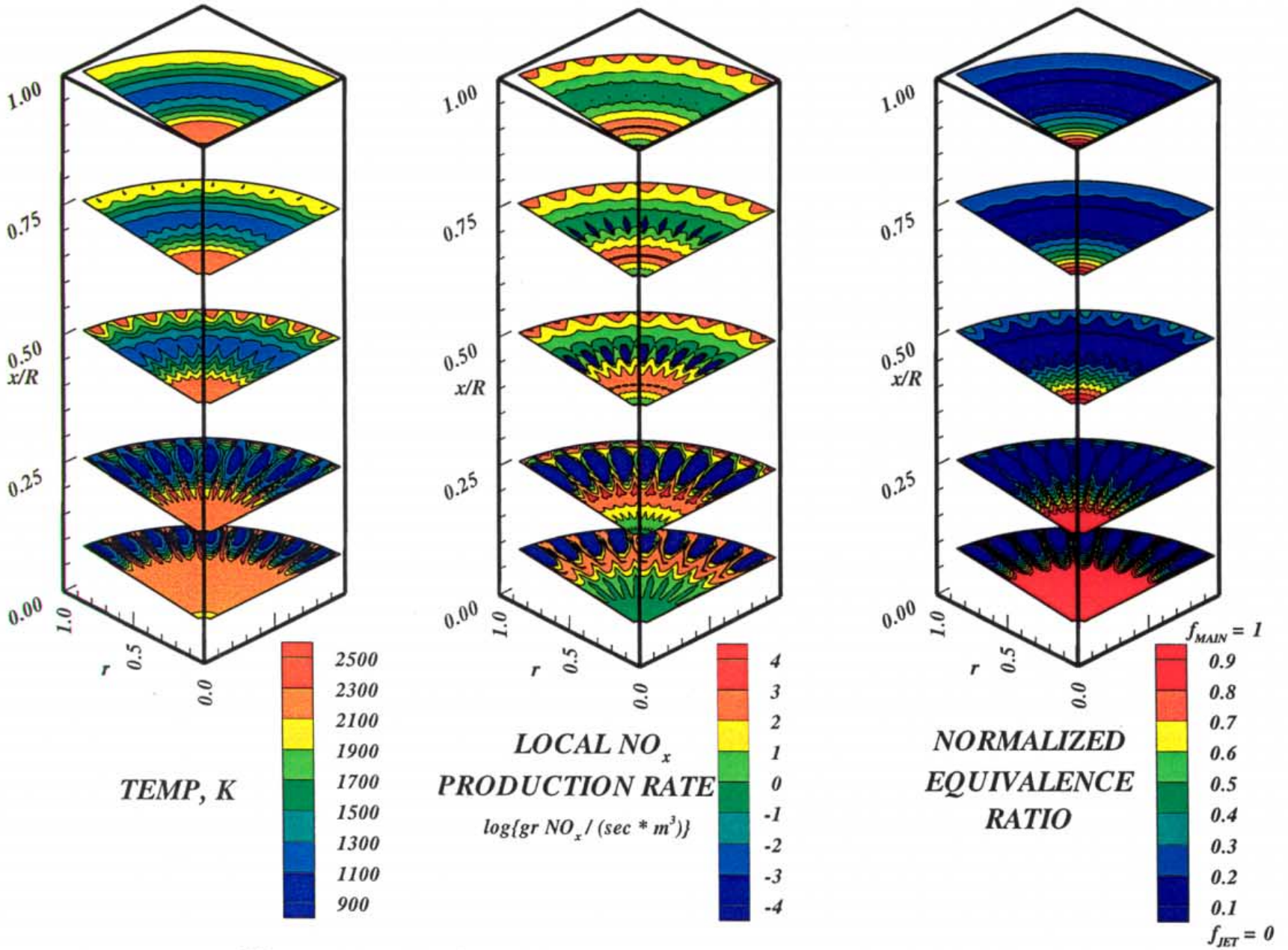

Figure-A57. Configuration HO-57, flow aligned slot L/W=4, 38 orifices /row
J=52.0, MR=2.96, DR=2.28, ϕ_{RZ} = 1.80, ϕ_{LZ} = 0.416 (9-adjacent sectors)

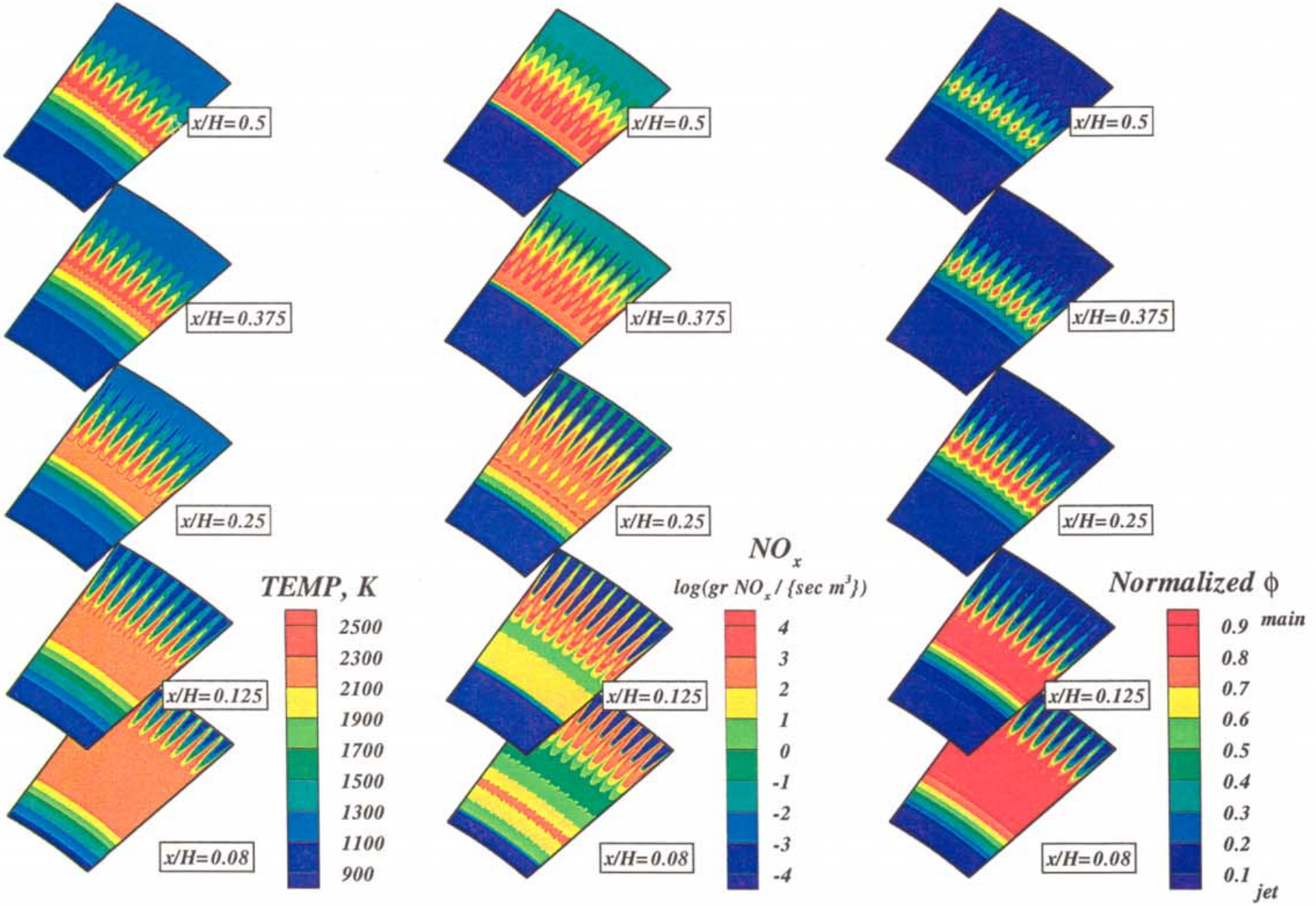

Figure-A58. Annular mixer configuration HO-58, flow aligned slot L/W=4, 299 per row (28 eq holes/row) J=52.0, MR=2.96, DR=2.28, ϕ_{RZ}=1.80, ϕ_{LZ}=0.416 (10 sectors)

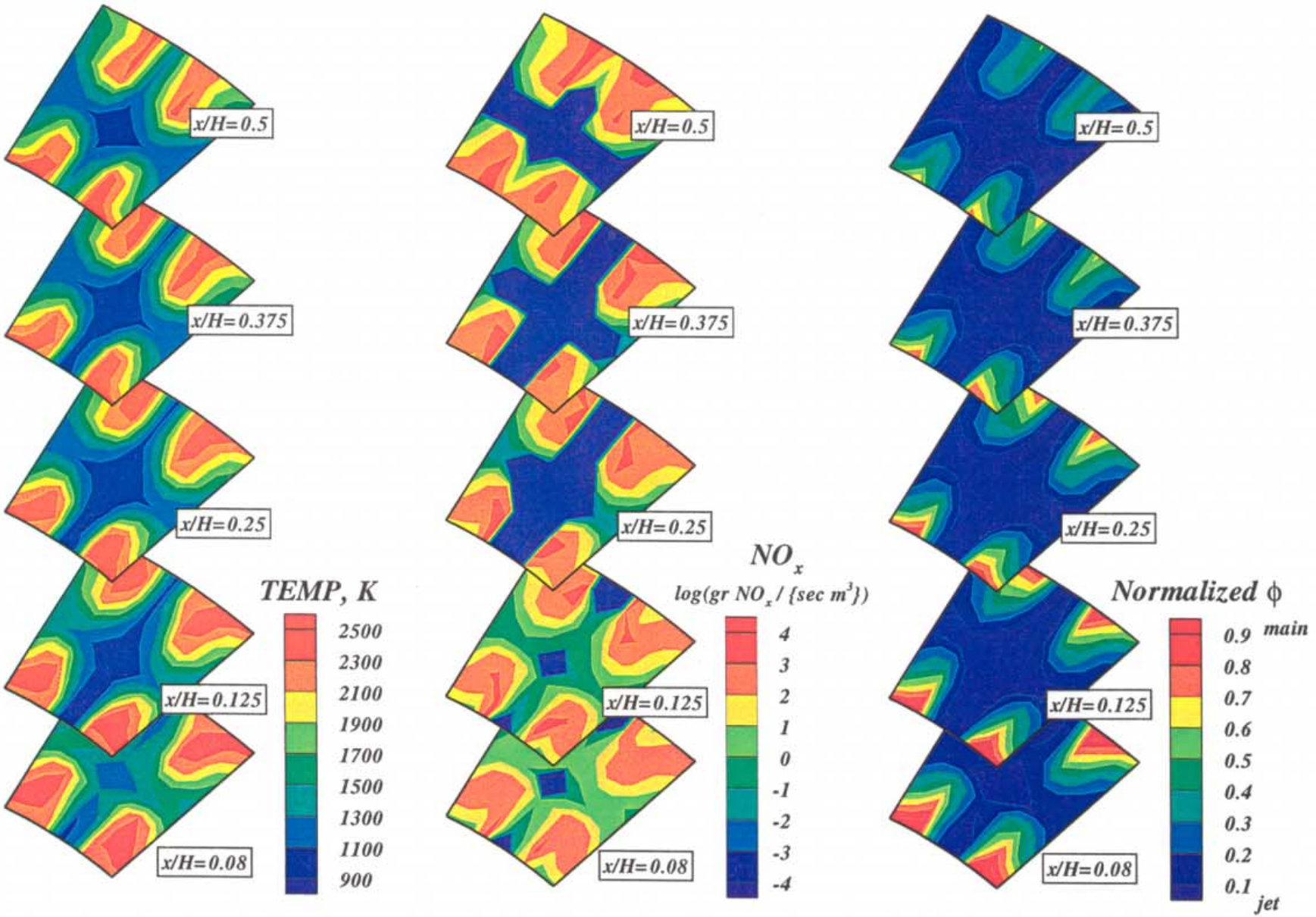

Figure-A59. Annular mixer configuration HO-59, flow aligned slot L/W=4, 21 per row (2 eq holes/row) J=52.0, MR=2.96, DR=2.28, ϕ_{RZ}=1.80, ϕ_{LZ}=0.416 (1 sector)

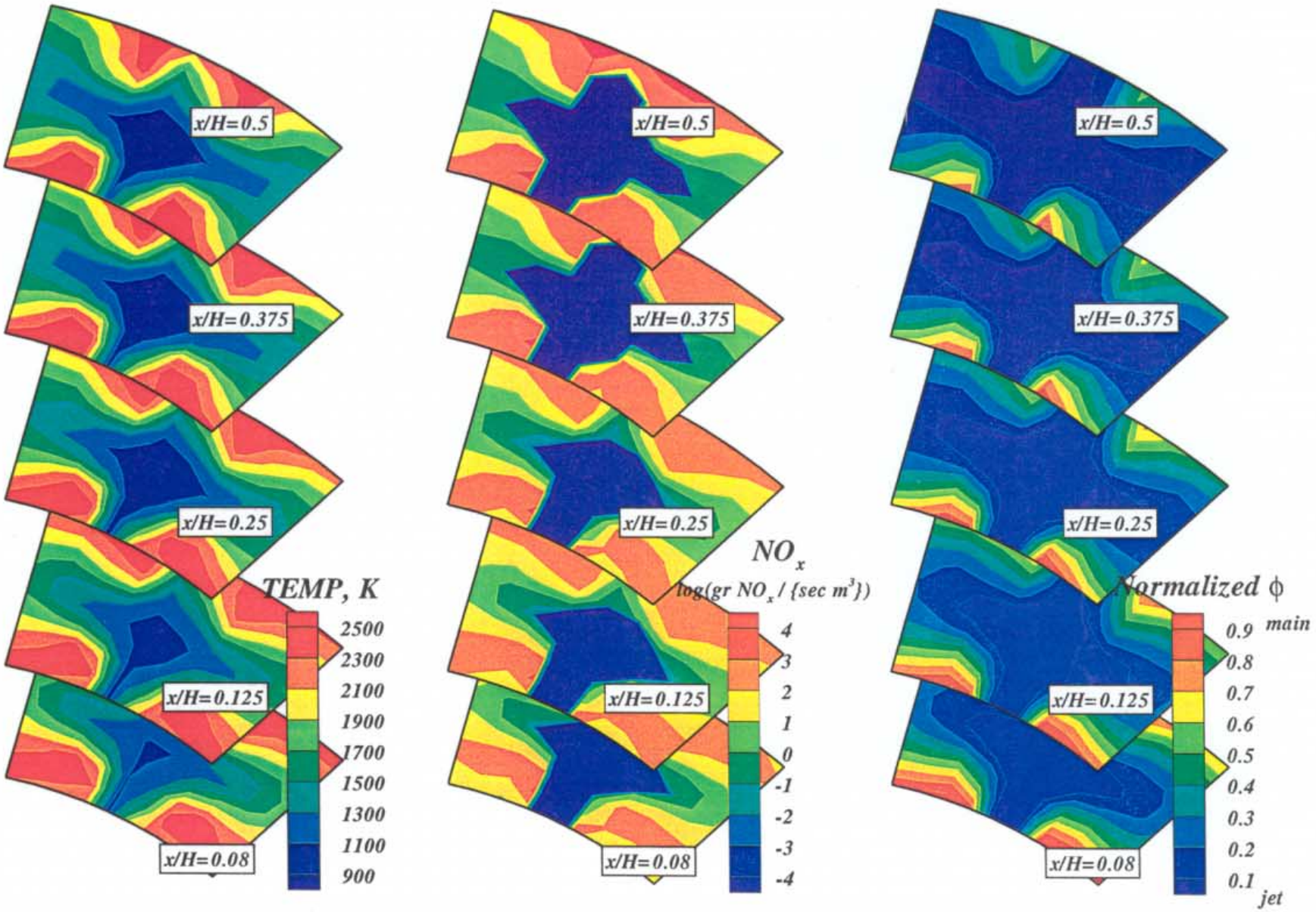

Figure-A60. Annular mixer configuration HO-60, flow aligned slot L/W=4, 11 per row (1 eq holes/row)
J=52.0, MR=2.96, DR=2.28, ϕ_{RZ}=1.80, ϕ_{LZ}=0.416 (1 sector)

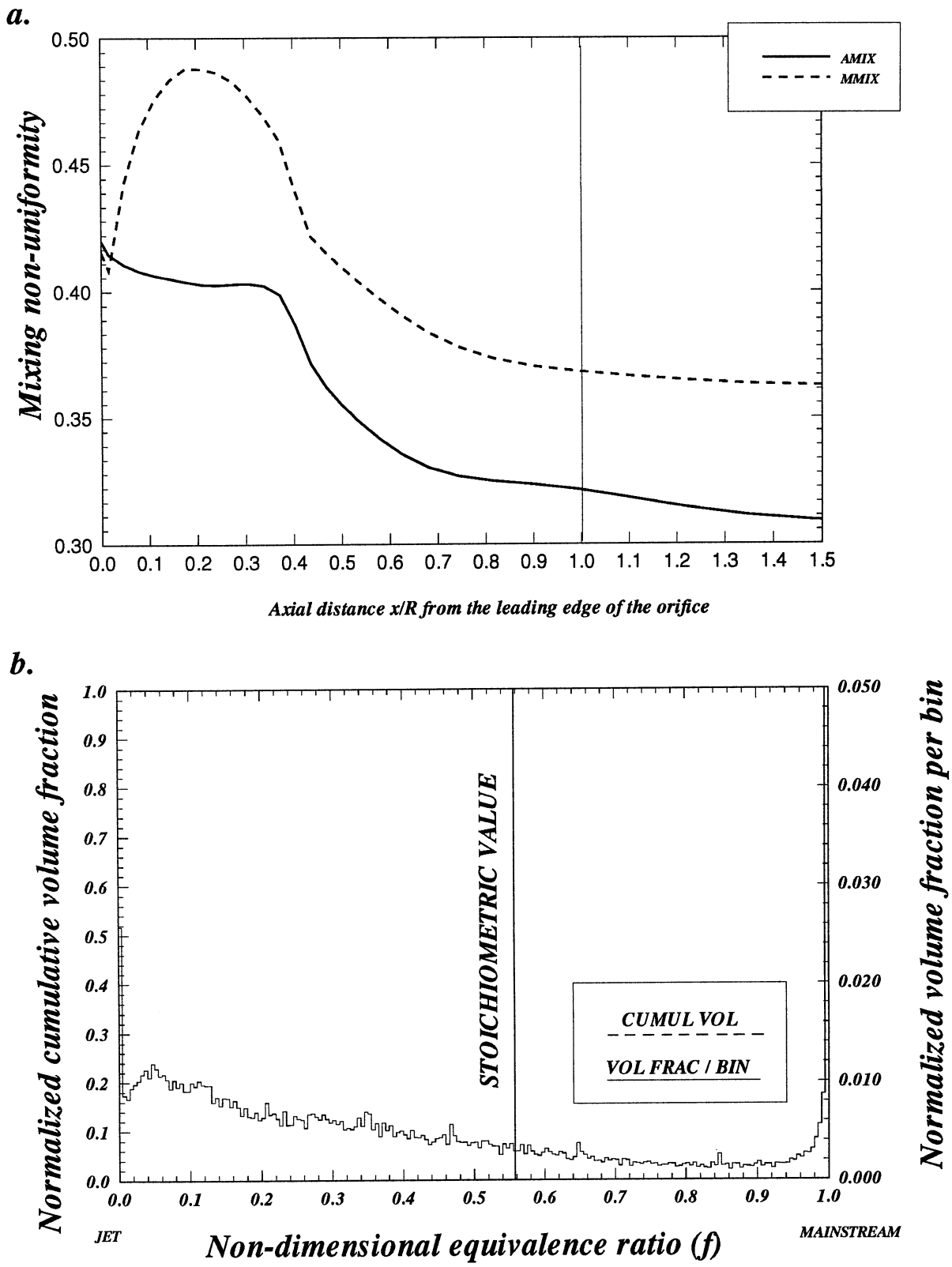

a. Planar deviations (AMIX and MMIX) results

b. mixing non-uniformity volume histograms for 0 < x/R < 1

Figure-B1. Configuration HO-1. Circular mixer, 6 round holes/row

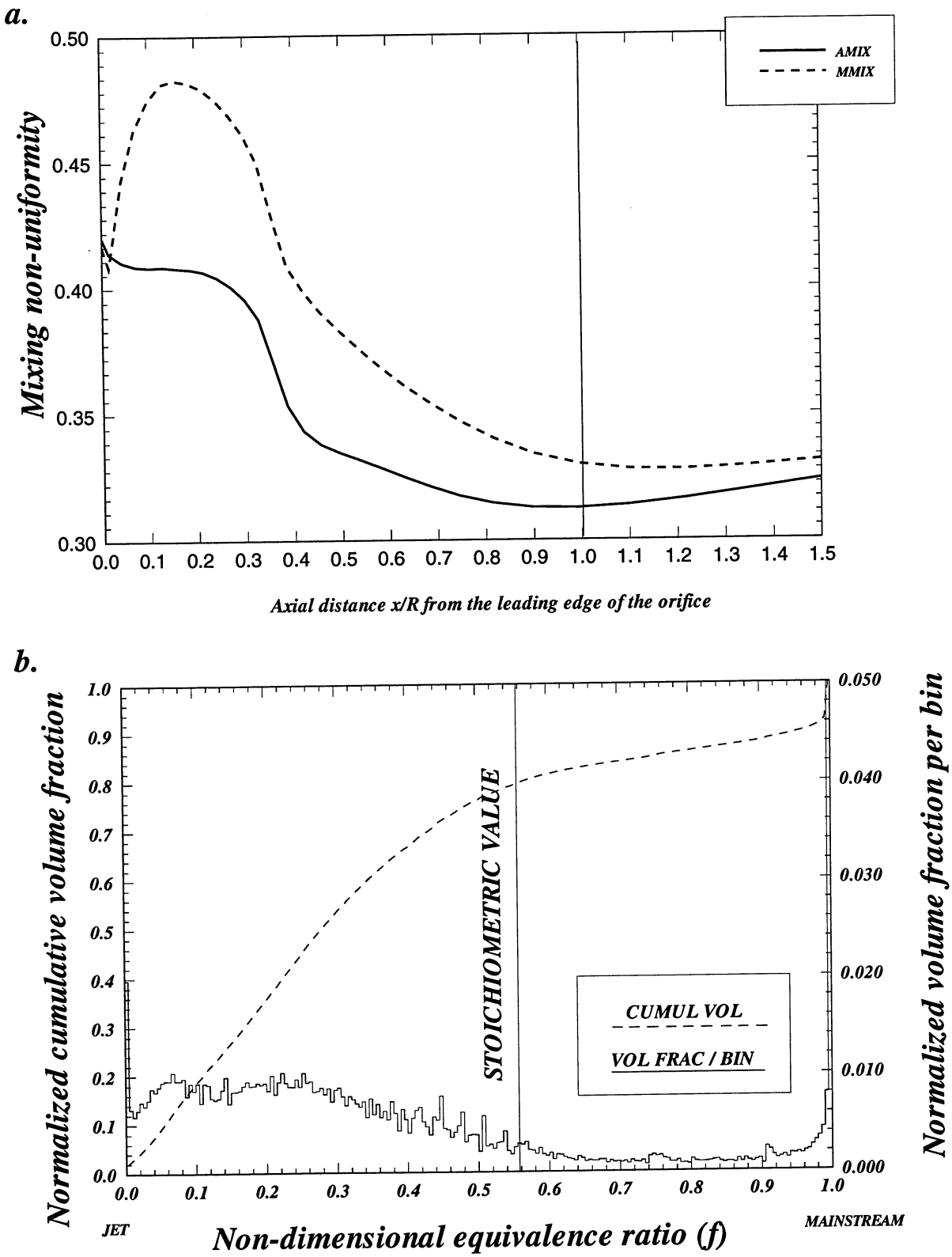

a. Planar deviations (AMIX and MMIX) results

b. mixing non-uniformity volume histograms for 0 < x/R < 1

Figure-B2. Configuration HO-2. Circular mixer, 67.5^0 slot L/W=4, 8 holes/row

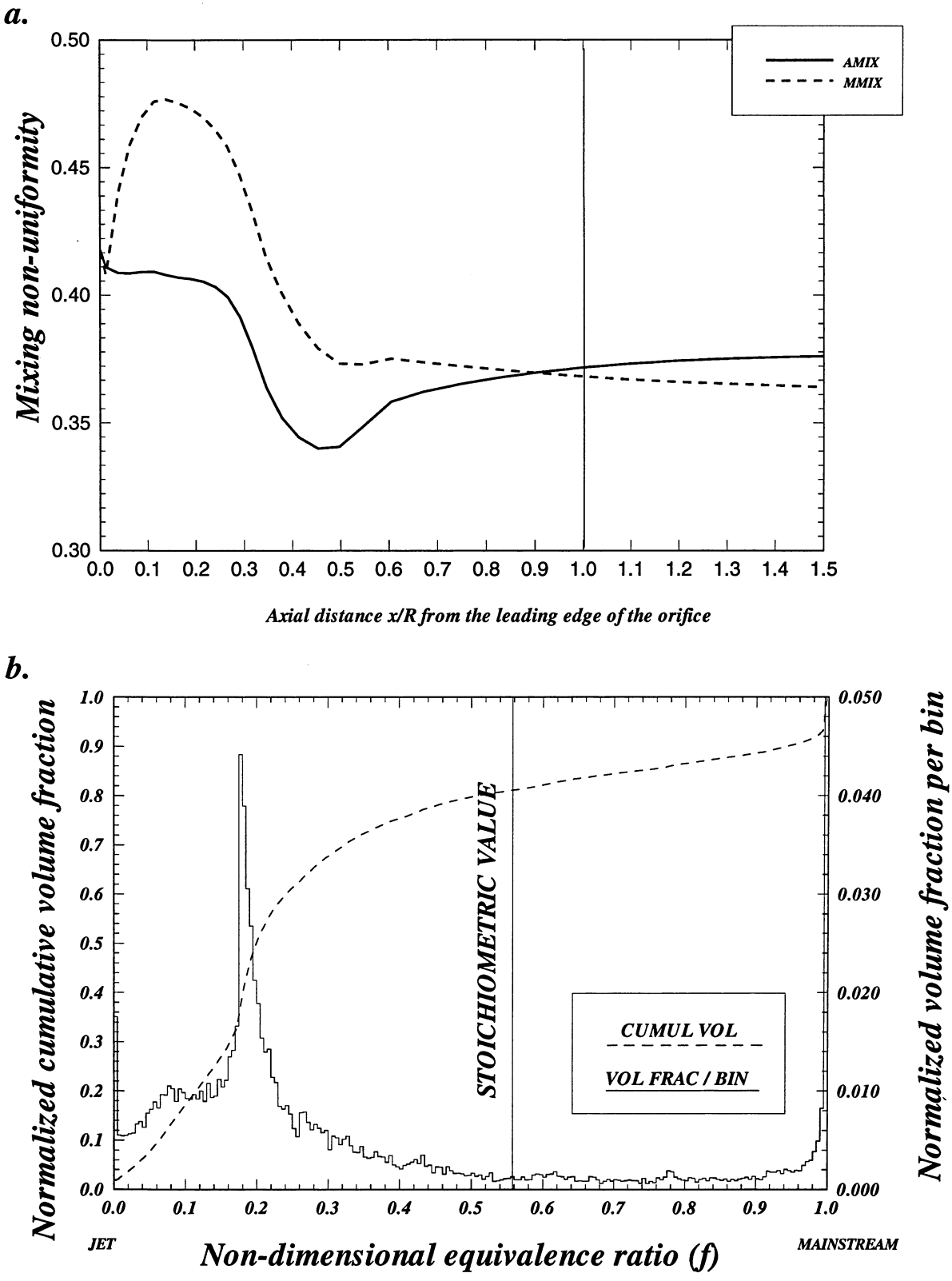

a. Planar deviations (AMIX and MMIX) results

b. mixing non-uniformity volume histograms for 0 < x/R < 1

Figure-B3. Configuration HO-3. Circular mixer, 67.5^0 slot L/W=4, 10 holes/row

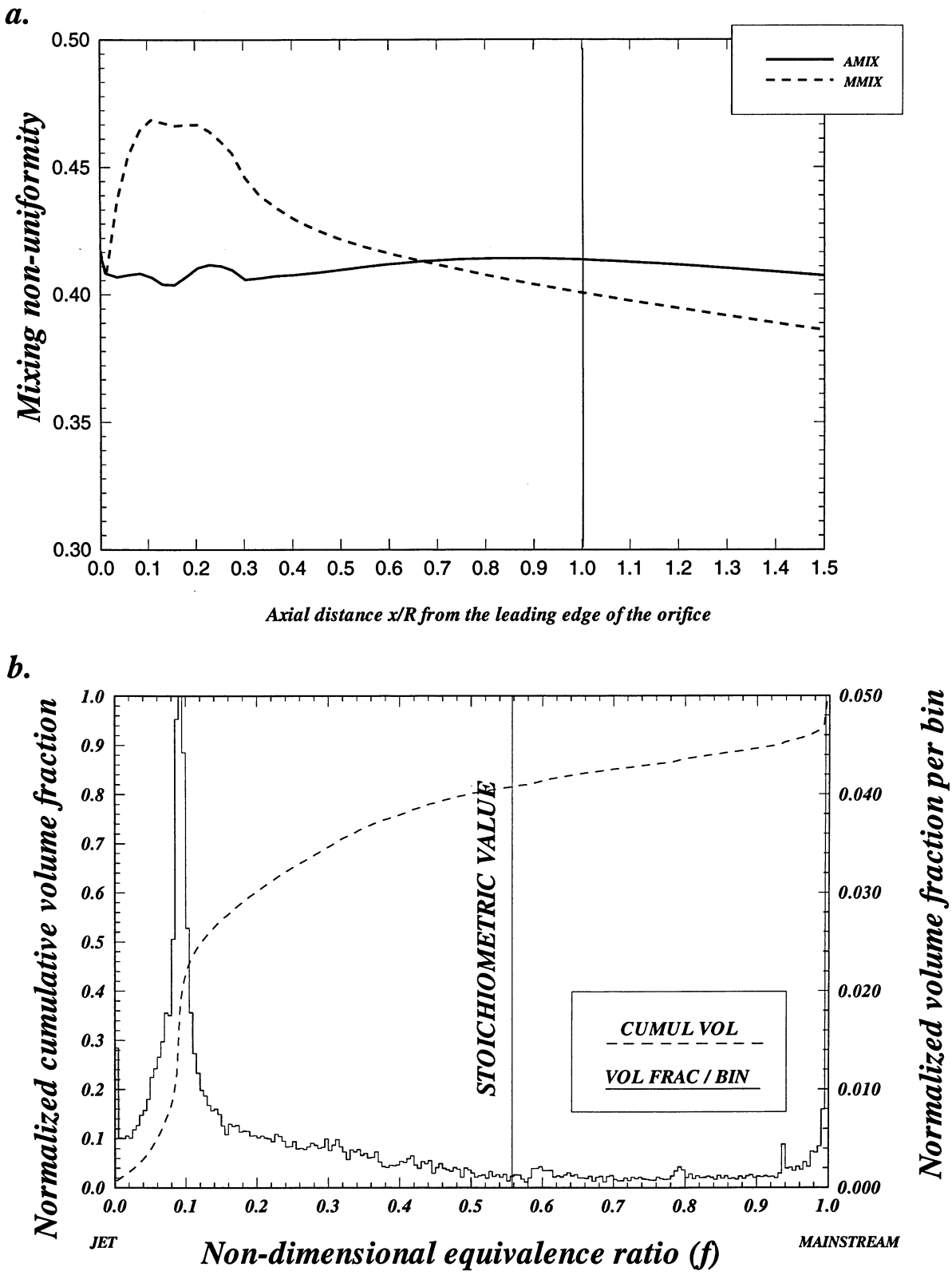

a. Planar deviations (AMIX and MMIX) results

b. mixing non-uniformity volume histograms for 0 < x/R < 1

Figure-B4. Configuration HO-4. Circular mixer, 67.5^0 slot L/W=4, 12 holes/row

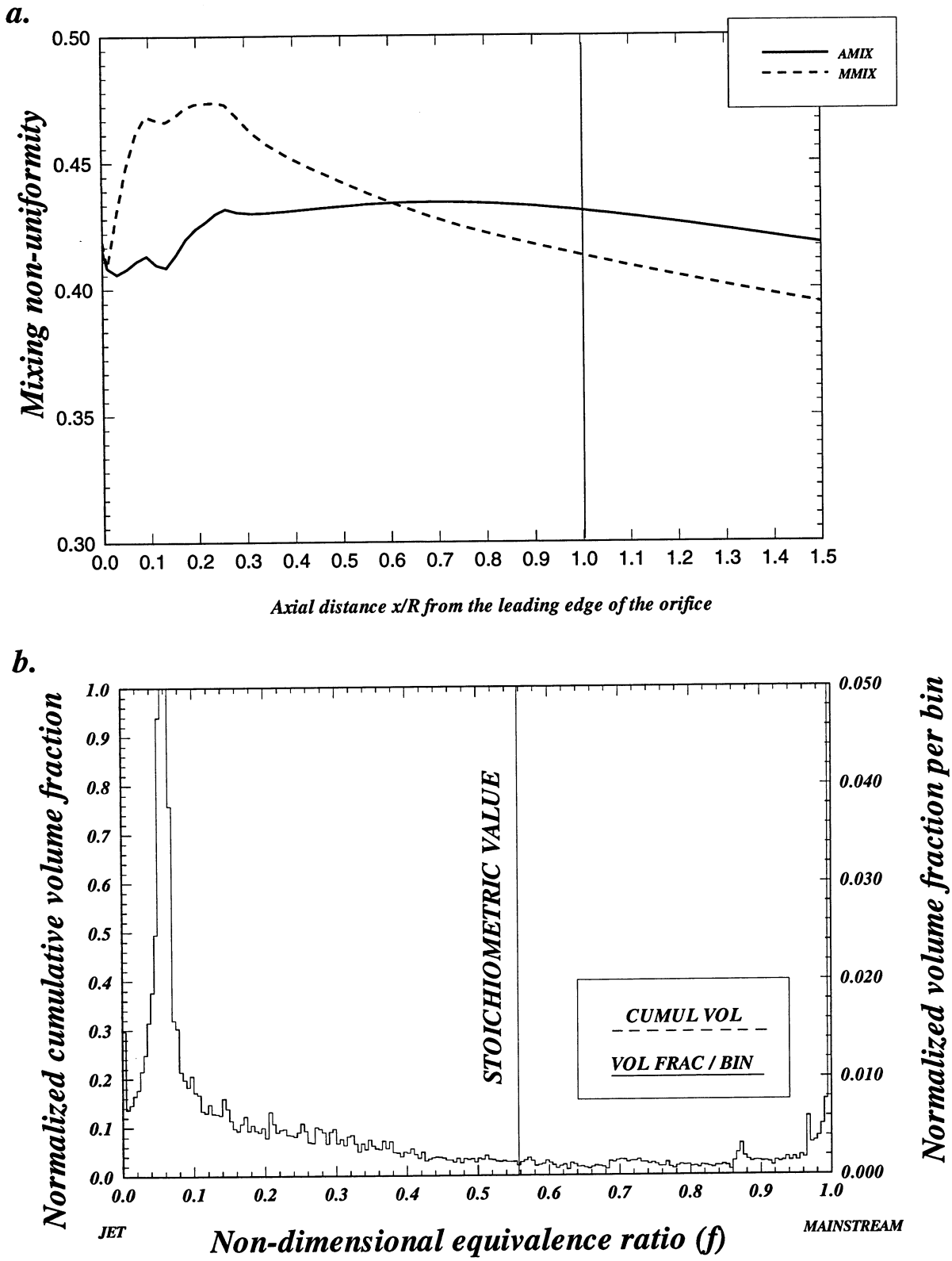

a. Planar deviations (AMIX and MMIX) results

b. mixing non-uniformity volume histograms for 0 < x/R < 1

Figure-B5. Configuration HO-5. Circular mixer, 67.5^0 slot L/W=4, 14 holes/row

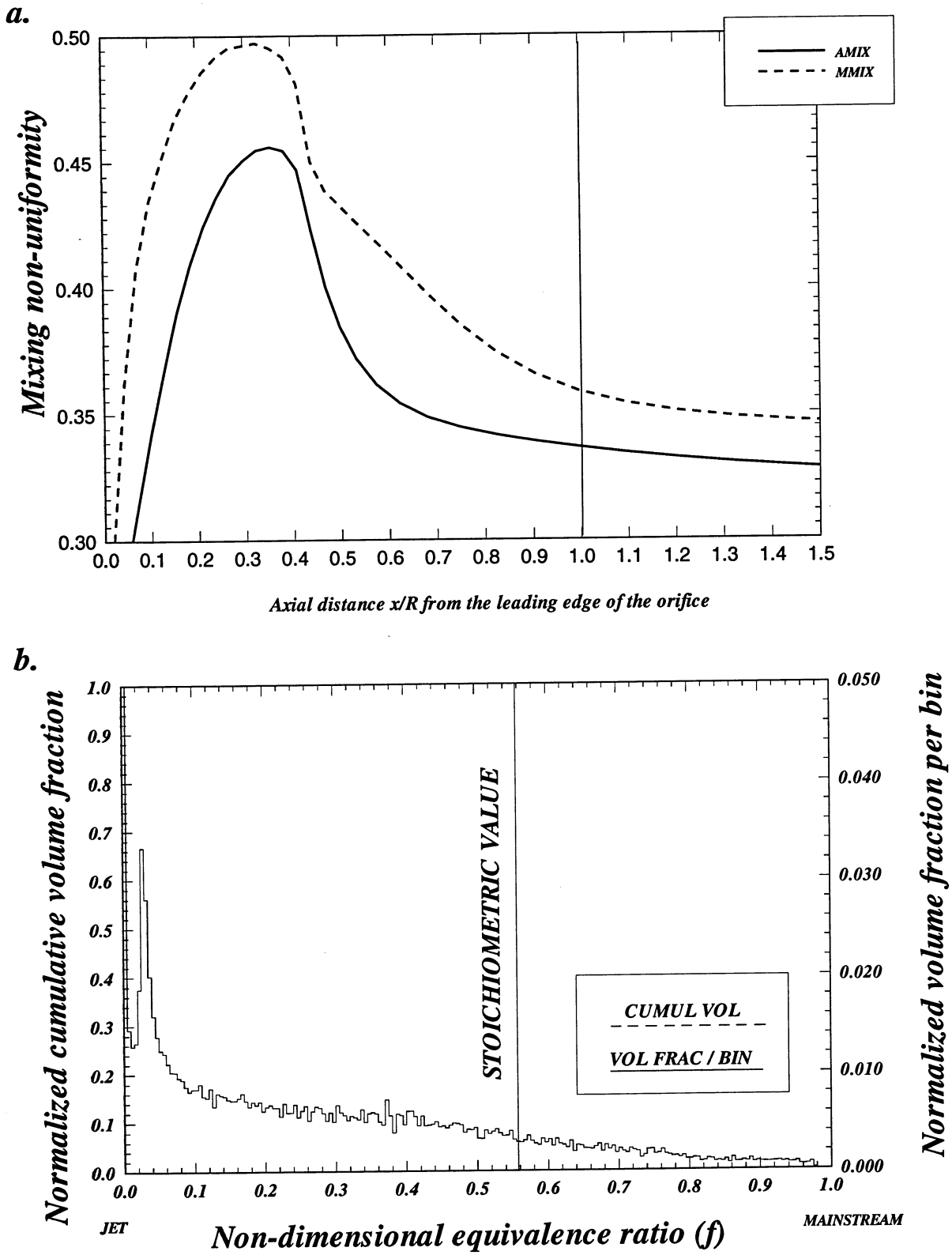

a. Planar deviations (AMIX and MMIX) results

b. mixing non-uniformity volume histograms for 0 < x/R < 1

Figure-B6. Configuration HO-6. Circular mixer, 6 round holes/row

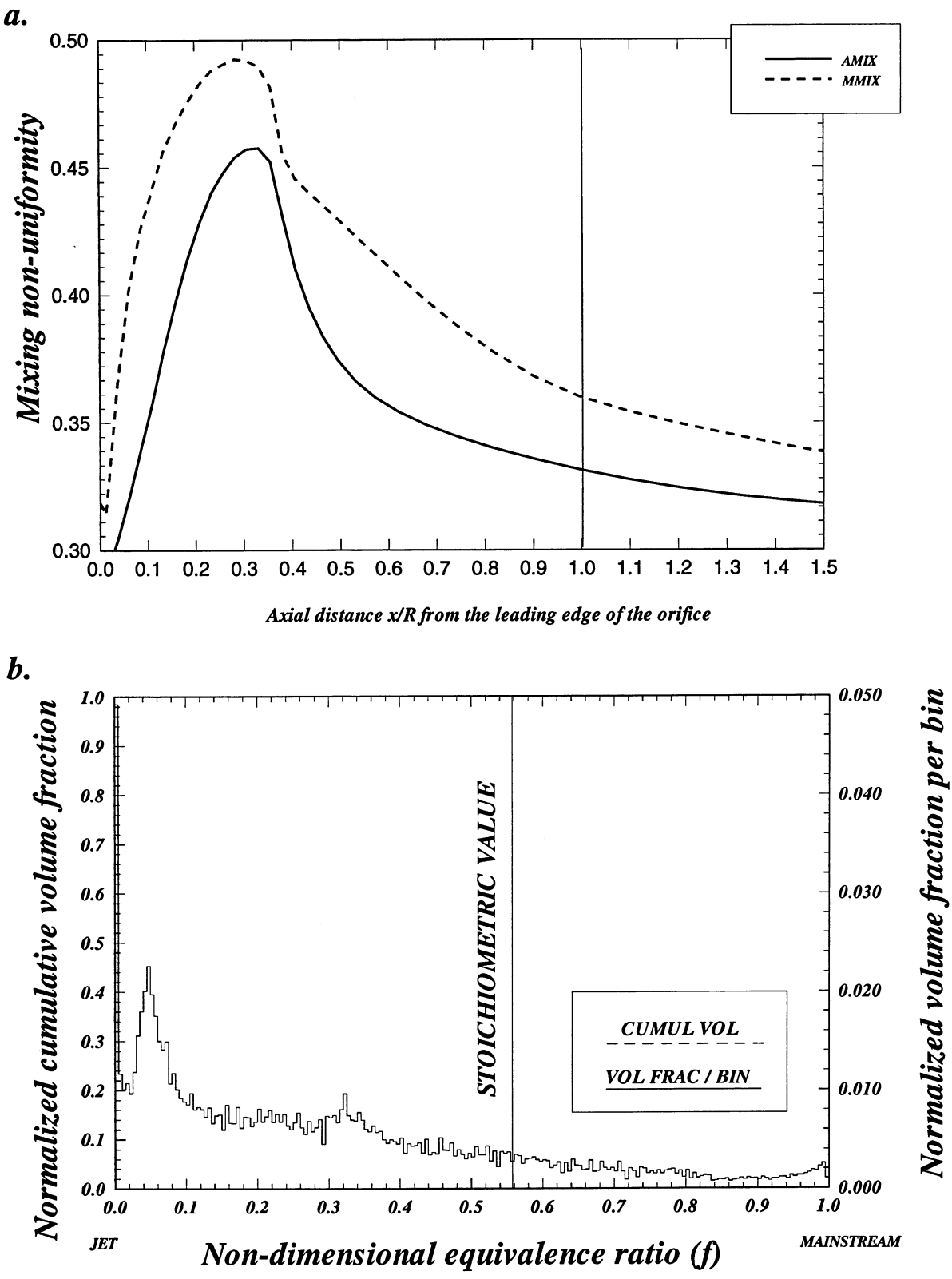

a. Planar deviations (AMIX and MMIX) results

b. mixing non-uniformity volume histograms for 0 < x/R < 1

Figure-B7. Configuration HO-7. Circular mixer, 8 round holes/row

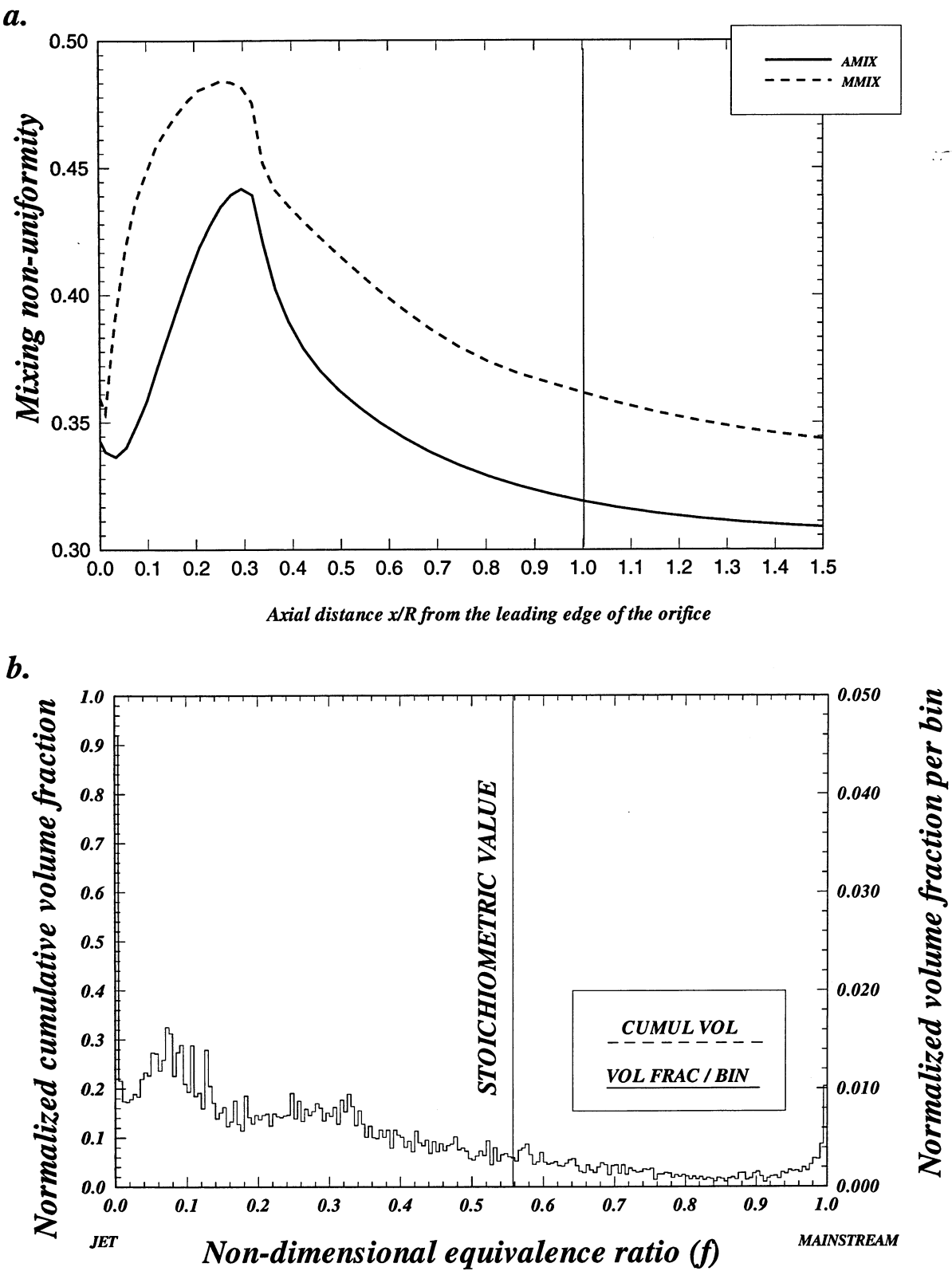

a. Planar deviations (AMIX and MMIX) results

b. mixing non-uniformity volume histograms for 0 < x/R < 1

Figure-B8. Configuration HO-8. Circular mixer, 10 round holes/row

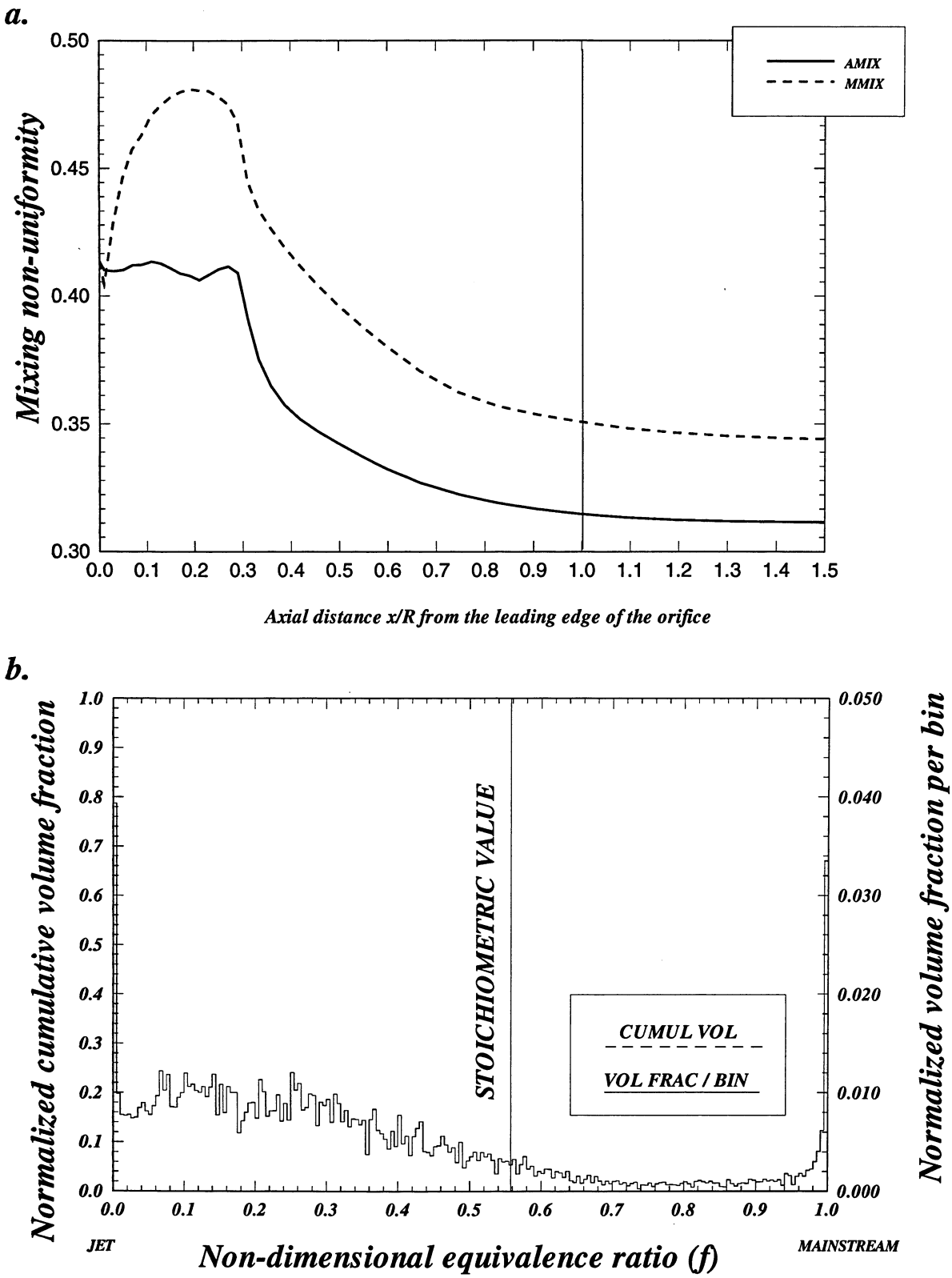

a. Planar deviations (AMIX and MMIX) results

b. mixing non-uniformity volume histograms for 0 < x/R < 1

Figure-B9. Configuration HO-9. Circular mixer, 12 round holes/row

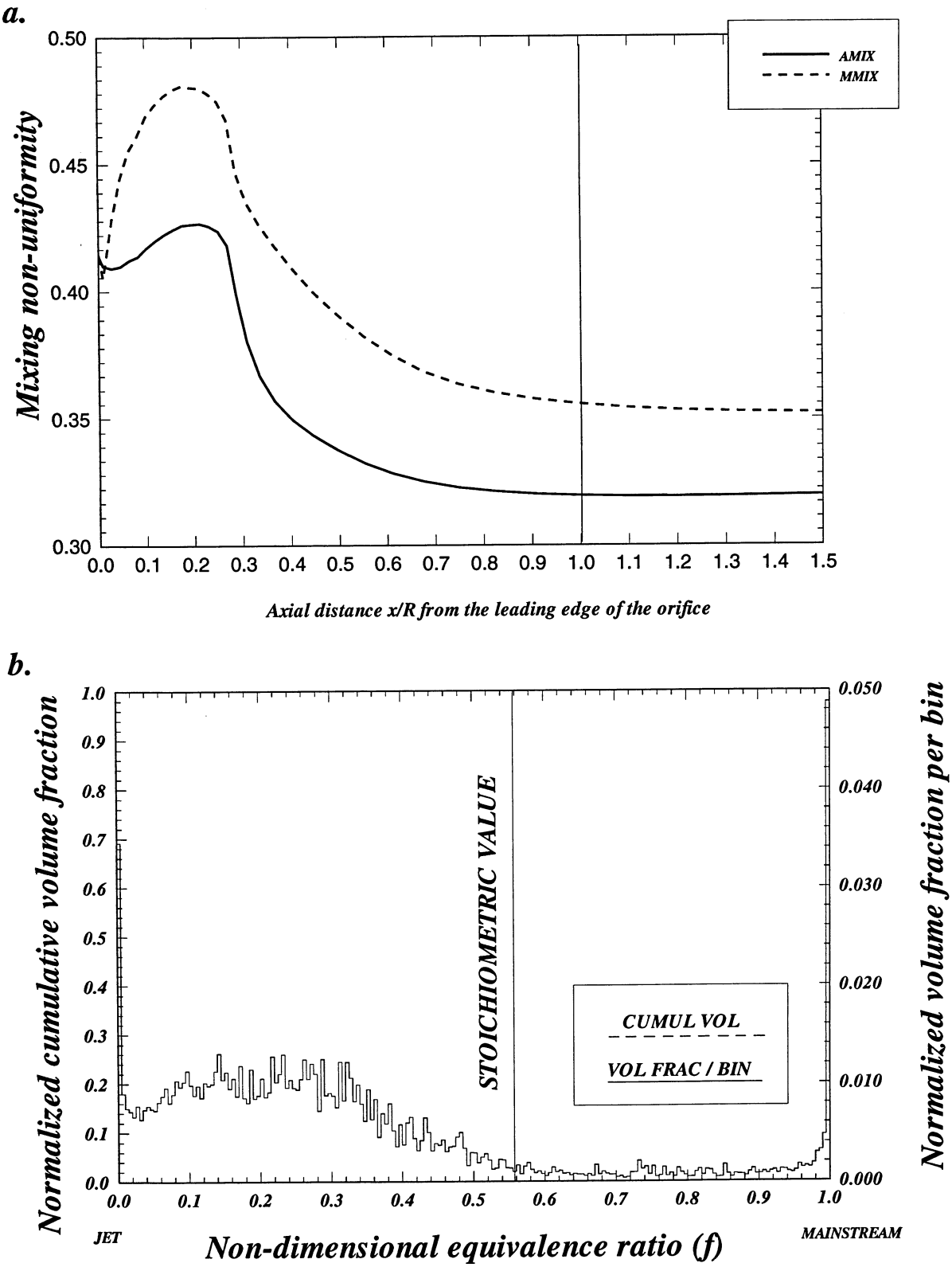

a. Planar deviations (AMIX and MMIX) results

b. mixing non-uniformity volume histograms for 0 < x/R < 1

Figure-B10. Configuration HO-10. Circular mixer, 14 round holes/row

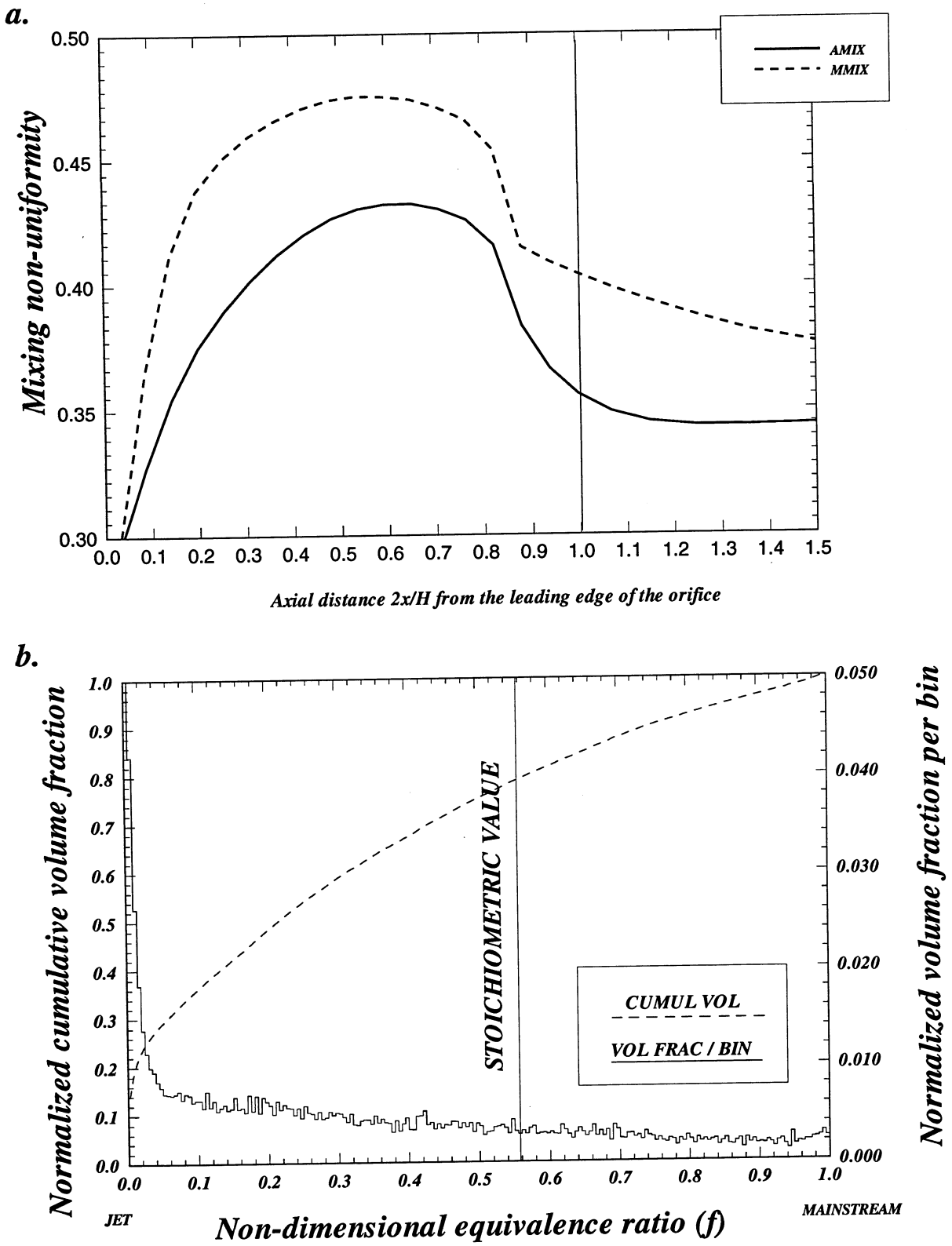

a. Planar deviations (AMIX and MMIX) results

b. mixing non-uniformity volume histograms for 0 < 2x/H < 1

Figure-B11. Configuration HO-11. Annular mixer, 6 round equivalent holes/row

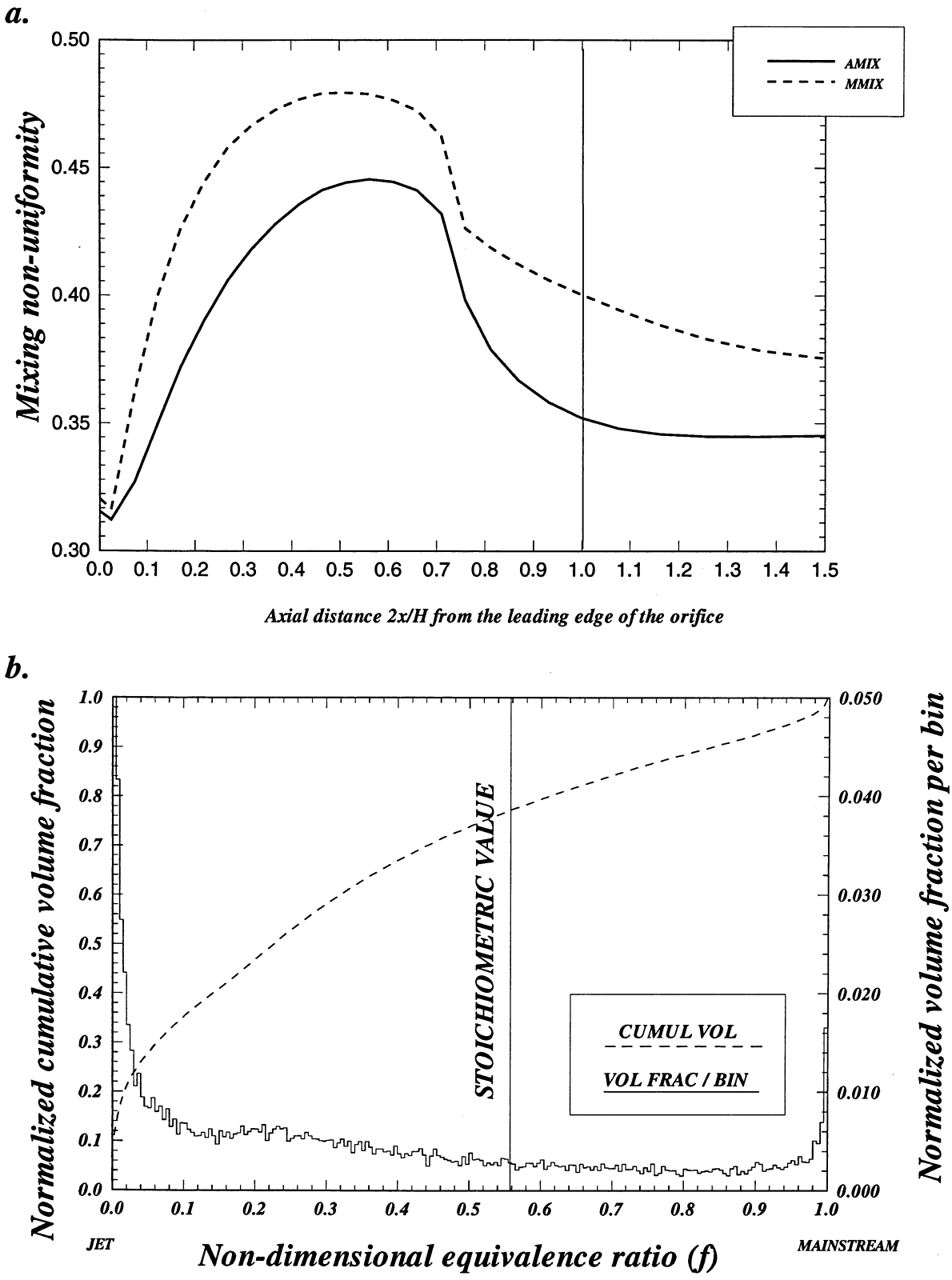

a. Planar deviations (AMIX and MMIX) results

b. mixing non-uniformity volume histograms for 0 < 2x/H < 1

Figure-B12. Configuration HO-12. Annular mixer, 8 round equivalent holes/row

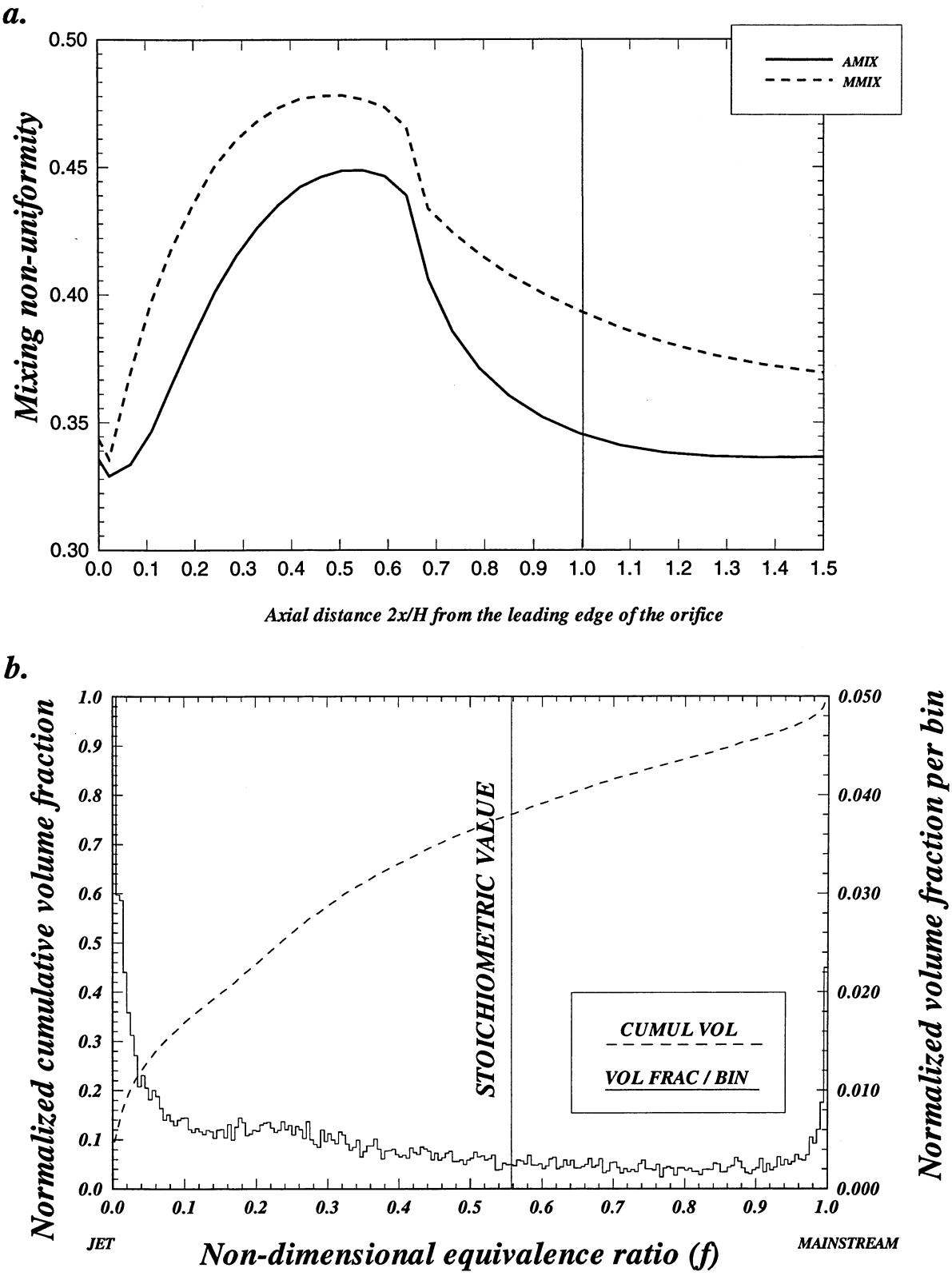

a. Planar deviations (AMIX and MMIX) results

b. mixing non-uniformity volume histograms for 0 < 2x/H < 1

Figure-B13. Configuration HO-13. Annular mixer, 10 round equivalent holes/row

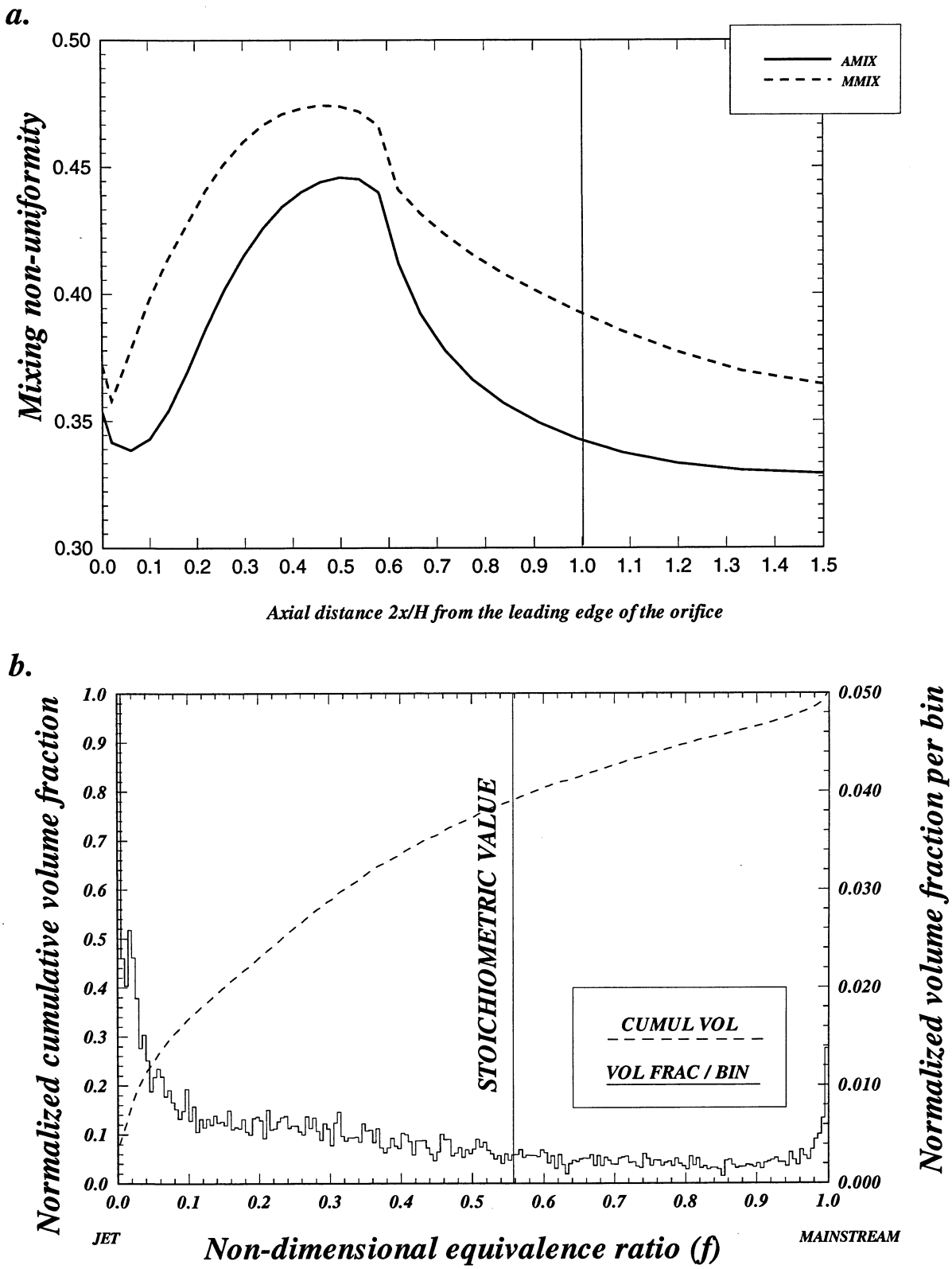

a. Planar deviations (AMIX and MMIX) results

b. mixing non-uniformity volume histograms for 0 < 2x/H < 1

Figure-B14. Configuration HO-14. Annular mixer, 12 round equivalent holes/row

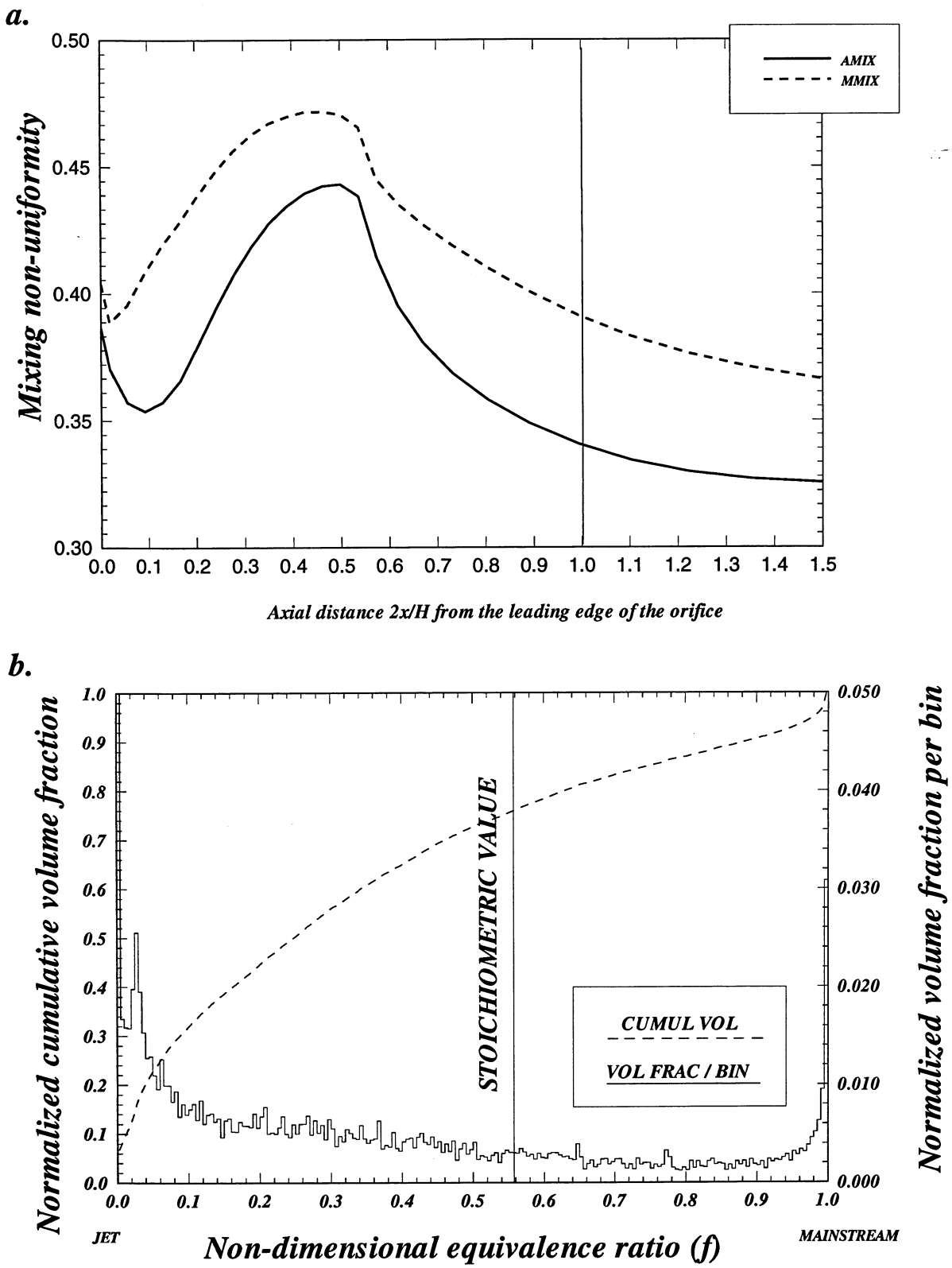

a. Planar deviations (AMIX and MMIX) results

b. mixing non-uniformity volume histograms for 0 < 2x/H < 1

Figure-B15. Configuration HO-15. Annular mixer, 14 round equivalent holes/row

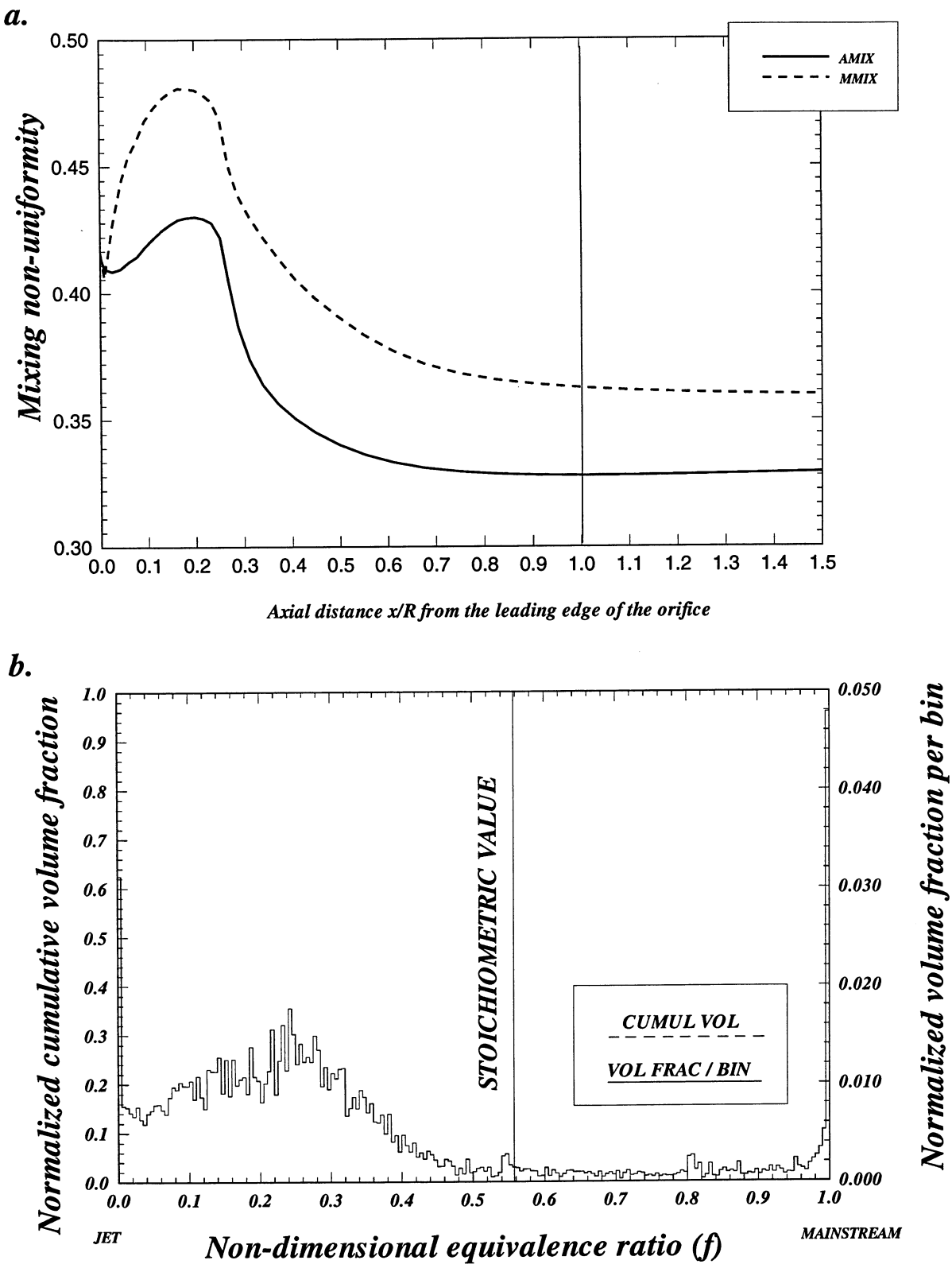

a. Planar deviations (AMIX and MMIX) results

b. mixing non-uniformity volume histograms for 0 < x/R < 1

Figure-B16. Configuration HO-16. Circular mixer, 16 round holes/row

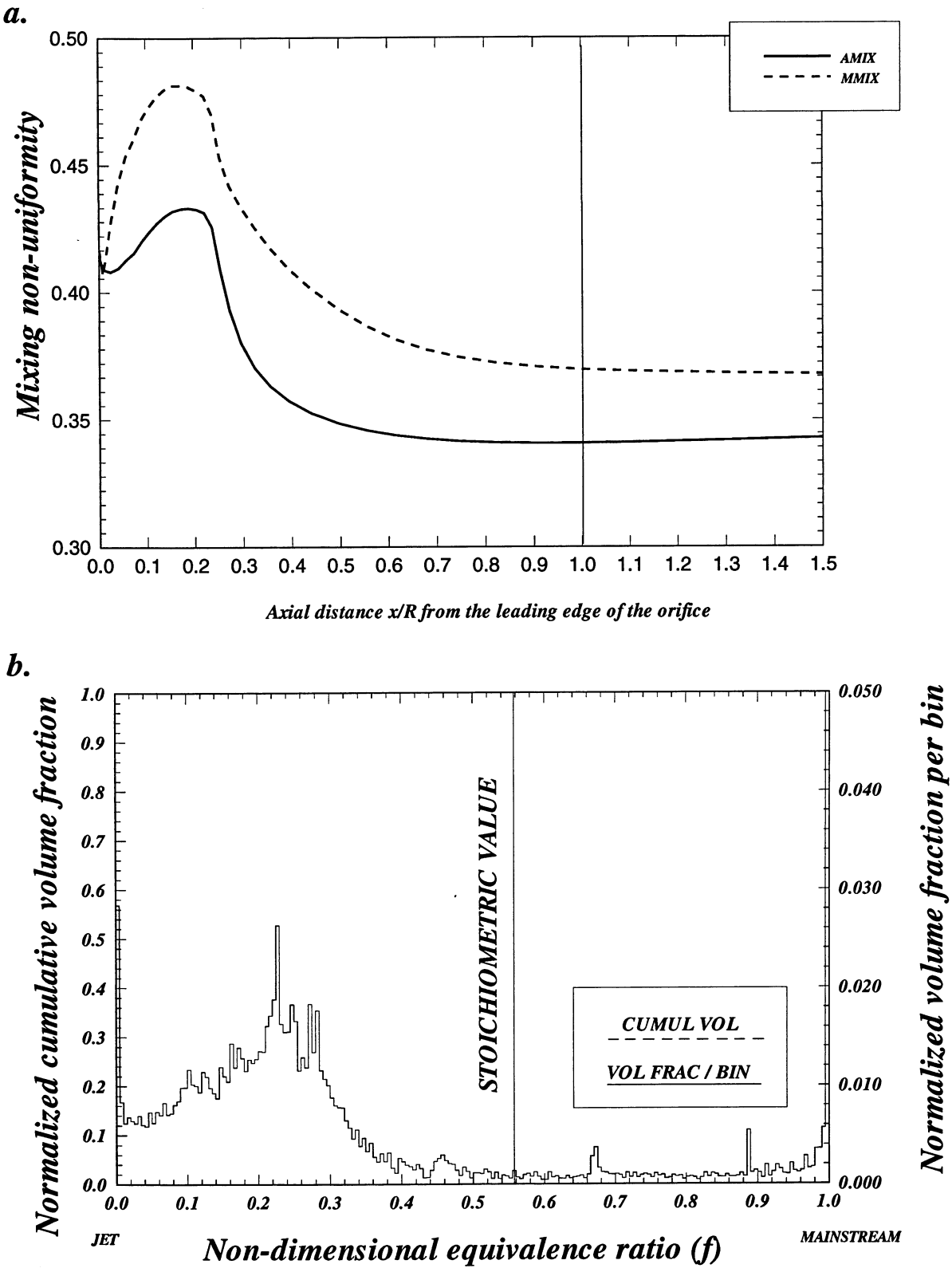

a. Planar deviations (AMIX and MMIX) results

b. mixing non-uniformity volume histograms for 0 < x/R < 1

Figure-B17. Configuration HO-17. Circular mixer, 18 round holes/row

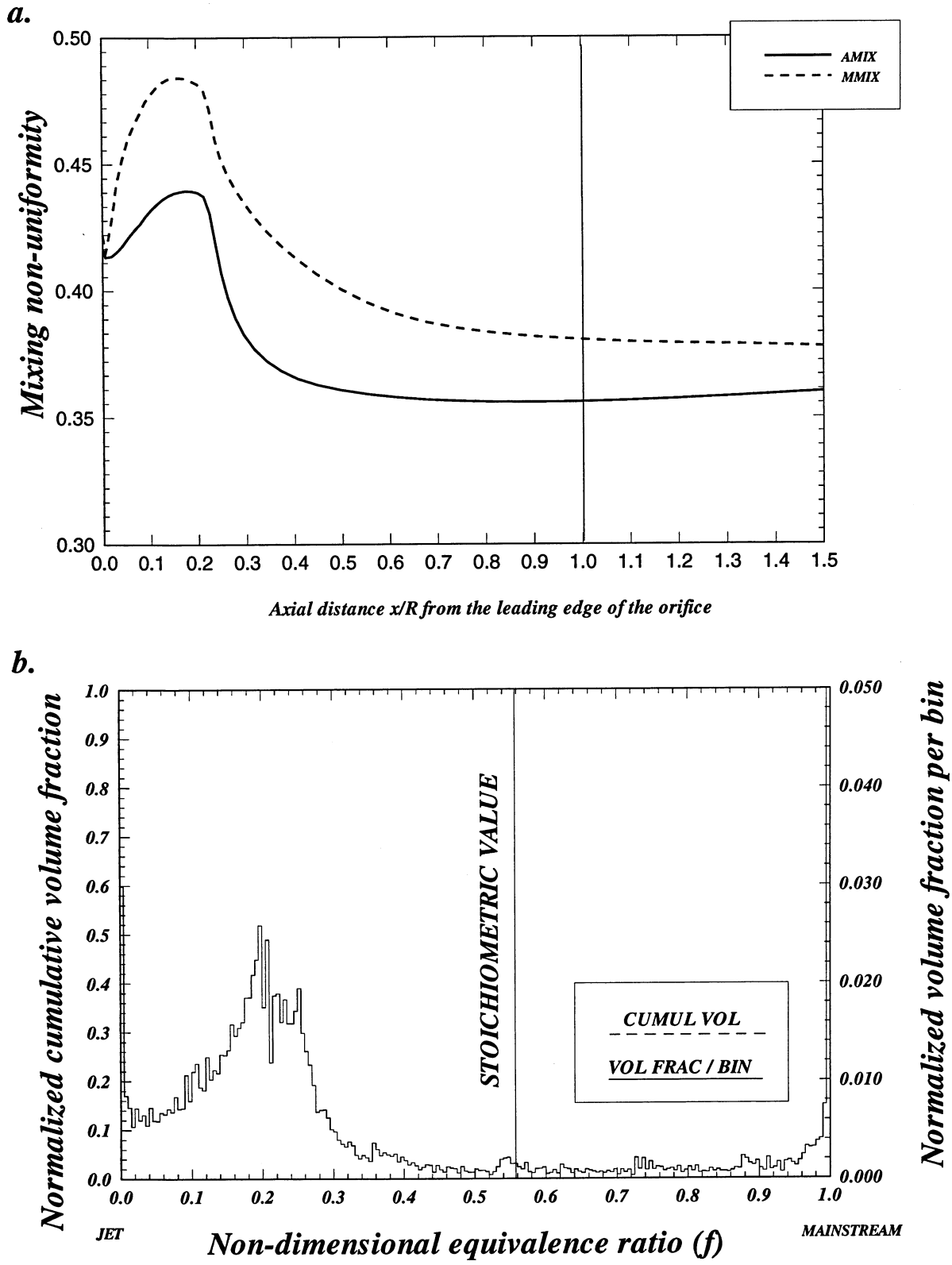

a. Planar deviations (AMIX and MMIX) results

b. mixing non-uniformity volume histograms for 0 < x/R < 1

Figure-B18. Configuration HO-18. Circular mixer, 20 round holes/row

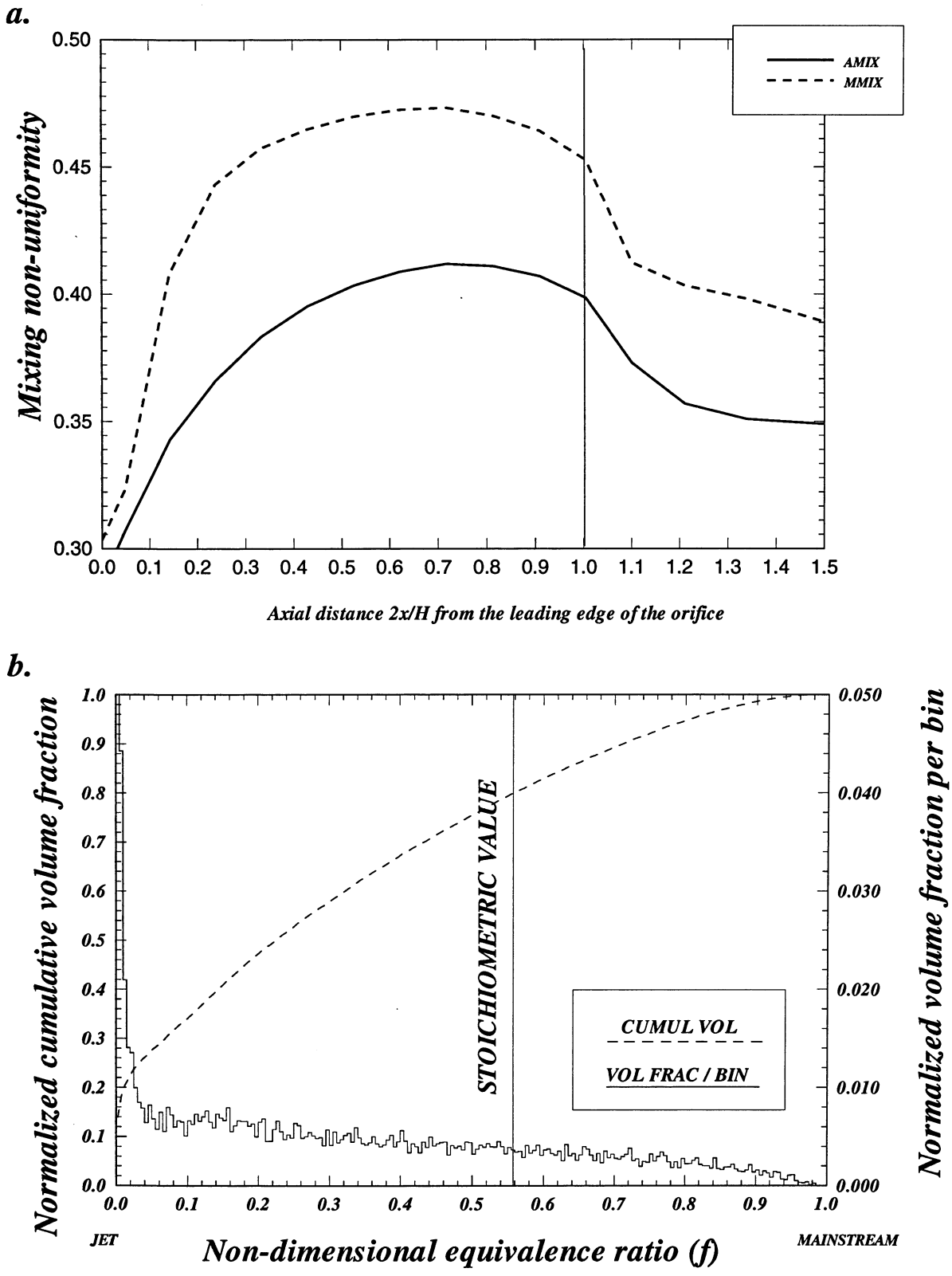

a. Planar deviations (AMIX and MMIX) results

b. mixing non-uniformity volume histograms for 0 < 2x/H < 1

Figure-B19. Configuration HO-19. Annular mixer, 4 round equivalent holes/row

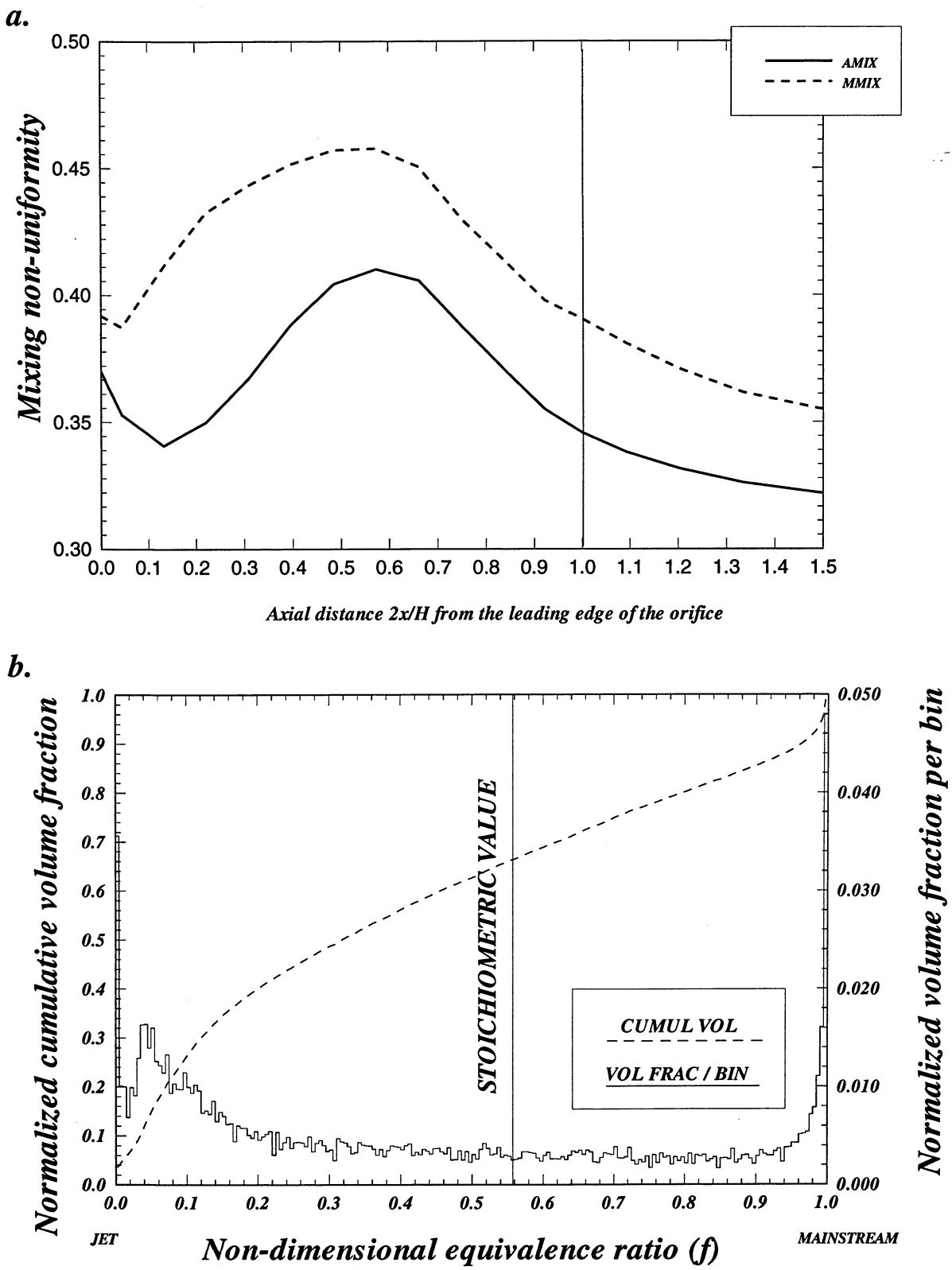

a. Planar deviations (AMIX and MMIX) results

b. mixing non-uniformity volume histograms for 0 < 2x/H < 1

Figure-B20. Configuration HO-20. Annular mixer, 67.5^0 slot L/W=4, 6 equiv holes/row

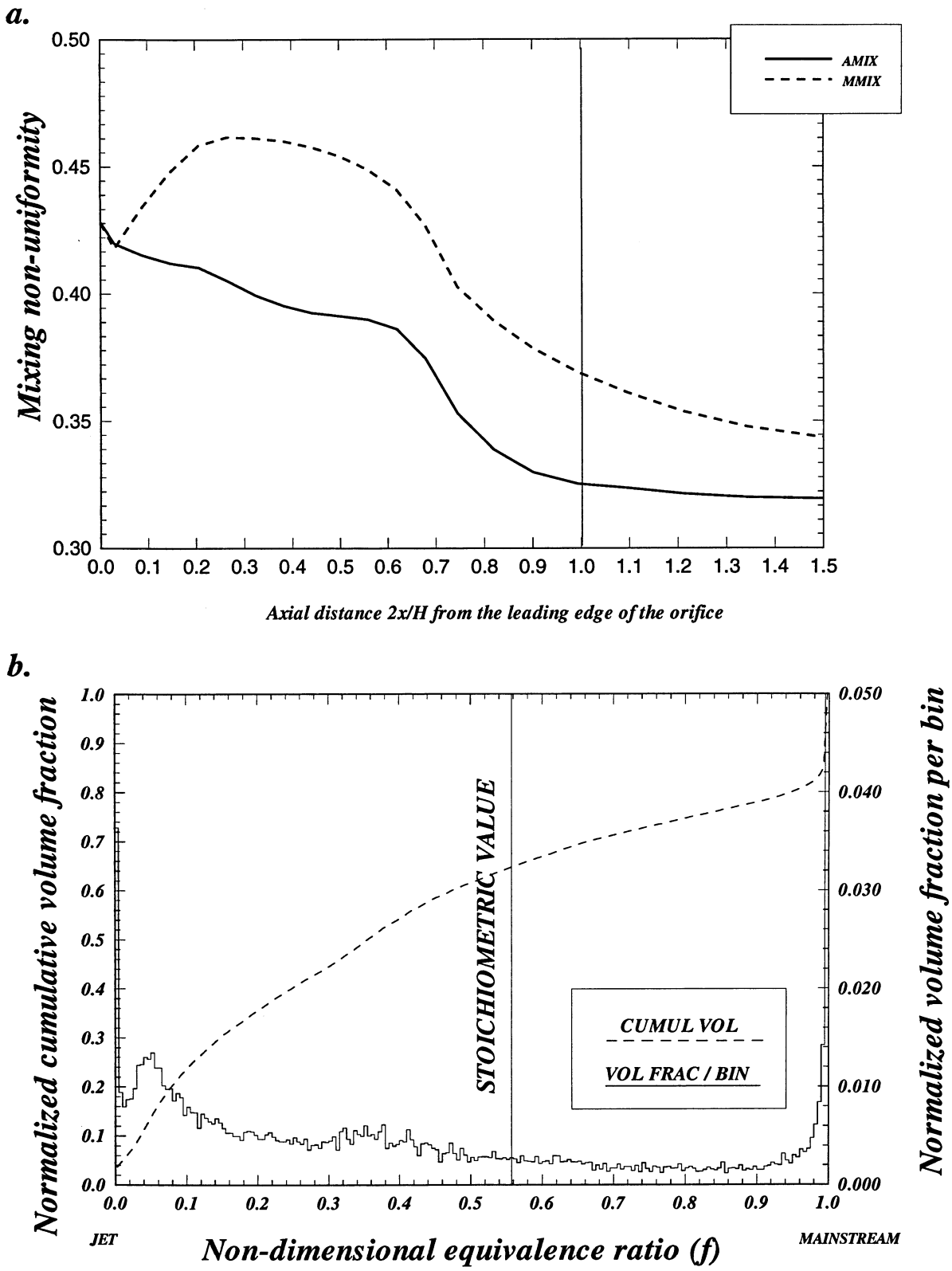

a. Planar deviations (AMIX and MMIX) results

b. mixing non-uniformity volume histograms for 0 < 2x/H < 1

Figure-B21. Configuration HO-21. Annular mixer, 67.5^0 slot L/W=4, 8 equiv holes/row

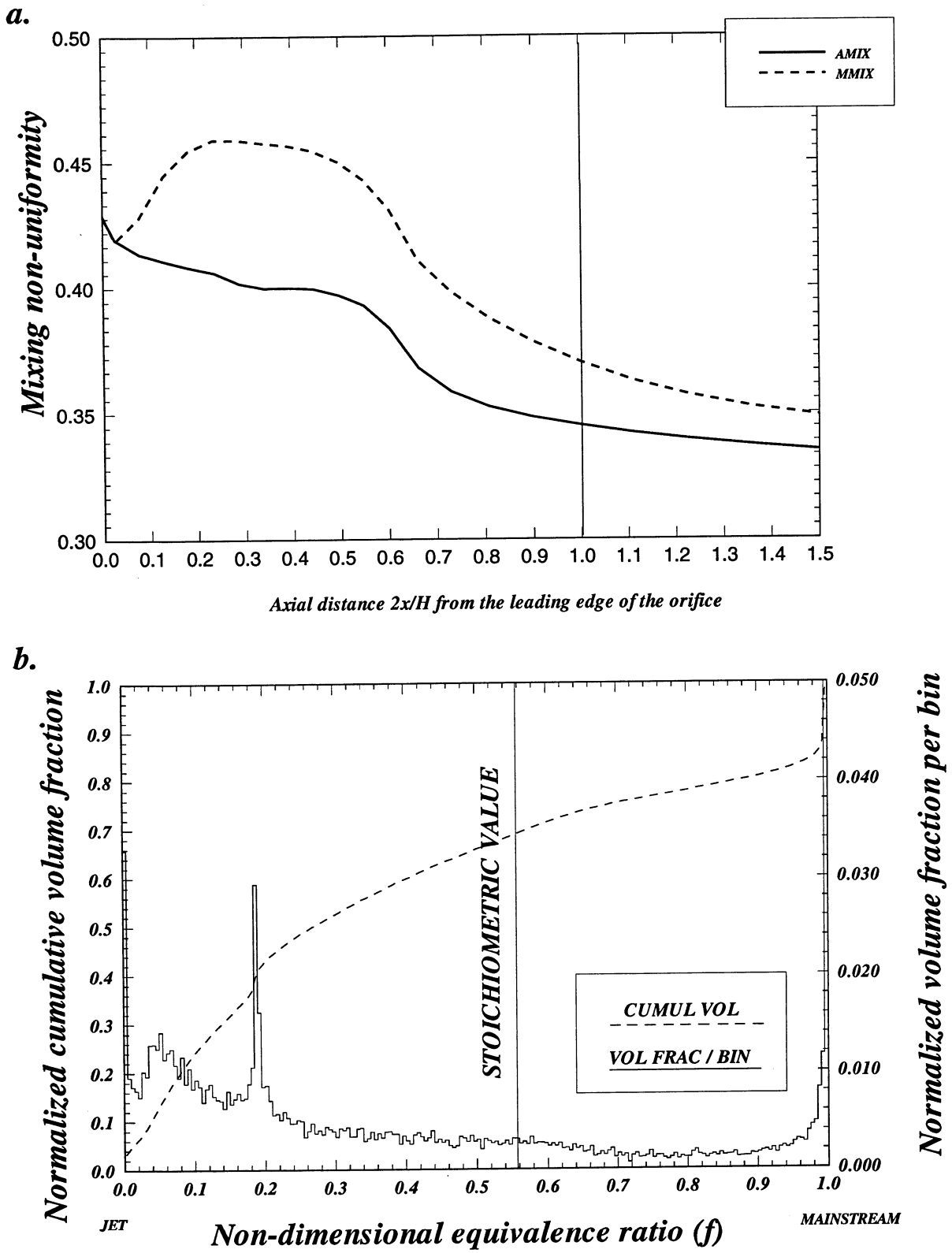

a. Planar deviations (AMIX and MMIX) results

b. mixing non-uniformity volume histograms for 0 < 2x/H < 1

Figure-B22. Configuration HO-22. Annular mixer, 67.5^0 slot L/W=4, 10 equiv holes/row

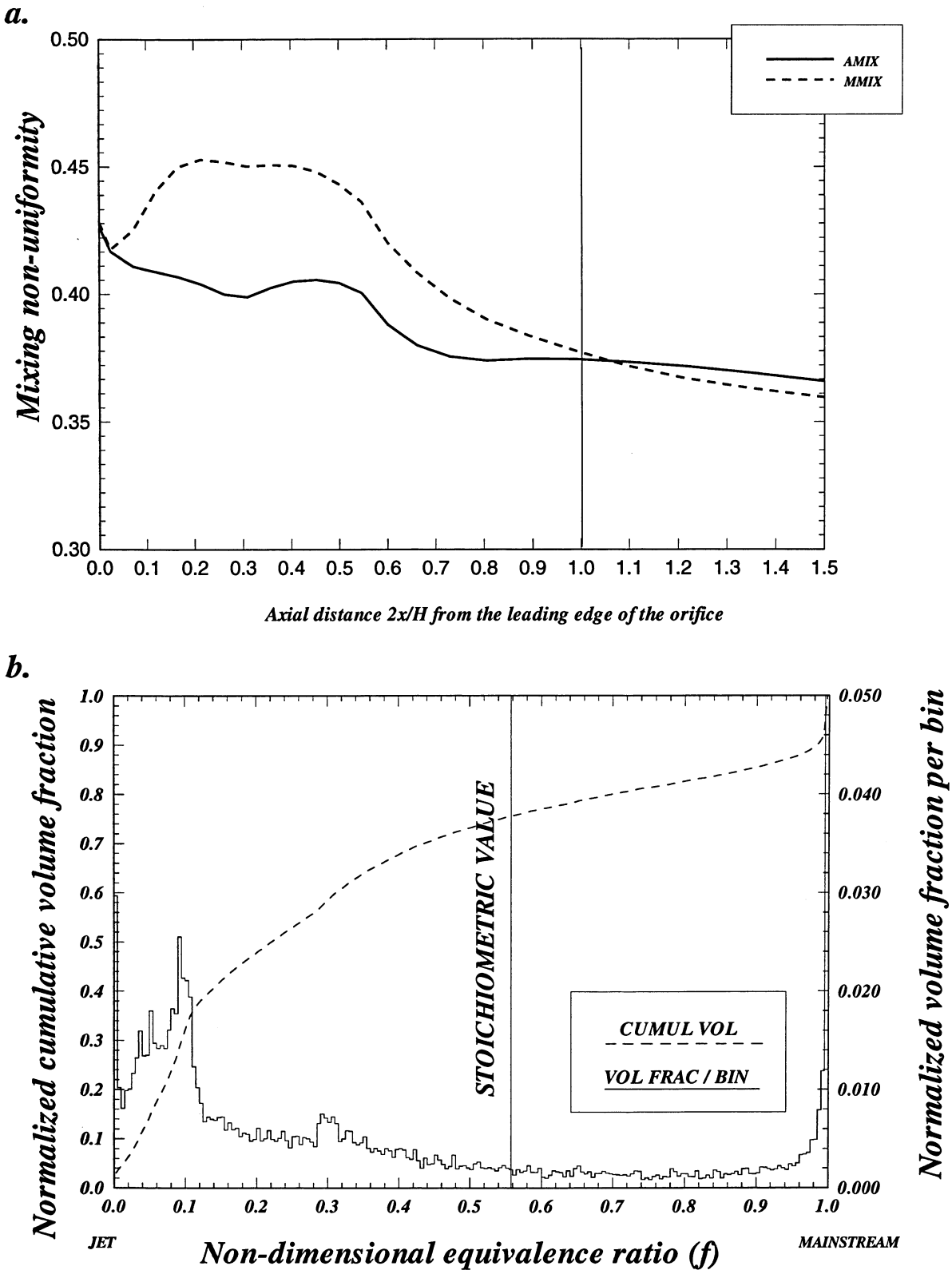

a. Planar deviations (AMIX and MMIX) results

b. mixing non-uniformity volume histograms for 0 < 2x/H < 1

Figure-B23. Configuration HO-23. Annular mixer, 67.5^0 slot L/W=4, 12 equiv holes/row

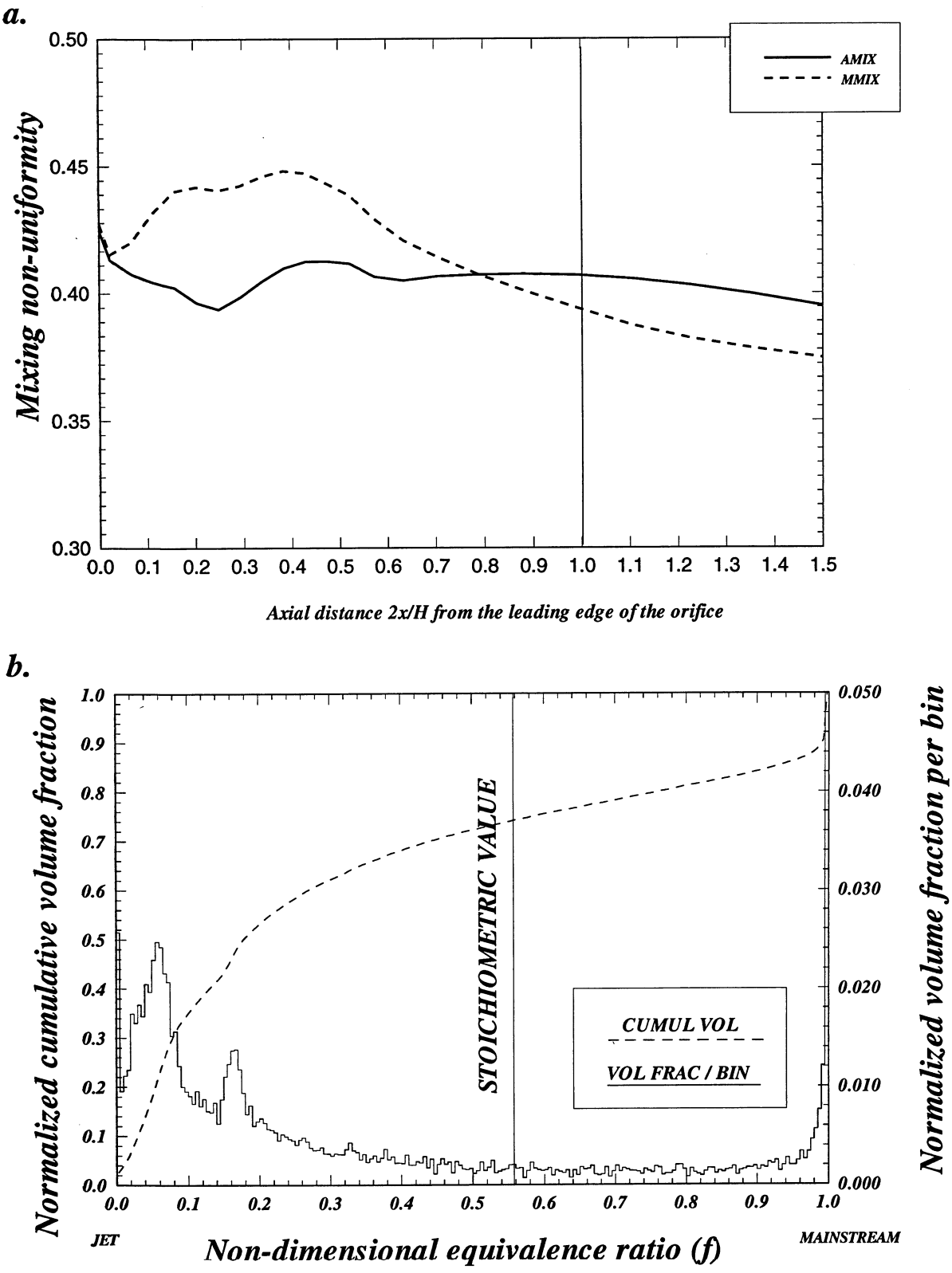

a. Planar deviations (AMIX and MMIX) results

b. mixing non-uniformity volume histograms for 0 < 2x/H < 1

Figure-B24. Configuration HO-24. Annular mixer, 67.5^0 slot L/W=4, 14 equiv holes/row

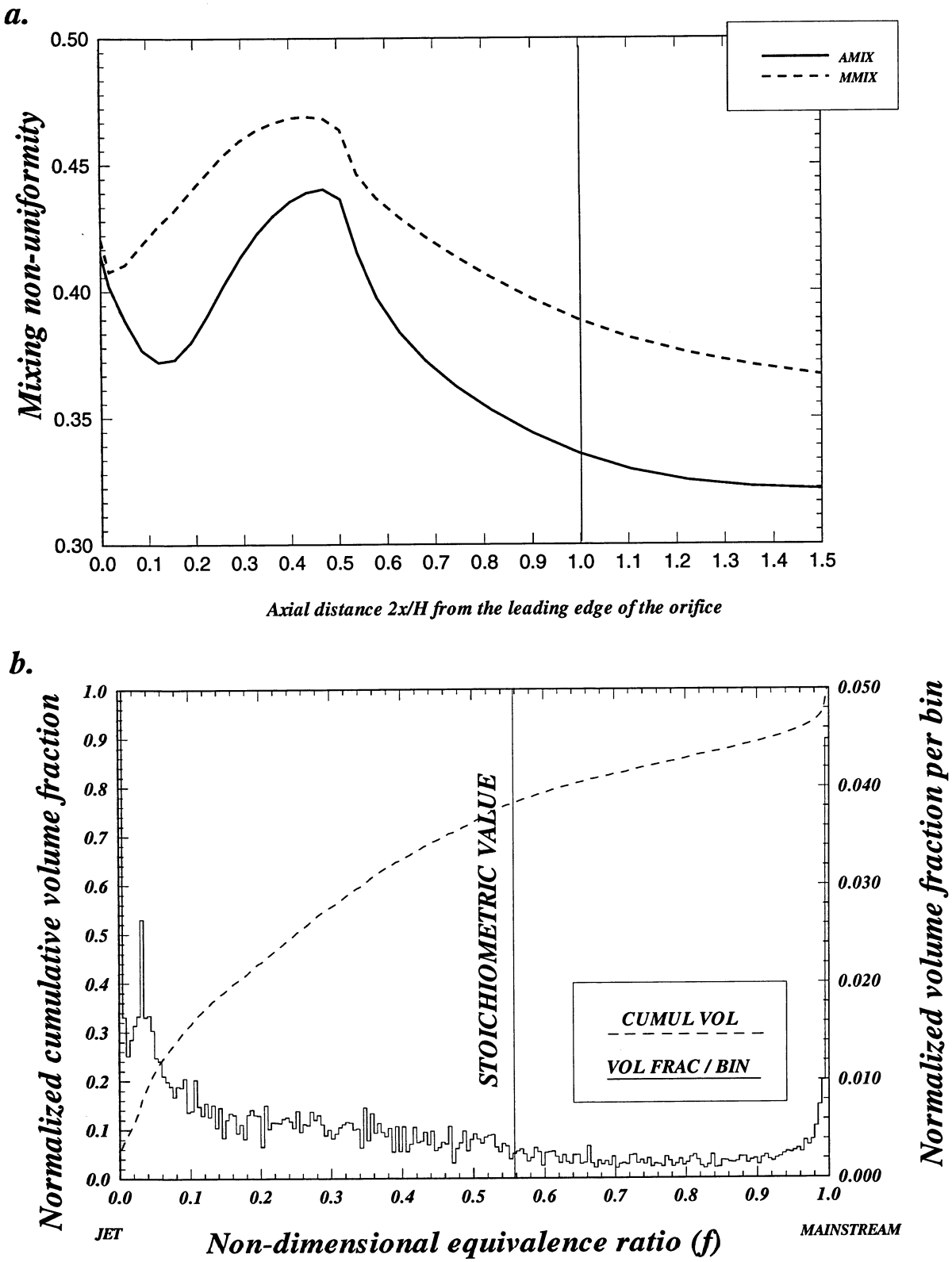

a. Planar deviations (AMIX and MMIX) results

b. mixing non-uniformity volume histograms for 0 < 2x/H < 1

Figure-B25. Configuration HO-25. Annular mixer, 16 round equivalent holes/row

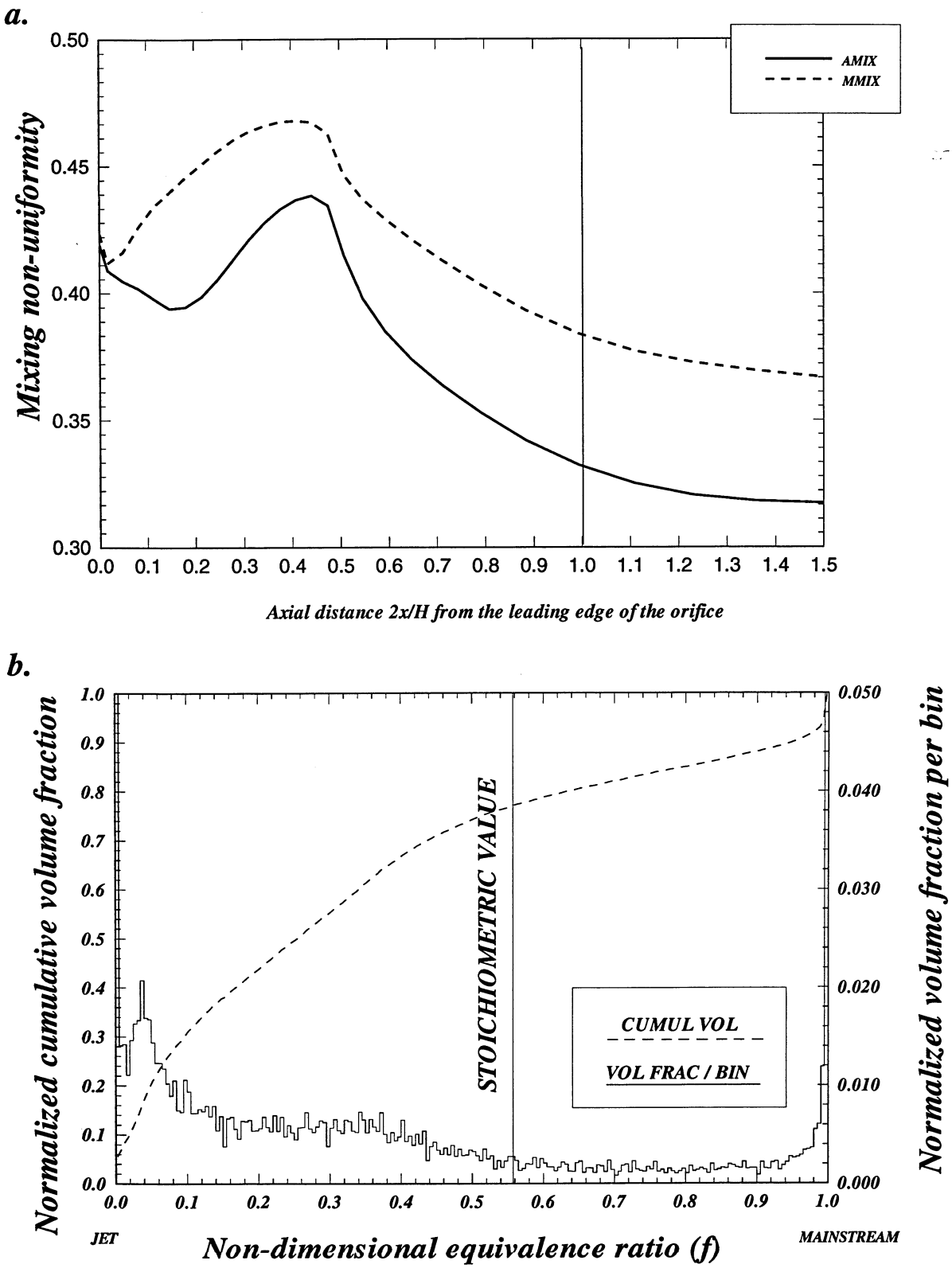

a. Planar deviations (AMIX and MMIX) results

b. mixing non-uniformity volume histograms for 0 < 2x/H < 1

Figure-B26. Configuration HO-26. Annular mixer, 18 round equivalent holes/row

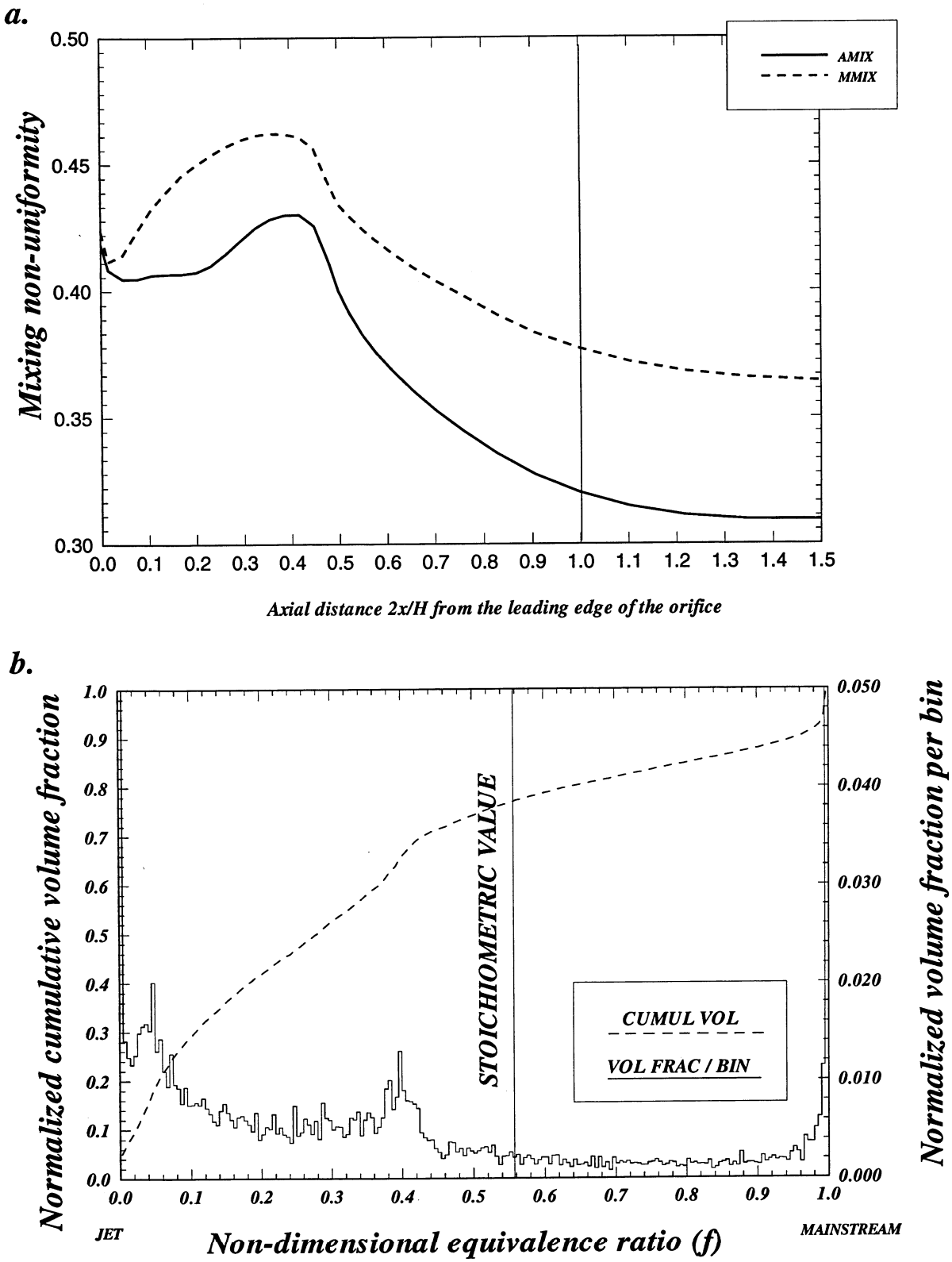

a. Planar deviations (AMIX and MMIX) results

b. mixing non-uniformity volume histograms for 0 < 2x/H < 1

Figure-B27. Configuration HO-27. Annular mixer, 20 round equivalent holes/row

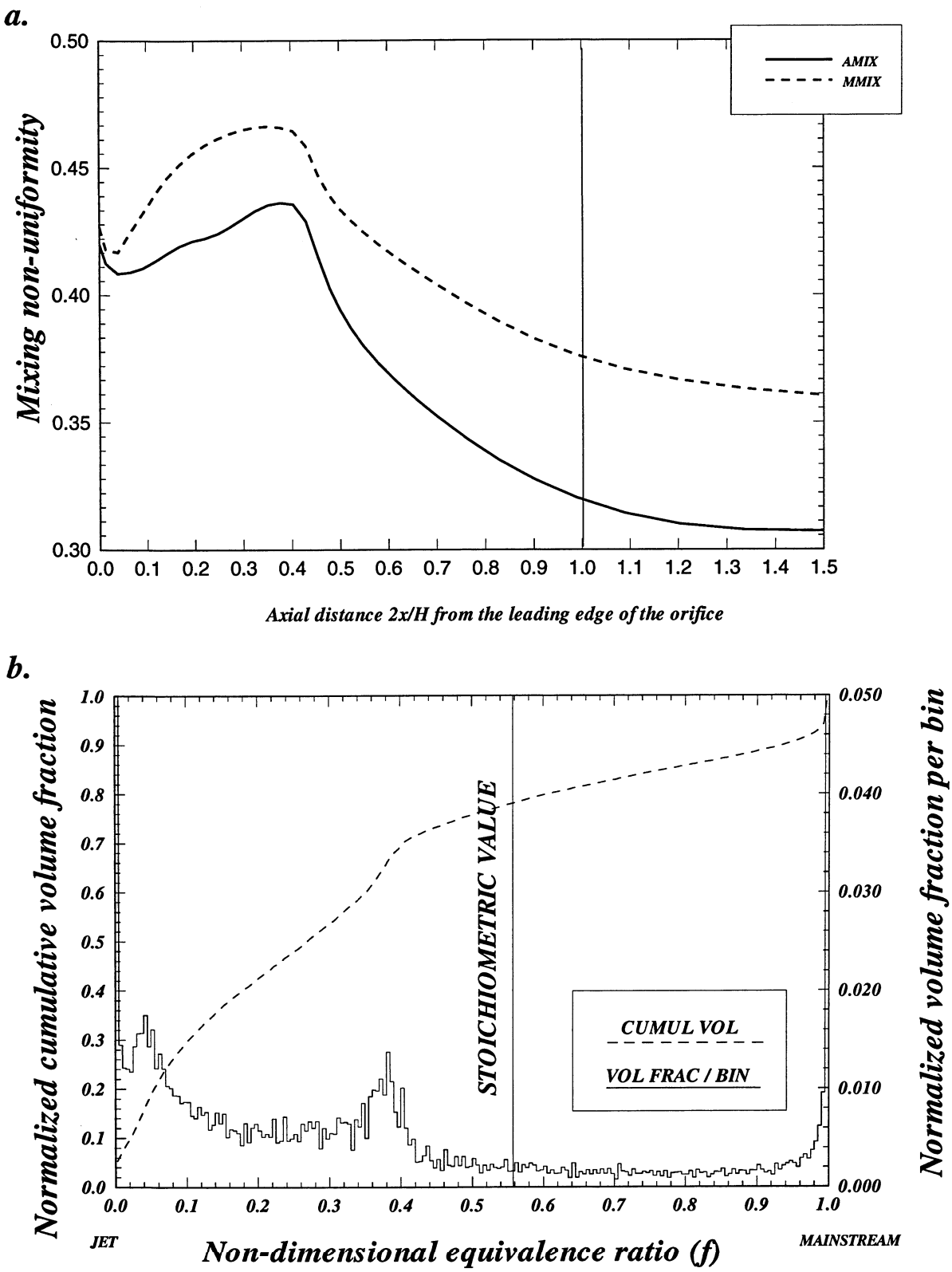

a. Planar deviations (AMIX and MMIX) results

b. mixing non-uniformity volume histograms for 0 < 2x/H < 1

Figure-B28. Configuration HO-28. Annular mixer, 22 round equivalent holes/row

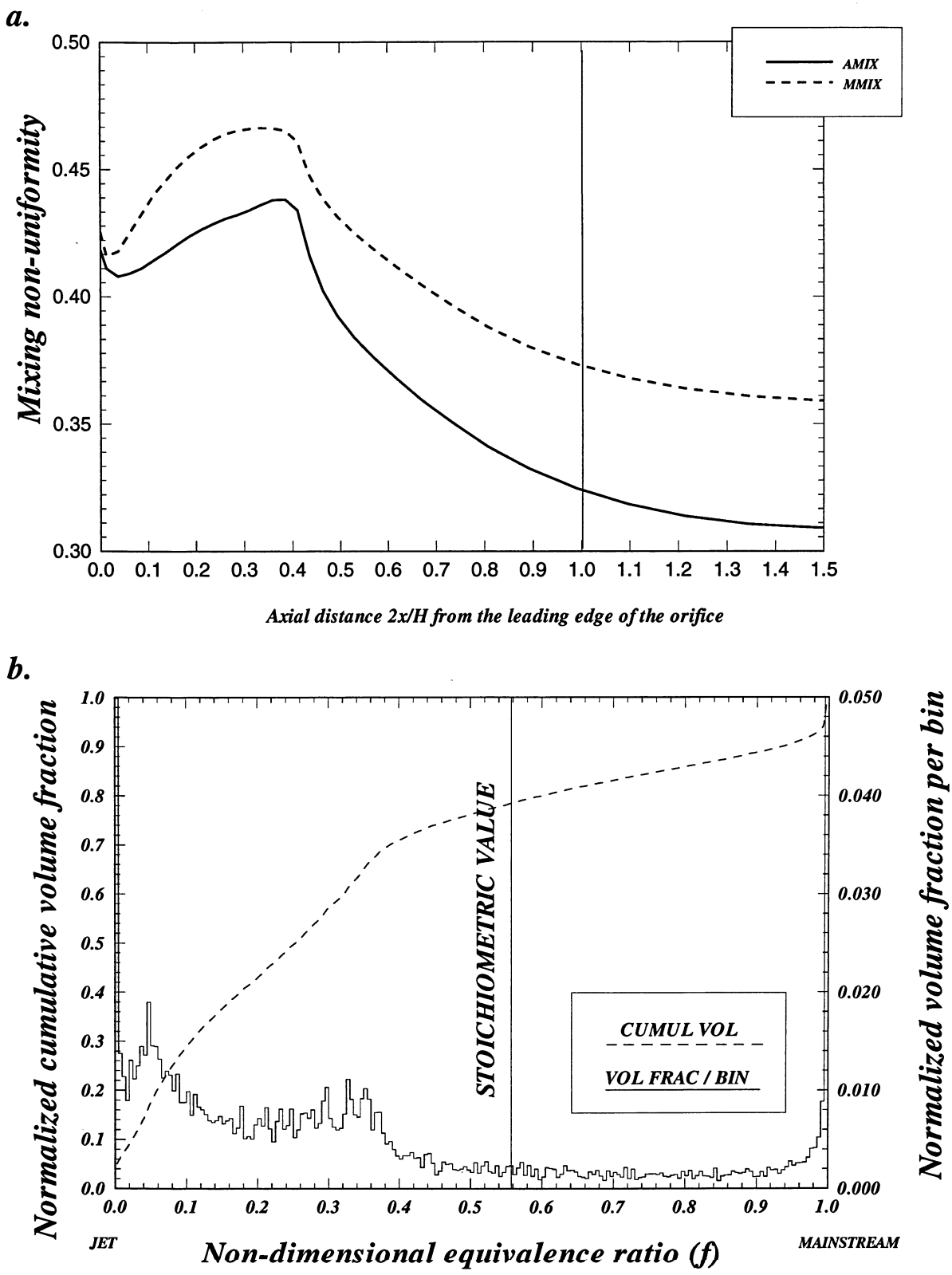

a. Planar deviations (AMIX and MMIX) results

b. mixing non-uniformity volume histograms for 0 < 2x/H < 1

Figure-B29. Configuration HO-29. Annular mixer, 24 round equivalent holes/row

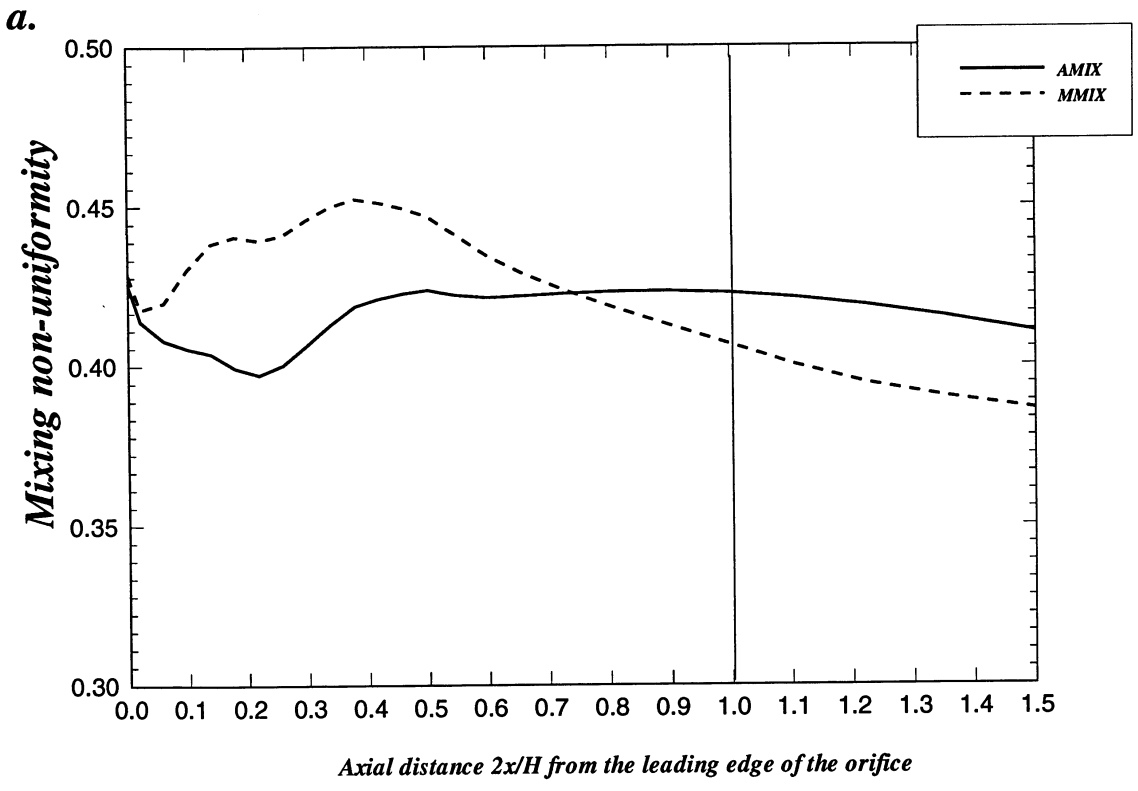

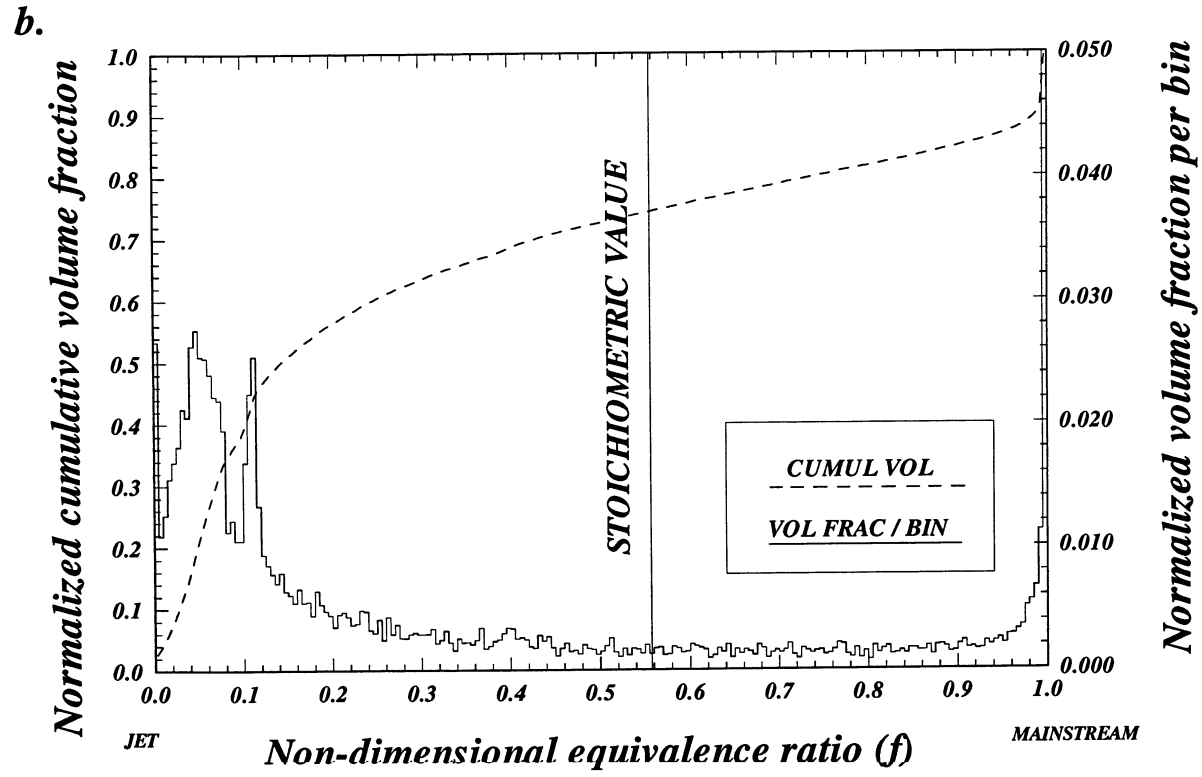

a. Planar deviations (AMIX and MMIX) results

b. mixing non-uniformity volume histograms for 0 < 2x/H < 1

Figure-B30. Configuration HO-30. Annular mixer, 67.5^0 slot L/W=4, 16 equiv holes/row

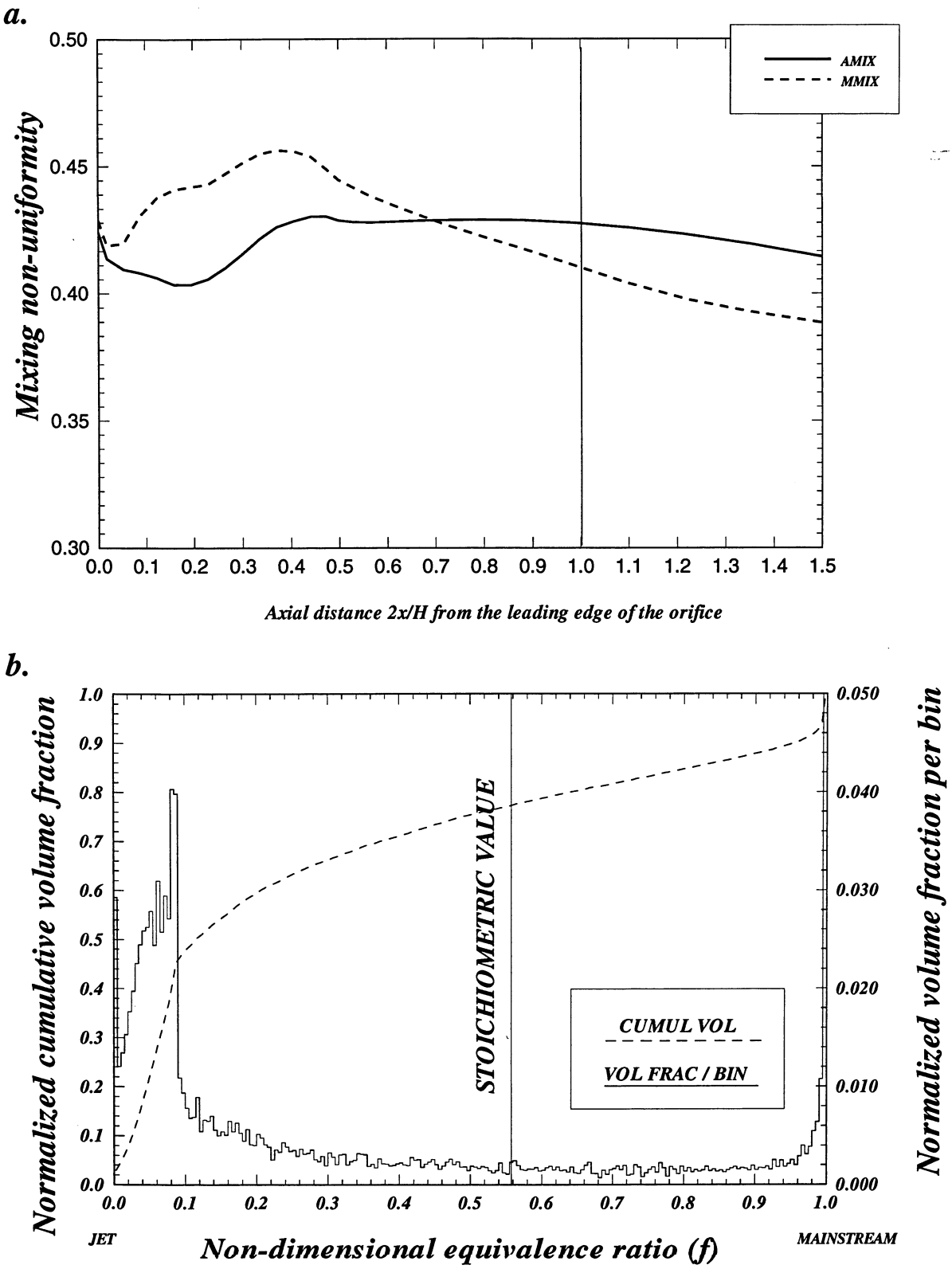

a. Planar deviations (AMIX and MMIX) results

b. mixing non-uniformity volume histograms for 0 < 2x/H < 1

Figure-B31. Configuration HO-31. Annular mixer, 67.5^0 slot L/W=4, 18 equiv holes/row

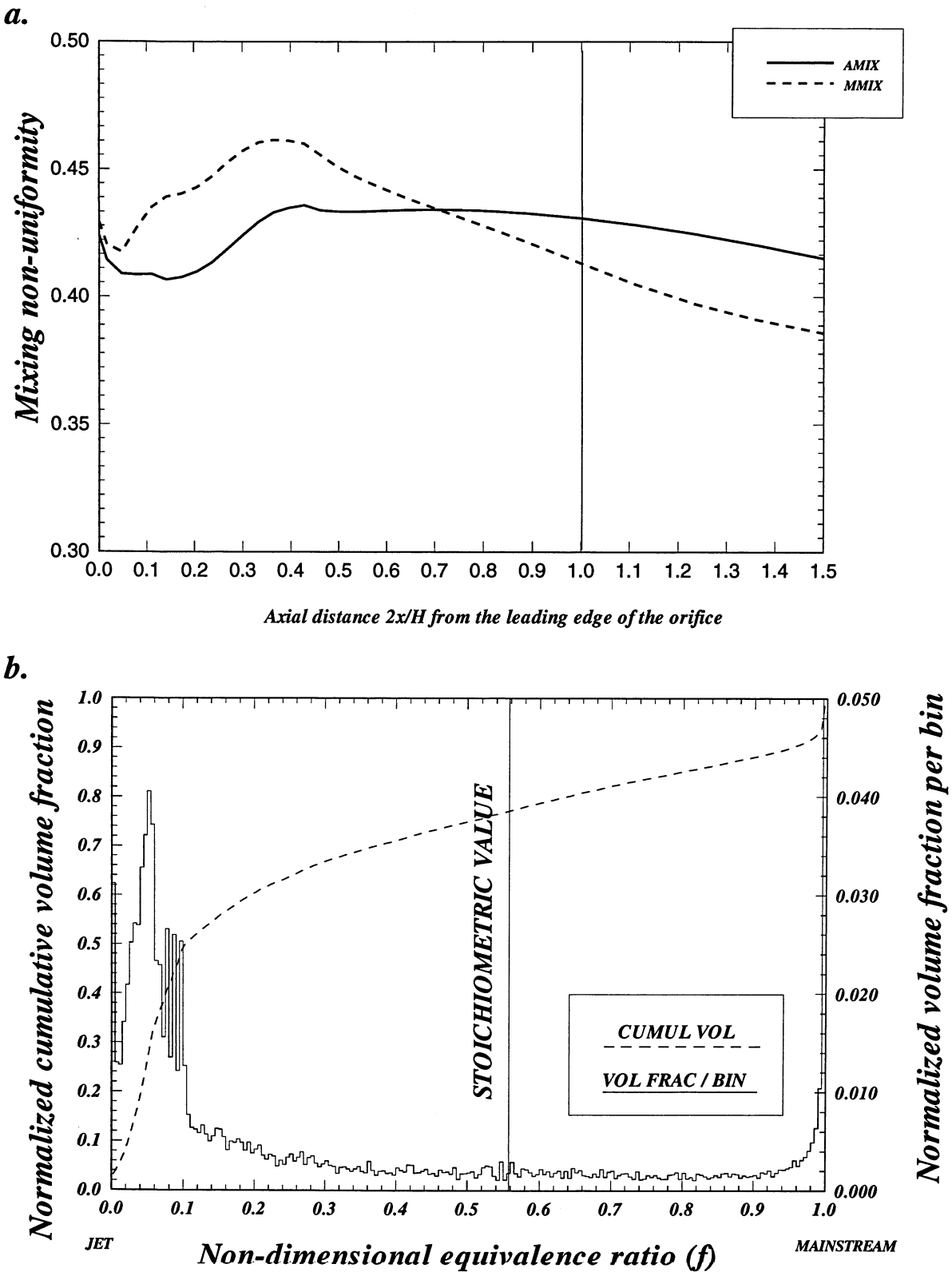

a. Planar deviations (AMIX and MMIX) results

b. mixing non-uniformity volume histograms for 0 < 2x/H < 1

Figure-B32. Configuration HO-32. Annular mixer, 67.5^0 slot L/W=4, 20 equiv holes/row

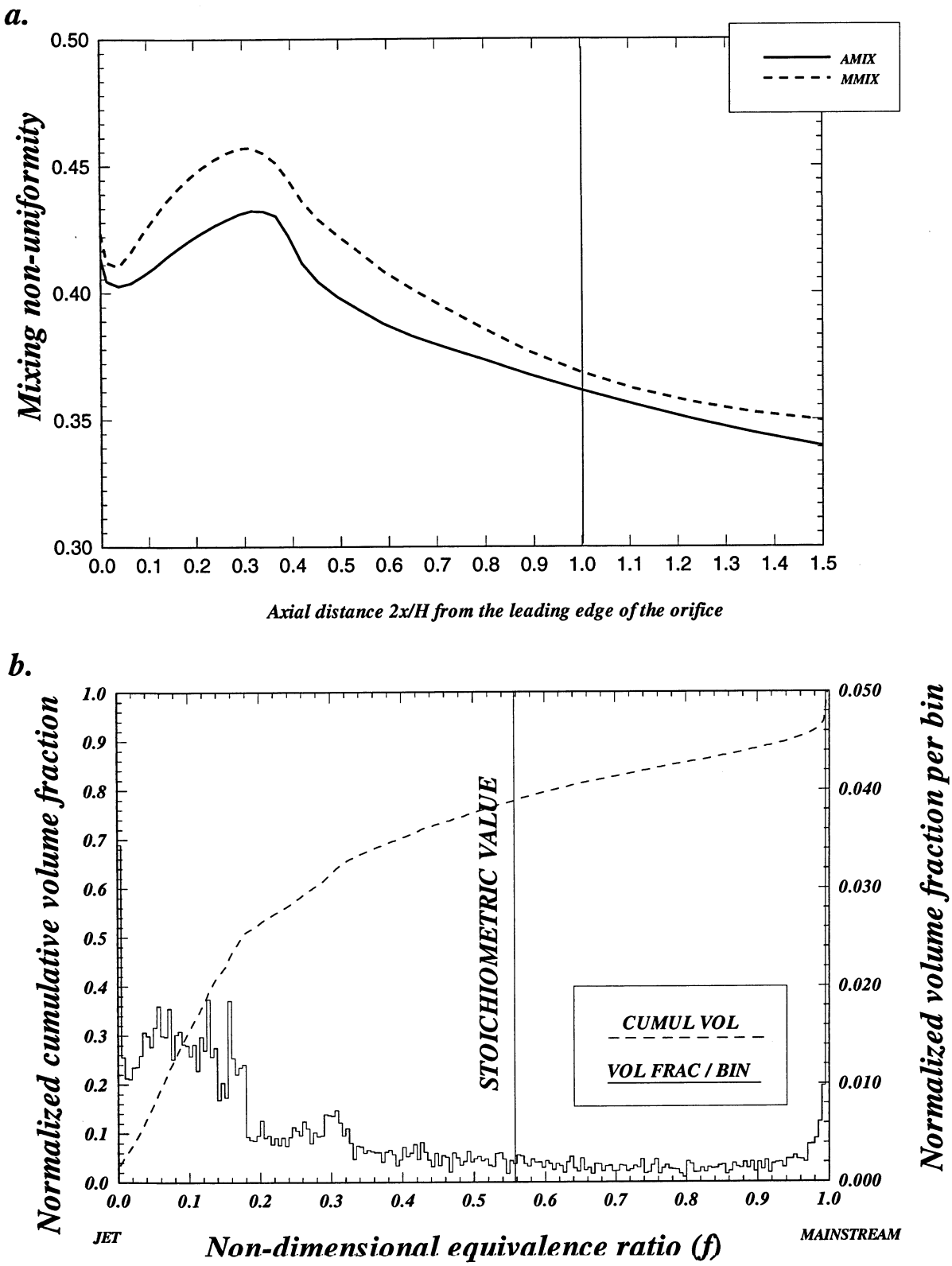

a. Planar deviations (AMIX and MMIX) results

b. mixing non-uniformity volume histograms for 0 < 2x/H < 1

Figure-B33. Configuration HO-33. Annular mixer, 30 round equivalent holes/row

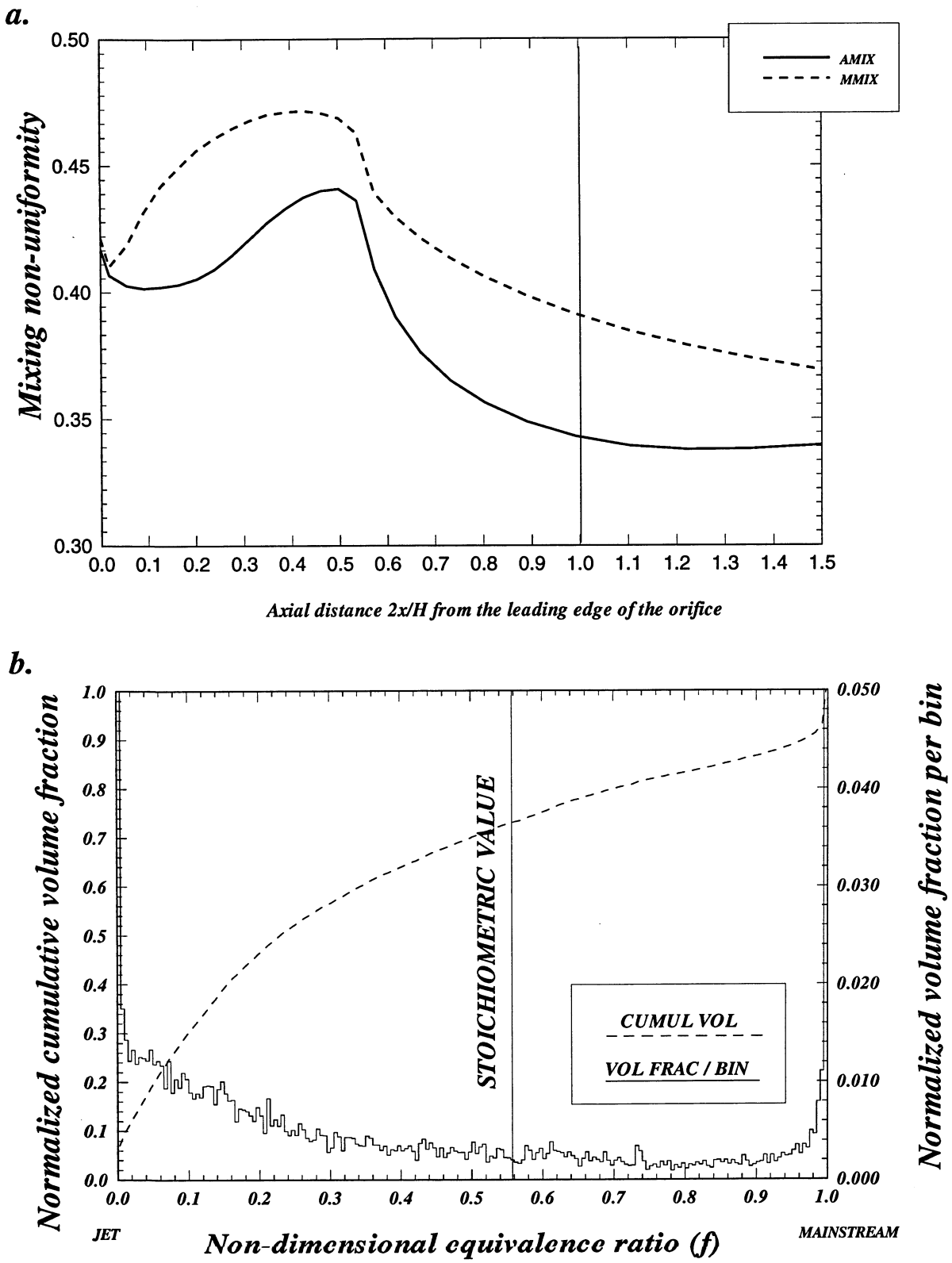

a. Planar deviations (AMIX and MMIX) results

b. mixing non-uniformity volume histograms for 0 < 2x/H < 1

Figure-B34. Configuration HO-34. Ann-staggered mixer, 14 round equiv holes/row

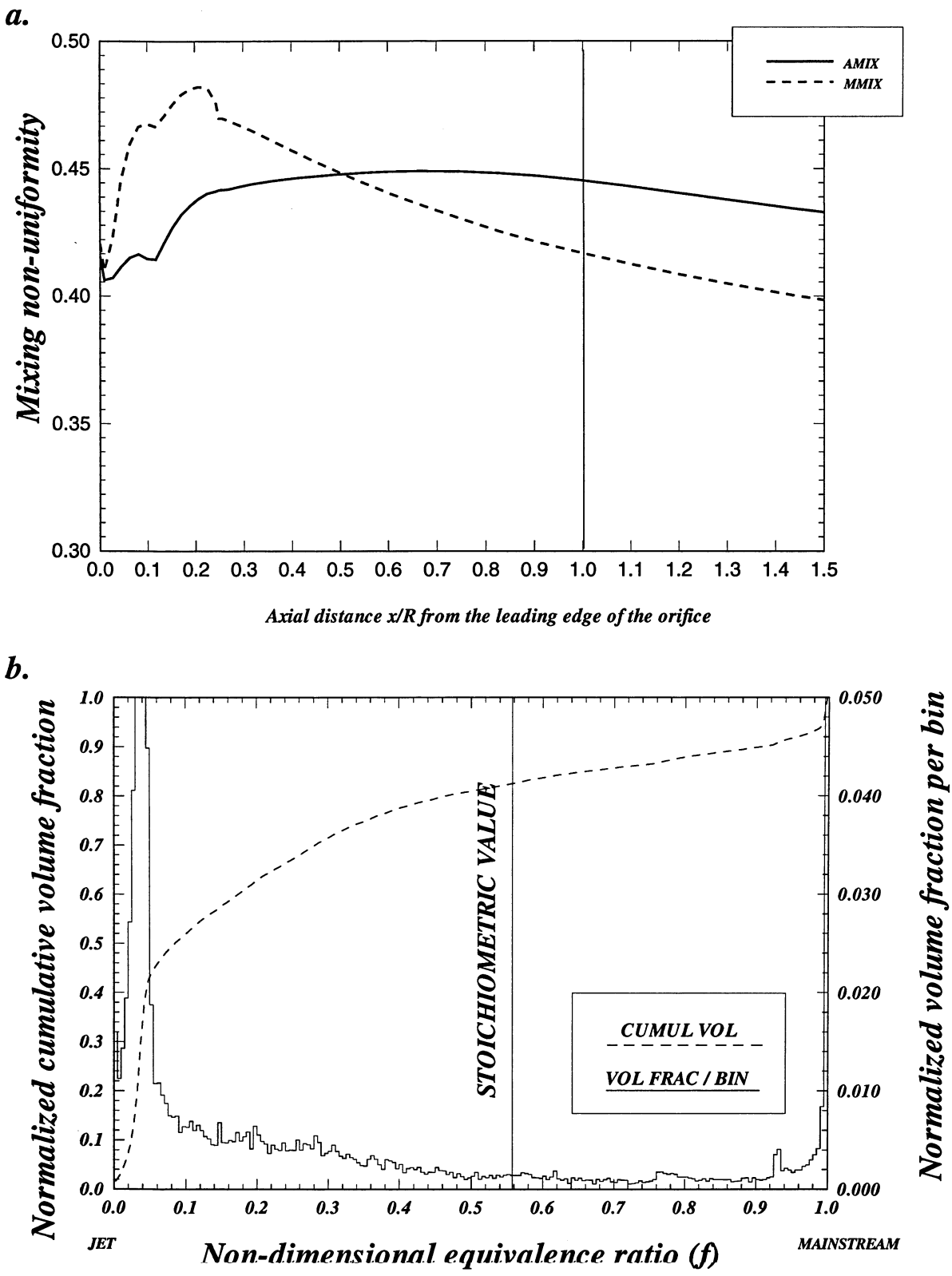

a. Planar deviations (AMIX and MMIX) results

b. mixing non-uniformity volume histograms for 0 < x/R < 1

Figure-B35. Configuration HO-35. Circular mixer, 67.5^0 slot L/W=4, 16 holes/row

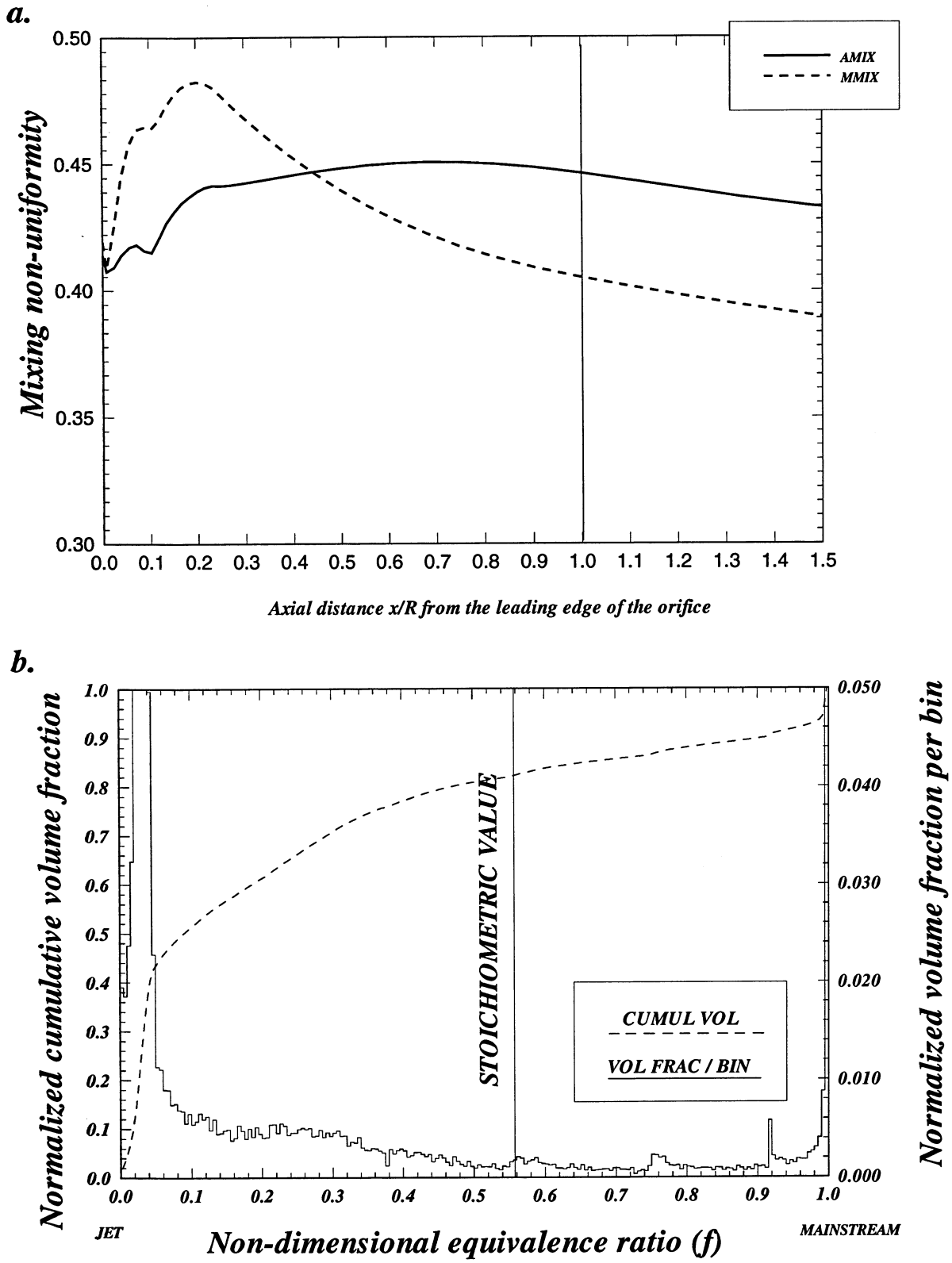

a. Planar deviations (AMIX and MMIX) results

b. mixing non-uniformity volume histograms for 0 < x/R < 1

Figure-B36. Configuration HO-36. Circular mixer, 67.5^0 slot L/W=4, 18 holes/row

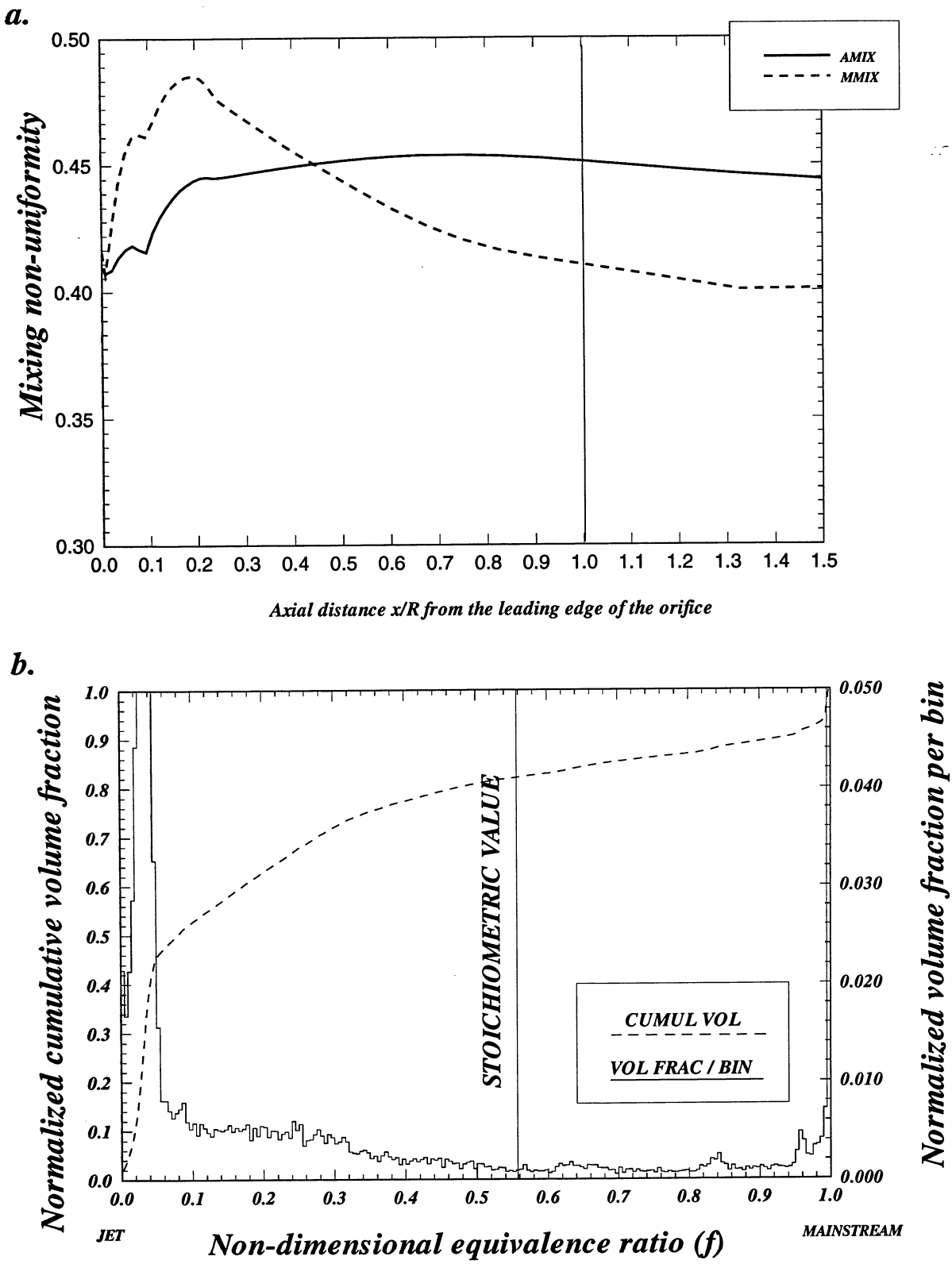

a. Planar deviations (AMIX and MMIX) results

b. mixing non-uniformity volume histograms for 0 < x/R < 1

Figure-B37. Configuration HO-37. Circular mixer, 67.5^0 slot L/W=4, 20 holes/row

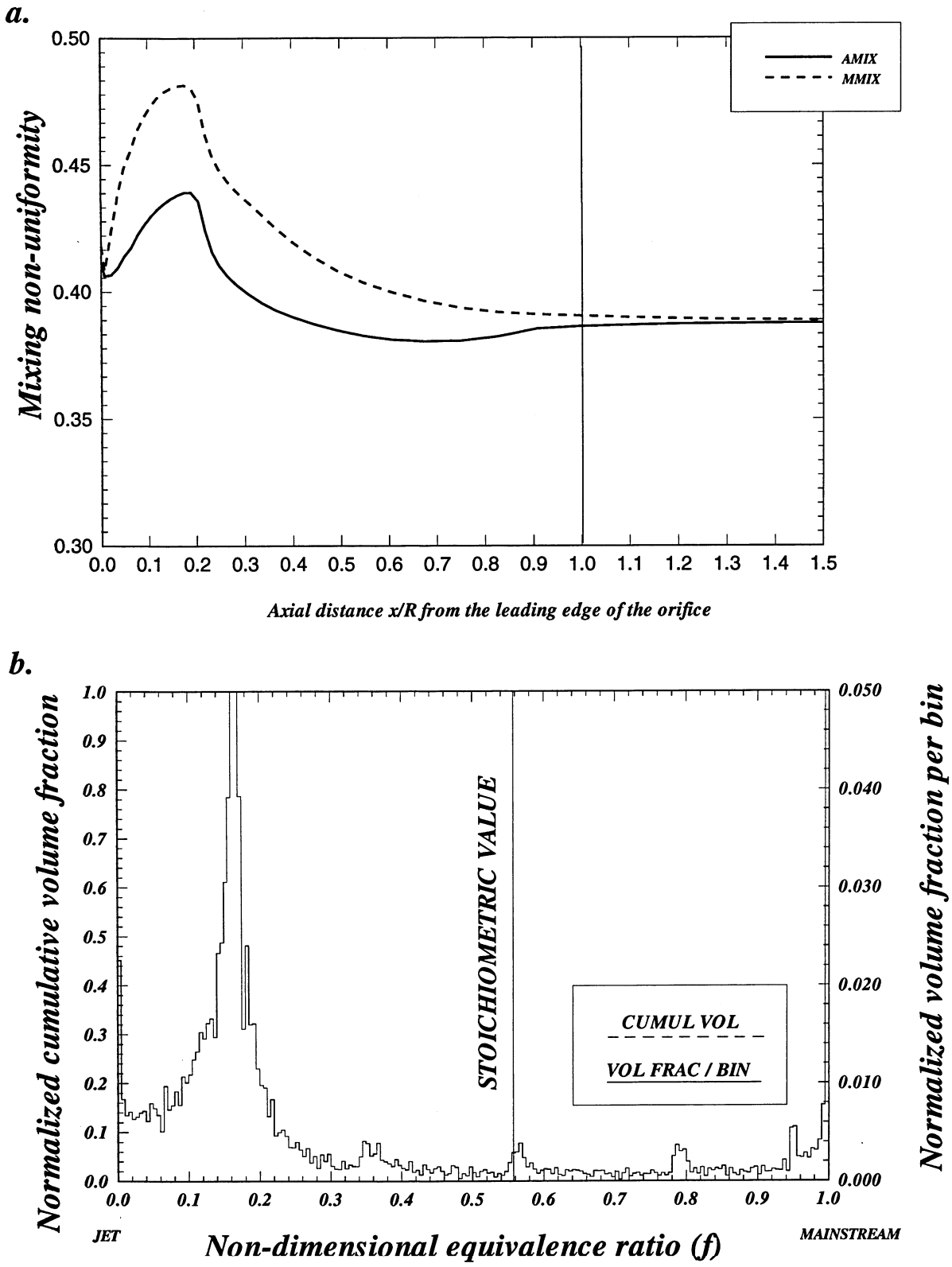

a. Planar deviations (AMIX and MMIX) results

b. mixing non-uniformity volume histograms for 0 < x/R < 1

Figure-B38. Configuration HO-38. Circular mixer, 24 round holes/row

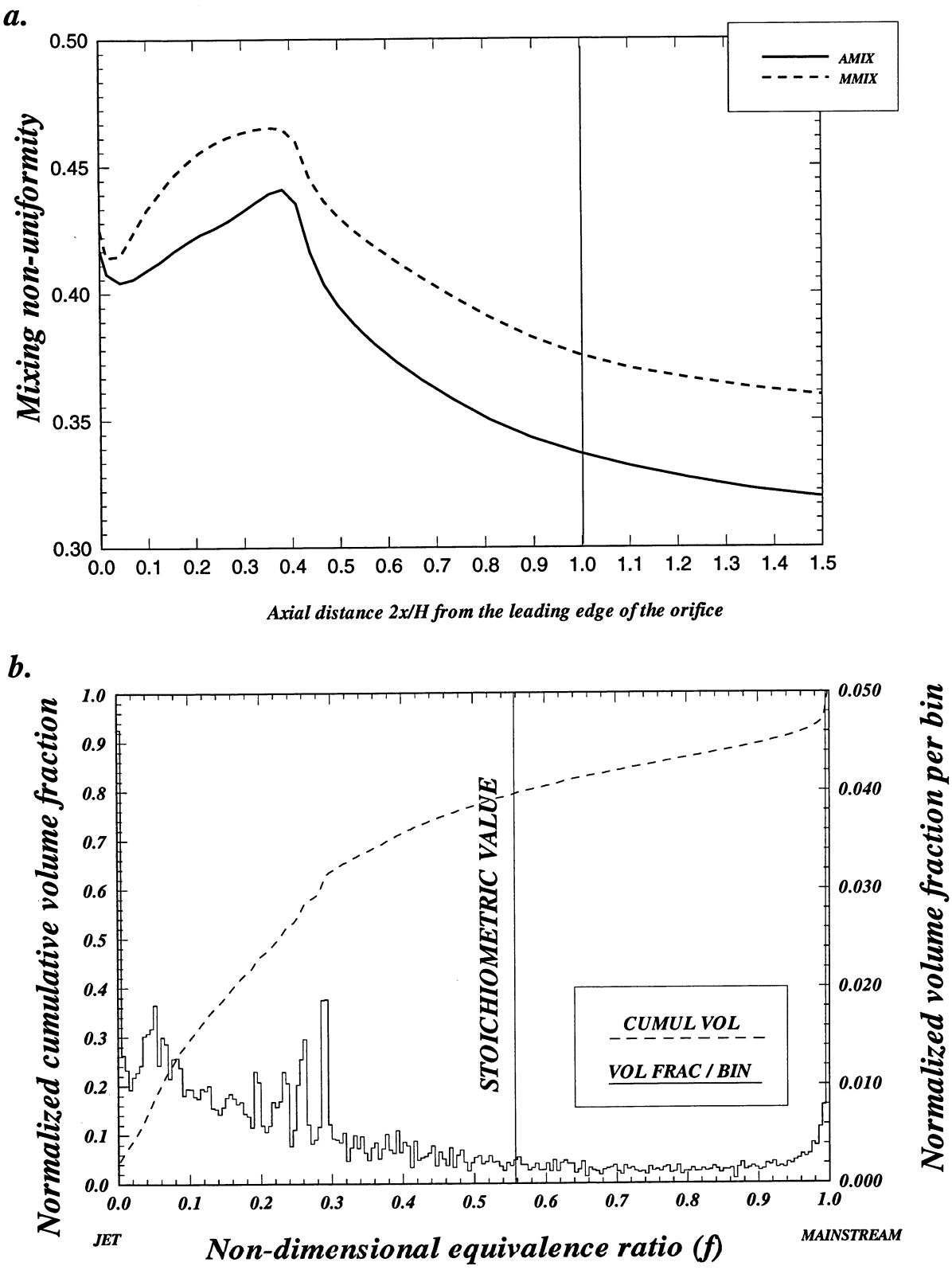

a. Planar deviations (AMIX and MMIX) results

b. mixing non-uniformity volume histograms for 0 < 2x/H < 1

Figure-B39. Configuration HO-39. Annular mixer, 6 round equivalent holes/row

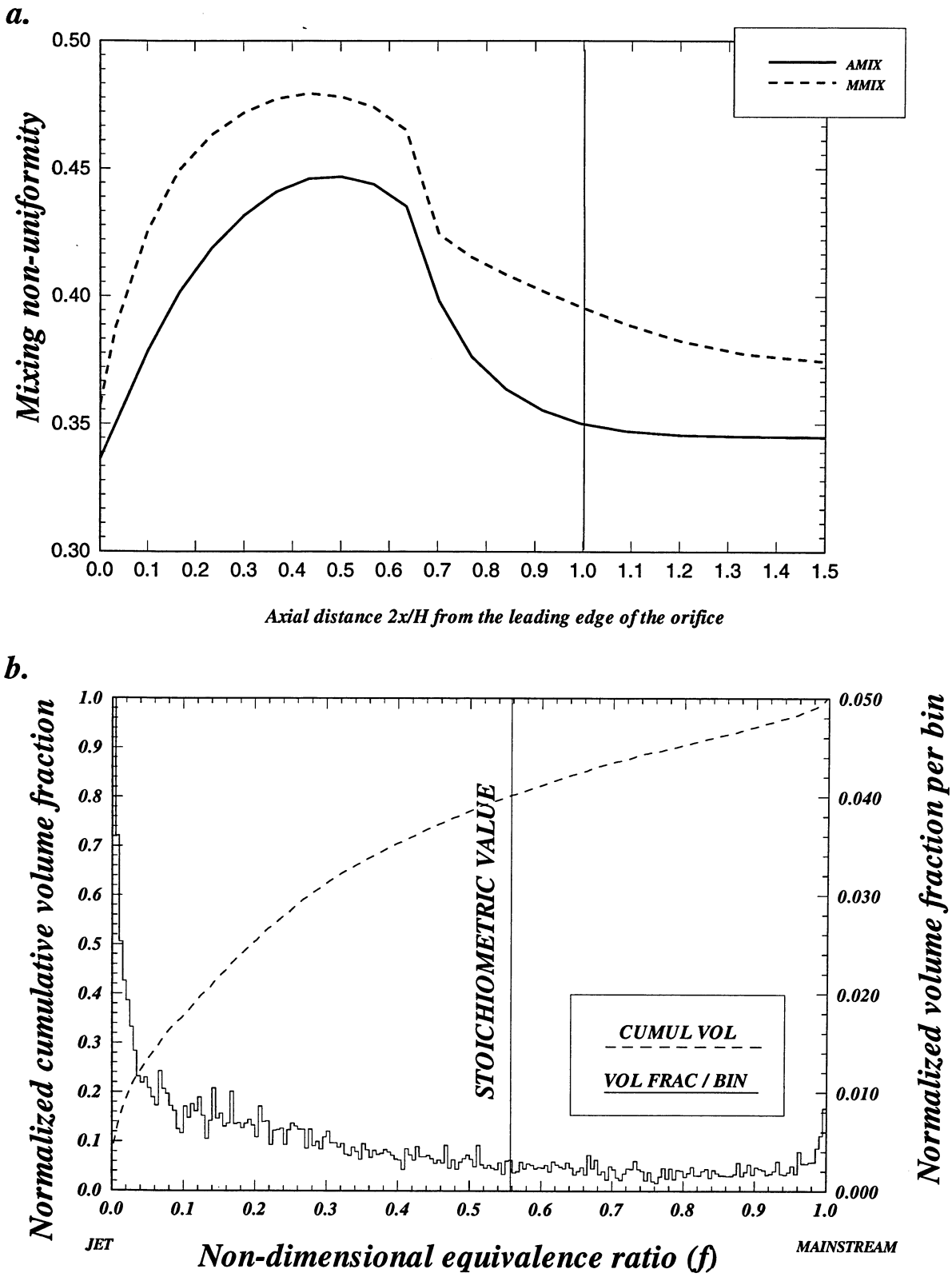

a. Planar deviations (AMIX and MMIX) results

b. mixing non-uniformity volume histograms for 0 < 2x/H < 1

Figure-B40. Configuration HO-40. Annular mixer, 2 round equivalent holes/row

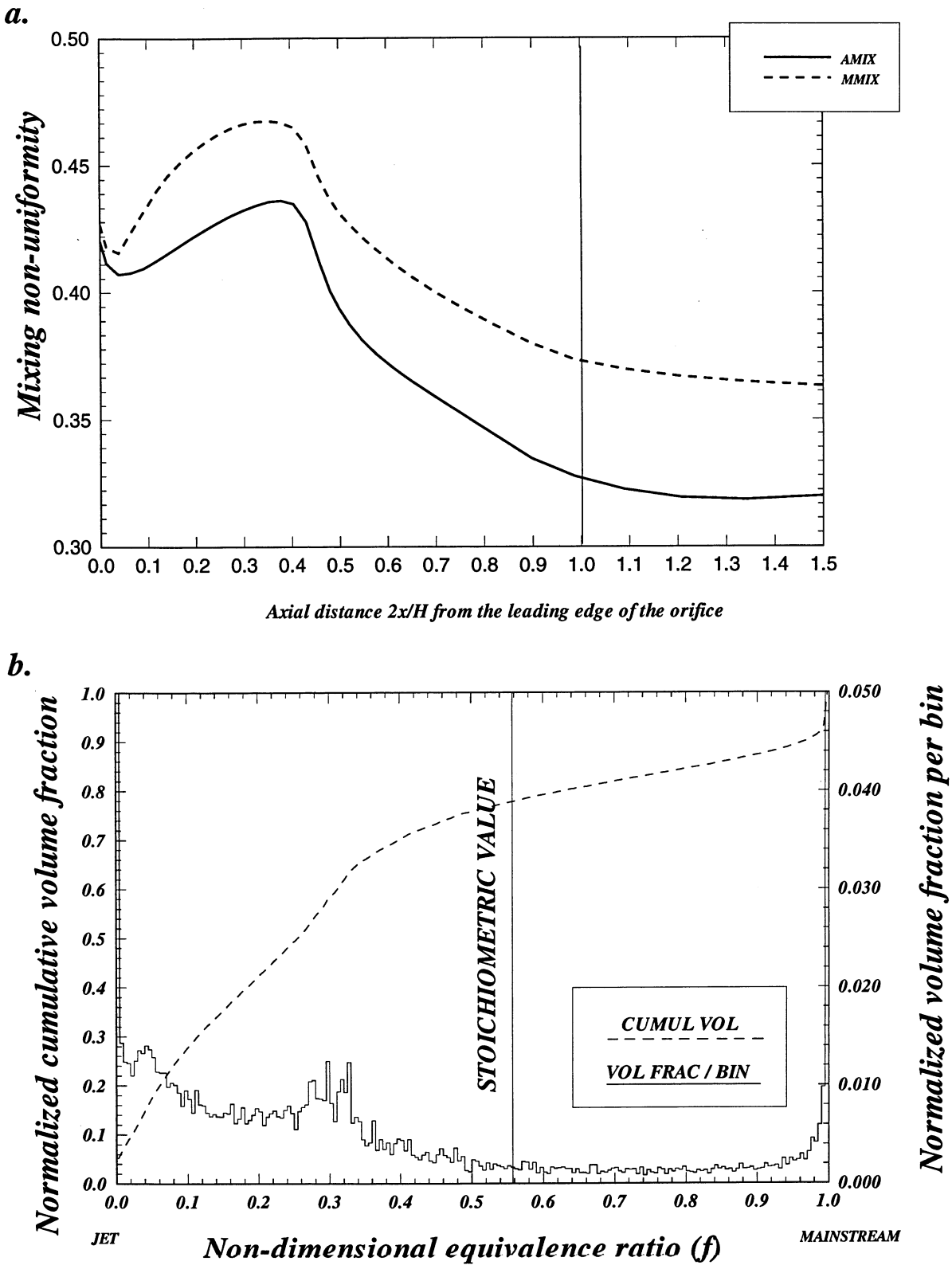

a. Planar deviations (AMIX and MMIX) results

b. mixing non-uniformity volume histograms for 0 < 2x/H < 1

Figure-B41. Configuration HO-41. Ann-staggered mixer, 22 round equivalent holes/row

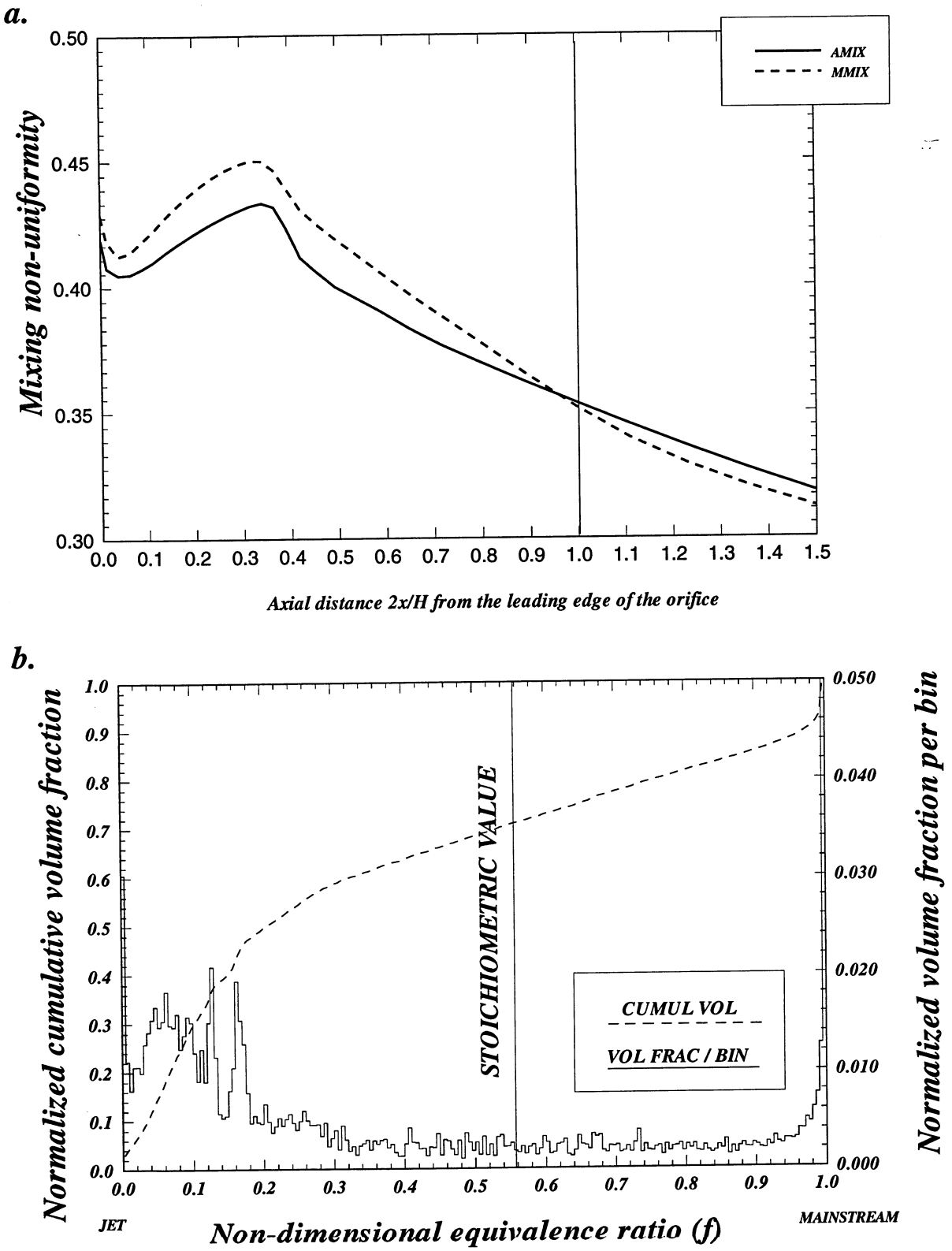

a. Planar deviations (AMIX and MMIX) results

b. mixing non-uniformity volume histograms for 0 < 2x/H < 1

Figure-B42. Configuration HO-42. Ann-staggered mixer, 30 round equivalent holes/row

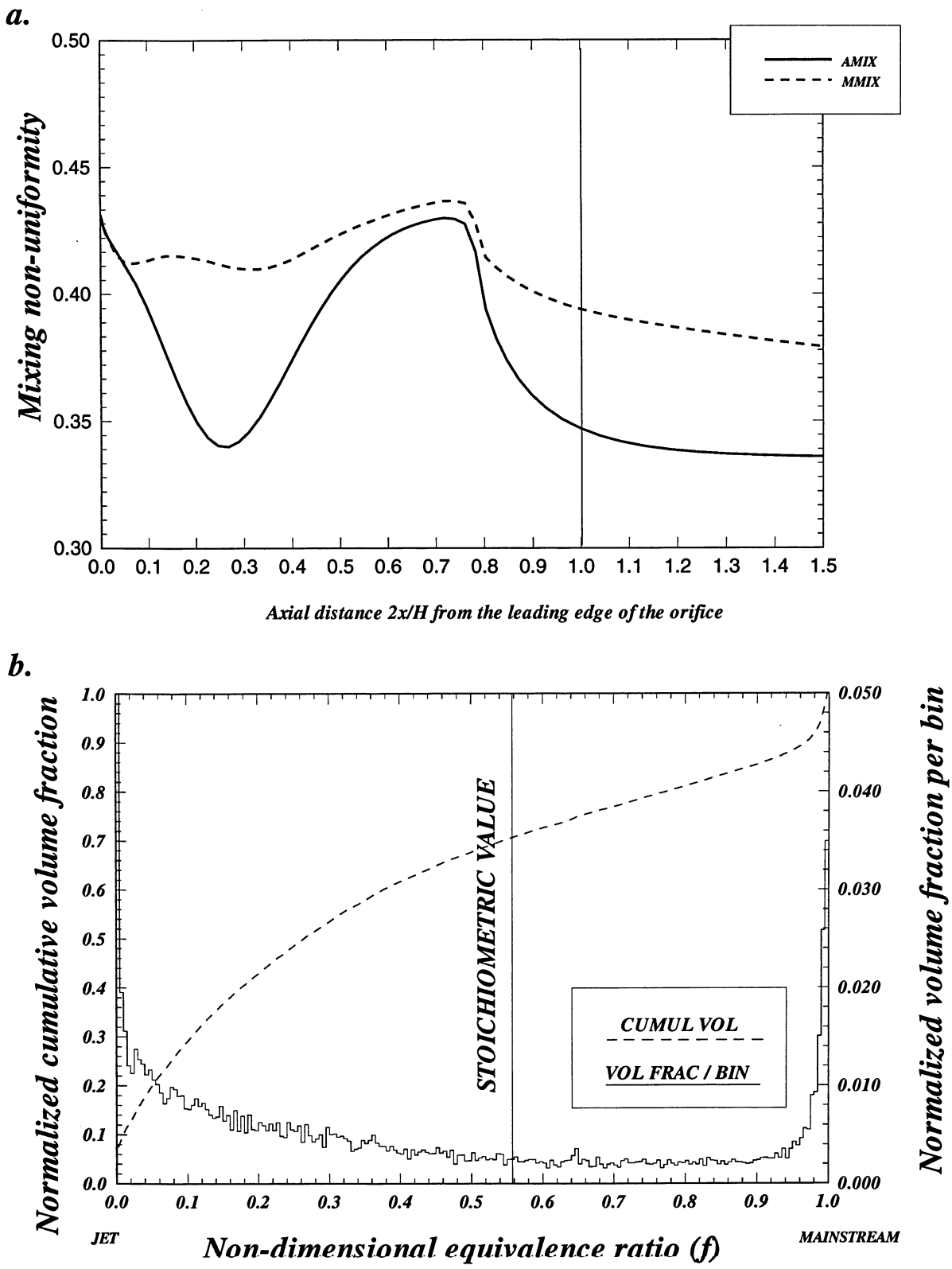

a. Planar deviations (AMIX and MMIX) results

b. mixing non-uniformity volume histograms for 0 < 2x/H < 1

Figure-B43. Configuration HO-43. Annular mixer,flow aligned slot L/W=4, 6 eq holes/row

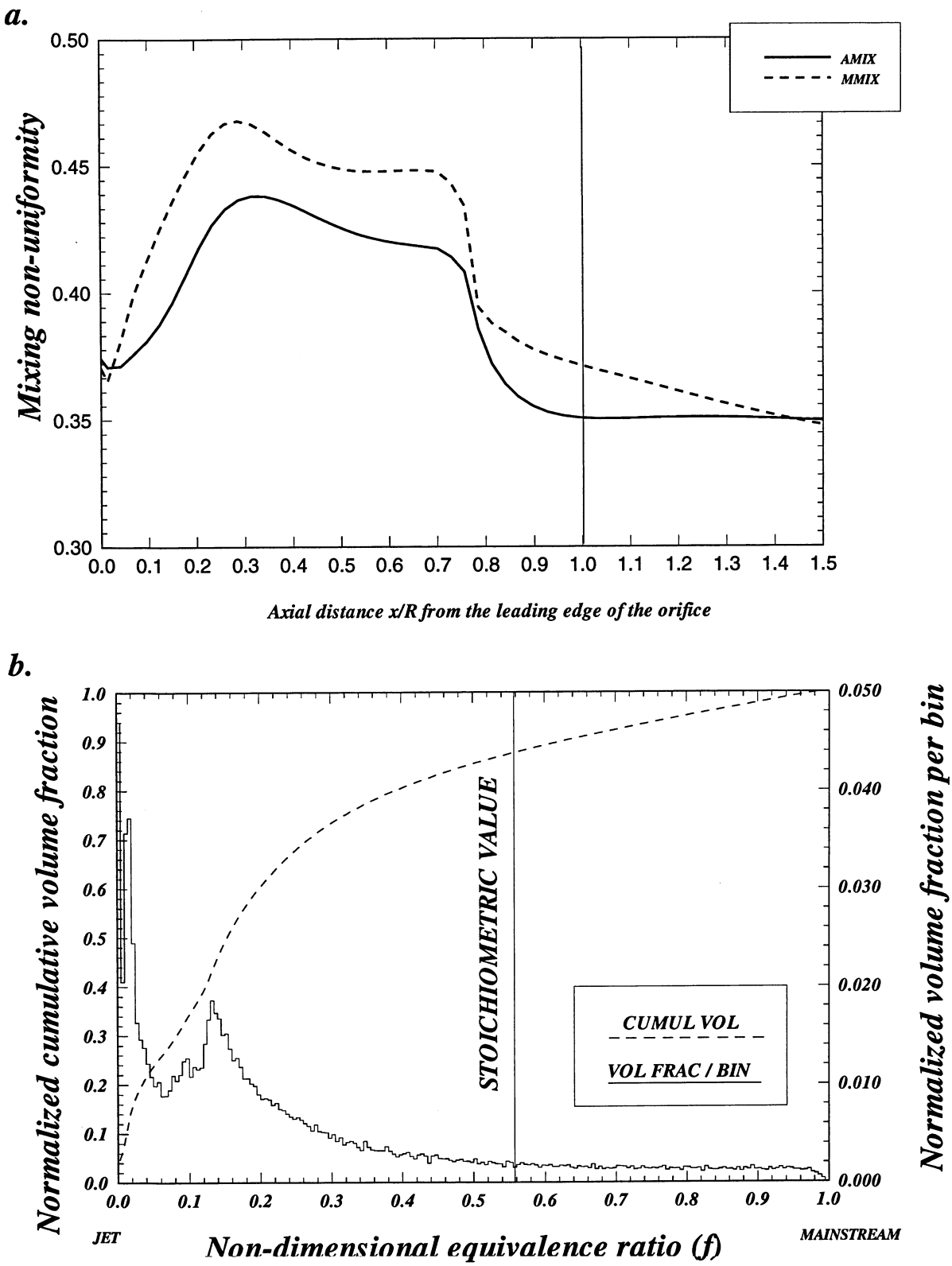

a. Planar deviations (AMIX and MMIX) results

b. mixing non-uniformity volume histograms for 0 < x/R < 1

Figure-B44. Configuration HO-44. Circular mixer, flow aligned slot L/W=4, 6 holes/row

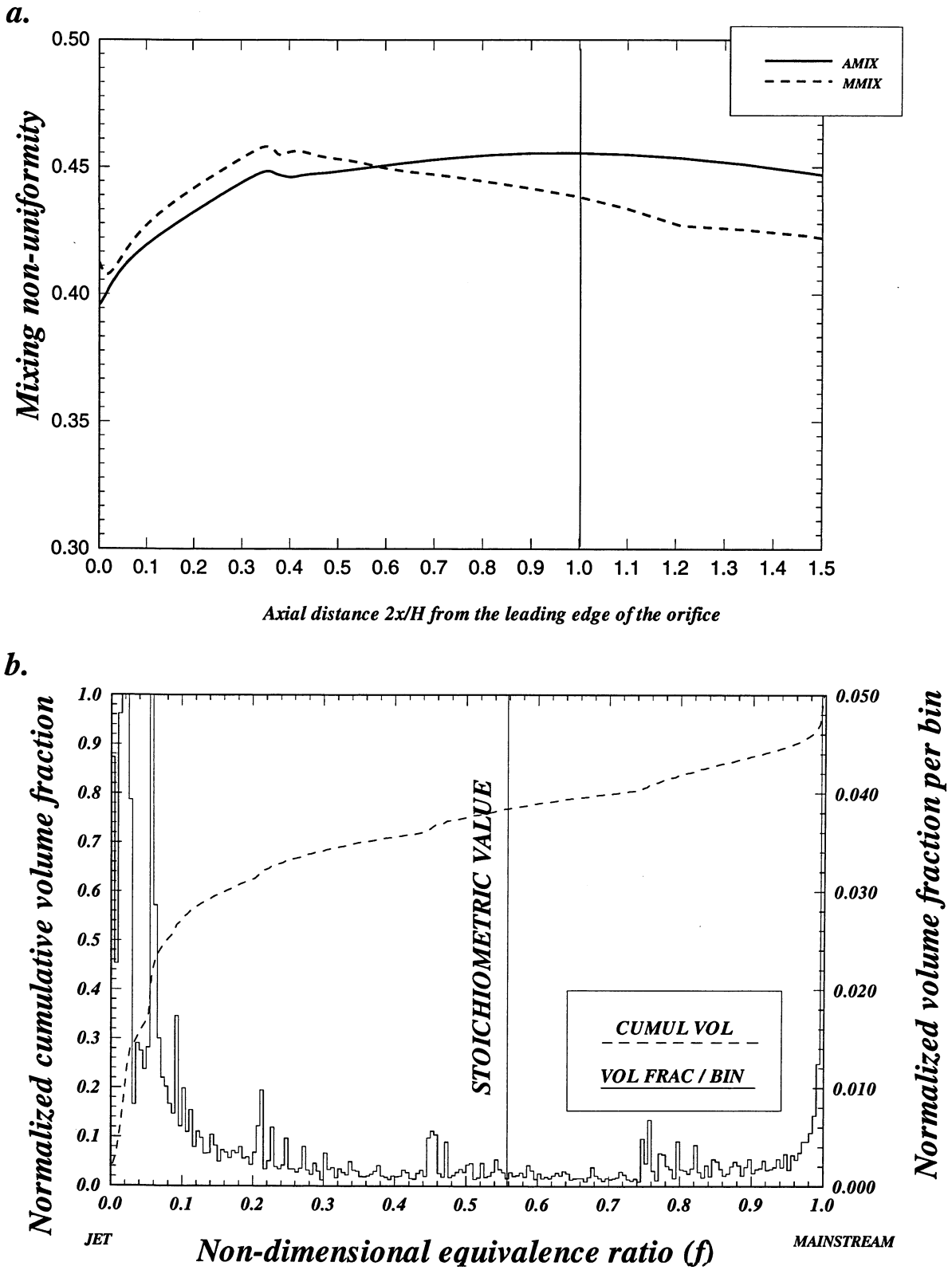

a. Planar deviations (AMIX and MMIX) results

b. mixing non-uniformity volume histograms for 0 < 2x/H < 1

Figure-B45. Configuration HO-45. Annular mixer,flow aligned slot L/W=4, 26 eq holes/row

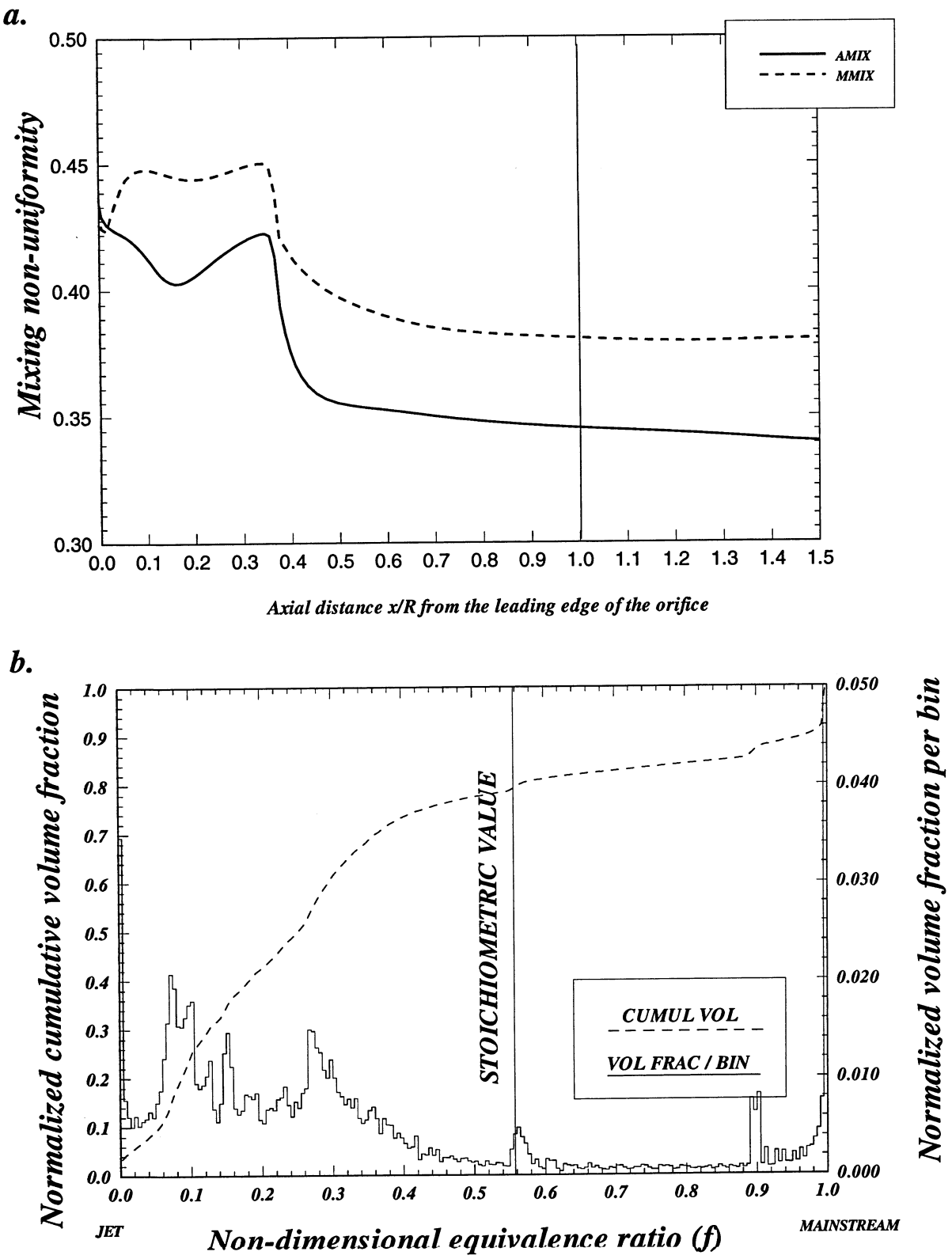

a. Planar deviations (AMIX and MMIX) results

b. mixing non-uniformity volume histograms for 0 < x/R < 1

Figure-B46. Configuration HO-46. Circular mixer, flow aligned slot L/W=4, 26 holes/row

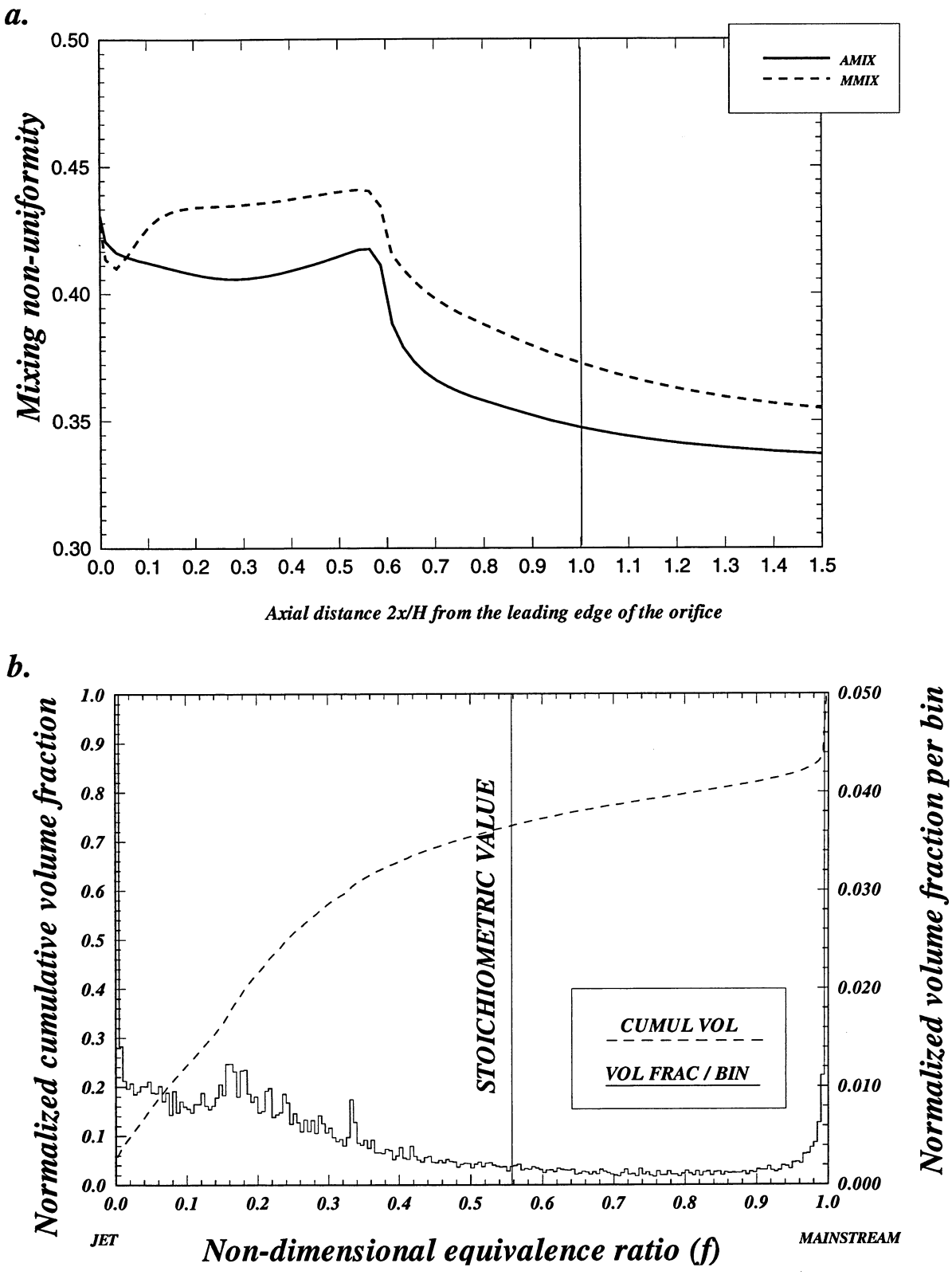

a. Planar deviations (AMIX and MMIX) results

b. mixing non-uniformity volume histograms for 0 < 2x/H < 1

Figure-B47. Configuration HO-47. Annular mixer,flow aligned slot L/W=4, 10 eq holes/row

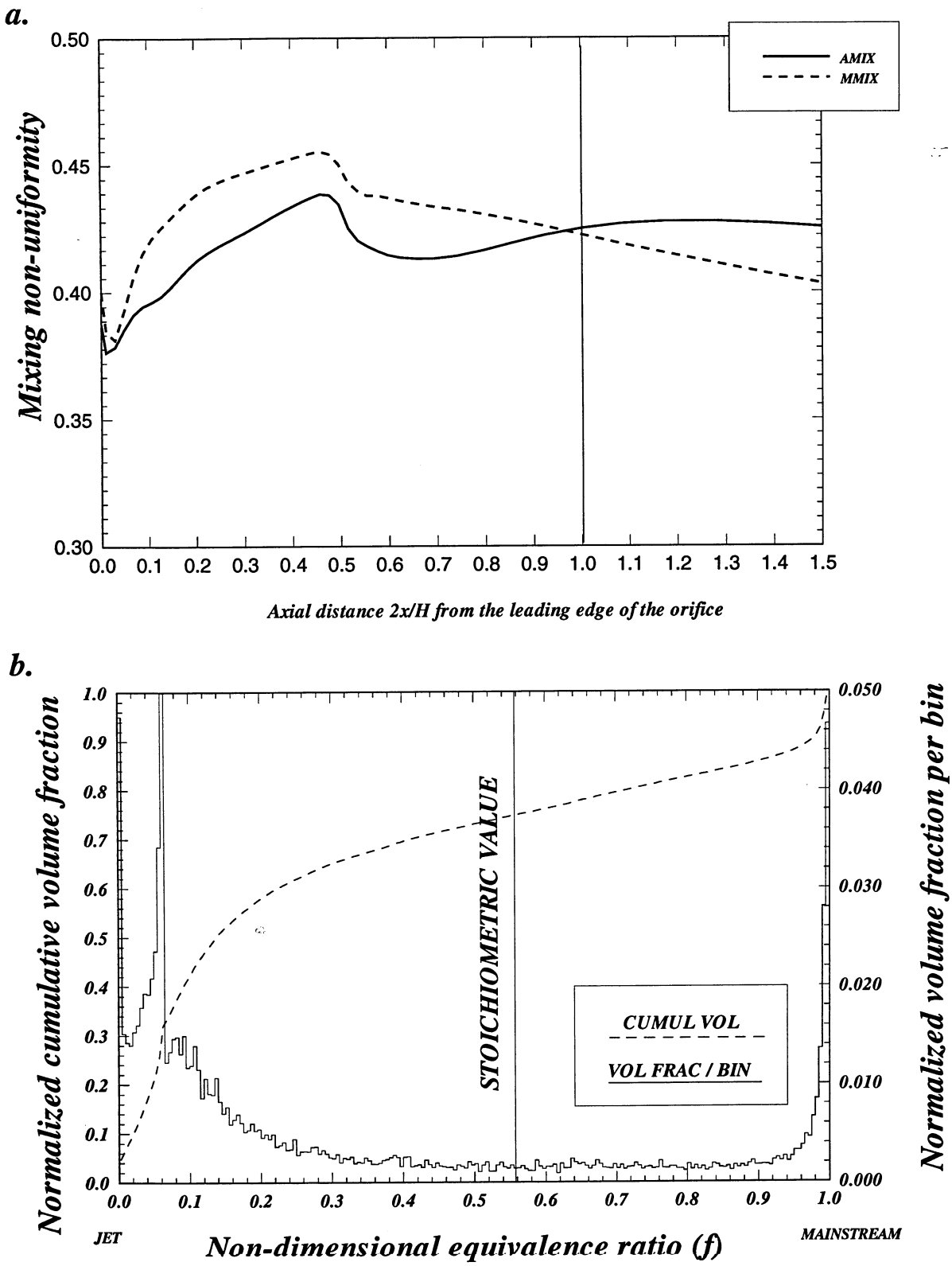

a. Planar deviations (AMIX and MMIX) results

b. mixing non-uniformity volume histograms for 0 < 2x/H < 1

Figure-B48. Configuration HO-48. Annular mixer,flow aligned slot L/W=4, 14 eq holes/row

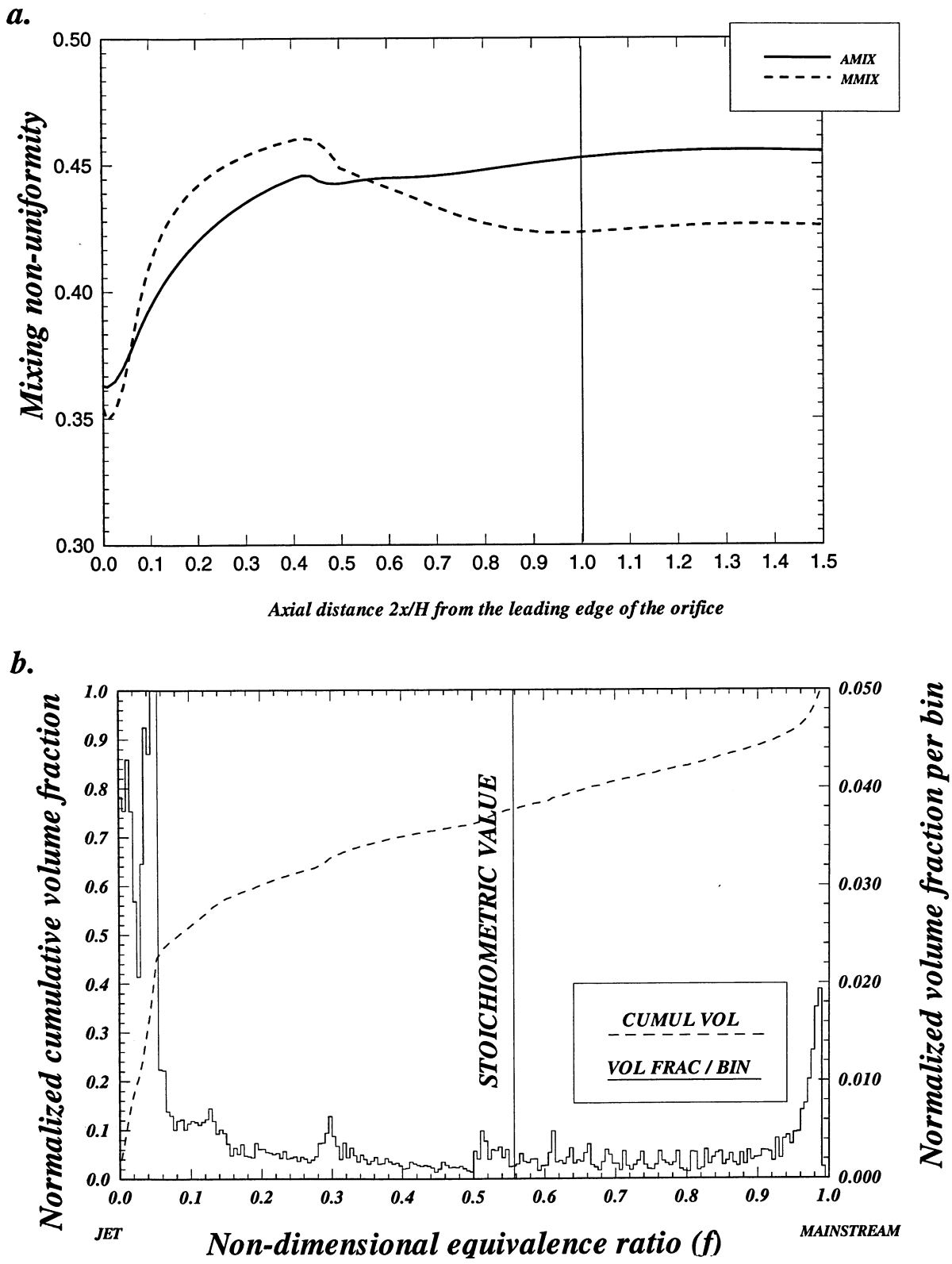

a. Planar deviations (AMIX and MMIX) results

b. mixing non-uniformity volume histograms for 0 < 2x/H < 1

Figure-B49. Configuration HO-49. Annular mixer,flow aligned slot L/W=4, 18 eq holes/row

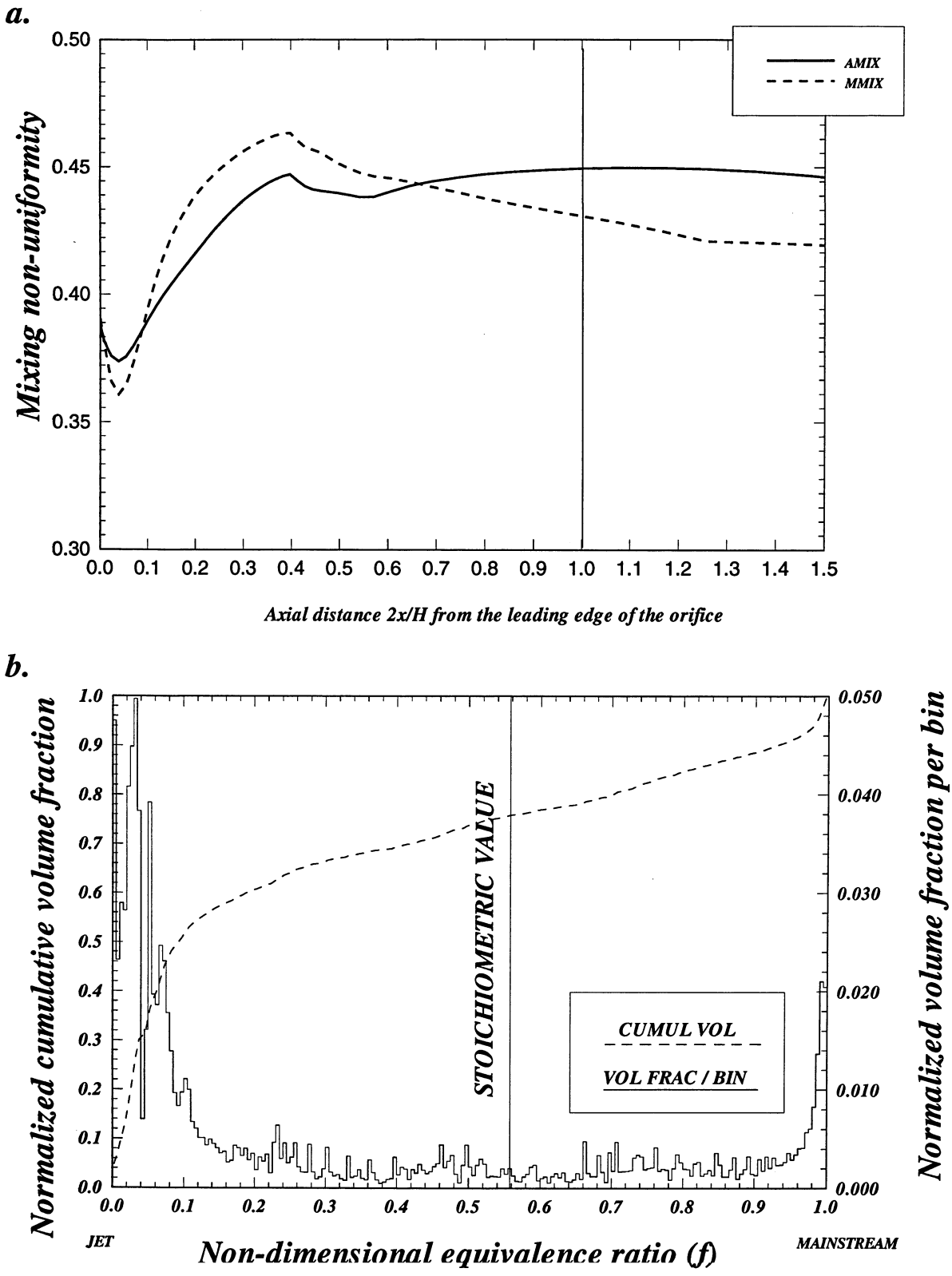

a. Planar deviations (AMIX and MMIX) results

b. mixing non-uniformity volume histograms for 0 < 2x/H < 1

Figure-B50. Configuration HO-50. Annular mixer,flow aligned slot L/W=4, 22 eq holes/row

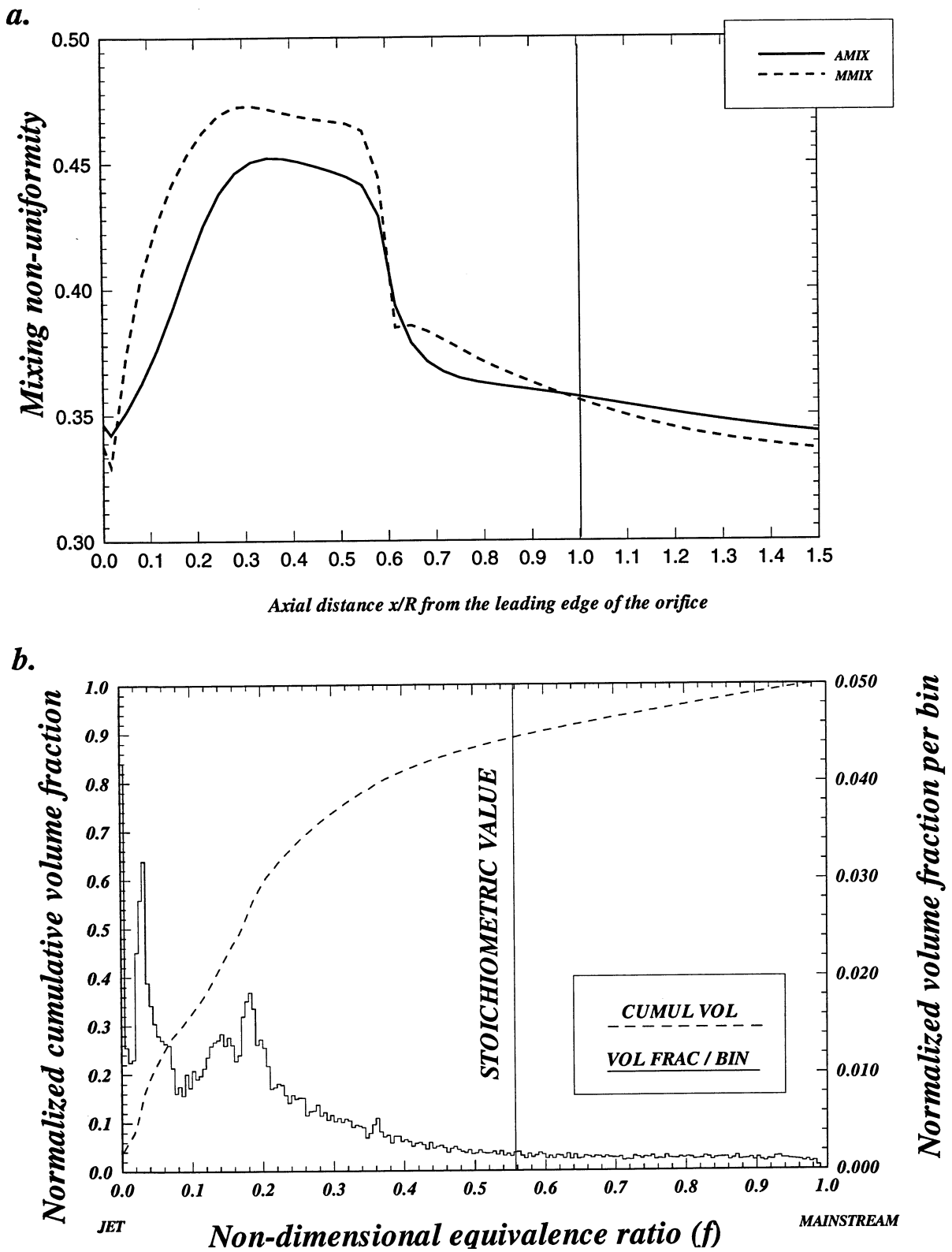

a. Planar deviations (AMIX and MMIX) results

b. mixing non-uniformity volume histograms for 0 < x/R < 1

Figure-B51. Configuration HO-51. Circular mixer, flow aligned slot L/W=4, 10 holes/row

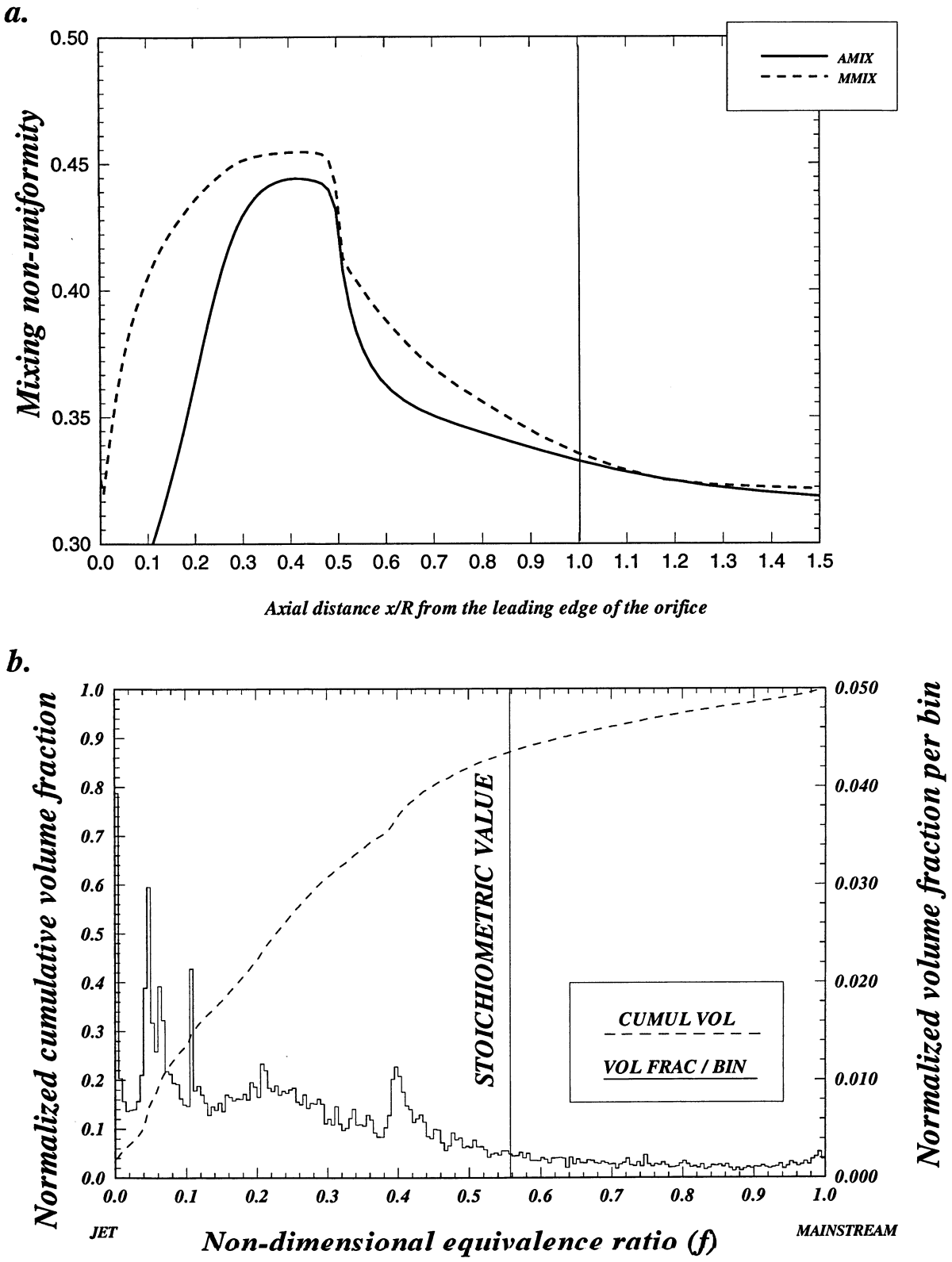

a. Planar deviations (AMIX and MMIX) results

b. mixing non-uniformity volume histograms for 0 < x/R < 1

Figure-B52. Configuration HO-52. Circular mixer, flow aligned slot L/W=4, 14 holes/row

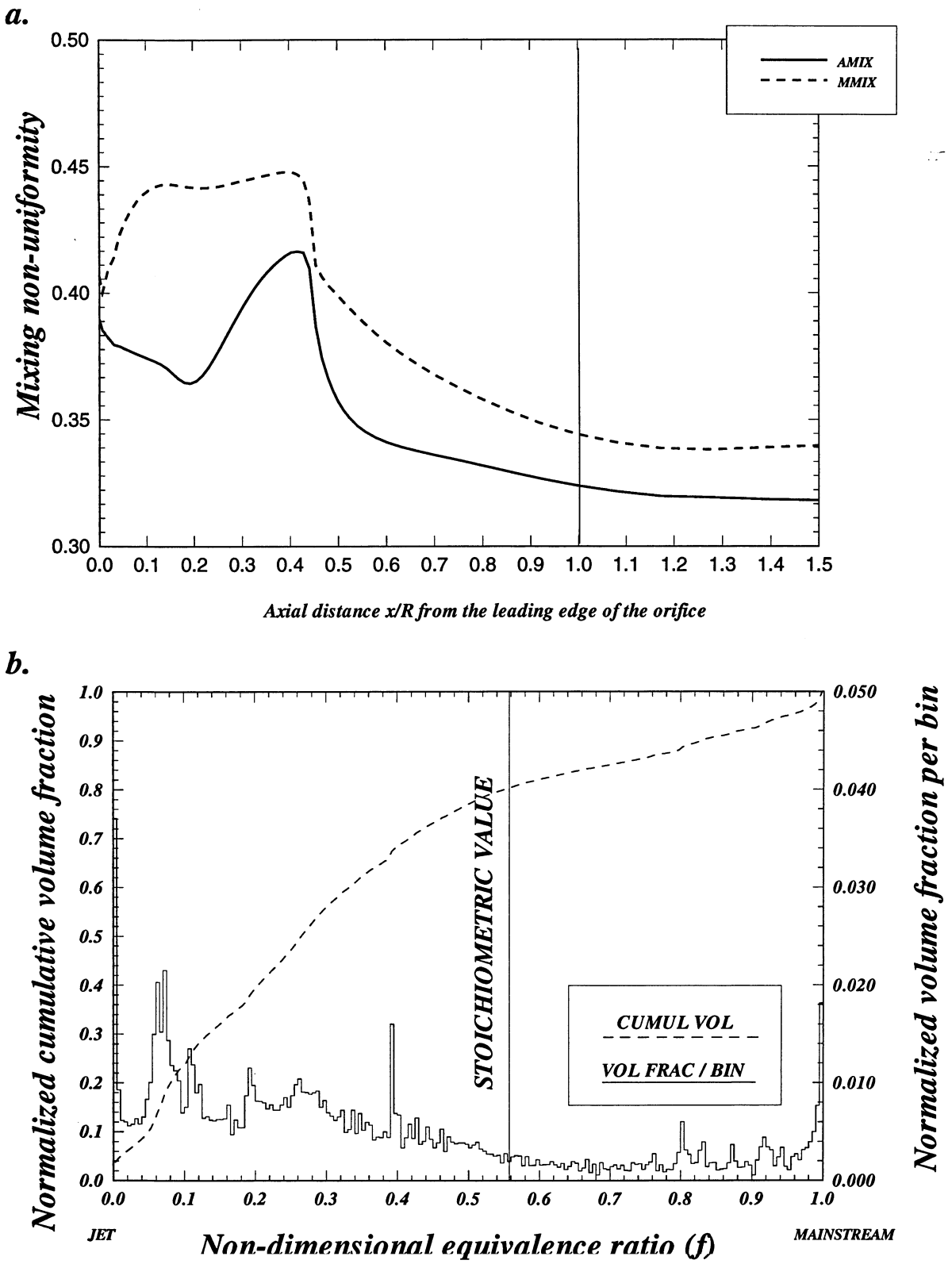

a. Planar deviations (AMIX and MMIX) results

b. mixing non-uniformity volume histograms for 0 < x/R < 1

Figure-B53. Configuration HO-53. Circular mixer, flow aligned slot L/W=4, 18 holes/row

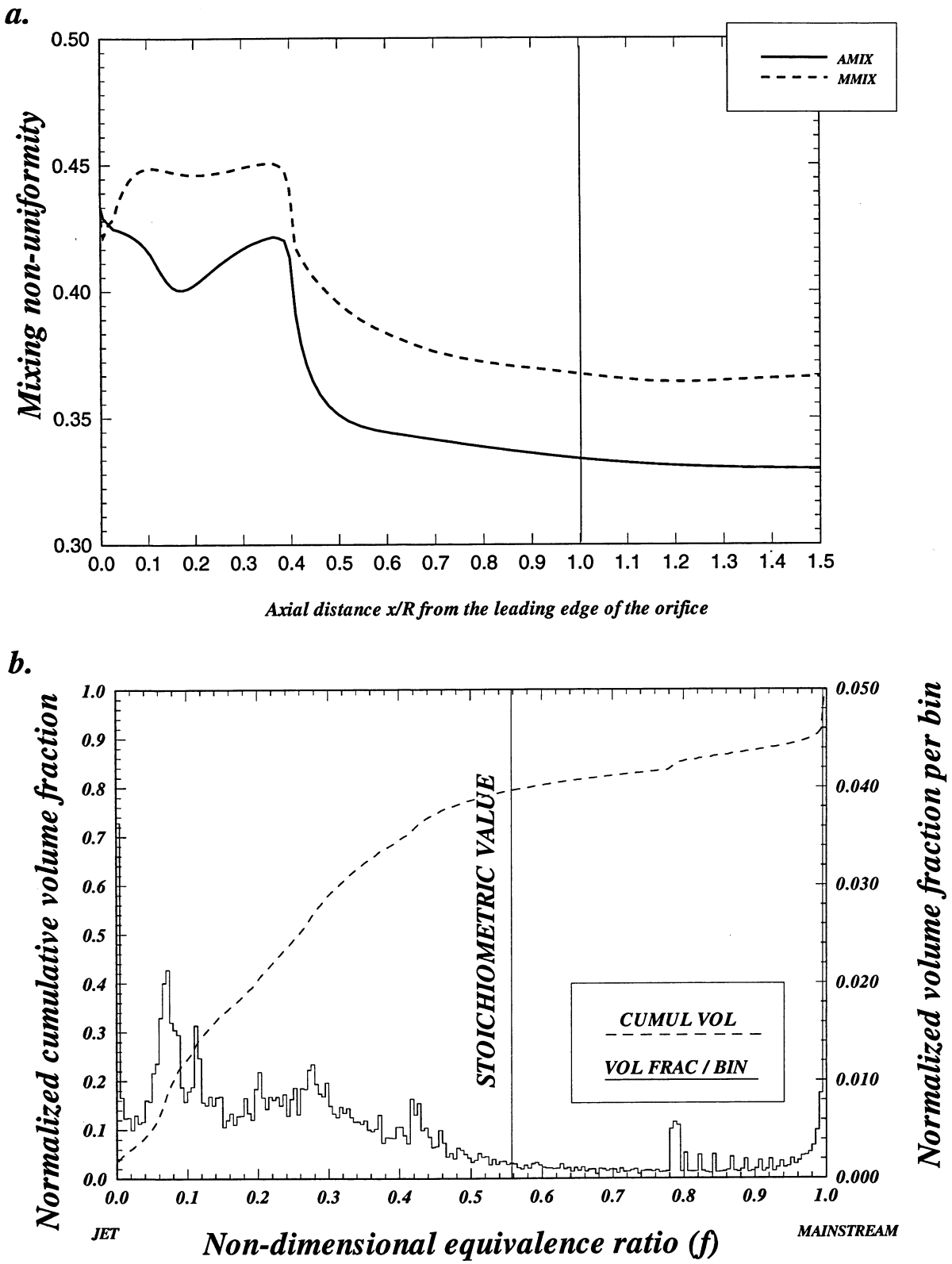

a. Planar deviations (AMIX and MMIX) results

b. mixing non-uniformity volume histograms for 0 < x/R < 1

Figure-B54. Configuration HO-54. Circular mixer, flow aligned slot L/W=4, 22 holes/row

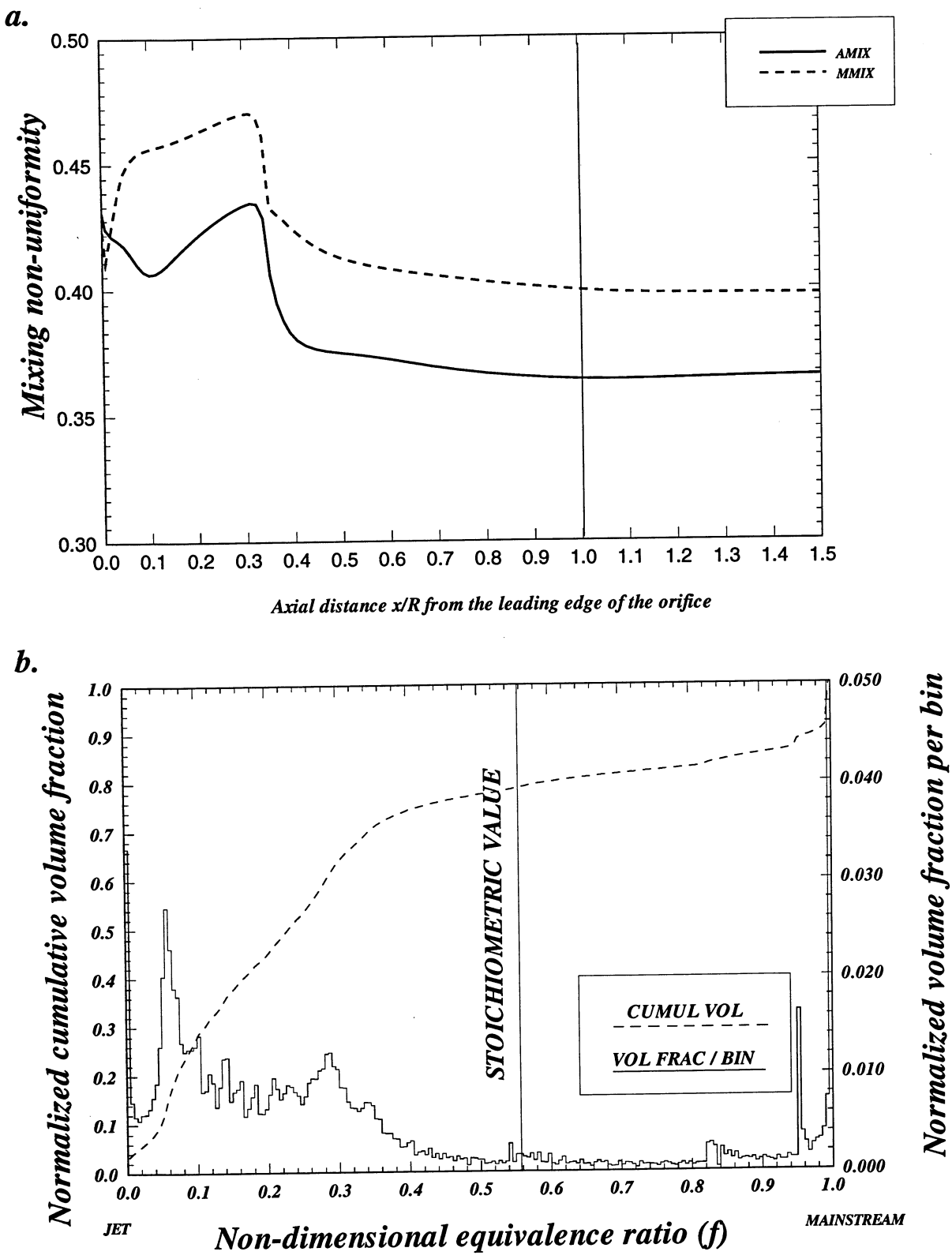

a. Planar deviations (AMIX and MMIX) results

b. mixing non-uniformity volume histograms for 0 < x/R < 1

Figure-B55. Configuration HO-55. Circular mixer, flow aligned slot L/W=4, 30 holes/row

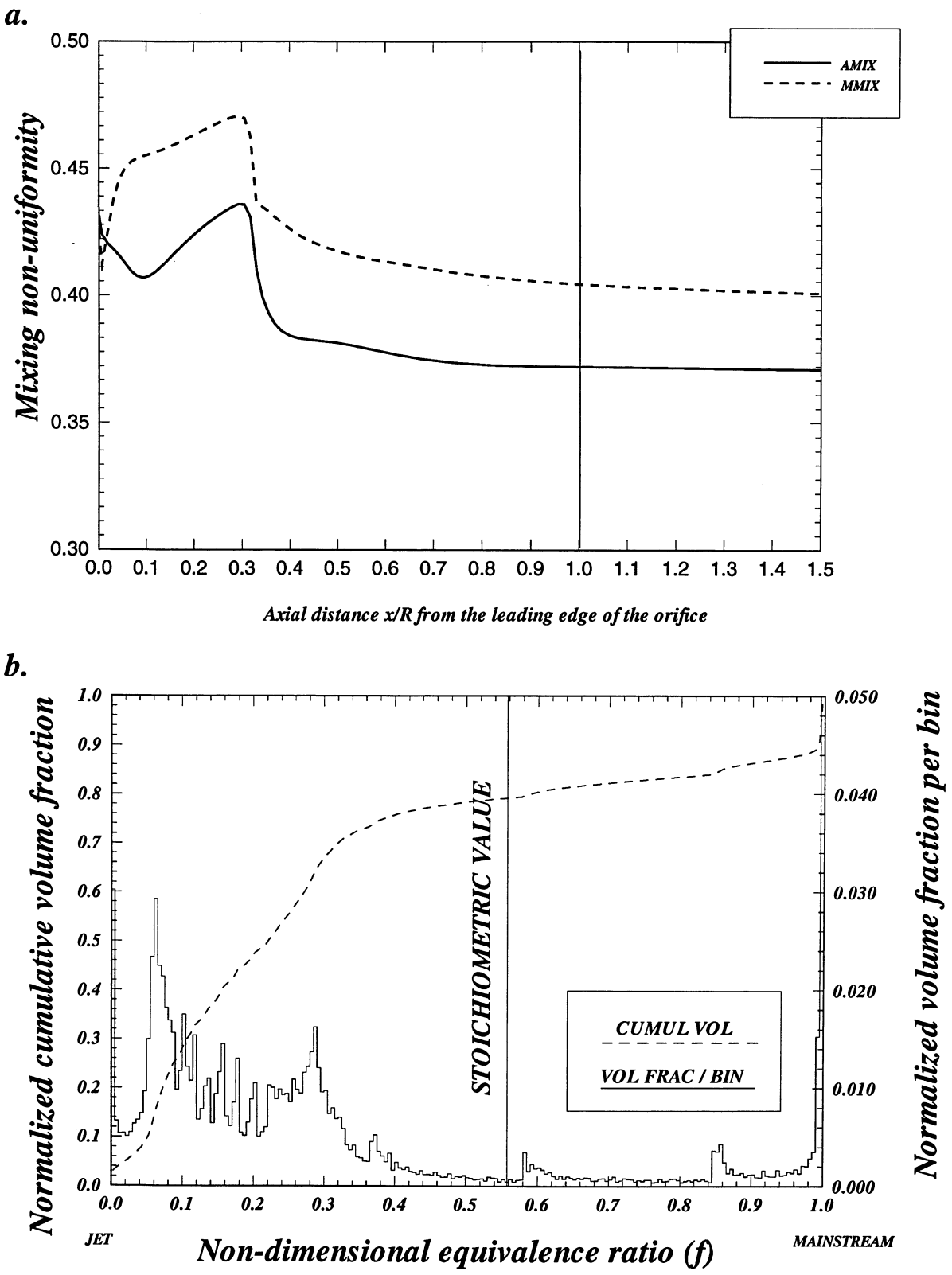

a. Planar deviations (AMIX and MMIX) results

b. mixing non-uniformity volume histograms for 0 < x/R < 1

Figure-B56. Configuration HO-56. Circular mixer, flow aligned slot L/W=4, 34 holes/row

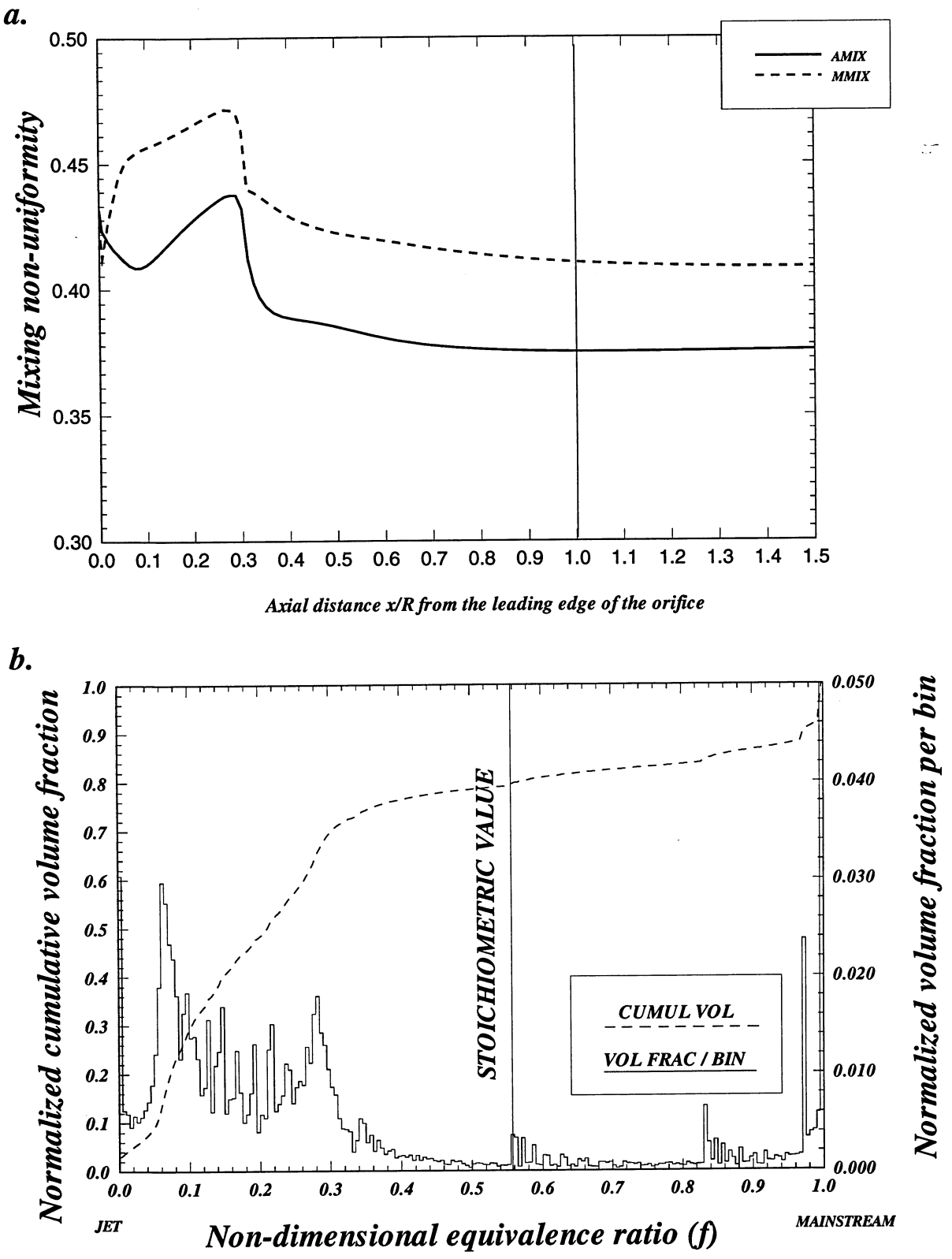

a. Planar deviations (AMIX and MMIX) results

b. mixing non-uniformity volume histograms for 0 < x/R < 1

Figure-B57. Configuration HO-57. Circular mixer, flow aligned slot L/W=4, 38 holes/row

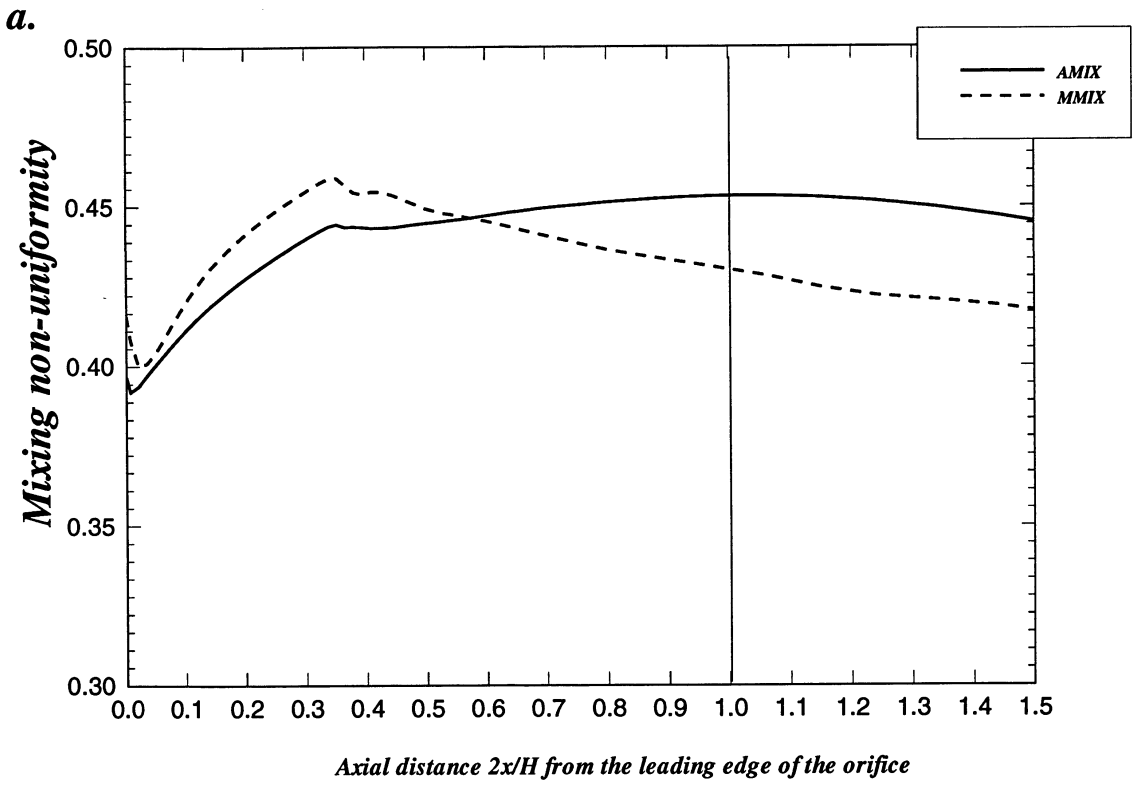

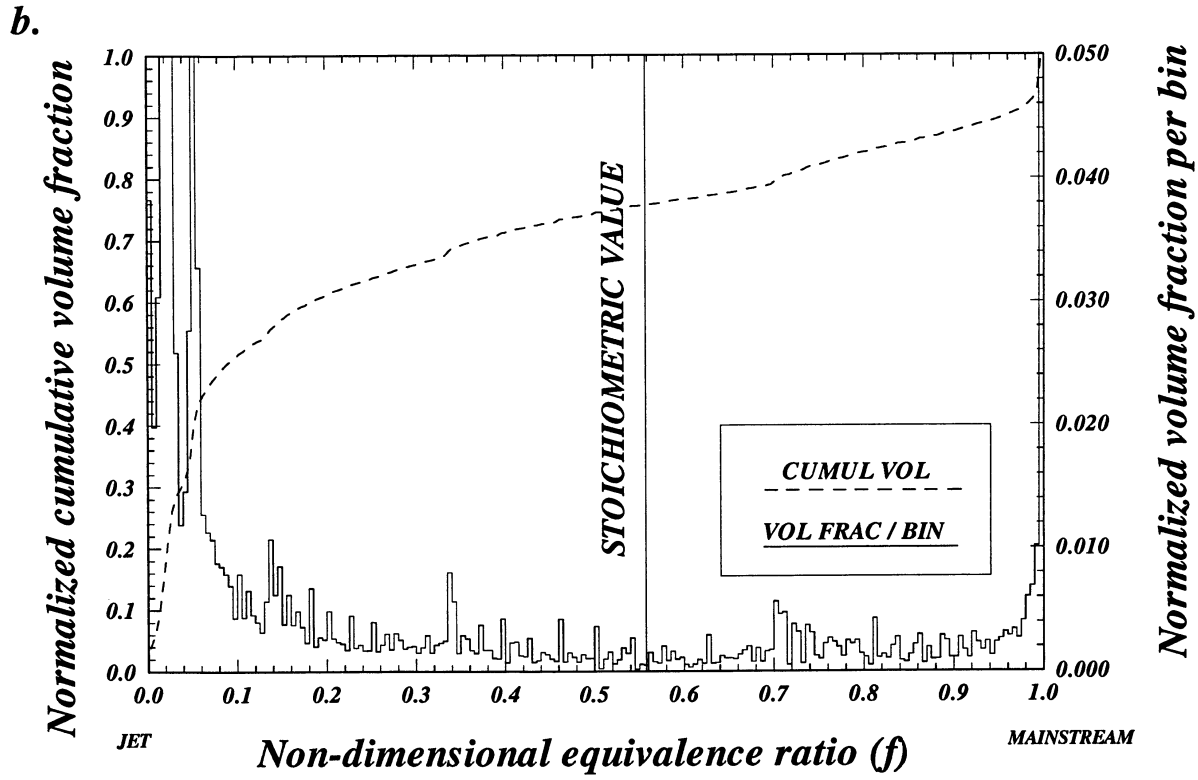

a. Planar deviations (AMIX and MMIX) results

b. mixing non-uniformity volume histograms for 0 < 2x/H < 1

Figure-B58. Configuration HO-58. Annular mixer,flow aligned slot L/W=4, 28 eq holes/row

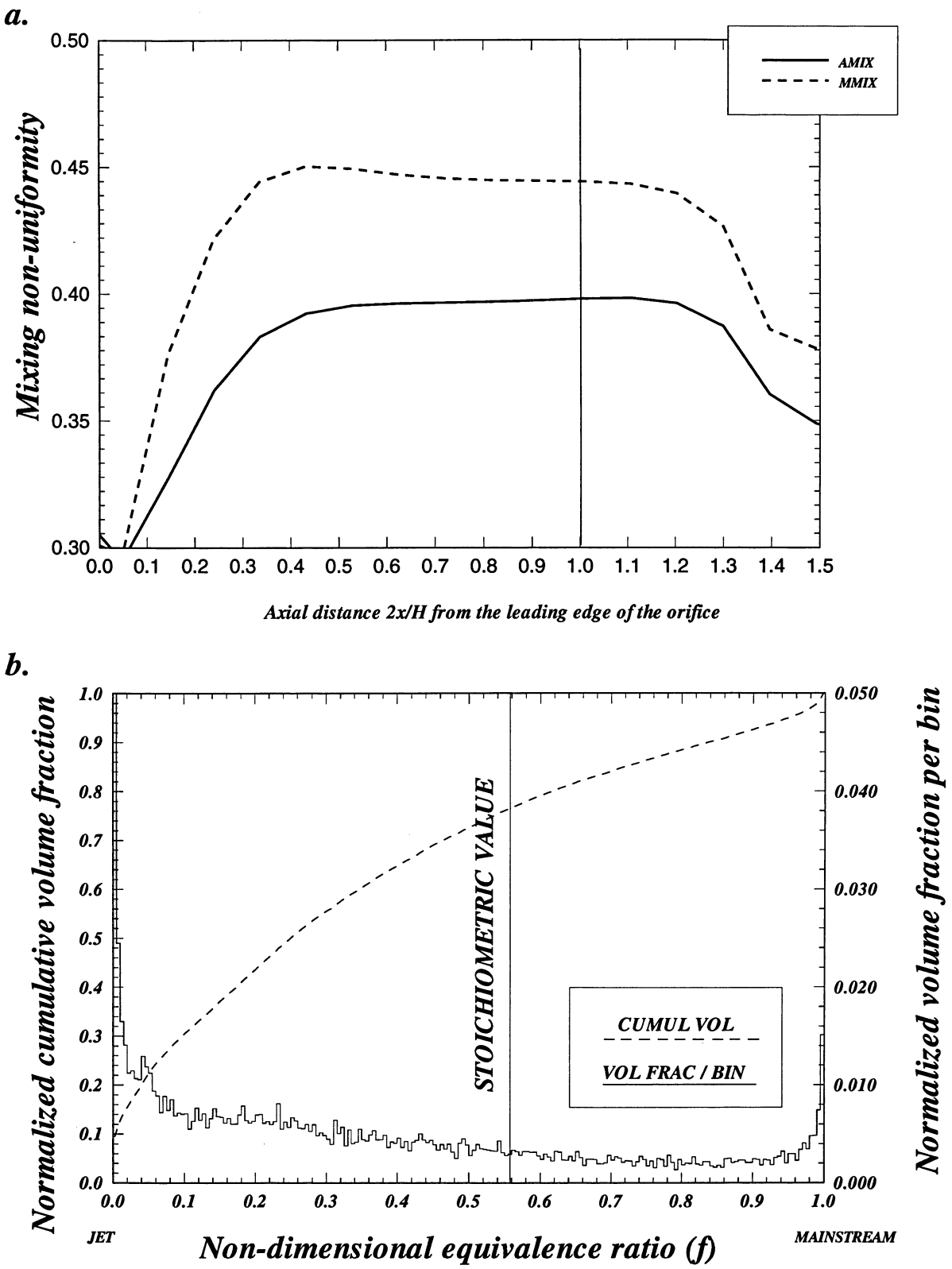

a. Planar deviations (AMIX and MMIX) results

b. mixing non-uniformity volume histograms for 0 < 2x/H < 1

Figure-B59. Configuration HO-59. Annular mixer,flow aligned slot L/W=4, 2 eq holes/row

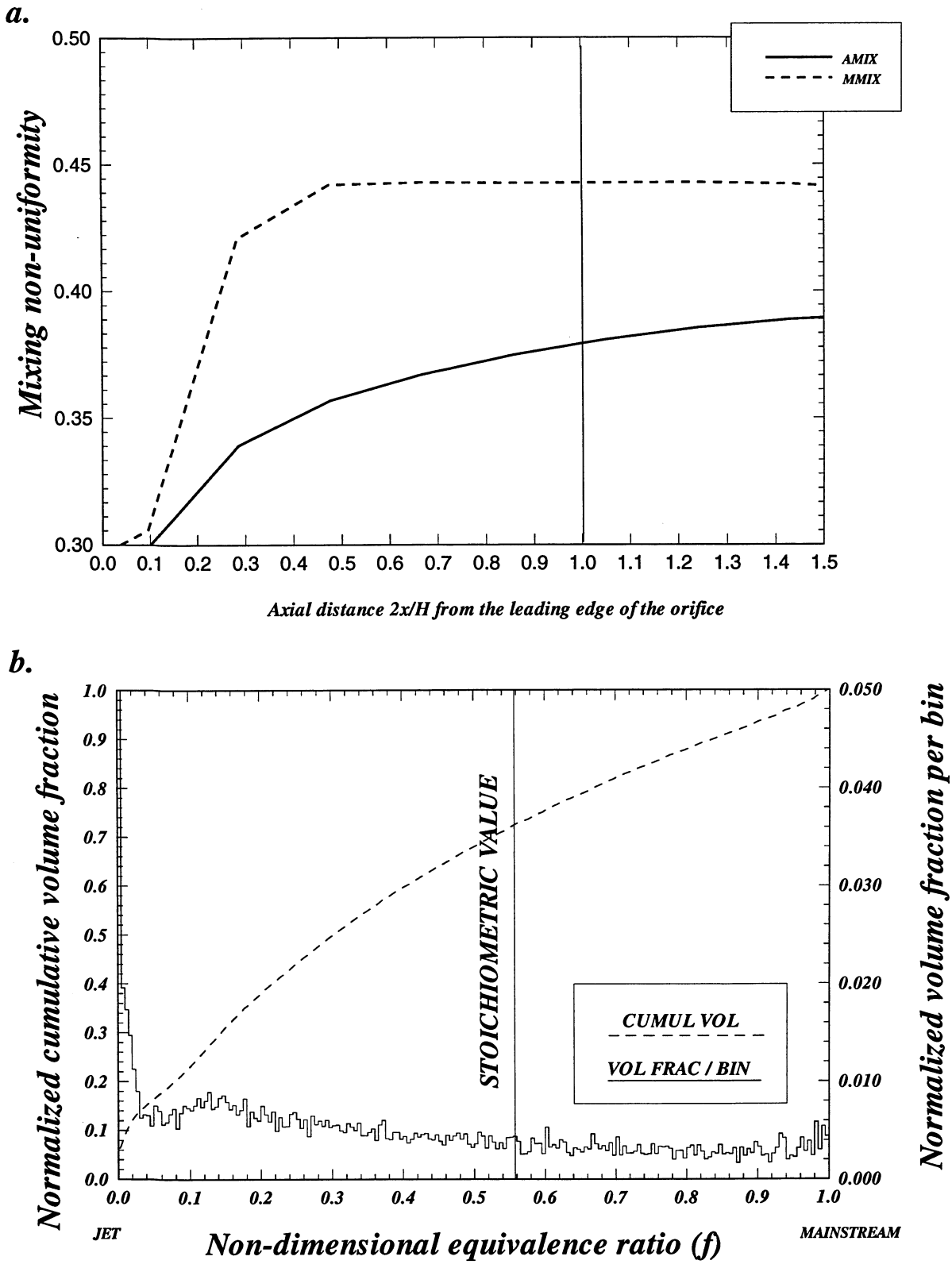

a. Planar deviations (AMIX and MMIX) results

b. mixing non-uniformity volume histograms for 0 < 2x/H < 1

Figure-B60. Configuration HO-60. Annular mixer,flow aligned slot L/W=4, 1 eq holes/row

REPORT DOCUMENTATION PAGE

Form Approved
OMB No. 0704-0188

1. AGENCY USE ONLY (*Leave blank*)	2. REPORT DATE	3. REPORT TYPE AND DATES COVERED
	December 2000	Final Contractor Report

4. TITLE AND SUBTITLE

Mixing and NOx Emission Calculations of Confined Reacting Jet Flows in Cylindrical and Annular Ducts

5. FUNDING NUMBERS

WU–714–01–4A–00
NAS3–25950
Task Order 1

6. AUTHOR(S)

Victor L. Oechsle and Christopher H. Connor

7. PERFORMING ORGANIZATION NAME(S) AND ADDRESS(ES)

Allison Engine Company
Indianapolis, Indiana

8. PERFORMING ORGANIZATION REPORT NUMBER

E–12579

9. SPONSORING/MONITORING AGENCY NAME(S) AND ADDRESS(ES)

National Aeronautics and Space Administration
Washington, DC 20546–0001

10. SPONSORING/MONITORING AGENCY REPORT NUMBER

NASA CR—2000-210672

11. SUPPLEMENTARY NOTES

This work was completed in 1992. Project Manager, James D. Holdeman, Turbomachinery and Propulsion Systems Division, NASA Glenn Research Center, organization code 5830, 216–433–5846.

12a. DISTRIBUTION/AVAILABILITY STATEMENT

Document Availability Change Notice

This document was published in December 2000 with an EAR restriction. It was changed April 2003 to Unclassified/Unlimited per DAA modified February 10, 2003.

Export Administration Regulations (EAR) Notice

This document contains information within the purview of the Export Administration Regulations (EAR), 15 CFR 730–774, and is export controlled. It may not be transferred to foreign nationals in the U.S. or abroad without specific approval of a knowledgeable NASA export control official, and/or unless an export license/license exception is obtained/available from the Bureau of Industry and Security, United States Department of Commerce. Violations of these regulations are punishable by fine, imprisonment, or both.

Unclassified - Unlimited
Subject Category: 07 Distribution: Nonstandard

This publication is available from the NASA Center for AeroSpace Information, 301–621–0390.

12b. DISTRIBUTION CODE

13. ABSTRACT ***(Maximum 200 words)***

Rapid mixing of cold lateral jets with hot cross-stream flows in confined configurations is of practical interest in gas turbine combustors as it strongly affects combustor exit temperature quality, and gaseous emissions in for example rich-lean combustion. It is therefore important to further improve our fundamental understanding of the important processes of diIution jet mixing especially when the injected jet mass flow rate exceeds that of the cross-stream. The results reported in this report describe some of the main flow characteristics which develop in the mixing process in a cylindrical duct. A three-dimensional CFD code has been used to predict the mixing flow field characteristics and NOx emission in a quench section of a RQL combustor. Sixty configurations have been analyzed in both circular and annular geometries in a fully reacting environment simulating the operating condition of an actual RQL gas turbine combustion liner. The evaluation matrix was constructed by varying the number of orifices per row and orifice shape. Other parameters such as J, MR, DR, and mixer sector orifice ACd were maintained constant throughout the entire study. The results indicate that the mixing flow field can be correlated with the NOx production if they are referenced with the stoichiometric equivalence ratio value and not the equilibrium value. The mixing flowfields in both circular and annular mixers are different. The penetration of equal jets in both annular and circular geometries is vastly different which significantly affects the performance of the mixing section. In the computational results with the circular mixer, most of the NOx formation occurred behind the orifice starting at the orifice wake region. General trends have been observed in the NOx production as the number of orifices is changed and this appears to be common for all hole configurations and mixer types (circular or annular). The performance of any orifice shape (in producing minimum NOx) appears to be acceptable if the number of orifices can be freely varied in order to attain the optimum jet penetration.

14. SUBJECT TERMS	15. NUMBER OF PAGES
Gas turbine; Combustors; RQL	180
	16. PRICE CODE
	A09

17. SECURITY CLASSIFICATION OF REPORT	18. SECURITY CLASSIFICATION OF THIS PAGE	19. SECURITY CLASSIFICATION OF ABSTRACT	20. LIMITATION OF ABSTRACT
Unclassified	Unclassified	Unclassified	